**Negative Capacitance for Ultra-low Power Computing**

by

Asif Islam Khan

A dissertation submitted in partial satisfaction of the

requirements for the degree of

Doctor of Philosophy

in

Engineering–Electrical Engineering and Computer Sciences

in the

Graduate Division

of the

University of California, Berkeley

Committee in charge:

Professor Sayeef Salahuddin, Chair
Professor Jeffrey Bokor
Professor Chenming C. Hu
Professor Junqiao Wu

Summer 2015

**Negative Capacitance for Ultra-low Power Computing**

## Abstract

Negative Capacitance for Ultra-low Power Computing

by

Asif Islam Khan

Doctor of Philosophy in Engineering–Electrical Engineering and Computer Sciences

University of California, Berkeley

Professor Sayeef Salahuddin, Chair

Owing to the fundamental physics of the Boltzmann distribution, the ever-increasing power dissipation in nanoscale transistors threatens an end to the almost-four-decade-old cadence of continued performance improvement in complementary metal-oxide-semiconductor (CMOS) technology. It is now agreed that the introduction of new physics into the operation of field-effect transistors–in other words, "reinventing the transistor"– is required to avert such a bottleneck. In this dissertation, we present the experimental demonstration of a novel physical phenomenon, called the negative capacitance effect in ferroelectric oxides, which could dramatically reduce power dissipation in nanoscale transistors. It was theoretically proposed in 2008 that by introducing a ferroelectric negative capacitance material into the gate oxide of a metal-oxide-semiconductor field-effect transistor (MOSFET), the subthreshold slope could be reduced below the fundamental Boltzmann limit of 60 mV/dec, which, in turn, could arbitrarily lower the power supply voltage and the power dissipation. The research presented in this dissertation establishes the theoretical concept of ferroelectric negative capacitance as an experimentally verified fact.

The main results presented in this dissertation are threefold. To start, we present the first direct measurement of negative capacitance in isolated, single crystalline, epitaxially grown thin film capacitors of ferroelectric $Pb(Zr_{0.2}Ti_{0.8})O_3$. By constructing a simple resistor-ferroelectric capacitor series circuit, we show that, during ferroelectric switching, the ferroelectric voltage decreases, while the stored charge in it increases, which directly shows a negative slope in the charge-voltage characteristics of a ferroelectric capacitor. Such a situation is completely opposite to what would be observed in a regular resistor-positive capacitor series circuit. This measurement could serve as a canonical test for negative capacitance in any novel material system. Secondly, in epitaxially grown ferroelectric $Pb(Zr_{0.2}Ti_{0.8})O_3$-dielectric $SrTiO_3$ heterostructure capacitors, we show that negative capacitance effect from the ferroelectric $Pb(Zr_{0.2}Ti_{0.8})O_3$ layer could result in an enhancement of the capacitance of bilayer heterostructure over that of the constituent dielectric $SrTiO_3$ layer. This observation apparently violates the fundamental law of circuit theory which states that the

equivalent capacitance of two capacitors connected in series is smaller than that of each of the constituent capacitors. Finally, we present a design framework for negative capacitance field-effect-transistors and project performance for such devices.

To
Jagadish Chandra Bose (1858-1937), the radio pioneer working in British India during the late 1800s and early 1900s.

# Contents

# List of Figures

# List of Tables

# Acknowledgments

I would like to thank my research advisor, Professor Sayeef Salahuddin, for guidance and mentorship throughout the years, for challenging me and providing me with an exciting research environment. I am immensely indebted to my co-advisors, Professors Ramamoorthy Ramesh and Chenming C. Hu. I would also like to thank Professors Jeffrey Bokor, Chenming C. Hu and Junqiao Wu for gladly accepting to be on my qualifying exam and dissertation committees, and for providing guidance and suggestions. Sincere thanks to Professors Tsu-Jae King Liu, Ali Javey and Eli Yablonovitch and Dr. Josephine Yuen for providing invaluable suggestions and comments during my time as a graduate student at Berkeley.

The research presented in this dissertation would not have been possible without the support from the funding agencies: the Office of Naval Research, FCRP Center for Materials, Structures and Devices, the Center for Low Energy Systems Technology (LEAST), one of the six SRC STARnet Centers, sponsored by MARCO and DARPA and the NSF Center for Energy Efficient Electronics Science ($E^3S$). I thank the agencies for the support. I am also very thankful to Qualcomm Incorporated for awarding me the Qualcomm Innovation Fellowship during 2012-13. I also thank Taiwan Semiconductor Manufacturing Company Limited for awarding me the silver award at the 5th TSMC Outstanding Student Research Competition in 2011.

I am grateful to Intel Corporations for the internship opportunity during the summer of 2013. I would like to thank Dr. Tahir Ghani, Dr. Dimitri Nikonov, Dr. Ian Young and Dr. Sasikanth Manipatruni for mentoring me and providing a glimpse of industrial research, in addition to hosting me in Portland, OR.

I have had the good fortune of interacting with some very bright and talented colleagues at Berkeley, and of learning a great deal from them. In particular, I would like to express my sincere thanks to Korok Chatterjee, Claudy Serrao, Chun Wing Yeung, Zhongyuan Lu, Debanjan Bhowmik, Jayakanth Ravichandran, Samuel Smith, Mohammad Ahosanul Karim, Dominic Labanowski, Varun Mishra, Kartik Ganapathi, Rehan Kapadia, Sapan Agarwal, Pu Yu, Cheng-I Lin, Saidur Bakaul, James Clarkson, Jinxing Zhang, Tania Roy, Mahmut Tosun, Muktadir Rahman, Suman Hossain, Justin Wong, Long You, and many more for collaborations and conversations at workplace. Through REU programs and $E^3S$ and COINS centers, I have had the good fortune to mentor a group of talented undergraduate students: Michelle J. Lee, Brian Wang, Sajid Nasir, Ibrahim Fattouh and Eric Lam from Berkeley, Shane Christopher from CUNY, Steven G. Drapcho from MIT, Marc Molina from UC Riverside, Stephen Meckler from PennState, Joaquin Resasco from U. Oklahoma, Hector Romo from UC Santa Cruz. I thank them all for the joy and the experience I received from mentoring them. Shirley Salanio, associate director for graduate matters and EE graduate advisor, and Charlotte Jones, administrative specialist at Berkeley, have always been there

to help me on numerous occasions, for which I am greatly indebted to them.

And last but not the least, words fail me in conveying indebtedness to my wife–Nadia Nusrat– whose love, affection, encouragement, and persistence had played the most important role towards my strides during Ph.D. I acknowledge the unconditional love and support from my parents: Shahidul Islam Khan and Anisa Ahmad, my sister: Fahrin Islam, my uncle: Rais Ahmad, my aunt: Farhana Ahmad and my cousin: Rumaisa Ahmad.

# Chapter 1

# ULTRA-LOW POWER COMPTUING: THE NEGATIVE CAPACITANCE APPROACH

## 1.1 Electronics at the Crossroads: The CMOS Power Dissipation Bottleneck

This era is defined by the Internet, the social media and mobile electronics. Close to 2.5 billion people–a number that has grown 566% since 2000–are online around the globe and nearly 70% of them use the Internet every day [1]. Every 60 seconds, 204 million emails are exchanged, 5 million searches are made on Google, 1.8 million "Like"s are generated on Facebook, 350 thousand tweets are made on Twitter, $272,000 of merchandise is sold on Amazon and 15 thousand tracks are downloaded in iTunes [1]. The vast traffic of these activities is managed by the massive data centers and cloud computing infrastructures. And the widespread proliferation of personal computing devices: smart phones, tablets, general purpose workstations, gaming stations etc. in the consumer end results in the symbiotic information ecosystem. Computing is more personal than ever playing a significant role in the economic, social, physical and intellectual pursuits of a human being. On average, the number of electronic devices a person in the US interacts per day is of $\sim$10 [2]. This number is going to increase to thousands with the upcoming paradigm of the "Internet of Things," where intelligence in the form of tiny stand-alone devices and sensors numbering in trillions will be seamlessly integrated into our environment. Within this paradigm, the number of data generating devices connected to the internet is expected to grow exponentially to 20 billion by 2020 [3]. A simplified view of the information ecosystem is shown in figure 1.1. "How much information is there stored by the mankind and what is the digital computation capability of our civilization?"-the answer to such questions yielded staggering estimations such as $2.9 \times 10^{20}$ optimally compressed bits and $6.4 \times 10^{18}$ instructions per second respectively for the year 2007 [4]. Between 1986 and 2007, the world's technological capacity to

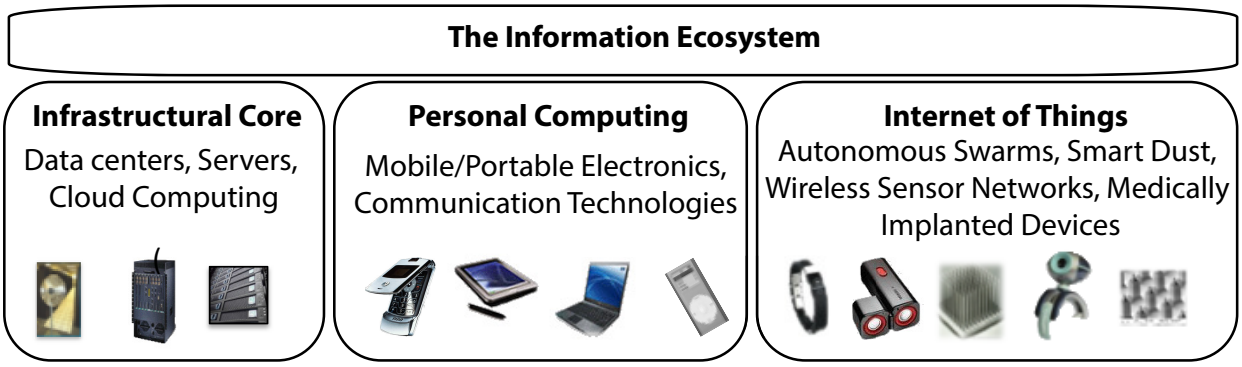


Figure 1.1: A bird's eye view of the information ecosystem.

compute information (instructions per second) has experienced 58% growth per year [4]. The storage of information in vast technological memories has experienced a growth rate of 23% per year [4]. These rates have increased even more since 2007. In summary, the prolieration of information paradigm has followed the path of accelerating returns.

However, power dissipation and management issues at the hardware level threatens the cadence of the information revolutions in the future years. The 12 million servers in 3 million data centers that drive all the online activities in the US consume 76 TW-hr of energy per year (figure 1.2(a))[1]. The total electric energy consumption of the US in 2011 was 4113 TW-hr [5]; data centers constitute ∼2% of the US electricity consumption. Now, if the current exponential growth pattern of information paradigms continues in the future, the power consumption will reach an unmanageable level in near future[6]. Along with the data center, the overall energy usage of the information infrastructure could reach one-third of total US energy consumption by the year 2025 [7, 8]. The carbon footprint of all the data centers worldwide is already equivalent to that of a mid-sized country such as Malaysia or Netherlands (figure 1.3) [6].

The relentless down-scaling of complementary metal-oxide-semiconductor (CMOS) transistor over past four decades has been the core driver for the information revolution. And the power dissipation crisis also originates at the transistor level. The transistor density has approximately doubled every 18 months in accordance with the Moore's law [11]. Figure 1.3(a) shows the evolution of CMOS half-pitch over last 20 years. However, also plotted in figure 1.3(a) is the evolution of power supply voltage. Although the physical dimensions has been scaled down exponentially, the power supply voltage has been stuck at around 1 V for almost 15 years. The microprocessor power density is proportional to the density, operating frequency and the square of the power supply voltage. The increase of microprocessor operating frequency resulted in the power density reach 100 W/cm$^2$ level, which is an order of magnitude higher than a typical hot plate. Increase of the power density beyond that level is

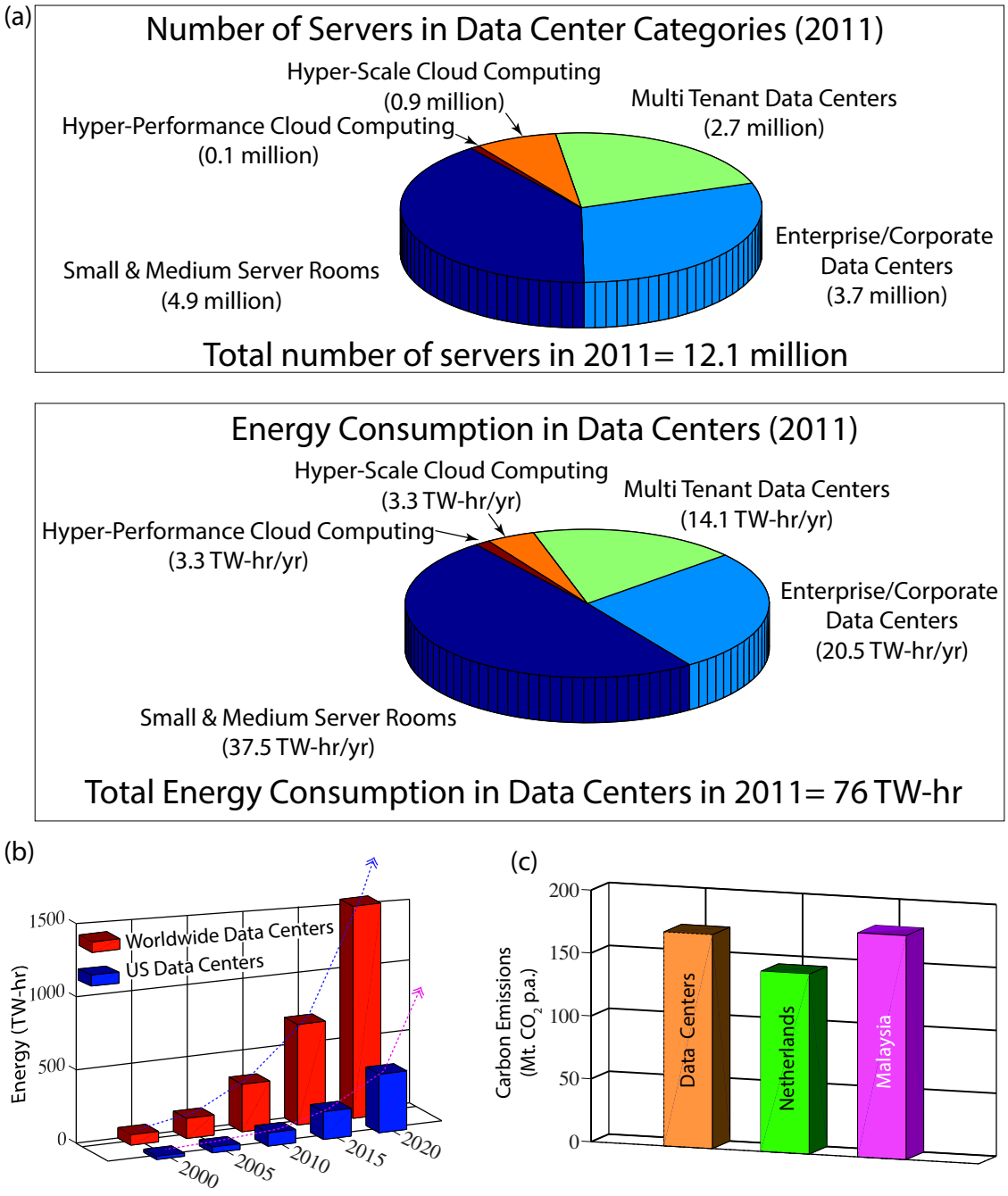


Figure 1.2: (a) The projected energy consumption of data centers. Adapted from reference [1]. (b) Carbon footprint of data centers. Adapted from reference [6].

unmanageable; as a result, the clock frequency stopped increasing beyond 3 GHz after 2005 [10].

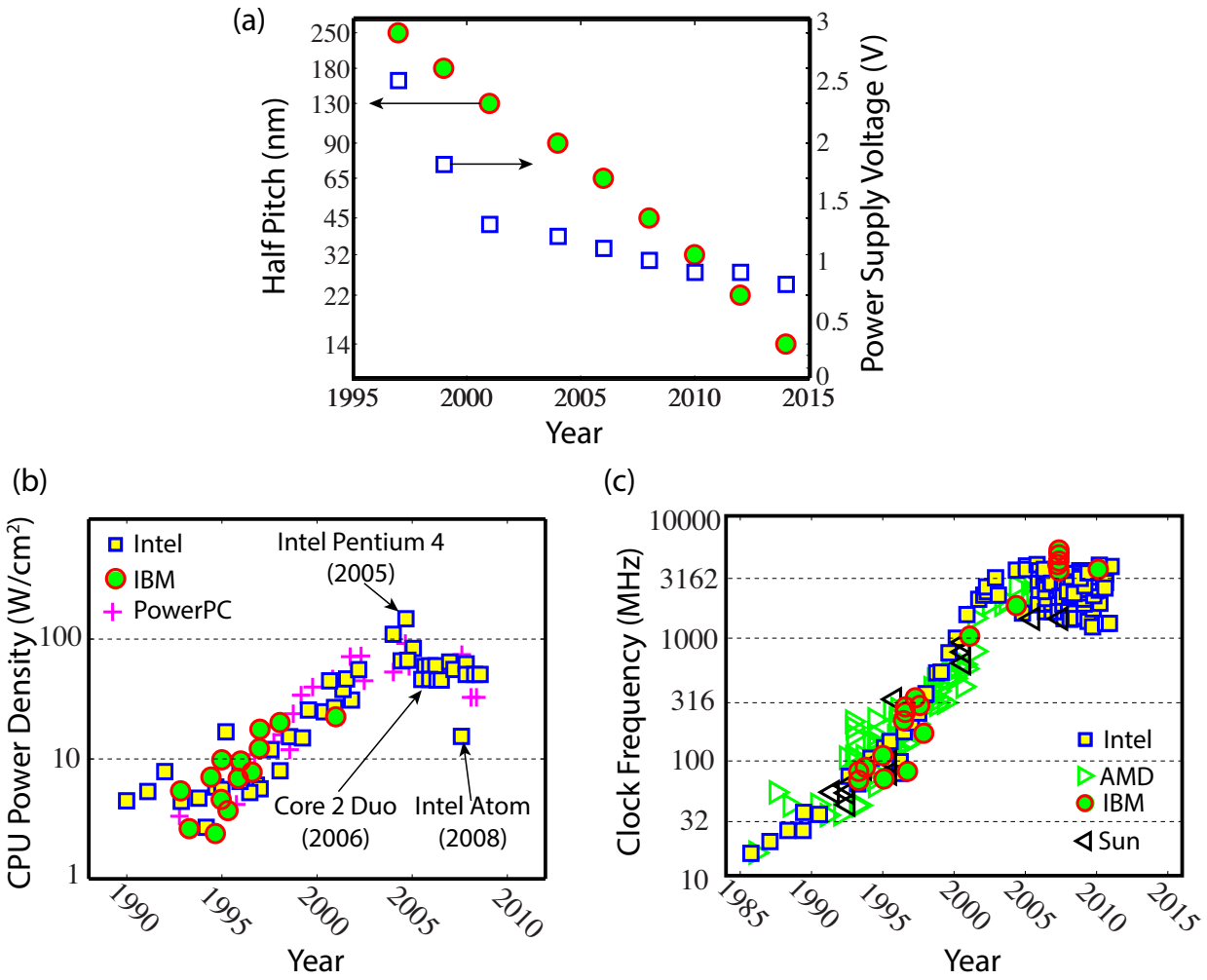


Figure 1.3: (a) The evolution of CMOS half-pitch over the last two decades [9]. (b,c) The evolution of CMOS power density (b) and microprocessor clock frequency (c) over the last two decades. Adapted from reference [10].

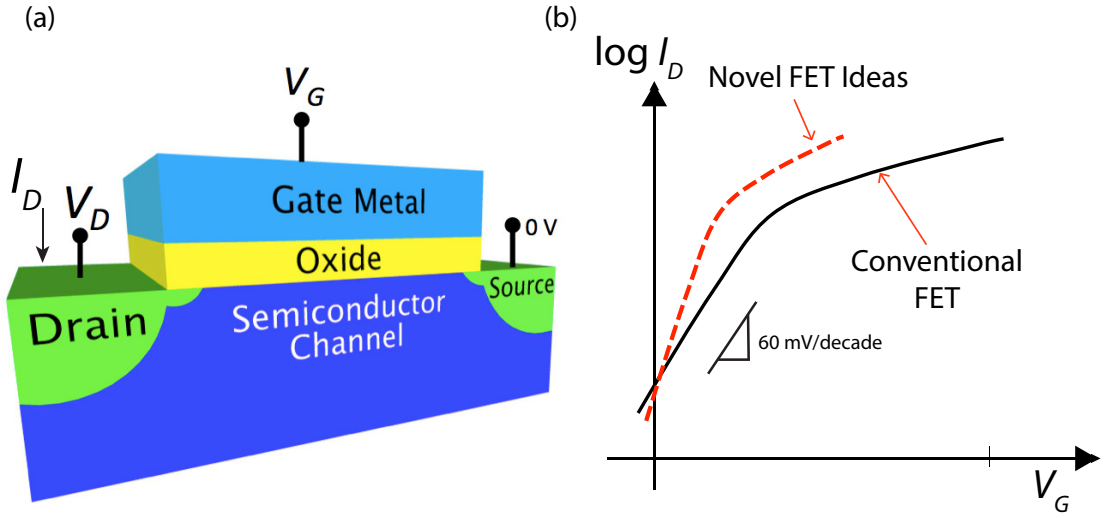


Figure 1.4: (a) Schematic diagram of a metal-oxide-semiconductor field-effect-transistor (MOSFET). (b) The output characteristics of a MOSFET. We are in search of a low-power device with less than 60 mV/decade of subthreshold swing.

The reason why the power supply voltage in microprocessors has not scaled at par with the transistor dimensions originates from the fundamental physics of transistor operation. The Boltzmann distribution dictates that, to increase the drain current $I_D$ by an order magnitude at room temperature, the gate voltage $V_G$ needs to be increased by at least $k_BTlog10$=60 mV, $k_B$ and $T$ being the Boltzmann constant and the temperature, respectively. Hence the lower limit of the sub-threshold slope $S$, defined as $\partial V_G/\partial log_{10}I_D$ is 60 mV/decade. To maintain a good on-off ratio of the current, ∼1 V needs to be applied at the gate. This limitation has been termed as the "Boltzmann Tyranny" and this is a fundamental physical bottleneck. However much engineering is put into a transistor design, the sub threshold slope cannot be lowered below this limit. It is now generally agreed that, without introducing new physics into the physics of transistor operation, this limitation cannot be overcome. As a result, there has been an industry-wide call for "reinventing the transistor" [12, 13, 14, 15]

To overcome this problem in the conventional transistors, a number of alternative approaches are currently being investigated. Examples include band-to-band tunneling field effect transistors (TFET) [16, 17], impact ionization metal oxide semiconductor transistors (IMOS)[18] and also nano-electro mechanical (NEM) switches[19, 20]. In these approaches the mechanism of transport, i.e., the way electrons flow in a transistor, is altered such that the minimum limit of $2.3k_BT/q$ can be avoided. In contrast, it was theoretically shown [21] that it may be possible to keep the mechanism of transport intact, but change the electrostatic gating in such a way that it steps up the surface potential of the transistor beyond what

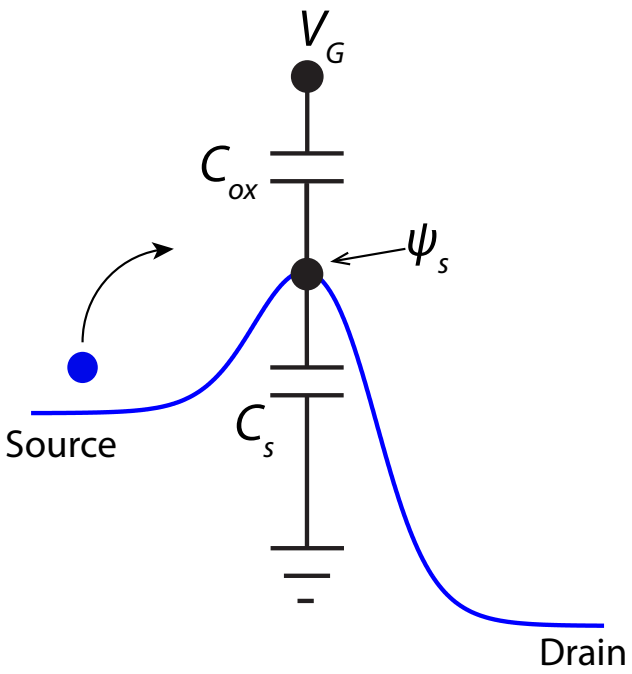


Figure 1.5: Potential profile in a nanoscale transistor. The capacitor network shows how the applied gate voltage is divided between the oxide insulator and the semiconductor.

is possible conventionally. The basic principle of such "active" gating relies on the ability to drive the ferroelectric material away from its local energy minimum to a non-equilibirum state where its capacitance ($dQ/dV$) is negative and stabilizing it there by adding a series capacitance. In the next several sections, we shall discuss this mechanism.

## 1.2 Negative Capacitance to Rescue

The idea for negative capacitance to reduce the sub threshold slope below 60 mV/decade was proposed in 2008. The proposal is to replace the gate oxide with a negative capacitance material [21]. To understand how negative capacitance may help reducing the supply voltage and hence energy dissipation in conventional transistors, we start by noting that a field effect transistor could be thought of a series combination of two capacitors: the gate oxide capacitor $C_{ox}$ and the semiconductor capacitor $C_s$ as shown in figure 1.5. In a conventional transistor, where $C_{ox}$ is a positive quantity, the equivalent capacitance of the series network would be smaller than that of each of the constituent capacitors. On the other hand, when $C_{ox}$ is negative, the equivalent capacitance would be larger than $C_s$ provided $|C_{ox}| > |C_s|$. This is surprising considering that in a series network of two ordinary capacitors the total capacitance must be smaller than either of the constituent capacitances. Now the reduction

in supply voltage can be understood in the following way: since the total capacitance is enhanced by having a negative $C_{ox}$, it requires less voltage to produce the same amount of charge $Q$ across the capacitors, $C_s$ and $C_{ox}$, both of which have the same $Q$ due to being in series. The current in the channel is proportional to the charge across $C_s$. This means that the same amount of current can now be produced with smaller voltage. Perhaps a more intriguing aspect of the network in Fig. 1.5 is the fact that the internal node voltage, $\psi_s$ is larger than gate voltage $V_G$ due to the presence of a negative $C_{ox}$. This makes the channel 'see' a larger voltage than what was actually applied. Recognizing that the Boltzmann factor is given by $e^{q\psi_s/k_BT}$, the minimum voltage required to increase current by one order of magnitude is $2.3k_BT/(rq)$. Conventionally, $r = \psi_s/V_G < 1$; but in this case, $r > 1$ since $C_{ox} < 0$. As a result the minimum voltage (to increase current by one order of magnitude) reduces below 60 mV at room temperature.

Mathematically, subthreshold swing $S$ is defined as:

$$S = \frac{\partial V_G}{\partial log_{10}(I_D)} = \left(\frac{\partial V_G}{\partial V_{in}}\right)\left(\frac{V_{in}}{\partial log_{10}(I_D)}\right) \tag{1.1}$$

In figure 1.4(b), the region below where the current saturates is known as the subthreshold region. $S$ provides an estimate for how steeply the current is increasing with voltage. The lower the value of $S$, the steeper the curve and vice versa. Going back to Equation 1.1, one would see that the expression can be written as a product of two terms. To understand these terms, lets look at figure 1.5 which also shows a simplistic view of the relationship between the capacitor network to the potential profile in a nanoscale transistor. Note that here the channel-drain or channel-source coupling capacitors are not drawn explicitly. These capacitances are rather lumped into the semiconductor capacitance itself. This treatment does not change the physical scenario that explained here. The internal node voltage, $\psi_s$, also called the surface potential, controls the current flow over the barrier. The second term determines the inverse of how much current flows as a function of $\psi_s$. This term is dictated by the Boltzmann factor $e^{q\psi_s/k_BT}$ and can only give an $S$ of $2.3k_BT/q$(=60 mV/decade) at room temperature. Clearly, as long as the transport mechanism of electrons is not altered from a barrier modulated transport, the second term is a fundamental one and provides only 60mV/decade of the subthreshold swing. This is the motivation behind TFET[16, 17], IMOS[18] and NEMFET[19, 20], as mentioned before, where the mode of transport is changed.

The negative capacitor approach effects the first term. This term is simply the ratio of supply voltage, $V_G$ to the internal node voltage, $\psi_s$ which can be written as

$$m = \frac{\partial V_G}{\partial \psi_s} = 1 + \frac{C_s}{C_{ox}} \tag{1.2}$$

This ratio, often called the 'body-factor' in the MOSFET literature, will always be larger than 1 because of the voltage divider rule in conventional capacitors. Thus ordinarily $S$ cannot be less than 60 mV/decade. However, if the conditions $C_{ox} < 0$ and $|C_{ox}| < |C_s|$, can be satisfied, $m$ could be made to be less than one leading to an overall $S$ which is less than 60 mV/decade. Obtaining an effective negative $C_{ox}$ is the main objective of this thesis.

## 1.3 Capacitance: Positive and Negative

A capacitor is a device that stored charge. Capacitance of a device $C$ is defined as the rate of increase of the charge $Q$ with the voltage $V$ ($C = dQ/dV$). Hence, by definition, for a negative capacitor, $Q$ decreases as $V$ is increased (see figure 1.6(a)). Alternatively, capacitance can also be defined in terms of the free energy $U$. For a negative capacitor, the energy landscape is an inverted parabola (see figure 1.6(b)). For a linear capacitor, $U = Q^2/2C$. In terms of free energy, the capacitance can be defined as follows.

$$C = \left[\frac{d^2U}{dQ^2}\right]^{-1} \tag{1.3}$$

The same relation holds also for a non-linear capacitor. In other words, the negative curvature region in the energy landscape of an insulating material corresponds to a negative capacitance.

## 1.4 How to realize negative capacitance: The case of Ferroelectric oxides

Which insulating materials have a negative curvature in their energy landscape? The energy landscape of a ferroelectric material is shown in figure 1.7. It has two degenerate energy minima. This means that the ferroelectric material could provide a non-zero polarization even without an applied electric field. In general, the total charge density in a given material can be written as $Q_A = \epsilon E + P$, where $\epsilon$ is the linear permittivity of the ferroelectric, $E$ is the external electric field and $P$ is the polarization. In typical ferroelectric materials, $P >> \epsilon E$ leading to $Q_A \approx P$. For this reason we shall use $P$ and $Q_A$ interchangeably. Since charge density is what we are interested in, we shall also drop the subscript $A$ and simply use $Q$ for charge density.

If we compare the characteristic ferroelectric energy landscape (figure 1.7) with that of an ordinary capacitor shown in figure 1.6(b), we would see that the curvature around $Q = 0$ of a ferroelectric is just the opposite of that of an ordinary capacitor. Remembering that the energy of an ordinary capacitor is given by $(Q^2/2C)$, this opposite curvature already hints

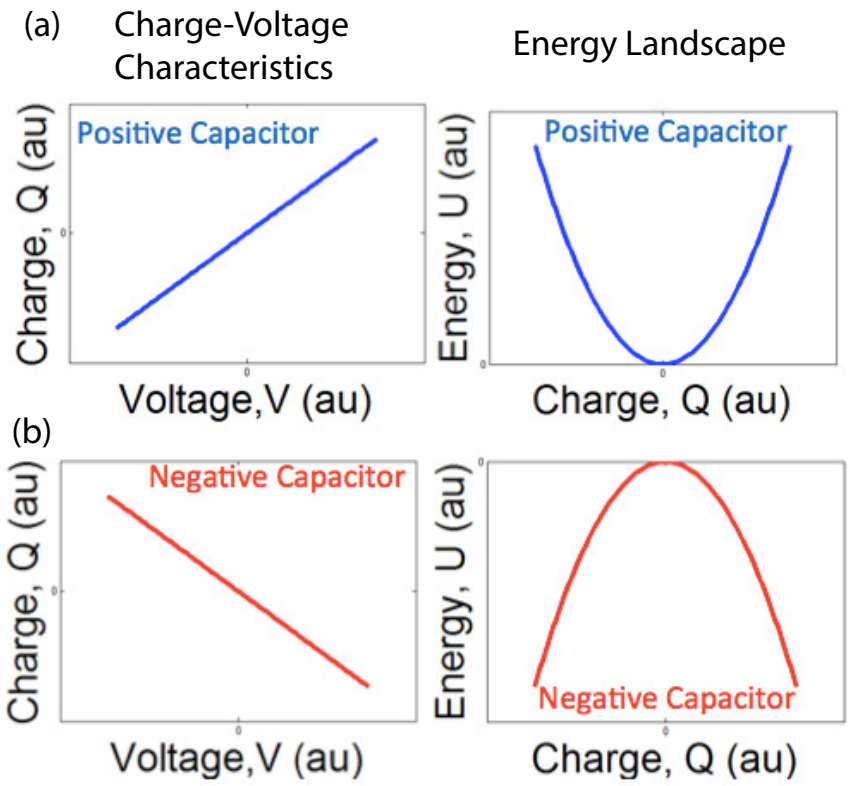


Figure 1.6: Charge-voltage characteristics and energy landscapes of a positive capacitance (a) and a negative capacitor (b).

at a negative capacitance for the ferroelectric material around $Q = 0$. Therefore, around this point, a ferroelectric material could provide a negative capacitance.

## 1.5 An Introduction To Ferroelectric Oxides

A ferroelectric is an insulating material with two or more discrete stable or metastable states of different nonzero electric polarization in zero applied lactic field, referred to as "spontaneous" polarization. For a system to be considered ferroelectric, it must be possible to switch between these states with an applied electric larger than the coercive field, which changes the relative energy of the states through the coupling to the field to the polarization. The polarization switch-ablity criteria for a ferroelectric material and, in fact, the term "ferroelectricity" was established through the work of Joseph Valasek, who, in 1921, demonstrated the hysteretic nature of the polarization of Rochelle salt: $NaKC_4H_4O_6{\cdot}4H_2O$

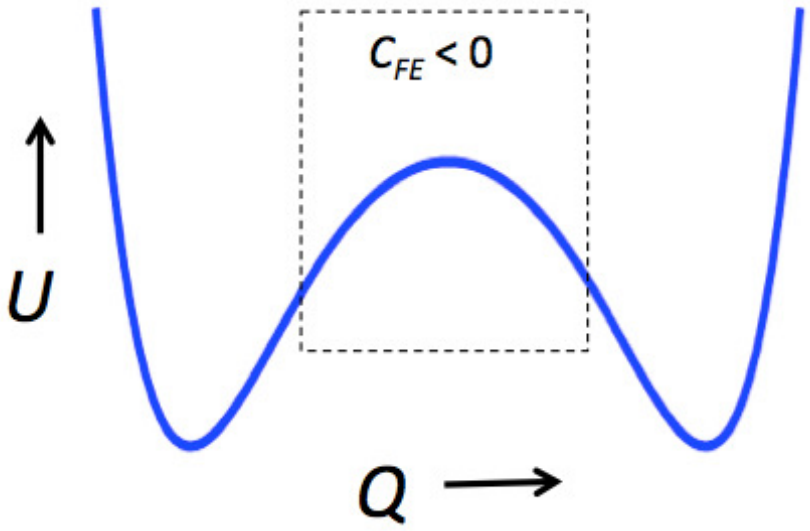


Figure 1.7: Energy landscape of a ferroelectric materials. The region under the dashed box corresponds to the negative capacitance state.

and its dependence on temperature [22]. Research in inorganic ferroelectric ceramics received an impetus during the WWII and the ferroelectric nature of the ceramic $BaTiO_3$ was first demonstrated in 1945 by applying an external field, electrically aligning, or "polling", the domains within the grains [22]. Research and development in piezoelectric transducers paved the way for research in other ferroelectic perovskite compounds from 1950 to the 1970s, most notably lead zirconate($PbZrO_3$):lead titanate ($PbTiO_3$) ceramic systems for their high Curie temperatures [22]. Ferroelectric material class can further be sub grouped into pyrochlores, perovskites, layer structures, tungsten bronze structure etc.

Non-centrosymmetry of the crystal structure plays an important role in ferroelectricity and negative capacitance phenomenon in ferroelectrics is essentially structurally driven. The noncentrosymmetric nature is essential in producing electric dipoles, and thus collectively the vector quantity: polarization. All crystals can be categorized into 32 different classes, or point groups, based on their symmetry elements as shown in figure 1.8 [23]. Among the 32 point groups, 11 classes are centrosymmetric and 21 are noncentrosymmetric. Of the 21 noncentrosymmetric point groups, 20 are piezoelectric classes, which consist of materials with the ability to electrically polarize when subjected to stress and strain [23]. Among the piezoelectric class, 10 are pyroelectric, consisting of materials that can develop spontaneous polarization and form permanent dipoles in the structure as a function of temperature. Ferroelectrics are a subgroup in pyroelectrics which not only possess unique, stable polar axes (piezoelectricity), and exhibit spontaneous polarization (pyroelectricity), but are also capable of reversing their polarization by an external electric field [23].

In this thesis, we will explore the negative capacitance effect only in tetragonal perovskite ferroelectrics. Perovskite ferroelectrics belong to a large class of materials called the complex oxides. Typical chemical symbol of perovskite complex oxide is $ABO_3$, where B is a transition metal element. Due to the partially filled/unfilled $d$ or $f$ orbitals in the transition metal element, a wide range of interesting properties are observed in complex oxide including high temperature superconductivity, ferroelectricity, antiferroelectricity, multiferroicity, colossal magnetoresistance, metal-insulator transition. Let us consider the case of a classical perovskite ferroelectric: $PbTiO_3$ (PTO). Figure 1.9(a) shows the unit cell of PTO. In this case, the central $Ti^{4+}$ is not at the center of the symmetry of the unit cell; rather it is off-centered and hence the crystal structure is non-centrosymmetric. This off-centering of the central ion results in a spontaneous dipole moment or electric polarization in the material. The unit cell of PTO is tetragonal (crystal class $P4mm$), which means that the one of the side of the cell is longer than the other two (*i.e.* $c > a$) and all the angles between the sides are 90°. The off-centering of the central ion $\delta$ is of the order of picometers resulting in the "spontaneous polarization" $P = q\delta/ca^2 = \sim 0.5$ C/m$^2$. The off-centering of the central atom in the two opposite directions corresponds to the two different minima of the ferroelectric energy landscape shown in figure 1.4. Figure 1.9(b) shows the switching of the polarization up on the application of a voltage larger than the coercive voltage. Figure 1.10 shows the polarization-voltage hysteresis characteristics of a ferroelectric capacitor and the energy landscape corresponding to different points of the hysteresis loop.

The properties of a ferroelectric material are strongly dependent on temperature. Above a critical temperature, called the Curie temperature, a ferroelectric material goes through a phase transition transforming into a paraelectric. In the paraelectric phase, the material does not have any spontaneous polarization and is akin to a regular dielectric. Figure 1.11(a,b) show the polarization and the dielectric constant respectively of a second order phase transition in ferroelectric material. At the Curie temperature $T_c$, the dielectric constant diverges. We will get back to the role of temperature dependent behavior in ferroelectric for exploring the negative capacitance properties later.

## 1.6 Landau Theory of Ferroelectrics and Negative Capacitance

The Landau theory is a symmetry based phenomenology that serves as a conceptual bridge between the microscopic models and the observed macroscopic phenomena. It assumes a spatial averaging of local fluctuations. As a result, it is particularly well suited to systems with long range interactions such as ferroelectrics and superconductors. In his classic 1937 papers, Landau noted that a system cannot change smoothly between two phases of differ-

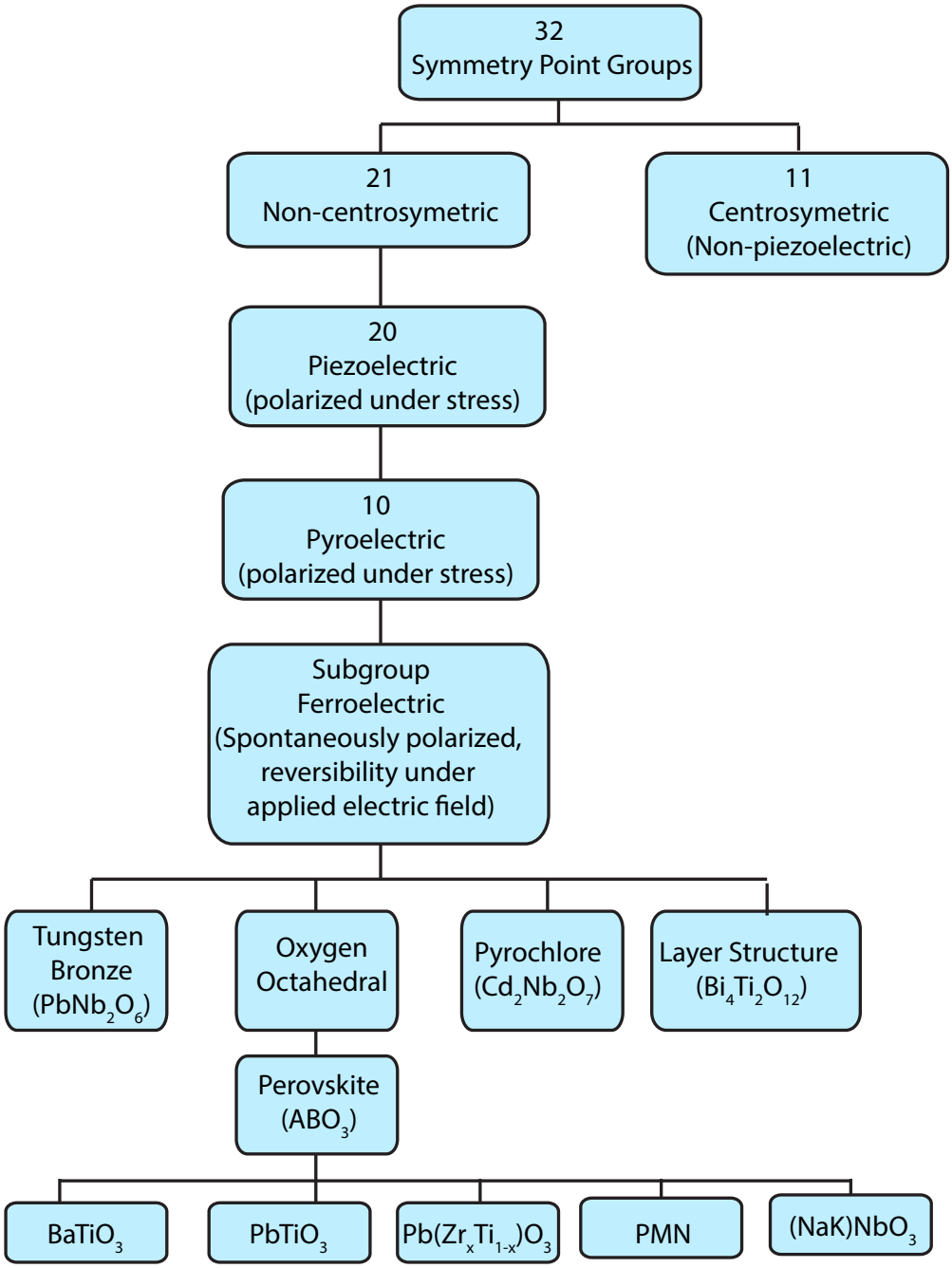


Figure 1.8: Relationship between the piezoelectric class and its subgroups within the 32 symmetric point groups.

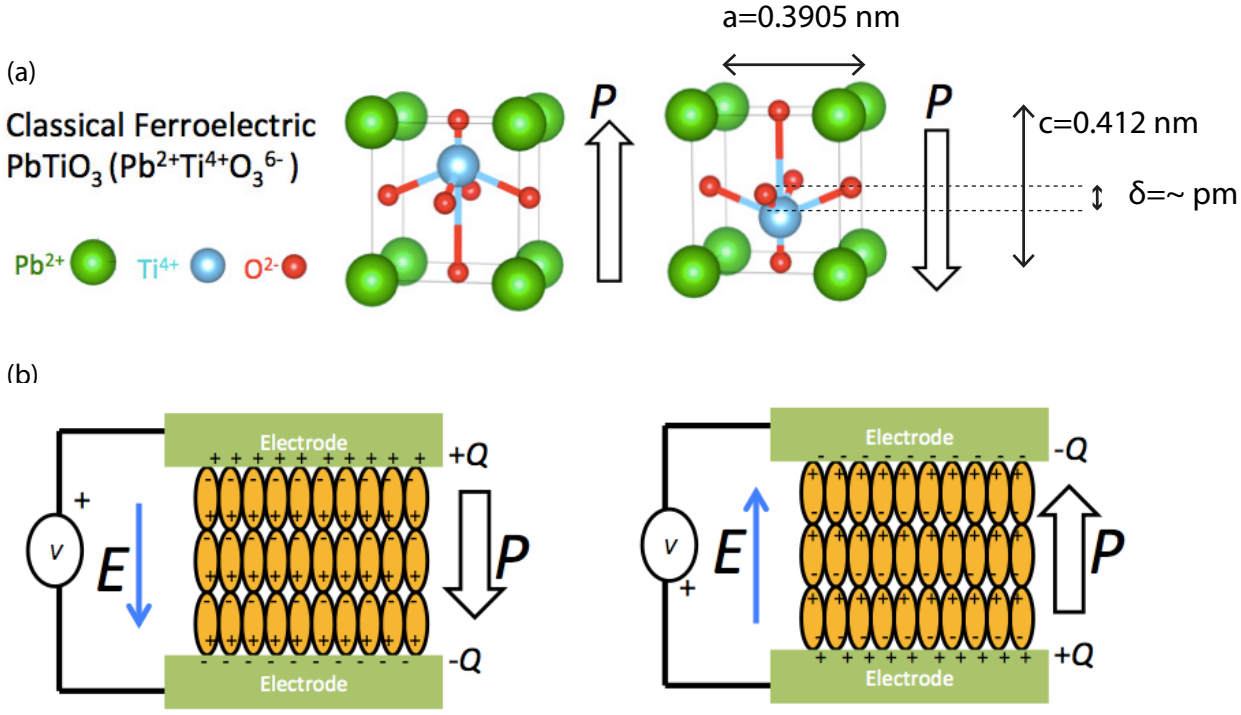


Figure 1.9: (a) Unit of cell of a classical ferroelectric $PbTiO_3$. The opposite off-centering of the central ion corresponding to the two different polarization states are shown. (b) The switching of the polarization of a ferroelectric capacitor upon the application of a voltage larger than the coercive voltage.

ent symmetries. Because the thermodynamic states of two phases that are symmetry-wise distinct must be the same at their shared transition line, the symmetry of one phase must be higher than that of the other. Landau then characterized the transition in terms of an order parameter, a physical entry that is zero in the high symmetry (disordered) phase and changes continuously to a finite value when the symmetry is lowered. For the case of a ferroelectric-paraelectric transition, this order parameters is the polarization and the high and low symmetry phases correspond to the paraelectric and the ferroelectric states respectively. The free energy of $U$ is then expanded as a power series of the order parameter $P$ where only symmetry compatible terms are retained. The state of the system is then found by minimizing the free energy $U(P)$ with respect to $P$ to obtain the spontaneous polarization $P_\circ$. The coefficients of the series expansion $U(P)$ can be determined from experiments or from first principle calculations.

For a ferroelectric, the free energy $U(P)$ can be represented as an even order polynomial of the polarization $P$, which is as follows.

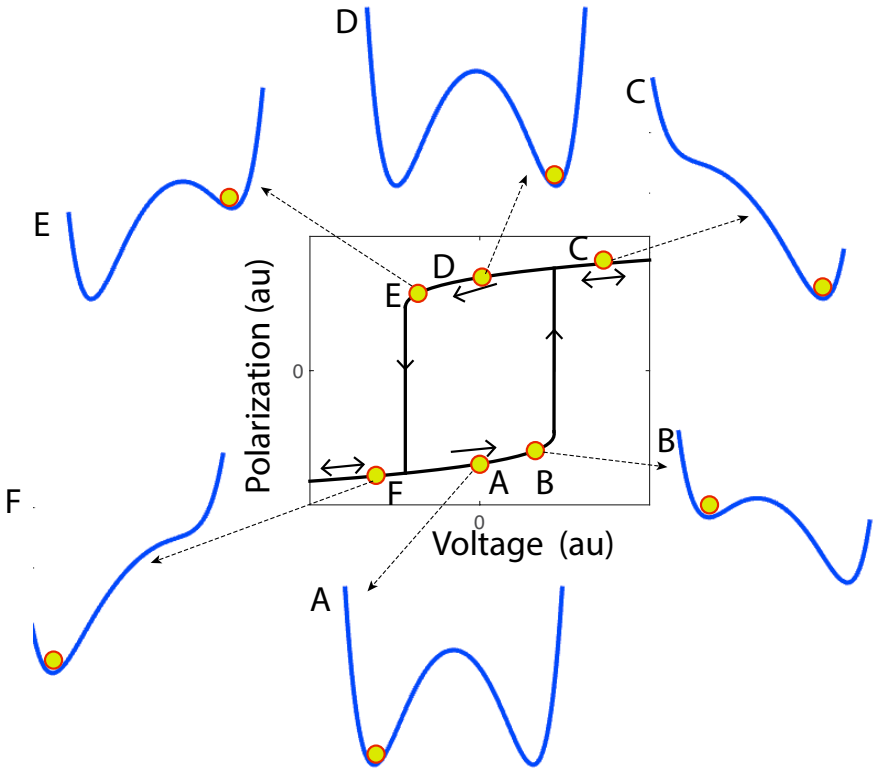


Figure 1.10: Polarization-voltage hysteresis characteristics of a ferroelectric capacitor. The energy landscapes at different points on the hysteresis curve are also shown.

$$U = \alpha P^2 + \beta P^4 + \gamma P^6 - EP \tag{1.4}$$

Here, $E = V/d$ is the applied electric field; $V$ and $d$ are the voltage applied across the ferroelectric and the ferroelectric thickness respectively. $\alpha$, $\beta$ and $\gamma$ are anisotropy constants. $\beta$ and $\gamma$ are temperature independent. $\gamma$ is a positive quantity; $\beta$ is positive and negative respectively for second order and first order phase transition. $\alpha = a_\circ(T - T_C)$, where $a_\circ$ is a temperature independent positive quantity and $T$ and $T_C$ are the temperature and the Curie temperature respectively. As a result, $\alpha < 0$ below the Curie temperature which results in the negative curvature of the energy landscape of a ferroelectric around $P = 0$ and hence the double well energy landscape. The temperature dependence of $\alpha$ results in the temperature dependent behavior of the ferroelectric as shown in figure 1.11. A quick look at equation 1.4 also reveals that an electric field tilts the energy landscape through the term $-EP$ which results in the evolution of the landscape with applied electric field/voltage as depicted in figure 1.10.

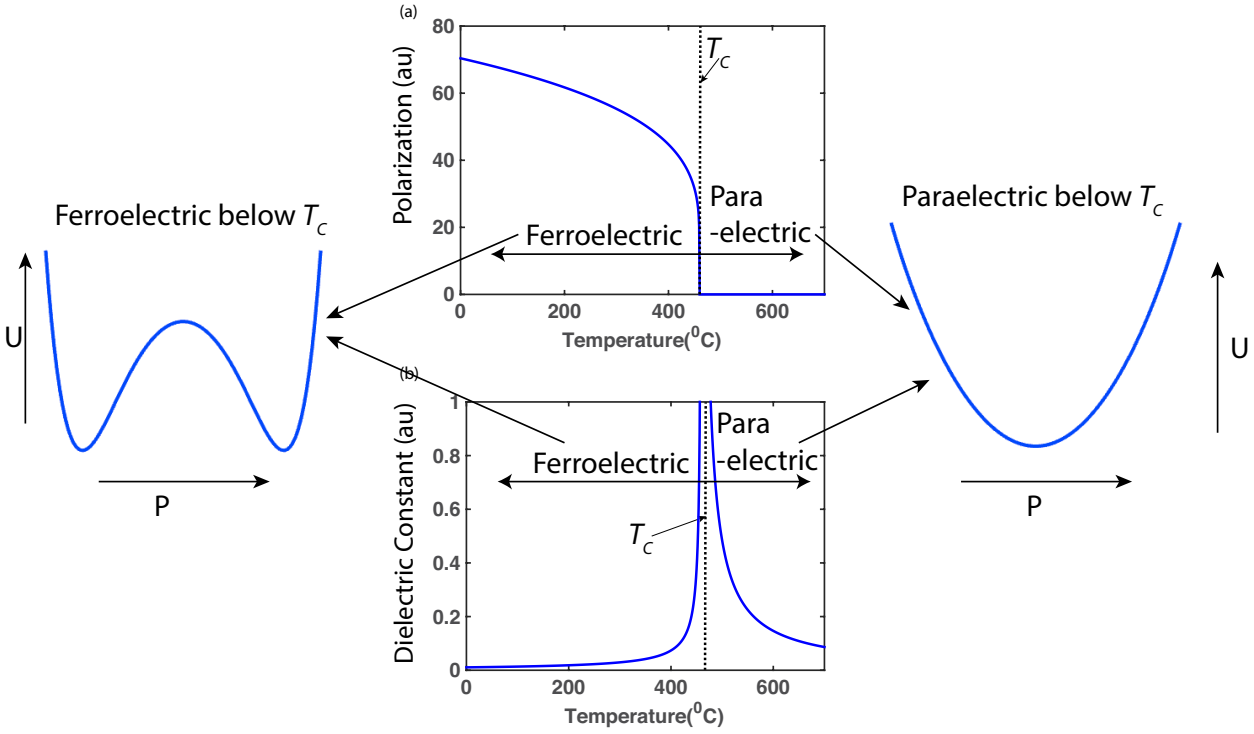


Figure 1.11: Evolution of the spontaneous polarization (a), the dielectric constant (b) and the energy landscape (c) as functions of temperature for a ferroelectric material with a second order phase transition.

Combining equations 1.3 and 1.4, the following equation for capacitance around $P$=$\sim$0 and at $T < T_C$ is obtained.

$$C = \frac{1}{2\alpha} = \frac{1}{2a_\circ(T - T_C)} < 0 \tag{1.5}$$

Furthermore, at equilibrium, $dU/dP = 0$, which, combined with equation 1.4, results in the following relation.

$$E = 2\alpha P + 4\beta P^3 + 6\gamma P^5 \tag{1.6}$$

Figure 1.12 shows the polarization-voltage characteristics of a ferroelectric capacitor obtained using equation 1.6. We note in figure 1.12 that, in accordance with the Landau theory of ferroelectrics, a ferroelectric capacitor has a non-linear charge-voltage characteristics in which

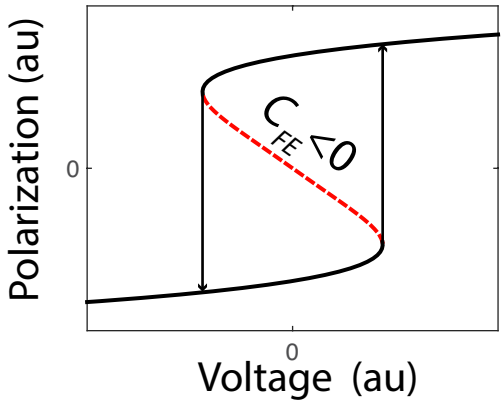


Figure 1.12: Charge (or polarization)-voltage characteristics of a ferroelectric material according to the Landau theory. The capacitance is negative in a certain region of charge and voltage which is indicated by the dotted line.

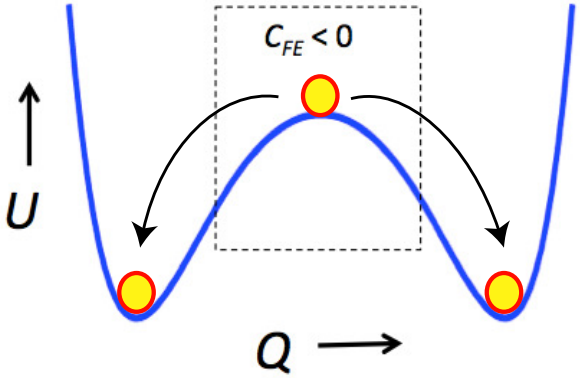


Figure 1.13: Negative capacitance state is unstable and the polarization spontaneously rolls downhill from a negative capacitance state to one of the minima making a direct measurement of the phenomenon experimentally difficult.

a negative capacitance can be obtained in a certain range of charge and voltage indicated by the red dashed curve.

## 1.7 Why has ferroelectric negative capacitance never been observed until now?

Ferroelectricity is an established discipline in physics and materials science with its origin back in the 1930s. The Landau theory of ferroelectricity has also been researched actively

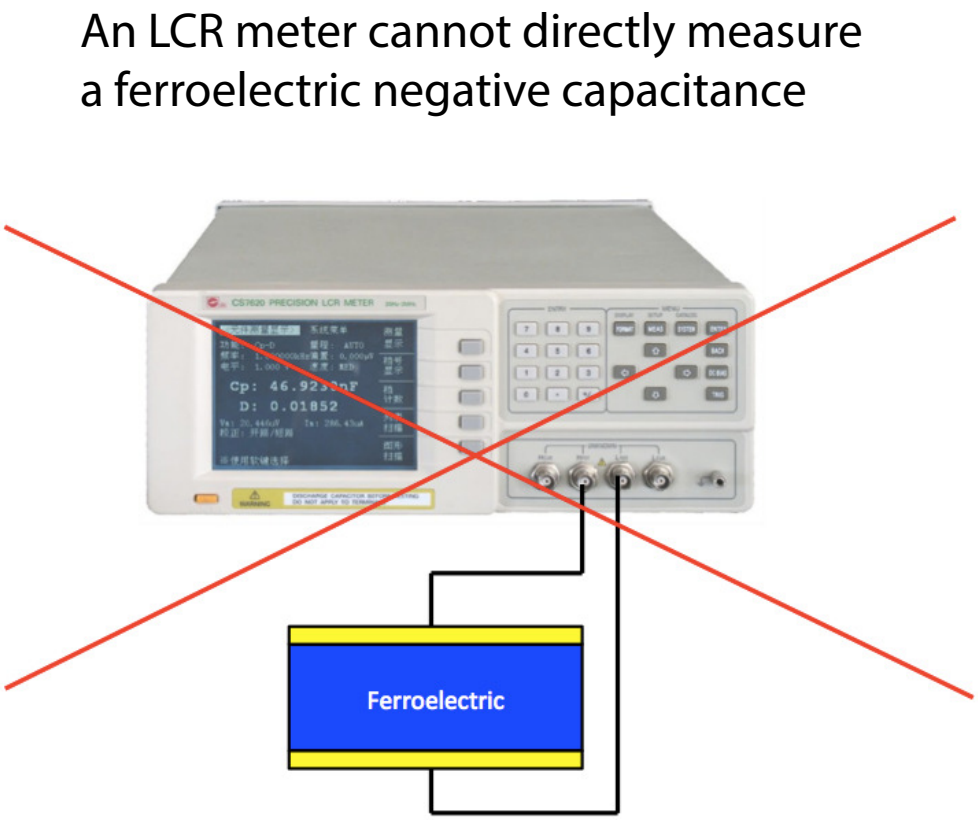


Figure 1.14: An LCR meter cannot directly measure a ferroelectric negative capaacitance

since 1930s. And ferroelectricity is a very active field of research with a publication rate of the order of ten thousand per year. Hence it begs the question "why has the negative capacitance phenomenon never been explicitly observed in ferroelectric materials until now?" One of the reasons is the unstable nature of the negative capacitance in a ferroelectric capacitor. If the polarization in placed in the unstable region of the energy landscape as shown in figure 1.13, the ferroelectric capacitor spontaneously self-charges and the polarization rolls downhill to one of the minima. This is also why, in the conventional experimental measurement of polarization-voltage characteristics where voltage is the control variable (see figure 1.12), the negative capacitance region is masked by a hysteresis region and sharp transitions between the two polarization states occur. As a result, a negative capacitance cannot be directly measured by connecting a ferroelectric capacitor to an LCR meter as shown in figure 1.14. It requires specialized experimental setup to directly measure the negative capacitance in a ferroelectric capacitor, which will be the topic of chapter 3.

Secondly, direct observation of negative capacitance in a ferroelectric material requires high structural quality of the film. We discuss the issue as well in chapter 3 section 3.15.

And finally, only now there is a significant technological interest in negative capacitance for reducing power dissipation in electronics and information paradigm, which makes it the right time to investigate this phenomenon with rigor. That being said, it is quite interesting that the negative capacitance effects were observed indirectly as early as 1956 [24, 25], although this fact was not explicitly mentioned in those early papers.

## 1.8 Scope and organization of the thesis

This thesis describes the research that transformed the theoretical concept of negative capacitance into an experimental reality during the time period 2008-2014. The thesis is divided into six chapters which are as follows.

1 *Chapter 1:* This chapter introduces the concept of negative capacitance and described this novel physical phenomenon could reduce the power dissipation in transistors.

2 *Chapter 2:* Chapter 2 describes the pulsed laser deposition of ferroelectric materials and standard electrical and structural characterization of ferroelectric $Pb(Zr_{0.2}Ti_{0.8})O_3$ thin films. This chapter sets the stage for the experimental measurements that detected negative capacitance described in chapters 3 and 4.

3 *Chapter 3:* Chapter 3 describes the first direct measurement of negative capacitance in an isolated ferroelectric capacitor. Two new concepts in negative capacitance and, in general, ferroelectricity have been proposed, namely the "characteristic negative capacitance transients" and the "dynamic hysteresis loops". The results are analyzed based on a simple 1-D Landau-Khalatnikov equation based model. The time-dynamic measurement technique presented in this chapter could be used a canonical test of negative capacitance for any alternative negative capacitance systems [26, 27, 28, 29, 30].

4 *Chapter 4:* Stabilization of the negative capacitance in ferroelectric $Pb(Zr_{0.2}Ti_{0.8})O_3$-dielectric $SrTiO_3$ heterostructures is experimentally demonstrated. In contrast to the classical theory of electrostatics, we observed that the equivalent capacitance of a series combination of a ferroelectric and a dielectric capacitor is larger than that of the constituent dielectric capacitor. This points to the fact the the ferroelectric capacitor acts as an effective negative capacitor in such a circuit. The results are analyzed based on a simple 1-D Landau-Devonshire model. The effects of temperature on the negative capacitance phenomena are also investigated in this chapter.

5 *Chapter 5:* Chapter 5 presents a design framework of negative capacitance field-effect-transistors (NCFET). A new mode of NCFET operation-called the antiferroelectric mode is proposed, where a significantly boost of the on-current and a sub-60 mV/dec subthreshold characteristics is obtained in exchange for a nominal hysteresis. The effects of different design parameters such ferroelectric thickness, source/drain overlap and gate length on the NCFET performance are also analyzed in this chapter.

5 *Chapter 6:* Finally, chapter 6 summarizes the key results presented in the thesis. Suggestions for future work are also made in this chapter.

# Chapter 2

# GROWTH AND CHARACTERIZATION OF FERROELECTRIC THIN FILMS USING PULSED LASER DEPOSITION TECHNIQUE

The first step towards investigating the negative capacitance phenomenon is to fabricate high quality ferroelectric capacitors. This chapter describes the deposition of ferroelectric films and presents detailed structural and standard electrical characterization. Started in 2008, the purpose of this research presented in this thesis was to experimentally demonstrate and explore the newly proposed physical phenomenon–ferroelectric negative capacitance; hence, we chose to work on the cleanest and simplest possible system in terms of both material systems and thin film growth. Towards that end, we took an epitaxial route to fabricate these films using the pulsed laser deposition technique, which ensures the highest structural and epitaxial quality. Also for the same reason, $Pb(Zr_{0.2}Ti_{0.8})O_3$ (PZT) was chosen as the ferroelectric, which is one of the most robust ferroelectric oxides known with one of the largest spontaneous polarizations. We will later show in chapter 3 that obtaining the highest quality ferroelectric films is the key to the first ever direct measurement of the negative capacitance effect. In summary, this chapter sets stage for the research described in the following chapters.

To explore the phase space of the negative capacitance phenomenon with respect to the structural and electrical characteristics, the properties of the PZT films were epitaxially strain tuned by depositing films on three different substrates, namely $SrTiO_3$ (STO), $DyScO_3$ (DSO) and $GdScO_3$ (GSO). Within the span and scope of our research, we found that compressively strained PZT films grown on STO substrates resulted in the desirable properties for negative capacitance, which was further researched for the purpose of negative

capacitance described in the later chapters. On the other hand, as a by-product of the negative capacitance research, a novel nanoscale strain functionality–voltage controlled reversible ferroelastic $c \rightarrow a$ and $a \rightarrow c$ switching–was observed for the first time in tensile strained PZT films as thin as 40 nm. These results are also described in this chapter briefly.

Sections 2.1-2.4 present a general introduction to the material systems and the pulsed laser deposition technique. In sections 2.5-2.8, we present the structural characterization of the PZT thin films using the atomic force microscopy technique and X-ray diffraction. Sections 2.9 and 2.10 present the standard electric characterization, namely the static hysteresis loop and the dielectric constant measurements. Section 2.11 details the effects of the epitaxial strain on the spontaneous polarization in the strained PZT films. In sections 2.12 and 2.13, we present the effects of strain relaxation on the dielectric properties of PZT films. Section 2.14 details the newly discovered voltage controlled ferroelastic switching in tensile strained PZT films grown on $GdScO_3$ substrates.

Most of the results presented in this chapter was reported in references [31, 32].

Table 2.1: Material systems used in this work.

| Material Class/Function | Material | Growth Technique |
|---|---|---|
| Ferroelectric | Lead zirconate titanate ($Pb(Zr_{0.2}Ti_{0.8})O_3$, PZT) | PLD |
| Dielectric | Strontium titanate | PLD |
| Bottom Metal Contact | Strontium ruthenate ($SrRuO_3$, SRO) | PLD |
| Substrate | Strontium titanate ($SrTiO_3$, STO), (001) orientation | PLD |
| | Dysprosium scandate ($DyScO_3$, DSO), (110) orientation | PLD |
| | Gadolinium scandate ($GdScO_3$, GSO), (110) orientation | PLD |
| Top metal contact | Gold Au | E-beam evaporation |

## 2.1 Material Systems and Device Structures

Material systems used in the research entailed in the thesis are listed in table 2.1. The different types capacitor heterostructures fabricated in this work along with the typical thicknesses of each of the layers in the devices are shown in figure 2.1. Growth, structural and standard electric characterization of ferroelectric films are described in this chapter. Negative capacitance measurements in the ferroelectric capacitor are detailed in chapter 3. Dielectric capacitor and ferroelectric-dielectric capacitor and are described in chapter 4.

## 2.2 Introduction to the Pulsed Laser Deposition Technique

Various thin-film growth techniques that have been used in the synthesis of epitaxial complex oxide thin films. Of these, the pulsed laser deposition (PLD) technique has emerged as the one of choice with several advantages related to the low set-up cost as well as the versatility it offers to synthesize a wide range of oxide material systems. It was the synthesis of high temperature superconductors via PLD in the late 1980's [33], followed by several pioneering works on oxide ferroelectrics [34, 35] in the early 1990's that initially brought PLD growth to the mainstream. Since then, major advancements over the last few decades including the integration of in-situ growth monitoring capabilities such as RHEED and others, have transformed PLD to a sophisticated thin-film growth technique that routinely enables the growth of high-quality epitaxial thin films with unit-cell level control of thickness, and even

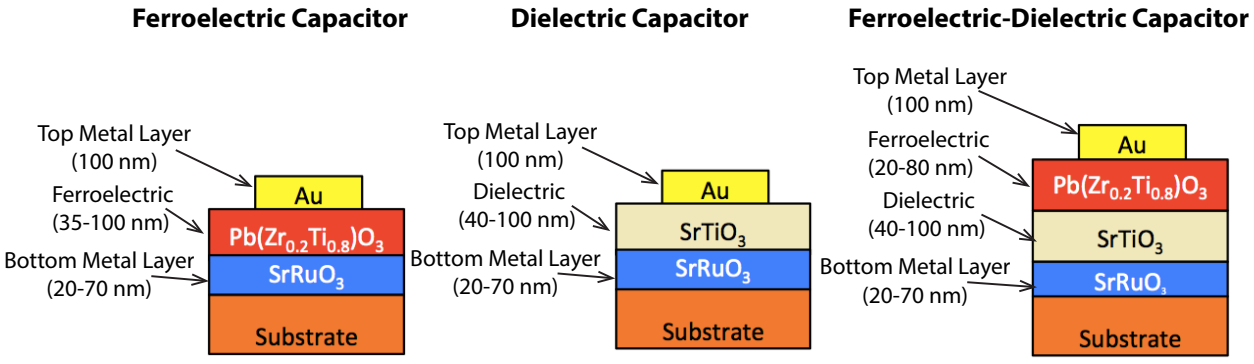


Figure 2.1: Schematic diagram of the capacitor heterostructures fabricated in this work.

the growth of artificial superlattices and nanostructures [36, 37]. However, despite the relatively easy set-up for a PLD system, the actual growth involves highly energetic and complex processes including laser-ablation, plume formation and propagation, plasma chemistry, as well as the out-of-equilibrium thin-film growth process that occurs at the substrate surface [38, 39, 40]. Consequently, careful control of PLD growth parameters are required to carefully tune the structure, crystallinity, stoichiometry and morphology of materials. This is particularly important for ferroelectric materials as it is well known that any of these factors can have a significant impact on the ferroelectric properties. Therefore, in this chapter, we begin with the general procedure of thin film deposition using the PLD set-up in our laboratory, followed by a description of growth optimization. We then move on to the detailed characterization of the structure, morphology, domain architecture, and ferroelectric properties of $Pb(Zr_{0.2}Ti_{0.8})O_3$ thin films and $Pb(Zr_{0.2}Ti_{0.8})O_3$-$SrTiO_3$ heterostructures.

## 2.3 General Procedure of Thin Film Deposition using the Pulsed Laser Deposition Technique

All thin film ferroelectric heterostructures studied in this dissertation were grown via PLD using a KrF excimer laser (Lambda Physik LPX205i, $\lambda = 248$ nm). The growth experiments were conducted in a vacuum chamber that is equipped with a target holder and substrate heater (figure 2.2). The steps of the deposition technique are as follows.

1. Substrate preparation: Prior to growth, the substrates are ultrasonicated for five minutes each in acetone and isopropanol, mounted on to the heater using silver paint (Leitsilber 200 silver paint from Ted Pella, Inc.), and allowed to cure at 60 °C for fifteen minutes.

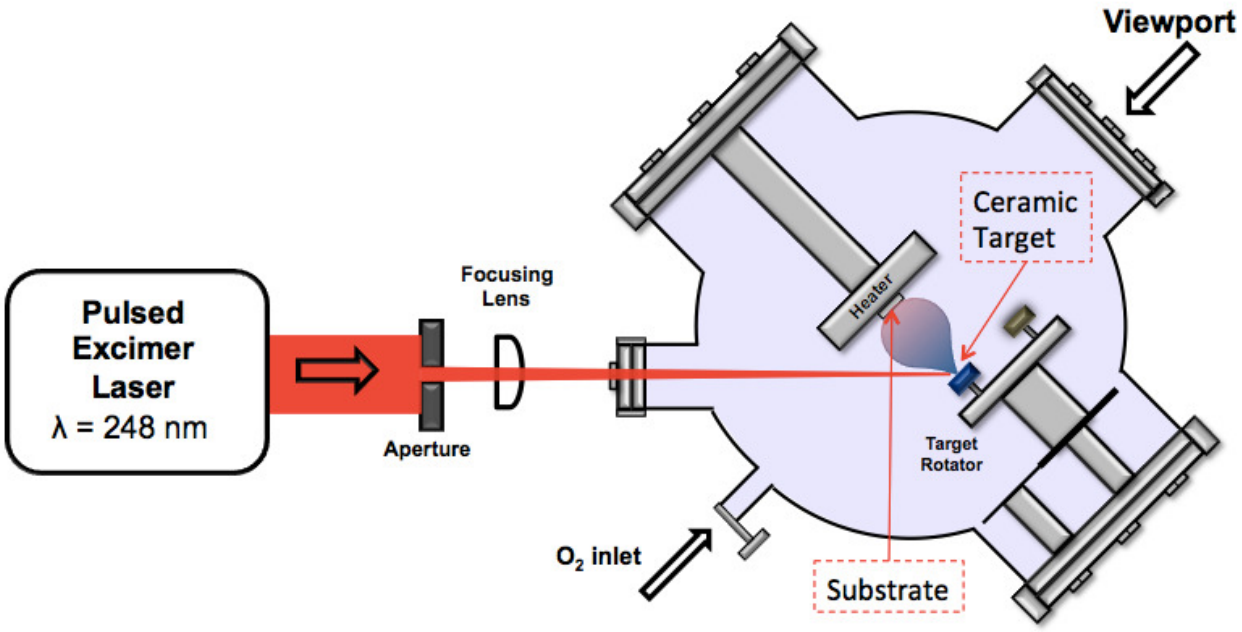


Figure 2.2: Schematic diagram of the pulsed-laser deposition system.

2. Target preparation: Targets of the desired composition are sanded, cleaned, and mounted on the target rotator assembly.

3. Pre-ablation of target: Prior to deposition, the target is pre-ablated to ensure that the target surface had reached steady state prior to growth.

4. Growth: An on-axis growth geometry with a target-substrate distance of 4-5 cm is used for all depositions. The chamber is pumped down to a base pressure of at least $5\times10^{-6}$ Torr following which it is backfilled with oxygen (99.995% pure) to the desired deposition pressure using a variable leak valve. The substrate is then heated to the growth temperature at a ramp rate of 20 °C per minute. Laser pulses with 50-200 mJ energy and ∼4 mm$^2$ spot size depending upon target material, its density, and the desired growth rate were used to ablate the targets. The laser pulse repetition rate was in the range of 1-20 Hz. For example, typically PZT and SRO targets were ablated at repetition rates of 5 and 15 for PZT and SRO respectively.

5. Cooling: Following growth, the chamber is filled with 760 Torr of oxygen to promote complete oxidation of films and is cooled at 2-10 °C/min to room temperature.

6. Deposition parameters: The growth variables involve several parameters including substrate temperature, chamber pressure, laser fluence, and laser repetition rates that have

been optimized for the thin-film systems under study.

7. Post deposition metallization: Gold top electrodes were ex-situ deposited by e-beam evaporation, and then patterned using standard lithographic technique into circular, triangular and square dots.

## 2.4 Optimization of Thin Film Growth using the Pulsed Laser Deposition Technique

In this section, we describe the optimization of thin film growth within the general procedure outlined in the previous section. The main advantage of the pulsed laser deposition over other techniques such as molecular beam epitaxy, RF sputtering, atomic layer deposition etc. is that growth conditions could be optimized in a quick time frame. This is especially true for high quality, epitaxial, single crystalline, thin film growth of complicated materials such as $Pb(Zr_{0.2}Ti_{0.8})O_3$. On the other hand, we found in our PLD set-up that optimal growth conditions tend to drift away within a time frame of one or two months, after which the growth needs be optimized again. We believe that the unstable nature of PLD growth conditions is primarily due to the following two reasons.

1. Drift in the laser pulse properties: The energy per pulse and the shape of the laser pulse of KrF excimer laser for given laser discharge voltage decreases with time. Let us give a practical example. Right after refilling the excimer laser, the pulse energy might be 120 mJ for the discharge voltage of 17 kV and a given optical setup. After 90 depositions in a month, the same discharge voltage of 17 kV yields only 80 mJ for the same optical setup. To achieve 120 mJ of energy per pulse, the discharge voltage might have to be increased to 22.5 kV. This is due to the fact the the laser discharge tube is filled with a low-pressure mixture of an inert Kr gas and a halogen or halide gas ($F_2$ in our case), and is additionally pressurized with an inert buffer gas of helium. The laser tube has two parallel electrodes running almost the entire length of the tube. The laser is pulsed by discharging across these electrodes. The resultant plasma contains a high concentration of an excited transient complex of KrF, which emits ultraviolet laser light. As a result, with the pulsing of the laser for PLD growth, Kr and $F_2$ partial pressure decrease. The discharge voltage have to be increased to get the same energy pulse as the partial pressures of Kr and $F_2$ reduce with time. The shape of laser pulse, which impinges on the ceramic target and can be recorded on thermal paper, also changes with the lowering of the partial pressures.

2. Non-uniform density of ceramic target: The non-uniformity of the density of the ceramic target also plays an important role. With subsequent growths from the same ceramic target, the target thins down due to sanding and ablation. As a result, after

10-15 growths, it may happen that a region of target gets exposed and subsequently ablated during growth to form the plasma plume which has a different density than the region which was initially exposed in the virgin target. The shape of plasma plume depends on the density of the exposed region of the ceramic target. In general, for the same material and same growth conditions, a dense target creates a larger plume then a less dense one. We observed that, after 10-15 growths, the shape of the plasma plume looks different for the same PLD parameters.

## Optimization Parameters:

The parameters for PLD growth are six-fold: (1) Substrate temperature, (2) Laser energy, (3) Laser spot size, (4) Laser repetition rate, (5) $O_2$ partial pressure during growth and (6) Cooling rate. In the following, we describe optimization of these PLD parameters.

1. Substrate Temperature: In general, the substrate temperature is decided based on epitaxial strain imposed by the substrate on the thin film. For a given combination of the material to be deposited and the substrate with different room temperature bulk lattice parameters and thermal expansion coefficients, the ideal temperature is the one at which the bulk lattice parameters of these materials are equal. High quality $SrRuO_3$ thin films, which serve as the bottom electrode in the heterostructures (see figure 2.1), could be grown on $SrTiO_3$ (002), $GdScO_3$ (110) and $DyScO_3$ (110) substrates at a large window of temperatures (550-850 °C), provided necessary optimization for all the other PLD parameters are done. On the other hand, in case of $Pb(Zr_{0.2}Ti_{0.8})O_3$, the optimal temperature window is rather limited. Due to the volatility of Pb, a lower growth temperature is required for the growth of stoichiometric PZT. Nonetheless, high quality PZT could be grown on on $SrTiO_3$ (002), $GdScO_3$ (110) and $DyScO_3$ (110) substrates at 580-630 °C. In our growth process, the substrate was generally held at 720 °C and 630 °C during the growth of SRO and PZT, respectively. For the growth of $SrTiO_3$ thin films on $SrRuO_3$ buffered substrates (*i.e.* for dielectric capacitor and ferroelectric-dielectric capacitor in figure 2.1), the growth temperature of STO films was the same as that for the SRO layer. As a PLD parameter, we found that substrate temperature was the most stable one. Hence, we generally kept the substrate temperature constant at the previously optimized value during a new optimization process.

2. Laser energy, spot size and repetition rate: These parameters tend to drift away most frequently. Hence, they are the most important optimization parameters. The laser energy per pulse is controlled by the discharge voltage and the laser spot size by optical setup. The laser energy per pulse and the repetition rate are more often changed during the course of an optimization routine. At an energy less than the optimal value, the thin films generally have pinholes. On the other hand, at an energy greater than the optimal value, the films generally develop mole-like structures. Similarly, a lower and higher than optimal value of repetition rate result in pinholes and mole-like

surface morphology. These effects are discussed in the example presented in the next subsection.

3. $O_2$ partial pressure: $O_2$ partial pressure is an important parameter for determining the insulating properties of ferroelectric or dielectric films. In general, for complex oxide deposition, $O_2$ partial pressure$\geq$50 mTorr is desirable for obtaining highly insulating PZT or STO films. The plasma plume is also more stable at a higher $O_2$ pressure. However, the plume is generally smaller at a higher $O_2$ pressure which decreases the film deposition rate. Like the substrate temperature, we generally kept the $O_2$ partial pressure constant at the previously optimized value during a new optimization process. For PZT and SRO, the $O_2$ partial pressure was 100 mTorr and, for STO, it was 200 mTorr.

4. Cooling rate: We found that a faster cooling rate (*i.e* $\geq$10 °C/min) generally improves the crystalline quality of the mono-domain PZT film grown on STO (002) and DSO (110) substrates with no detectable effect on the surface topography. For example, the PZT (002) full-width-at-half-maximum in X-ray diffraction rocking curve measurements in the fast cooled PZT films is generally smaller than that in slow cooled ones (*i.e* cooled at $\leq$5 °C/min). As such, fast cooled PZT films generally have less misfit dislocations and are strained to the substrates to a greater extent than that for slow cooled films of similar thicknesses. However, we also found that fast cooled samples tend to be more leaky. On the other hand, we found that, for 40 nm PZT films grown on $GdSCO_3$ (110) substrates, slow cooling results in $c/a$-type ferroelastic domain structures while fast cooling results in $c$-axis oriented mono-domain films. In general, the cooling rate was fixed at 5 °C/min and we did not change it during a new optimization process.

## An example of PLD Optimization Procedure

In our PLD setup, the optimal growth conditions for PZT drifted more frequently than those for SRO and STO. In this subsection, we present a real-life example of optimization of PZT growth on $SrTiO_3$ (002) substrate. Integral to the optimization procedure is the analysis of surface topography of the film using the atomic force microscopy (AFM) between subsequent growth iterations. We found that the surface morphology is the best indicator for film quality for the purpose of optimization. In this example, we show PZT growth optimization on STO substrates with respect to the most important PLD parameters: laser energy and repetition rate. In most cases, 5-15 growth iterations with different laser energies and repetition rates with all the other PLD parameters kept at the previously optimized values lead to optimized growth conditions for the new circumstances. In this particular instance, the initial growth conditions {100 mJ, 2 Hz} yielded PZT films with pinholes. The brute force approach is to explore the phase space of thin film quality with respect to the PLD parameters by performing growth iterations for different combinations of the

Table 2.2: A typical chart for the phase space of thin film quality with respect to the PLD parameters we used during PLD optimization. Populating this chart with thin film quality for each combination of the PLD parameters gives an idea about the new optimization window

| Laser energy per pulse→ Laser repetition rate ↓ | 2 Hz | 5 Hz | 10 Hz | 15 Hz |
|---|---|---|---|---|
| 80 mJ | | | | |
| 90 mJ | | | | |
| 100 mJ | | | | |
| 110 mJ | | | | |
| 120 mJ | | | | |

laser energy and the repetition rate. Table 2.2 shows a typical chart for the optimization. Populating this chart with thin film quality for each combination of the PLD parameters gives an idea about the new optimization window. The appearance of pinholes for the initial growth conditions: {100 mJ, 2 Hz} indicated that the laser energy and/or the repetition rate needed to be increased. Keeping all other PLD parameters the same, we first did growth iterations with repetition rates of 5 Hz, 10 Hz and 15 Hz. It was observed that, at 5 Hz, the film still had pinholes although less than that for 2 Hz. The 10 Hz film had moles (outgrowths). At 15 Hz, the moles got much bigger and denser. Hence, for the second iteration, we fixed the laser repetition rate at 5 Hz and grew three more films at the laser energies of 90 mJ, 110 mJ and 120 mJ. 90 mJ increased the density of pinholes, while 120 mJ created moles. 110 mJ resulted in a smooth surface without any pinholes and moles. Thusly, the new optimization {110 mJ, 5 Hz} was obtained.

## 2.5 Growth of Ferroelectric $Pb(Zr_{0.2}Ti_{0.8})O_3$ Thin Films

Lead zirconate titanate 20-80: $Pb(Zr_{0.2}Ti_{0.8})O_3$ (PZT) is a tetragonal perovskite (space group $P4mm$) with bulk tetragonal lattice parameters of $a_{PZT}$=$b_{PZT}$=3.93 $\dot{A}$ and $c_{PZT}$=4.13 $\dot{A}$ [41, 42]. It is a robust ferroelectric with spontaneous polarization $P_\circ$=$\sim$80 $\mu C/cm^2$, one of the highest values among all ferroelectrics. Figure 2.5(b) shows that the in-plane lattice parameter of PZT is conveniently placed in the spectrum of lattice parameters of commercially available substrates, $SrTiO_3$ (STO), $DyScO_3$ (DSO) and $GdScO_3$ (GSO) so that both compressive (STO) and tensile (DSO and GSO) strain can be applied by epitaxy [43]. Table 2.3 lists the in-plane pseudo-cubic lattice parameters of the substrates and epitaxial strain imposed on PZT by these substrates. For electrical measurements, PZT thin films were grown

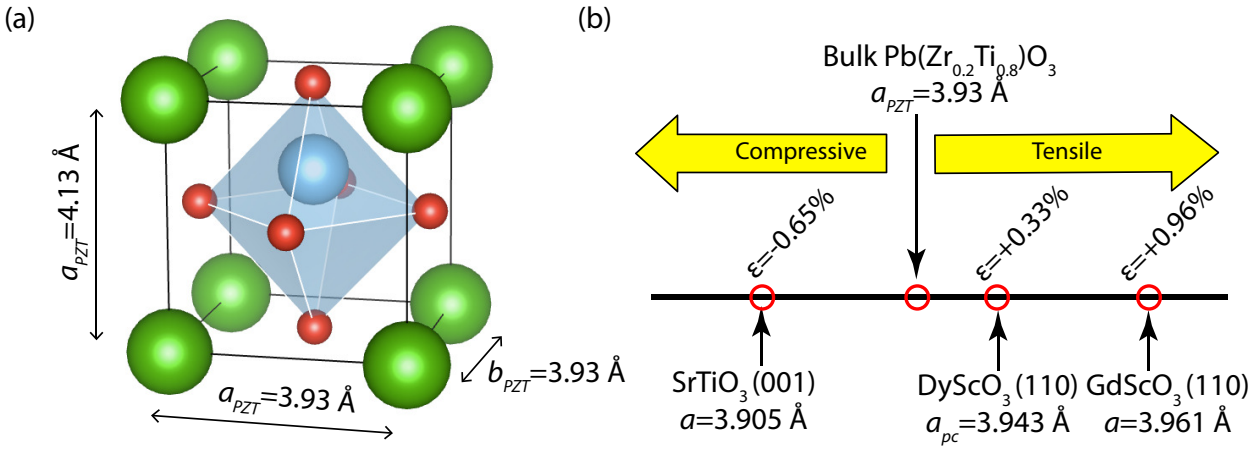


Figure 2.3: (a) Bulk lattice parameters of PZT. (b) Comparison of in-plane pseudo-cubic lattice constants of PZT and three different substrates, $SrTiO_3$ (001), $DyScO_3$ (110) and $GdScO_3$ (110).

on metallic $SrRuO_3$ (SRO) buffered substrates. SRO has a pseudocubic crystal structure with lattice parameter of 3.93 $\dot{A}$. During growth, the substrate was held at 720 °C for SRO and STO and at 630 °C for PZT. Lower growth temperature of PZT is adopted to prevent the evaporation of volatile Pb. PZT and SRO were grown in an oxygen environment at 100 mTorr.

Table 2.3: Epitaxial strain imposed by different substrates on PZT. Bulk in-plane lattice parameter of PZT is $a_{PZT}$=$b_{PZT}$=3.93 $\mathring{A}$.

| Substrate | In-plane pseudo-cubic lattice parameter $\mathring{A}$ | Epitaxial Strain |
|---|---|---|
| Strontium titanate ($SrTiO_3$, STO), (001) orientation | 3.905 | Compressive, -0.65% |
| Dysprosium scandate ($DyScO_3$, DSO), (110) orientation | 3.943 | Tensile, +0.33% |
| Gadolinium scandate ($GdScO_3$, GSO), (110) orientation | 3.961 | Tensile, +0.96% |

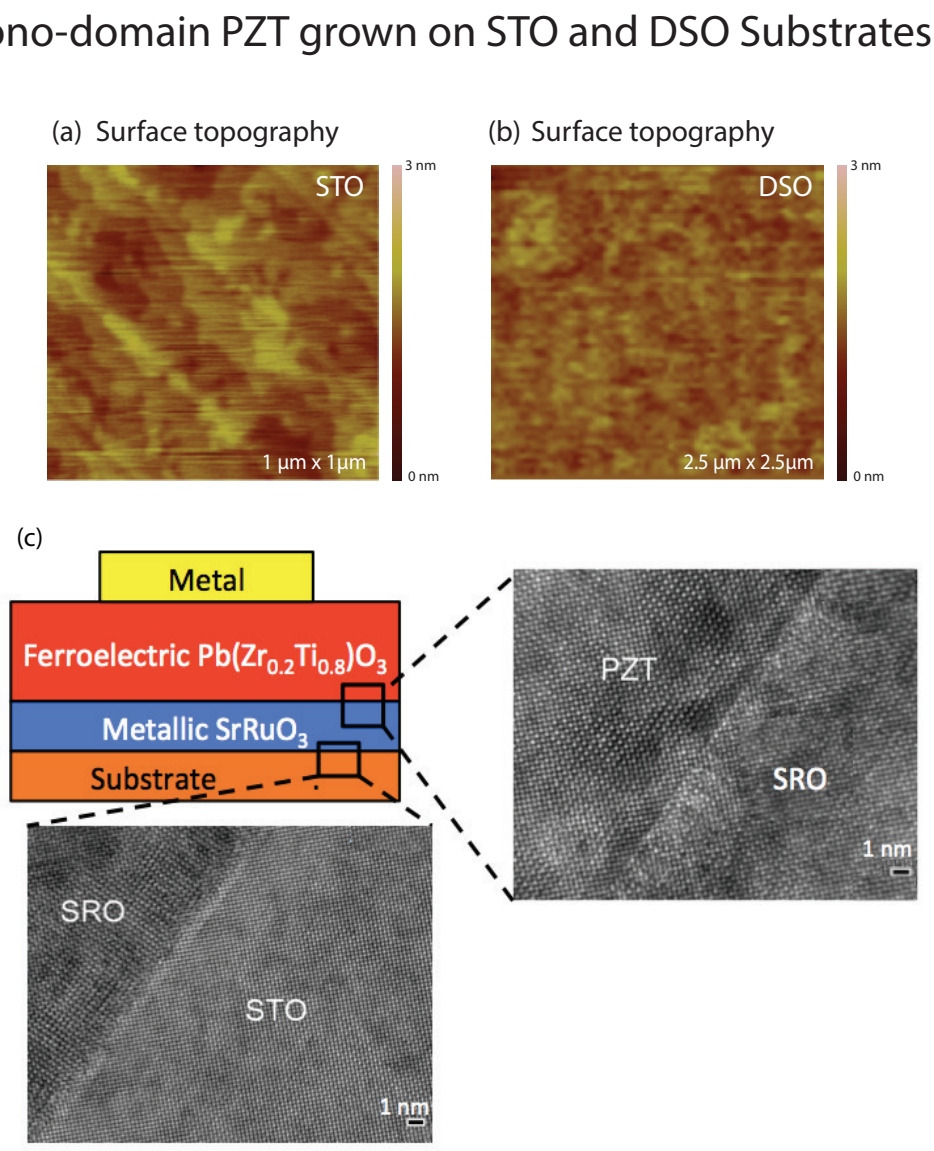


Figure 2.4: (a,b) Surface topography of PZT(40 nm)/SRO heterostructures on STO (a), DSO (b) substrates. (c) HRTEM image of representative PZT/SRO heterostructure on STO substrate

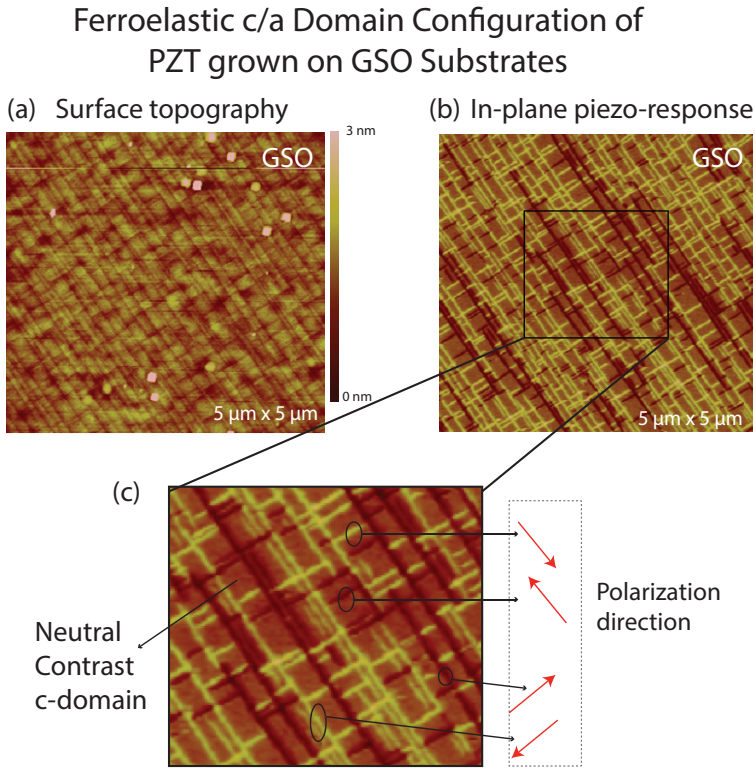


Figure 2.5: (a,b) AFM surface topography (a) and in-plane PFM image (b) of PZT(40 nm)/SRO heterostructures on GSO substrates. (c) Blown up image of a region in the in-plane PFM image shown in figure b. The in-plane contrasts (dark or bright) ensue only when there is an in-plane polarization component perpendicular to the AFM tip scan direction. In figure c, the PFM tip scan direction is along the X axis. The dark and bright contrast correspond the cases where the in-plane polarization component along the $Y$-axis is aligned along $+Y$ and $-Y$-directions respectively. A neutral contrast corresponds to the $c$-domain. Furthermore, the in-plane polarization is perpendicular to the stripe axis of the $a$-domain. The polarization directions in different regions are indicated as well.

## 2.6 Structural Characterization: Atomic Force, Piezo-response Force and Transmission Electron Microscopy

The surface topography obtained using atomic force microscopic technique of 40 nm PZT films grown on SRO buffered STO and DSO substrates are shown in figure 2.5(a,b) respectively. The roughness of all these samples are less than 0.3 nm. High resolution transmission electron microscopy (HRTEM) cross-sectional image of representative PZT/SRO heterostructure on STO substrate is shown in figure 2.5(c). These results of heterostructures grown on STO and DSO substrates confirm that these samples are mono-domain with the $c$-axis lattice parameter aligned along the out-of-plane direction with no undesired secondary. On the other hand, the GSO pseudo cubic template ($a_{pc} \approx b_{pc}$=3.968 Å)[44] imposes a +0.96% tensile misfit strain on PZT films. This tensile strain stabilizes a distinct ferroelastic $c_c/a_c$ type domain structures, where a dense square network of crossed narrow $a$-domains is embedded into a ferroelectric matrix with the tetragonal $c$-axis oriented perpendicular to the substrate. Figure 2.5(a,b) show the AFM surface topography and in-plane piezo-response force microscopy (PFM) image of the same 5 $\mu$m $\times$ 5 $\mu$m region on a 40 nm PZT film grown on SRO buffered GSO substrate. An interesting stripe like feature in figure 2.5(a) and the corresponding contrast in the in-plane PFM image in figure 2.5(b) are due to the $a$-domains present in the 40 nm PZT film grown on GSO. Figure 2.6(a) shows the out-of-plane and the in-plane PFM image on a 1.3 $\mu$m $\times$ 1.3 $\mu$m region on the same PZT film grown on GSO substrate and figure 2.6(b) shows the corresponding cross-sectional TEM image. Similar domain structure has previously been observed in PZT, but only for much thicker films ($\geq$ 100 nm)[45, 46, 47, 48, 49, 50, 51]. Figure 2.6(b) shows that the a-domains have a wedge-like shape, which is tapered at the PZT-SRO interface and the width of the $a$-domain is $\sim$15 nm at the free surface.

## 2.7 Structural Characterization: X-Ray Diffraction

In the previous section, we presented AFM, PFM and TEM based studies, which show that the epitaxial strain imposed by STO and DSO substrates results in a mono-domain structure in PZT film in the thickness range:30-80 nm, while the tensile strain from the GSO (110) substrates result in a polydomain ferroelastic $c_c/a_c$ domain configuration in the same thickness range. In this section, we study the X-ray diffraction spectrum of these films. Figure 2.7 shows the X-ray diffraction (XRD) spectrum around (002) reflections of PZT heterostructures grown on different substrates. We observe in figure 2.7 that as the substrate is changed from GSO to DSO and then to STO, the (002) peak of the PZT thin film systematically moves towards larger $2\theta$ values indicating the elongation of the PZT unit cell along the $c$-axis direction with an increasing compressive strain (or a decreasing tensile strain). Figure 2.8(a,b,c) show the reciprocal space maps (RSMs) around (103) reflections of

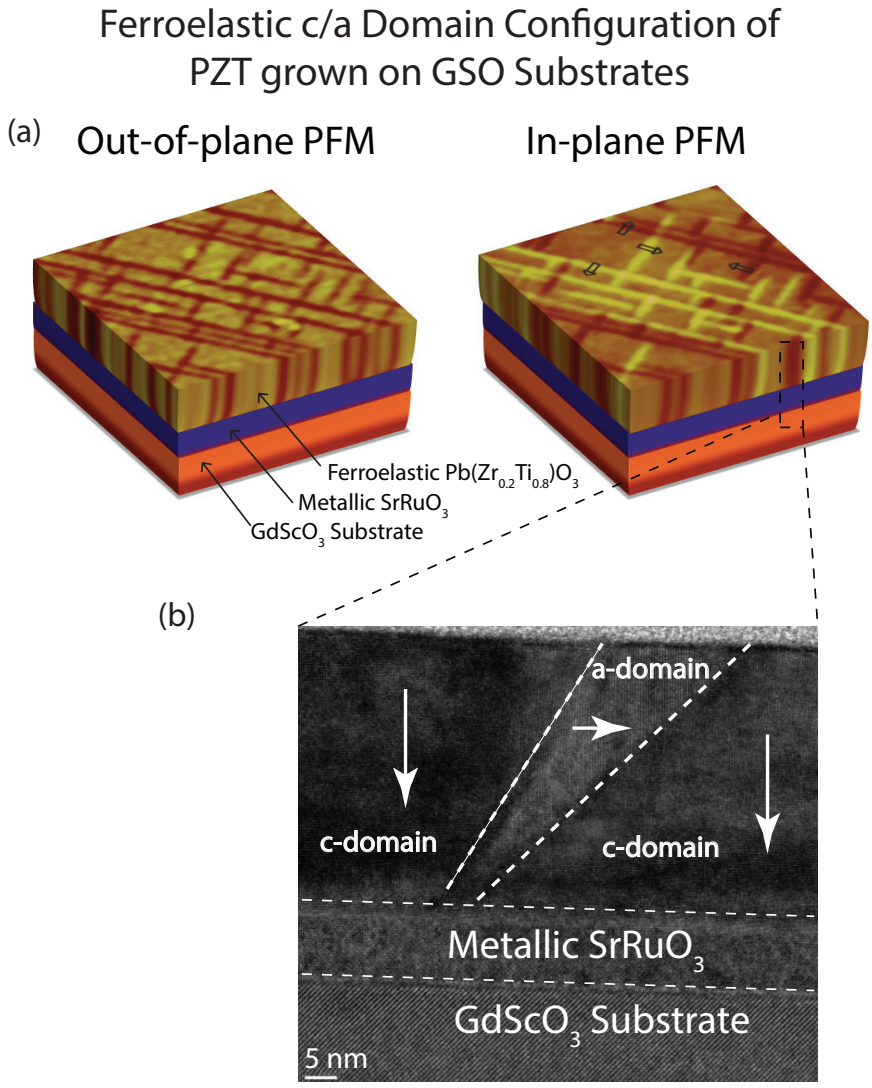


Figure 2.6: (a) The out-of-plane and in-plane PFM images of a 1.3 $\mu$m $\times$ 1.3 $\mu$m area of PZT film grown on GSO substrate in the as-grown state. The stripe-like features are the a-domains. (b) Cross-sectional TEM image of a 40 nm PZT film grown on GSO substrate. The polarization directions in c- and a-domains are indicated using arrows.

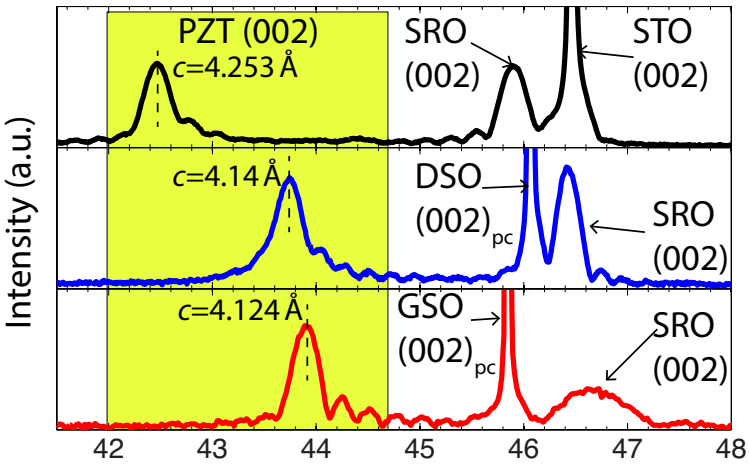


Figure 2.7: X-ray diffraction spectrum of 40 nm PZT fims grown on SRO buffered STO (001), DSO (110), and GSO (110) substrates. "pc" in subscript notation in the Miller indices refer to "pseudo-cubic."

the heterostructures grown on STO, DSO and GSO substrates, respectively. In (103) RSMs of the PZT grown on STO and DSO substrates shown in figure 2.8(a,b), the reflections corresponding to only the *c*-domains are observed, which further confirms the mono-domain structure of 40 nm PZT film grown on STO and DSO substrates. We note in figure 2.8(c,d) that satellite peaks corresponding to *a*- domains in the PZT films grown on GSO substrate are also observed. Nonetheless, we observe in figure 2.8(a,b,c) that the (103) peaks of PZT *c*-domain, SRO and substrate align along a constant $Q_x$ line confirming that, within the resolution limit of the X-ray diffractometer, there is no observable relaxation of the epitaxial strain in the PZT and the SRO layers in these samples. This is true even for the case of the polydomain PZT film grown on GSO, where the volume fraction of the *a*-domain calculated from the RSM and PFM images (d) is ∼3%. .

## 2.8 Calculation of PZT Average Lattice Parameters from X-Ray Diffraction Techniques

### (002) and (013) reflections from the *c*-domains:

Figure 2.9(a) and 2.9(b) show the schematic diagrams of the unit cells of a *c*- and an *a*-domain respectively. The (002) and (013) planes of the *c*-axis oriented unit cell and the (002) and (013) planes of the *a*-axis oriented unit cell are shown in figure 2.9(a) and 2.9(b) respectively. The lattice parameters along different axes are also indicated in figure 2.9(a,b).

For the *c*-domains, the (002) and (013) reflections occur at

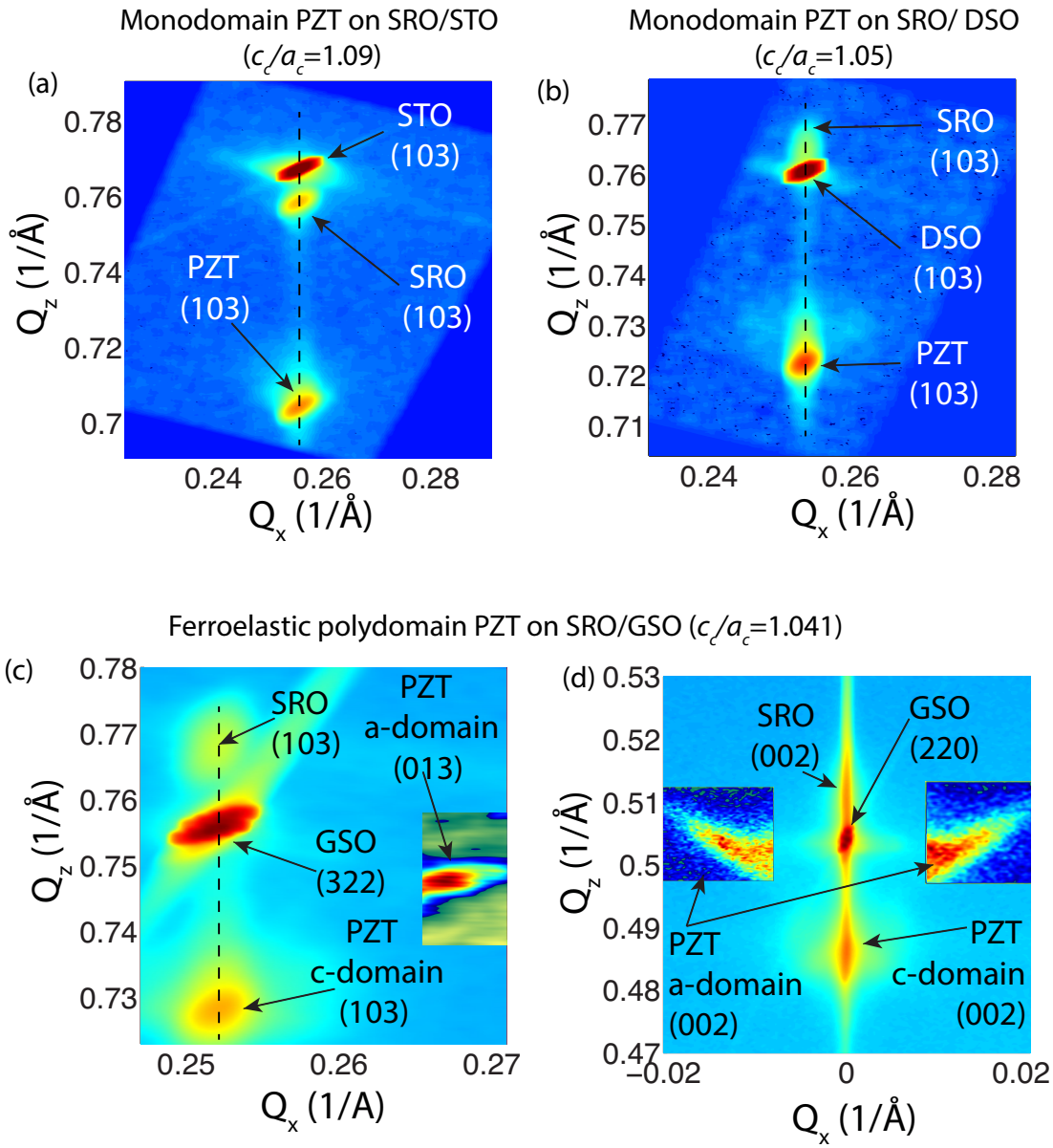


Figure 2.8: (a,b,c) Reciprocal space maps around (103) peaks of PZT(40 nm)/SRO heterostructures grown on STO (a), DSO (b) and GSO (c). (d) Reciprocal space maps around (002) peaks of PZT(40 nm)/SRO heterostructures grown on GSO.

$$(Q_x, Q_y, Q_z)_{(002)} \equiv (0, 0, \frac{2}{c_c}) \tag{2.1}$$

$$(Q_x, Q_y, Q_z)_{(013)} \equiv (0, \frac{1}{a_c}, \frac{3}{c_c}) \tag{2.2}$$

The average lattice parameters of the $c$-domains of the PZT samples grown on different substrates and whose RSM's are plotted in figure 2.10 are calculated using equation 2.1 and 2.2 and are listed in table 2.3.

## (002) reflections from the $a$-domains:

The structural continuity at the interface between $c$- and $a$-domains requires that $a$-domains are rotated at an angle $\alpha$ with respect to the interface. For the (002) plane, the real space direction vectors, $\vec{a_i}$ $(i \equiv 1, 2, 3)$ are given as:

$$\vec{a_1} = a_a\hat{x}; \vec{a_2} = c_a \cos\alpha\hat{y} + c_a \sin\alpha\hat{z}; \vec{a_3} = -\frac{a_a}{2}\sin\alpha\hat{y} + \frac{a_a}{2}\cos\alpha\hat{z} \tag{2.3}$$

Here, $\vec{a_1}$ and $\vec{a_2}$ lie in the (002) plane and $\vec{a_3}$ is perpendicular to the (002) plane. The reciprocal lattice vector $\vec{Q}$ is given by $\vec{Q} = (\vec{a_1} \times \vec{a_2})/V$ where, $V = a_a^2 c_a/2$. This leads to $(Q_x, Q_y, Q_z)_{(002)} \equiv (0, -\frac{2}{a_a}\sin\alpha, \frac{2}{a_a}\cos\alpha)$ and a corresponding contour equation of

$$Q^2_{y,(002)} + Q^2_{z,(002)} = (\frac{2}{a_a})^2 \tag{2.4}$$

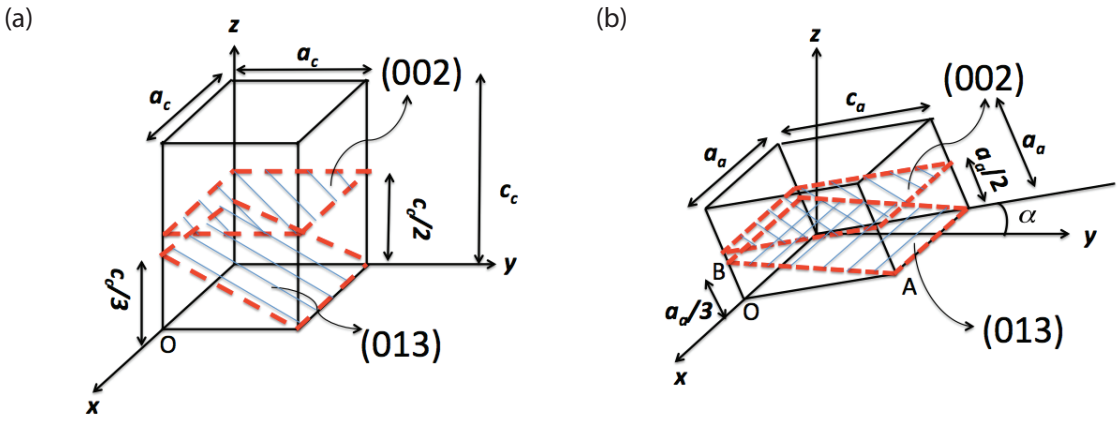


Figure 2.9: (a,b) Schematic diagram of the unit cells of a $c$- (a) and an $a$-domain (b). The (002) and (013) planes of the $c$-axis oriented unit cell and the (002) and (013) planes of the $a$-axis oriented unit cell are shown in figure (a) and (b) respectively. The lattice parameters along different axes are also indicated.

Table 2.4: Lattice parameters and strain.

| Substrate | Strain (%) | $c_c$ (Å) | $a_c$ (Å) | $c_a$ (Å) | $a_a$ (Å) | $c_c/a_c$ |
|---|---|---|---|---|---|---|
| STO (001) | -0.65 | 4.257 | 3.905 | – | – | 1.09 |
| DSO (110) | +0.33 | 4.14 | 3.943 | – | – | 1.05 |
| GSO (110) | +0.96 | 4.124 | 3.961 | 4.08 | 3.973 | 1.041 |

The constant $\alpha$ contour is given by:

$$\alpha = \pm \tan^{-1} \frac{Q_{y,(002)}}{Q_{z,(002)}} \tag{2.5}$$

### (013) reflections from the $a$-domains:

For the (013) plane, the real space direction vectors, $\vec{a_i}$ are given by:

$$\vec{a_1} = (-\frac{a_a}{3}\sin\alpha - c_a\cos\alpha)\hat{y} + (\frac{a_a}{3}\cos\alpha - c_a\sin\alpha)\hat{z}; \vec{a_2} = a_a\hat{x}; \vec{a_3} = \frac{\vec{a_1}\times\vec{a_2}}{|\vec{a_1}\times\vec{a_2}|}d_{013} \tag{2.6}$$

where $d_{013}$ is the distance between subsequent (013) planes. From this, the reciprocal lattice vectors are found to be $(Q_x, Q_y, Q_z)_{(013)} \equiv (0, (\frac{1}{c_a}\cos\alpha - \frac{3}{a_a}\sin\alpha), (\frac{1}{c_a}\sin\alpha + \frac{3}{a_a}\cos\alpha))$ which leads to a contour equation of

$$Q^2_{y,(013)} + Q^2_{z,(013)} = (\frac{1}{c_a})^2 + (\frac{3}{a_a})^2 \tag{2.7}$$

### Estimation of the average lattice parameters:

The zoomed-in versions of the (002) and (013) reflection lobes corresponding to $a$-domains of the 40 nm PZT film grown on SRO/GSO in figure 2.8(d,c), respectively are replotted in figure 2.10(a,b), respectively. The average $a$-domain $a$-axis lattice parameter, $a_a$ is calculated by drawing the constant $a_a$ contour (equation 2.4) through the peak intensity points of the $a$-domain (002) lobes in figure 2.10(a). Using this $a_a$ value, the corresponding average $a$-domain $c$-axis lattice parameter, $c_a$ is calculated by drawing the constant $(c_a, a_a)$ contour (equation 2.7) through the peak of the $a$-domain (013) lobe in figure 2.10(b).

## 2.9 Effects of Epitaxial Strain on PZT $c$-domain Structural Parameters

Table 2.4 list of the average lattice parameters of the $c$-domain ($c_c$, $a_c$) and the $a$-domain ($c_a$, $a_a$) of the 40 nm PZT films grown on SRO buffered substrates. Figure 2.11(a) plots

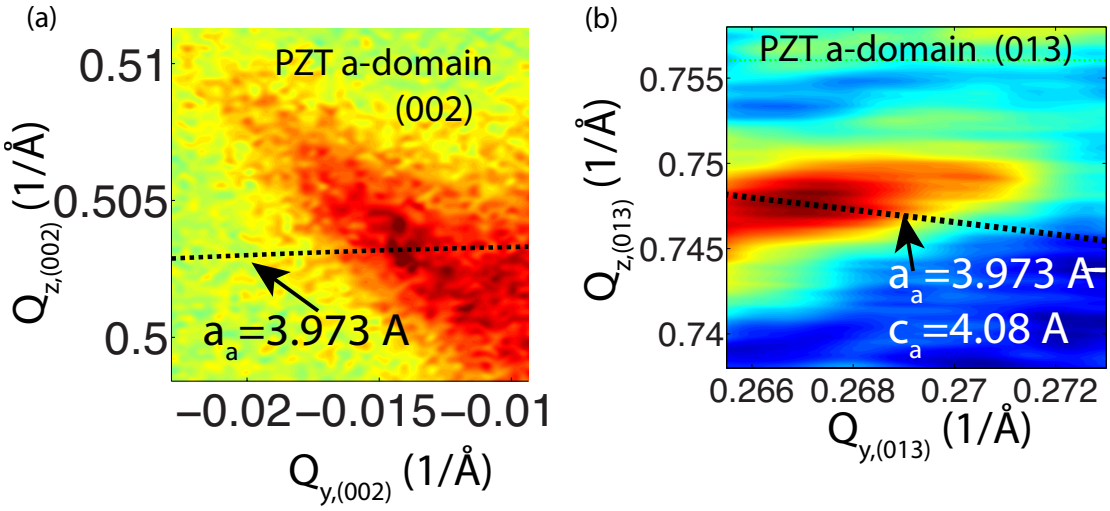


Figure 2.10: (a,b) The *a*-domain lobes corresponding to (002) (a) and (013) (b) reflections.

the *c*-axis lattice parameter of PZT *c*-domain as a function of the substrate in-plane lattice parameter. The PZT tetragonality $c_c/a_c$ is plotted as a function of the epitaxial strain in figure 2.11(b). Figure 2.11(b) shows that the strain driven structural modification is such that the tetragonality systematically decreases with an increasing tensile strain (or a decreasing compressive strain) as expected for a material with a positive Poisson ratio. Figure 2.11(b) indeed confirms that the tetragonality is sensitive to the epitaxial strain.

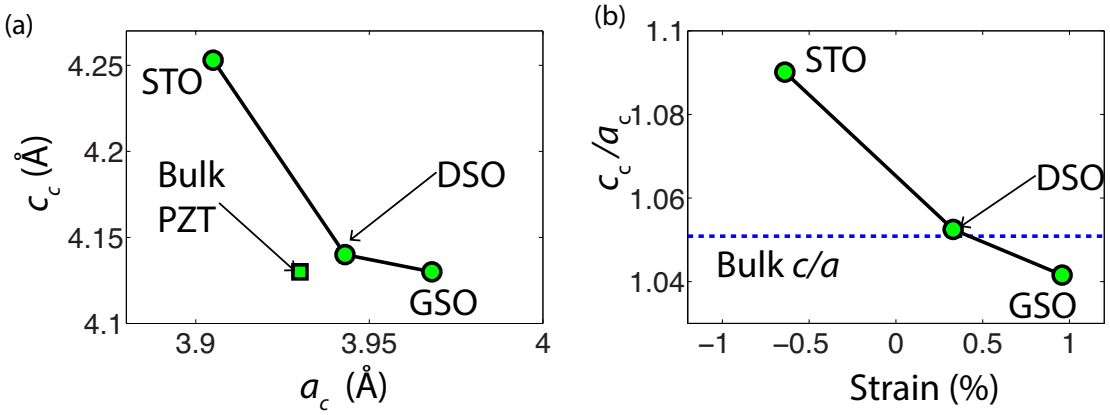


Figure 2.11: (a) PZT c-axis parameter as a function of the substrate in-plane lattice parameter. (b) Tetragonality of PZT thin films as a function of epitaxial strain.

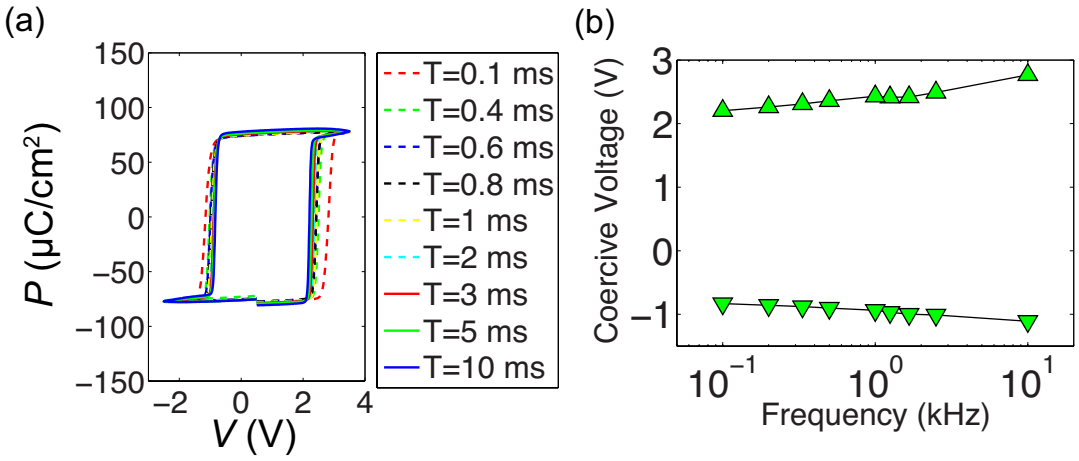


Figure 2.12: (a) The polarization ($P$)-voltage ($V$) hysteresis curve of the ferroelectric at different loop periods ($T$) measured using a Sawyer-Tower type setup. (b) Coercive voltages as functions of the measurement frequency ($=1/T$).

## 2.10 Measurement of the Spontaneous Polarization

The ferroelectric hysteresis loop is traditionally measured using the Sawyer-Tower technique [52]. Figure 2.12(a) shows the ferroelectric hysteresis loop of a PZT film grown on SRO buffered STO (001) substrate at different loop periods ($T$) measured by this technique using a Radiant Precision Multiferroic tester. The spontaneous polarization $P_\circ$ is measured to $\sim$82 $\mu$C/cm$^2$. Similar values of $P_\circ$ was reported by reference [53]. Figure 2.12(b) shows the coercive voltages as functions of the measurement frequency ($=1/T$).

## 2.11 Dielectric characterization and frequency dispersion

Figure 2.14(a, b, c, d) show the dielectric constant-voltage and the admittance angle-voltage characteristics of the PZT(60 nm)/SRO(60 nm)/STO(001) at 1 kHz, 10 kHz, 100 kHz and 1 MHz respectively. In figure 2.14(a-d), we observe that the admittance angle is $\sim 90^0$ at all frequencies.

Another technique that is widely used to characterize the defects in ferroelectrics is the Rayleigh analysis [54, 55, 56]. The basis of this analysis is that, due to the movement of the defects in response to an AC electric field $E_0$, the dielectric constant of a ferroelectric increases as $E_0$ increases even when $E_0$ is smaller the coercive field. Figure 2.15 shows the dielectric constant $\varepsilon_r$ as a function the AC electric field $E_0$ at 10 kHz. We observe that as

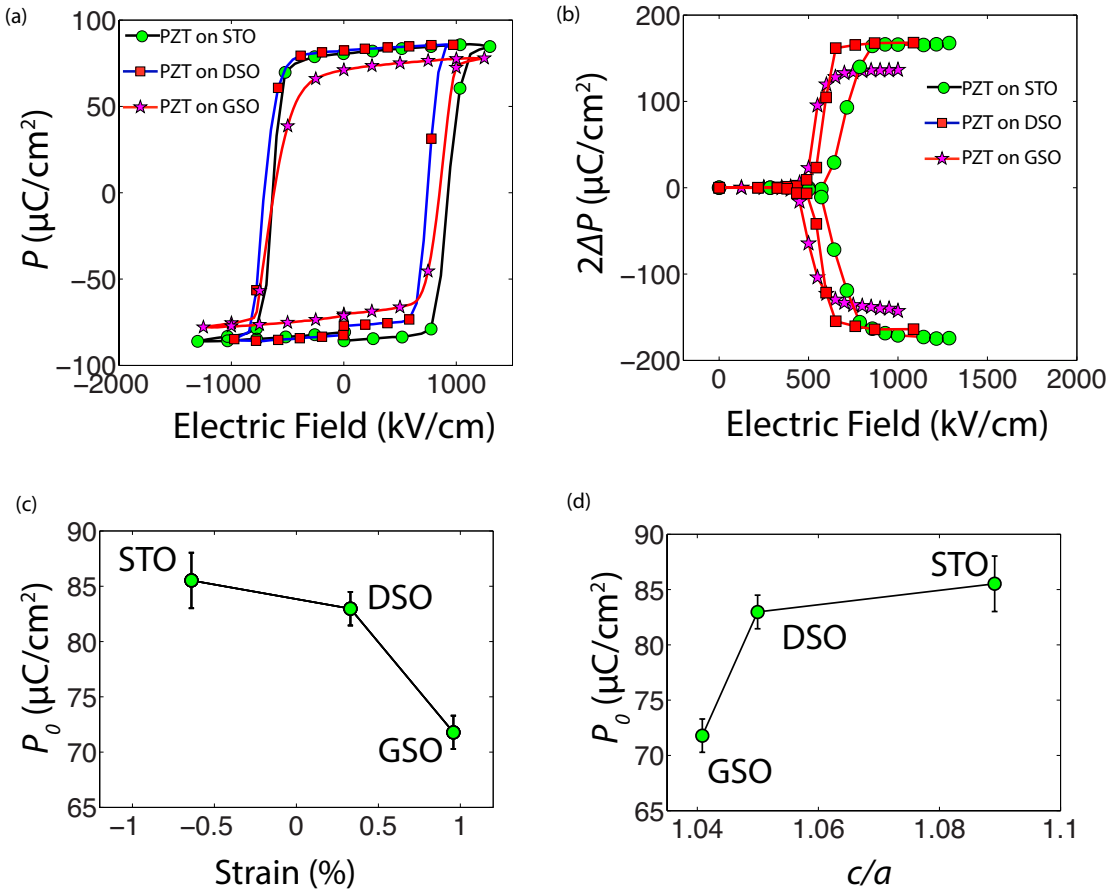


Figure 2.13: (a) Ferroelectric polarization ($P$)-electric field ($E$) characteristics of PZT samples grown on different substrates. (b) Switchable ferroelectric polarization ($2\Delta P$) measured using the PUND schemes a function of electric field ($E$) of PZT samples grown on different substrates. (c) Remnant polarization measured from PUND measurements $P_0$ as a function of $c_c/a_c$. The PZT error bar refer to the standard deviation of $P_0$ over a device set in the same sample. (d) $P_0$ as a function of the tetragonality.

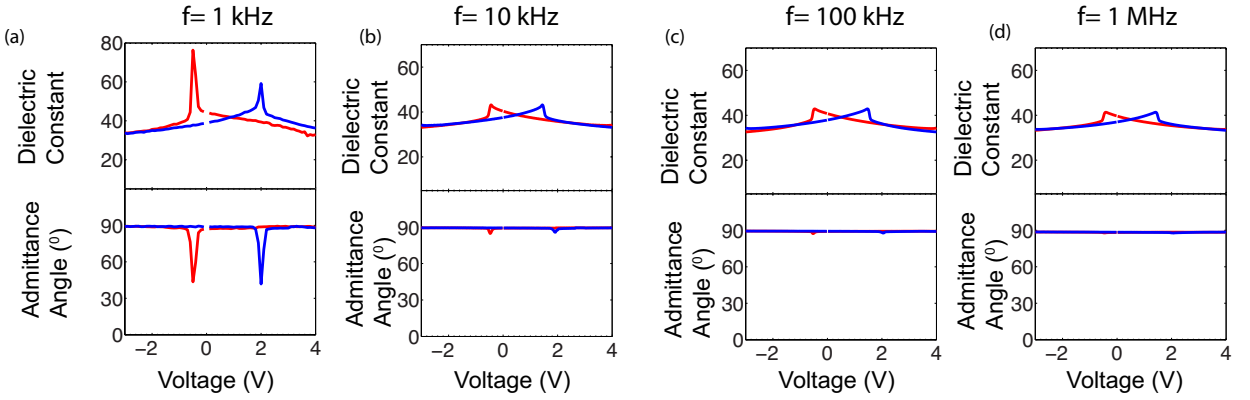


Figure 2.14: (a,b,c,d) Dielectric constant-voltage and the admittance angle-voltage characteristics of the PZT sample at 1 kHz (a), 10 kHz (b), 100 kHz (c) and 1 MHz (d).

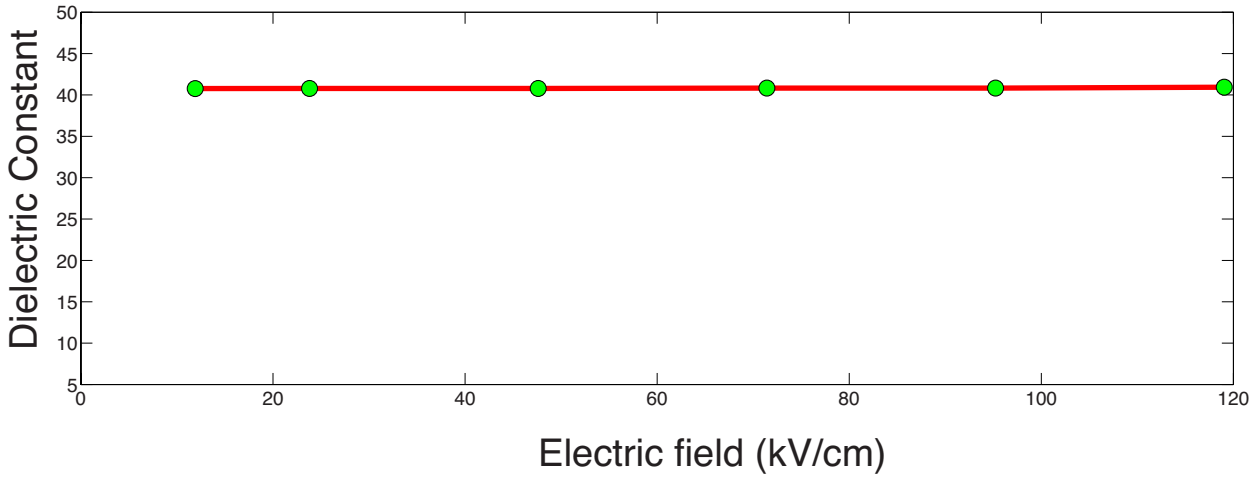


Figure 2.15: The dielectric constant $\varepsilon_r$ as a function the AC electric field $E_0$ at 10 kHz.

the AC electric field is increased from 10 kV/cm to ∼120 kV/cm, the dielectric constant increases by a mere 0.4% for this sample.

## 2.12 Effects of Epitaxial Strain on PZT Spontaneous Polarization

Figure 2.13(a) shows the polarization-electric field hysteresis loops for 40 nm PZT films grown on SRO buffered STO (001), DSO (110) and GSO (110) substrates measured with a Sawyer-Tower circuit (using a Radiant Precision Multiferroic test system). Because the

Sawyer-Tower type measurement of ferroelectric hysteresis can be corrupted by leakage effects, the positive up negative down (PUND) scheme was also employed to measure the remnant polarization with the same test system. Figure 2.13(b) shows PUND measurements for the samples. Figure 2.13(a,b) show that the remnant polarization of PZT on GSO ($\sim$69 $\mu$C/cm$^2$) is lower than that on both DSO and STO. Given the $a$-domains constitute $\sim$4% of the entire PZT volume, the polarization of PZT $c$-domains is $\sim$72 $\mu$C/cm$^2$. Figure 2.13(c,d) plot the remnant polarization $P_0$ as a function of the epitaxial strain and the tetragonality, respectively. We note in figure 2.10(d) that, as the substrate is changed from GSO to DSO with the corresponding change of $c_c/a_c$-1 from 0.041 to 0.05 ($\sim$16% increase) of the c-axis oriented domains, remnant polarization increases by $\sim$20%. In comparison, when the substrate is changed from DSO to STO with the corresponding change of $c_c/a_c$-1 from 0.05 to 0.089 ($\sim$74% increase), remnant polarization increases by $\sim$3%. This points to the fact that, while the tetragonality is significantly sensitive to epitaxial strain, the strain sensitivity of ferroelectric polarization is significantly less in the range $c_c/a_c$=1.05-1.09 than in the range $c_c/a_c$=1.041-1.05.

It is important to note that the effects of epitaxial strain on ferroelectricity have been widely studied. Polarization-strain coupling in ferroelectric materials is not fully understood yet and there are open questions, such as what the origins are of the differences in the strain sensitivity of ferroelectricity in different material systems. The coupling between strain and ferroelectricity is of intrinsic nature, the theoretical basis of which lies in the Landau-Ginzburg theory [57]. Epitaxial strain renormalizes the second- and the fourth-order polarization terms of the Gibbs free energy expansion, leading to a modification of the paraelectric-ferroelectric phase transition temperature and hence ferroelectric polarization [57]. Strain sensitive ferroelectricity in $BaTiO_3$ and $SrTiO_3$ is a wonderful testament to this theory [58, 43]. However, highly polar ferroelectrics such as $Pb(Zr_{0.2}Ti_{0.8})O_3$ is an interesting exception where such strong sensitivity to epitaxial strain does not hold true [59, 60]. At this point, it is interesting to compare our results with those in Lee *et al.* [60]. Lee *et al.*[60] studied the evolution of the strain in epitaxial PZT in the thickness range 15-200 nm and the control of the tetragonality of $c$-axis oriented PZT thin films grown on STO was achieved by controlled strain relaxation with increasing PZT thickness. It was shown that in the PZT tetragonality range $c_c/a_c$=1.05-1.09, the polarization is nearly independent of the strain ($P_0 \approx 82$ $\mu$C/cm$^2$). On the other hand, we took recourse to a second method of controlling the tetragonality, where we kept the thickness the same but varied the epitaxial strain by changing the substrate. In this case, it is possible to study the polarization-strain coupling in epitaxial films with minimal misfit dislocations though our choice a film thickness (40 nm) which is below the strain relaxation length. Nonetheless, our work extends the study by Lee *et al.*[60] of the nature of polarization-strain coupling in PZT into the tetragonality range $c_c/a_c$=1.041-1.05. Our work shows that, while, in the tetragonality range $c_c/a_c$ = 1.05-1.09, PZT remnant polarization is nearly independent of the tetragonality, as it has been reported previously, in the range $c_c/a_c$ = 1.041-1.05, remnant polarization is found to show a much stronger functional dependence. This points to the fact that the strain sensitivity of the

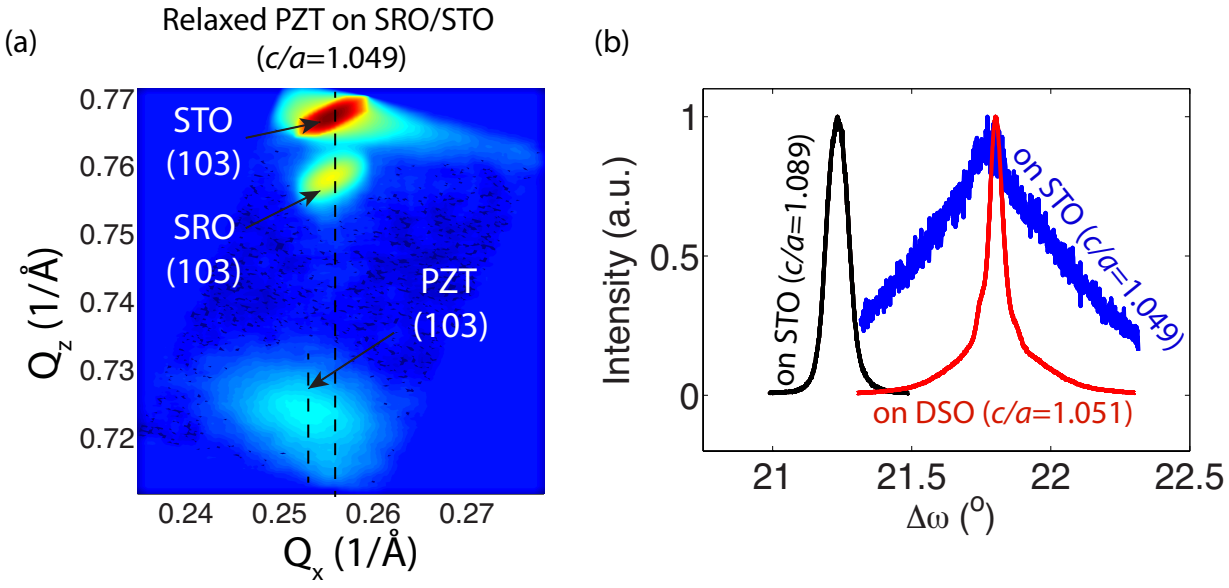


Figure 2.16: (a,b,c,d) Dielectric constant-voltage and the admittance angle-voltage characteristics of the PZT sample at 1 kHz (a), 10 kHz (b), 100 kHz (c) and 1 MHz (d).

polarization even in the same ferroelectric material can depend on the value of tetragonality and the sensitivity is larger for smaller values of the tetragonality.

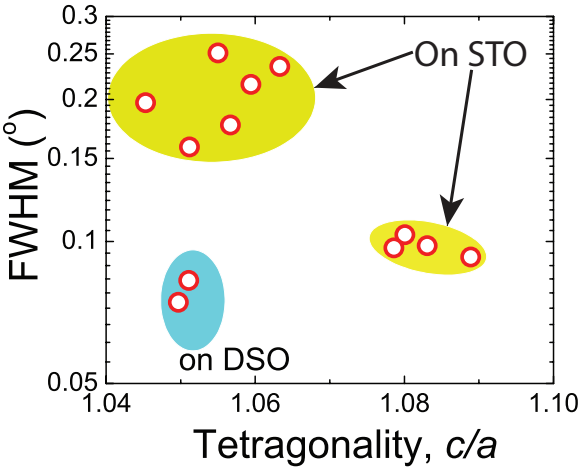


Figure 2.17: FWHM around PZT (002) peaks as a function of tetragonality ($c_c/a_c$) for PZT (40 nm)/SRO heterostructures grown on STO and DSO substrates.

## 2.13 Strain Relaxed PZT Films grown on STO (001) Substrates

We observed that PZT films often becomes strain relaxed due to minute variation of growth conditions when grown on STO (001) substrates. Figure 2.16(a) shows the reciprocal space map of a relaxed 40 nm PZT film grown on SRO buffered STO substrate around (103) peaks. We observe in figure 2.16(a) that the PZT (103) peak occurs at a smaller $Q_x$ than the STO (103) peak in this sample indicating that the PZT layer is not epitaxially coherent to the substrate. This is in contrast with the (103) RSM of 40 nm PZT film grown on SRO buffered STO substrate shown in figure 2.8(a), where the PZT film was fully strained to the substrate. Figure 2.16(b) shows the rocking curve measurements around the PZT (002) peaks in fully strained 40 nm PZT films grown on STO and DSO substrates and the 40 nm relaxed PZT film grown on STO substrate. We observe in figure 2.16(b) that the relaxed PZT film has a full-width-at-half-maximum (FWHM) much larger than those for both of the other two strained PZT films. The FWHM is a measure of the crystalline quality of a film. The relaxation of strain in thin films generally occurs through the formation of misfit dislocations which degrade the crystalline quality, thereby increasing the FWHM. The defect microstructure in ferroelectric thin films was studied in details in Ref. [61, 62]. These misfit dislocations are generally located at the interface between SRO and PZT layers,[61] which results in a significant distortion of local strain field. Using X-ray micro diffraction techniques on 30 nm $Pb(Zr_{0.3}Ti_{0.7})O_3$ films grown on SRO buffered STO (001) substrates, Do *et al.*[63] showed that in the regions of the ferroelectric film where a significant relaxation of strain occurs, the $Pb(Zr_{0.3}Ti_{0.7})O_3$ (002) reflection becomes broader in rocking curve measurements and the out-of-plane lattice parameter decreases by 0.3%, which is in agreement with our observations.

We indeed observed that even when 40 nm PZT films were grown directly on STO substrates without SRO buffer layers, the tetragonality of PZT films obtained from different growth runs varied in the range 1.045-1.09. In order to understand this variation, we note that the strain relaxation length of PZT on STO, $l_{PZT-STO}$, has been reported to be ∼40 nm [60]. In epitaxial growth processes, as the film thickness approaches the strain relaxation length, minute alteration of the kinetics caused by the slight variations of process parameters might often cause the epitaxial strain to relax. Hence we attribute this variation of strain state (strained or relaxed) in our 40 nm PZT films on STO to the stochastic variation of our PLD process parameters. We did not observe such a variation in the lattice parameter of our $Pb(Zr_{0.2}Ti_{0.8}$ films thicker than 80 nm grown on STO substrates and those thick samples were found to be relaxed with $c \approx 4.14\ \dot{A}$ and $c/a \approx 1.045$ (results not shown). We also note that the tetragonality of 40 nm PZT films on STO reported by different groups lies in the range 1.045-1.09 (for example $c_c/a_c$=1.045 [64], 1.087 [60] and 1.075 [65]). This is further underpinned by the fact that in PZT samples grown on DSO substrates (strain relaxation length> 40 nm due to the smaller lattice mismatch) under the same growth conditions, such

a large variation in PZT lattice parameters was not observed. Figure 2.17 plots the FWHM around the PZT (002) peak of a set of PZT films grown on SRO buffered STO and DSO substrates as a function of PZT $c_c/a_c$. In figure 2.17, we observe that the PZT films on STO with $c_c/a_c$ in the range 1.07-1.089 consistently show a narrower FHWM (FWHM $\leq\sim 0.1^0$) than those of the samples with $c_c/a_c$ in the range 1.045-1.007 (FWHM$\geq\sim 0.15^0$). This suggests that there is a significant increase in the defect and dislocation density as $c_c/a_c$ of PZT grown on STO goes below 1.07. We also note in figure 2.17 that 40 nm PZT films grown on DSO substrates consistently show FWHM $\leq 0.1^0$. This rules out the possibility that there might be an intrinsic connection between the $c_c/a_c$ value and the FWHM.

## 2.14 Comparison of Dielectric Properties of Strained and Relaxed PZT Films grown on STO (001) Substrates

In this section, we compare the dielectric properties of strained and relaxed PZT films. Figure 2.18(a) shows the dielectric constant $\varepsilon_r$ of the PZT films as a function of the electric field at 100 kHz. We refer to the cross point of the up- and the down-sweep of the $\varepsilon_r$-electric field curves as the nominal $\varepsilon_r$ of a sample. Figure 2.18(b,c) show the frequency dispersion of the dielectric constant of the samples. In figure 2.18(c), the dielectric constant is normalized with respect to the dielectric constant of the respective sample at 1 MHz. Both of the strained samples on STO and DSO show a frequency dispersion $((\varepsilon_{r,10kHz} - \varepsilon_{r,1MHz})/\varepsilon_{r,1MHz}))$ of $\sim$4%, whereas the relaxed sample on STO shows a frequency dispersion of $\sim$12%. Figure 2.18(d) shows the frequency dispersion as a function of the tetragonality, $c_c/a_c$. Figure 2.18(d) clearly shows that there is a drastic increase in the frequency dispersion as $c_c/a_c$ of PZT films grown on STO decreases below 1.07. The frequency dispersion of $\varepsilon_r$ is usually attributed to the extrinsic mechanisms such as defects and dislocations in insulating thin films. This aforementioned trend of frequency dispersion underpins the fact that the extrinsic mechanisms become more dominant for $c/a$ <1.07 in PZT films grown on STO as was observed in figure 2.17.

The Rayleigh relations are frequently employed to study the extrinsic contributions due to defects to the dielectric response in ferroelectric films [55, 66]. In this analysis, the dependence of the dielectric constant on the sub-coercive AC electric field excitation $E_0$ is studied using the following relation.

$$\varepsilon_r - \varepsilon_r^0 = \alpha E_0 \tag{2.8}$$

where $\varepsilon_r^0$ and $\alpha$ are the intrinsic component of the dielectric constant and the Ralyleigh coefficient respectively. $\alpha$ is a measure of the extrinsic contributions to the dielectric properties. The larger the value of $\alpha$, the more dominant the effects of defects on the overall electrical

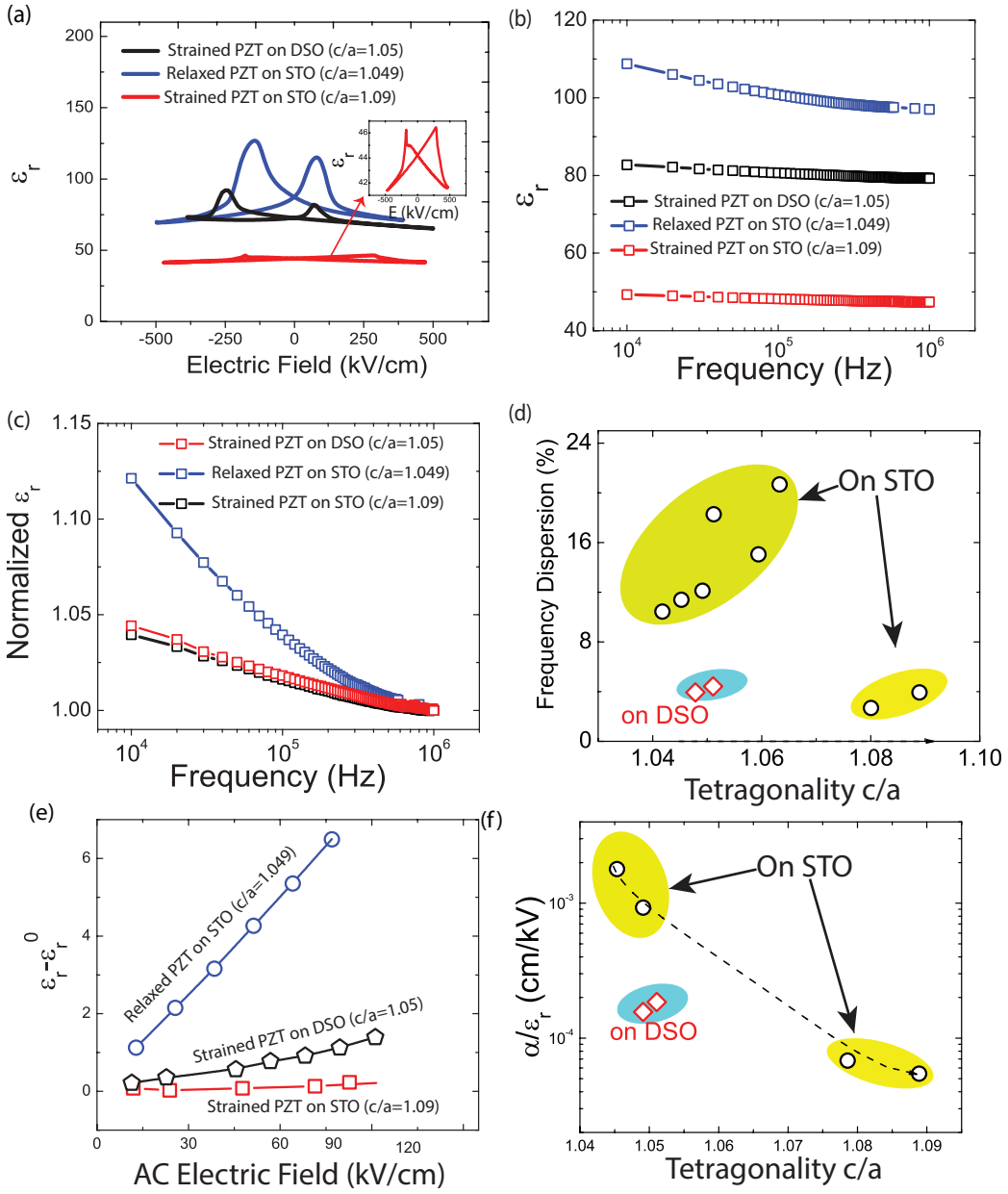


Figure 2.18: (a) Comparison of dielectric constant ($\varepsilon_r$)-electric field characteristics of strained PZT films grown on STO and DSO substrates and a relaxed PZT film grown on STO substrate. (b,c) Dielectric constant (b) and normalized dielectric constant (c) as functions of the frequency. (d) Frequency dispersion of the PZT films as a function of the tetragonality $c_c/a_c$. (e) Comparison of $(\varepsilon_r - \varepsilon_{r,0})$-AC electric electric field characteristics of strained PZT films grown on STO and DSO substrates and a relaxed PZT film grown on STO substrate. (f) $\alpha/\varepsilon_r$ of PZT samples as a function of tetragonality $c_c/a_c$.

properties of the film. Figure 2.19(e) plots $\varepsilon_r - \varepsilon_r^0$ as a function of $E_0$ for the PZT samples at 100 kHz. It is clear that that $\varepsilon_r$ is more sensitive to the AC electric field excitation in the relaxed PZT film than in the strained ones. Figure 2.19(e) shows the variation of $\alpha/\varepsilon_r$ as a function of tetragonality. We observe in figure 2.19(e) that $\alpha/\varepsilon_r$ is almost an order of magnitude higher in the relaxed PZT films compared to that in strained films.

Previous studies on the effects of strain relaxation in PZT films showed that the remnant polarization and the phase transition temperature depend weakly on the strain state of the film [60, 64]. On the other hand, our results indicate that the dielectric properties of ferroelectric films are more strongly affected by extrinsic mechanisms such as defects and dislocations. Given that strain relaxation plays an important role in the fatigue mechanism of epitaxial ferroelectric thin films [63], similar dielectric characterization can provide useful insights in the study of fatigue. Nonetheless, in this study, we investigated the correlation between the structural and the dielectric properties in a set of 40 nm PZT films that are either strained or relaxed to the misfit substrates. A drastic increase in defect and dislocation density due to strain relaxation is observed in epitaxial PZT films with tetragonality $c/a < 1.07$ grown on STO substrates, which results in a significant frequency dispersion of the dielectric constant and a strong Rayleigh type behavior in those samples. For a given combination of a ferroelectric thin film and a substrate, tetragonality $c_c/a_c$ is a quantitative measure of the degree to which epitaxial strain has been relaxed in the film and the extent of extrinsic contributions to the dielectric properties can be predicted from the value of $c_c/a_c$.

## 2.15 Voltage Controlled Ferroelastic Switching in Polydomain PZT Films grown on SRO buffered GSO (110) Substrates

In sections 2.5 and 2.6, we have seen that the tensile strain imposed by the GSO (110) substrate stabilizes an interesting $c/a$ type polydomain structure. In this section, we study

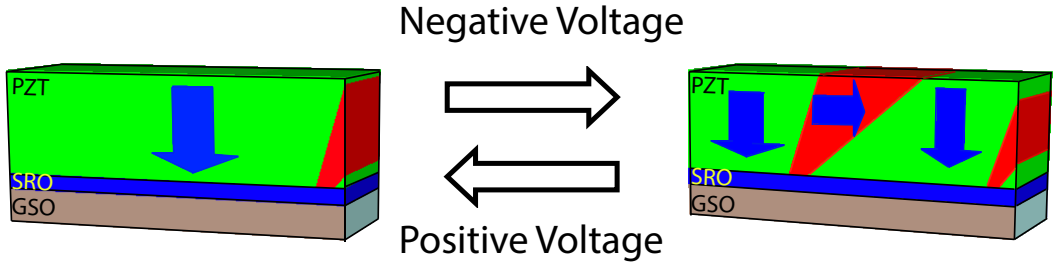


Figure 2.19: Schematic illustration of voltage controlled ferroelastic switching in polydomain PZT films grown on SRO buffered GSO (110) substrates.

the response of this ferroelastic domain structure to an electric field applied through a conducting AFM tip. To investigate the response of the ferroelastic domain to an out-of-plane electric field, we applied different DC voltages on the same area of the films via a conducting scanning atomic force microscopy (AFM) tip. The bottom $SrRuO_3$ electrode was connected to the electrical ground. The surface topography, the in-plane and out-of-plane piezoresponse were recorded after each voltage.

## Observation of Ferroelastic $c \rightarrow a$ Switching

Figure 2.20 compares the domain configuration of the same 2 $\mu$m x 2 $\mu$m region in the as-grown state and after -2 V and -2.5 V were applied on the entire region. New ferroelastic

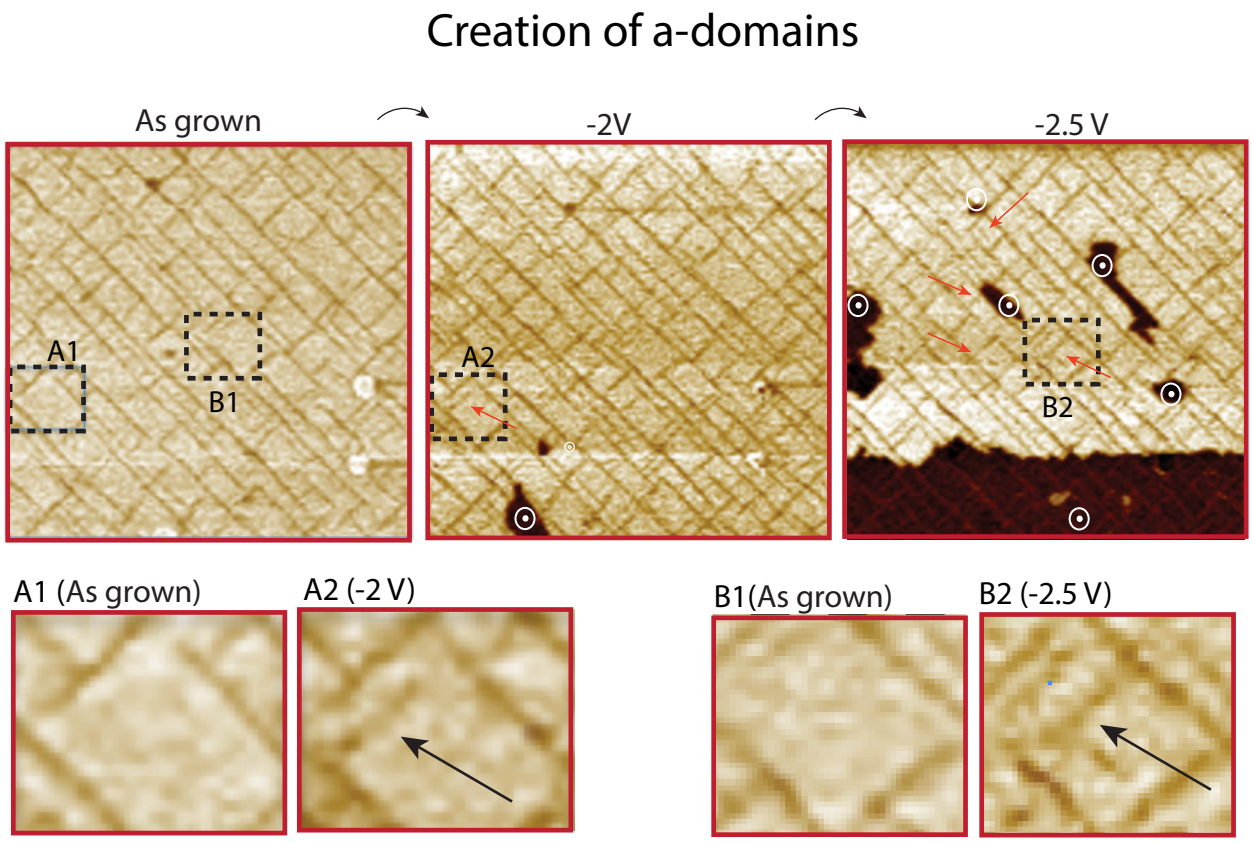


Figure 2.20: *Decoupling of ferroelastic switching from a concurrent ferroelectric switching.* Comparison of the out-of-plane PFM snapshots of the same 2 $\mu$m x 2 $\mu$m area of the 40 nm PZT film in the as-grown state and after the subsequent application of -2 V and -2.5 V on the entire region. The regions where ferroelastic $a$-domain are created are indicated by arrows. Close up out-of-plane PFM images of two regions corresponding to the boxes {A1, A2} and {B1, B2} are also shown.

$a$-domain forms at -2 V and -2.5 V in the regions corresponding to the dashed boxes {A1, A2} and {B1, B2} and the arrows in figure 2.20. Note that the ferroelectric polarization in the $c$-domains in the as-grown state points towards the PZT-SRO interface. The out-of-plane component of the electric field due to the application of the negative voltage at the conducting AFM tip is aligned antiparallel with the $c$-domain polarization. The coercive voltage for ferroelectric 180° switching varies from point to point on the surface of the sample. In some regions, the $c$-domain polarization switches by 180° at -2 V and -2.5 V (noted by $\odot$ in Figure 2.20). However, no reversal of $c$-domain polarization is observed in the region, where new $a$-domains formed. The out-of-plane PFM images corresponding to the intermediate voltage steps are shown in figure 2.21 and the new $a$-domains are indicated by arrows. We observe in figure 2.21 that the critical voltage for ferroelastic $c \rightarrow a$ switching is $\sim$-2 V. To eliminate the possibility that a 180° switching occurs in the surrounding region of the new $a$-domain upon the application of the -2 V bias followed by a rapid ferroelectric back switching upon the removal of the DC voltage, we imaged a region while applying a negative DC voltage on which a AC voltage was superimposed. Figure 2.22(a) shows the out-of-plane piezo-magnitude and -phase of a 2 $\mu$m$\times$ 2 $\mu$m region in the as-grown state measured by applying 0.5 V (peak-to-peak) AC on the tip. In figure 2.22(b), we show the piezo-magnitude and -phase of the same region as -2 V DC+0.5 V (peak-to-peak) AC was applied. Comparing figure 2.22(a,b), we observe that in the regions where new $a$-domains formed (indicated by arrows), no 180° degree switching of the surrounding $c$-domain matrix is observed. These observations reveal that the reversal of $c$-domain polarization is not necessary for an electric field induced ferroelastic $c \rightarrow a$ switching.

## Reversible $c \rightarrow a$ and $a \rightarrow c$ Switching

The new $a$-domains created thusly can be annihilated by applying a positive DC bias such that the resulting out-of-plane electric field is aligned with the as-grown $c$-domain polarization. Figure 2.23(a) compares the out-of-plane PFM images of the same 2 $\mu$m $\times$ 2 $\mu$m region in the as-grown state and after the successive application of -2 V and +4.5 V. In Figure 2.23, we observe that some of the new $a$-domains formed at -2 V (enclosed by dashed boxes) are annihilated at +4.5 V. The critical voltage for ferroelastic $a \rightarrow c$ switching $V_{a \rightarrow c}$ is $\sim$+3.5 V (see Figure 2.24 for the PFM sequence). In Figure 2.23(b), we show PFM snapshots of a 300 nm$\times$ 200 nm region, where an $a$-domain is reversibly created and annihilated twice by applying a voltage sequence -2 V$\rightarrow$+4 V $\rightarrow$-2 V$\rightarrow$+4 V locally. This indicates that although the $a$-domains form at apparently random places, once created these domains can be reversibly annihilated and created by applying positive and negative DC voltages respectively at the conducting AFM tip.

## Stability of new formed $a$-domains

Figure 2.25 compares the out-of-plane PFM snapshots of a 2 $\mu$m $\times$ 2 $\mu$m region on the 40 nm PZT sample in the as-grown state and after -2 V was applied on the entire region. We

note in Figure 2.25 that even after 16 hours, the new $a$-domains formed at -2 V are intact.

## Effects of Contact Force on the Ferroelastic Switching

In order to eliminate the possibility that the local indentation due to the conducting AFM tip might cause a ferroelastic and/or ferroelectric switching,[67, 68] we also studied the effect of the contact force on ferroelastic domain pattern. The conversion factor for the photo-detector deflection signal $DFL$ to the movement of the cantilever in the $z$-direction $\Delta z$ was experimentally measured. $DFL$ was typically set at 1-2 nA for which $\Delta z$=12.5-25 nm. For PFM experiments, we used MikroMasch NSC-35 cantilevers (coated with Ti-Pt) for which the nominal force constant $k$ is ∼14 N/m. Based on this, the typical value of the contact force during the PFM scans is estimated to be $k \times \Delta z$= ∼175-350 nN. Figure 2.26 shows the out-of-plane PFM images for different contact forces in the range 100-700 nN. We observe in Figure 2.26 that even at a contact force of 700 nN, no change in the ferroelastic domain pattern is observed. This is in agreement with the observation in Gao *et al.*[68] that the ferroelastic switching was observed only when the loading force was $> 6$ $\mu$N. The additional force imposed by a biased tip can also be estimated using the relation, $F = QV$, $F, Q, E$ being the force, charge on the tip and the tip voltage respectively. The total charge on the tip $Q = \varepsilon_0 \varepsilon_r AV/d$, where $\varepsilon_0$, $\varepsilon_r$, $A$ and $d$ are the vacuum permitivity, the relative permittivity of PZT, the area of the tip and the PZT thickness respectively. Taking $\varepsilon_r$=100, $A = \pi \times$ 30 nm$^2$, $V$=4 V and $d$=40 nm, $F$ is calculated to ∼25 nN. Based on the results shown in Figure 2.26, it is clear that the force applied by the biased tip results in neither a ferroelectric nor a ferroelastic switching. Thus the creation and annihilation of the $a$-domain observed in our experiments are solely due to the electric field.

## Coupled Ferroelastic-Ferroelectric Switching

When the $c$-domains are ferroelectrically switched by applying a voltage larger than their coercivity, some of the pre-existing $a$-domains get erased and some new $a$-domains are created resulting in a complete reconstruction of the ferroelastic domain pattern. Figure 2.27 shows the topography and the out-of-plane piezo-response of the same 1.5 $\mu$m x 1.5 $\mu$m region in the as-grown state and after -4 V, +4 V and -4 V were successively applied on the same region of the 40 nm PZT sample. We note in Figure 3 that a dramatic reconstruction of the domain pattern occurs after each 180° switching. Most importantly, after the $c$-domain polarization is switched back to the as-grown direction by the voltage sequence -4 V→+4 V, the ferroelastic domain pattern does not come back to as-grown pattern.

## Significance of the Voltage Controlled Decoupled Ferroelastic Switching

Significance of the voltage controlled decoupled ferroelastic switching presented in this section lies in the fact that ferroelasticity–the spontaneous emergence of strain order parameter

is fundamental to the study of ferroicity [69, 70, 71]. In ferroelectric films, domains can be extremely thin spanning only a couple of nanometers [72, 73, 74]. Due to the lattice-polarization coupling, ferroelectric materials are also ferroelastic. Of the wide range of domain types observed in ferroelectric films, many are categorized as ferroelastic domains. The movement of the ferroelastic domains can lead to a strain that is of the order of lattice tetragonality and a piezoelectric response significantly larger than that obtained in single domain crystals can be achieved in ferroelastically twinned ferroelectrics.[45] Ferroelastic domains play an important role in the coupling between the electric field and the magnetization in magneto-electric multiferroic materials, such as $BiFeO_3$ [75], and heterostructures such as CoFe-$BaTiO_3$ [76], which offer a promising route for ultra-low power voltage controlled magnetic switching for spintronic applications. The domain walls that separate the adjacent domain also exhibit a wide range of exotic nanoscale phenomena exemplified by electronic conductivity of domain walls embedded into insulating parent materials [77, 78, 79, 73], and generation of large photovoltage in domain walls [80]. Interesting nanoscale phenomena such as formation of topological features (for example, flux-closure vortex structures[81, 82] and ferroelastic pair structures[83]) and ferroelastic vertex-vertex interactions over hundreds of nanometers[84] have been reported recently. The emerging paradigm of domain wall nanoelectronics aims at the controlled manipulation of these nanoscale features and nanodomains in ferroelectric films [85]. Thus, a proper understanding of ferroelectric and ferroelastic switching mechanisms is fundamentally important.

A certain degree of control has been reported in regard to manipulation of ferroelastic nanodomains in ferroelectric thin films [73, 45, 86, 87, 47, 88, 89, 68, 90, 91, 81, 83, 92, 93, 94, 95, 96]. Yet, this topic has remained a challenging and controversial one. The nature of electric field induced mobility of ferroelastic domain walls is elusive due to multiple reasons.

1 In previous studies, the creation of ferroelastic *a*-domains was observed only when there is a concurrent ferroelectric 180° switching of the surrounding *c*-domain. For example, Nagarajan *et al.* showed that movement of otherwise immobile ferroelastic domains in epitaxial $Pb(Zr_{0.2}Ti_{0.8})O_3$ films can be obtained through coupled ferroelastic-ferroelectric switching by patterning the thin films into discrete islands of high aspect ratio.[45] Afterwards, Chen *et al.* reported coupled ferroelastic-ferroelectric switching in continuous PZT thin films.[89] By now, similar switching has been reported by multiple groups [45, 86, 97, 73]. In single-crystal like epitaxial $Pb(Zr_{0.2}Ti_{0.8})O_3$ films, Li *et al.* showed that the pre-existing *a*-domains split into fine patterns of *a*- and *c*-domain stripes during the ferroelectric 180° switching of the *c*-domains [87]. Nonetheless, the coupled nature of ferroelastic and ferroelectric switching adds complexity to the process of ferroelastic *a*-domain creation in terms of understanding.

2 A coupled ferroelastic switching mechanism is not reversible. For example, Le Rhun *et al.* showed that after the rearrangement of the ferroelastic domain pattern in PZT

films by a ferroelectric 180° switching of the as-grown *c*-domain polarization state by a negative voltage pulse, the application of a subsequent positive voltage pulse such that the *c*-domain polarization switches back to the as-grown direction does not bring back the initial domain configuration; rather the system stabilizes in a completely different ferroelastic domain pattern.[86] Ivry *et al.* reported that the striped patterns of alternate *a*- and *c*-domains in polycrystalline $Pb(Zr_{0.3}Ti_{0.7})O_3$ thin films are irreversibly reoriented through coupled ferroelectric-ferroelastic switching when subsequent positive and negative voltages, which are larger than the coercivity of the average out-of-plane polarization, are applied [90]. Similar observations were also made in tensile strained PZT thin films[98] and in polycrystalline bilayer heterostructures of $Pb(Zr_{0.3}Ti_{0.7})O_3$-$Pb(Zr_{0.7}Ti_{0.3})O_3$ [92].

In perspective, we have reported a new degree of nanoscale control of the ferroelastic switching process toward the reversible creation and annihilation of *a*-axis oriented ferroelastic ∼10 nm wide nanodomains in archetypal ferroelectric $Pb(Zr_{0.2}Ti_{0.8})O_3$ (PZT) thin films by using the piezo-response force microscopy (PFM) technique. We have shown for the first time that a voltage controlled ferroelastic $c \rightarrow a$ switching can be achieved without a concurrent ferroelectric $180^0$ switching of the surrounding *c*-domain matrix in PZT films, which are epitaxially strain tuned by (110) oriented $GdScO_3$ (GSO) substrates. By decoupling ferroelastic $c \rightarrow a$ switching from a simultaneous ferroelectric switching, we further show that it is possible to erase a newly formed *a*-domain by the application of a voltage of opposite polarity leading to the demonstration of a reversible creation and annihilation of ferroelastic *a*-domains. In contrast to the previous reports where only coupled and irreversible ferroelastic-ferroelectric switching was observed, the observation of the decoupling of these two mechanisms in this work allows us to develop an understanding of the ferroelastic switching process based on a simple phenomenological energy barrier type model.

## 2.16 Growth and Structural Characterization Ferroelectric $Pb(Zr_{0.2}Ti_{0.8})O_3$-Dielectric $SrTiO_3$ Heterostructures

Ferroelectric $Pb(Zr_{0.2}Ti_{0.8})O_3$-dielectric $SrTiO_3$ heterostructures were grown on $SrTiO_3$ (001) substrates. In there heterostructures, the thickness of PZT, STO and SRO layers varied between 25-70 nm, 45-60 nm and 25-30 nm, respectively. First the STO/SRO heterostructure was grown at 720 °C. Afterwards, the heterostructure was cooled down at 5 °C to 630 ° and the PZT layer was grown. PZT and SRO were grown in an oxygen environment at 100 mTorr and STO in 250 mTorr. The repetition rate of PZT, STO and SRO was 15, 5 and 15, respectively. Laser pulses with 50-200 mJ energy and ∼4 $mm^2$ spot size was used during the growth of PZT/STO/SRO heterostructures. The general procedure outlined in section

2.3 was followed for the growth of these samples.

Figure 2.28 shows the AFM surface topography of typical PZT-STO sample surfaces. The typical RMS roughness is less than 0.5 nm for these samples. Figure 2.29 shows the XRD $\theta - 2\theta$ spectrum around (002) reflections of a PZT (42 nm)/STO (28 nm)/SRO (30 nm) and a PZT (39 nm)/SRO (30 nm) sample. The (002) reflection from the STO thin film is buried within the STO (002) substrate peak. No secondary peaks are observed in the XRD spectrum of PZT/STO/SRO heterostructure shown in figure 2.29, which indicates that the non-existence of any secondary phases of PZT and STO in these films. Figure 2.30 presents cross-sectional HRTEM images of different interfaces of a PZT-STO sample. PZT/STO film on SRO-buffered STO have in-plane epitaxy to the substrate with atomically sharp interfaces. The HRTEM characterization also confirms the $c$-axis orientation of the PZT films without any contribution from the $a$-axis oriented domains and impurity phases.

The negative capacitance phenomena in these ferroelectric-dielectric heterostructures are investigated in chapter 4.

## 2.17 Conclusions

1 We have studied the effects of epitaxial strain on spontaneous polarization of strained 40 nm $Pb(Zr_{0.2}Ti_{0.8})O_3$ films by growing them on three different substrates, names $SrTiO_3$ (001), $DyScO_3$ (110) and $GdScO_3$. Our work shows that, while, in the tetragonality range $c_c/a_c$ = 1.05-1.09, PZT remnant polarization is nearly independent of the tetragonality, in the range $c_c/a_c$ = 1.041-1.05, remnant polarization is found to show a much stronger functional dependence. This points to the fact that the strain sensitivity of the polarization even in the same ferroelectric material can depend on the value of tetragonality and the sensitivity is larger for smaller values of the tetragonality.

2 We also studied the effects of strain relaxation of dielectric properties of 40 nm $Pb(Zr_{0.2}Ti_{0.8})O_3$ films grown on $SrTiO_3$ substrates. A drastic increase in defect and dislocation density due to strain relaxation is observed in epitaxial PZT films with tetragonality $c/a <$ 1.07 grown on STO substrates, which results in a significant frequency dispersion of the dielectric constant and a strong Rayleigh type behavior in those samples. For a given combination of a ferroelectric thin film and a substrate, tetragonality $c_c/a_c$ is a quantitative measure of the degree to which epitaxial strain has been relaxed in the film and the extent of extrinsic contributions to the dielectric properties can be predicted from the value of $c_c/a_c$.

3 We have reported for the first time a voltage controlled reversible creation and annihilation of $a$-axis oriented $\sim$10 nm wide ferroelastic nanodomains without a concurrent

ferroelectric 180° switching of the surrounding *c*-domain matrix in archetypal ferroelectric $Pb(Zr_{0.2}Ti_{0.8})O_3$ thin films by using the piezo-response force microscopy technique. In previous studies, the coupled nature of ferroelectric switching and ferroelastic rotation has made it difficult to differentiate the underlying physics of ferroelastic domain wall movement. Our observation of distinct thresholds for ferroelectric and ferroelastic switching allowed us investigate the ferroelastic switching cleanly and demonstrate a new degree of nanoscale control over the ferroelastic nanodomains.

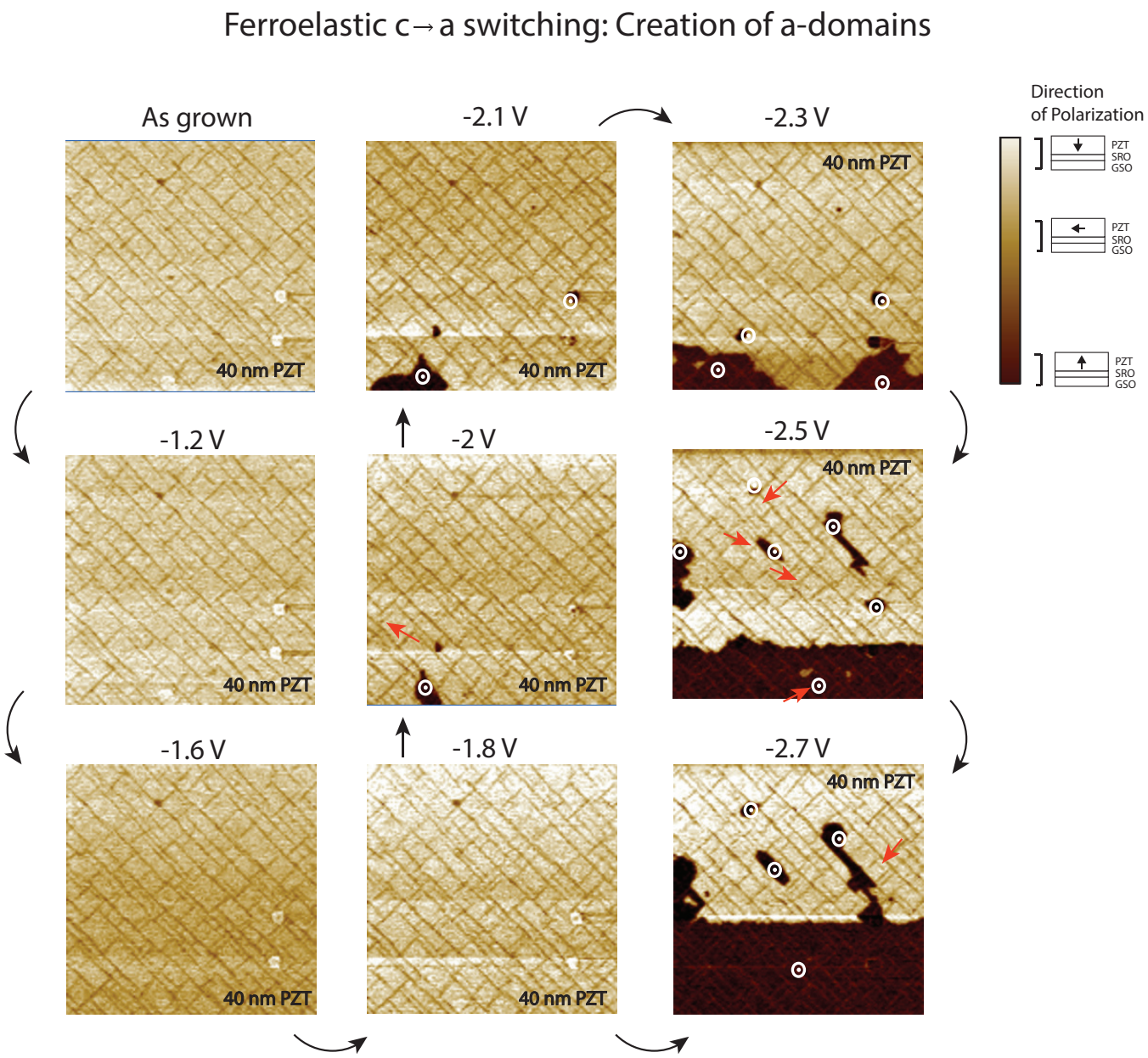


Figure 2.21: *Ferroelastic $c \rightarrow a$ switching:* The out-of-plane PFM snapshots for the 40 nm film after subsequently increasing negative DC voltages are applied on the same 2 $\mu$m x 2 $\mu$m area.

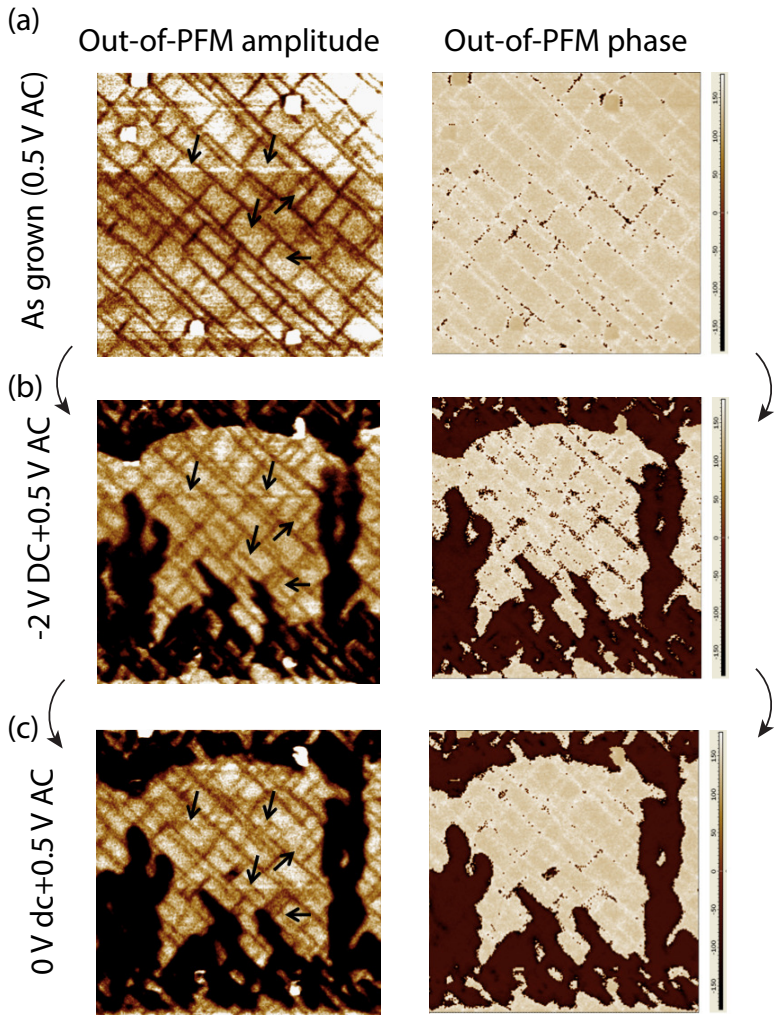


Figure 2.22: (a) The out-of-plane piezo-magnitude and -phase of a 2 $\mu$m$\times$ 2 $\mu$m region in the as-grown state measured by applying 0.5 V (peak-to-peak) AC on the tip. (b) The piezo-magnitude and -phase of the same region as -2 V DC+0.5 V (peak-to-peak) AC is applied on the entire region. (c) The piezo-magnitude and -phase of the same region with 0 V DC+0.5 V (peak-to-peak) AC applied after -2 V have been applied in the entire region.

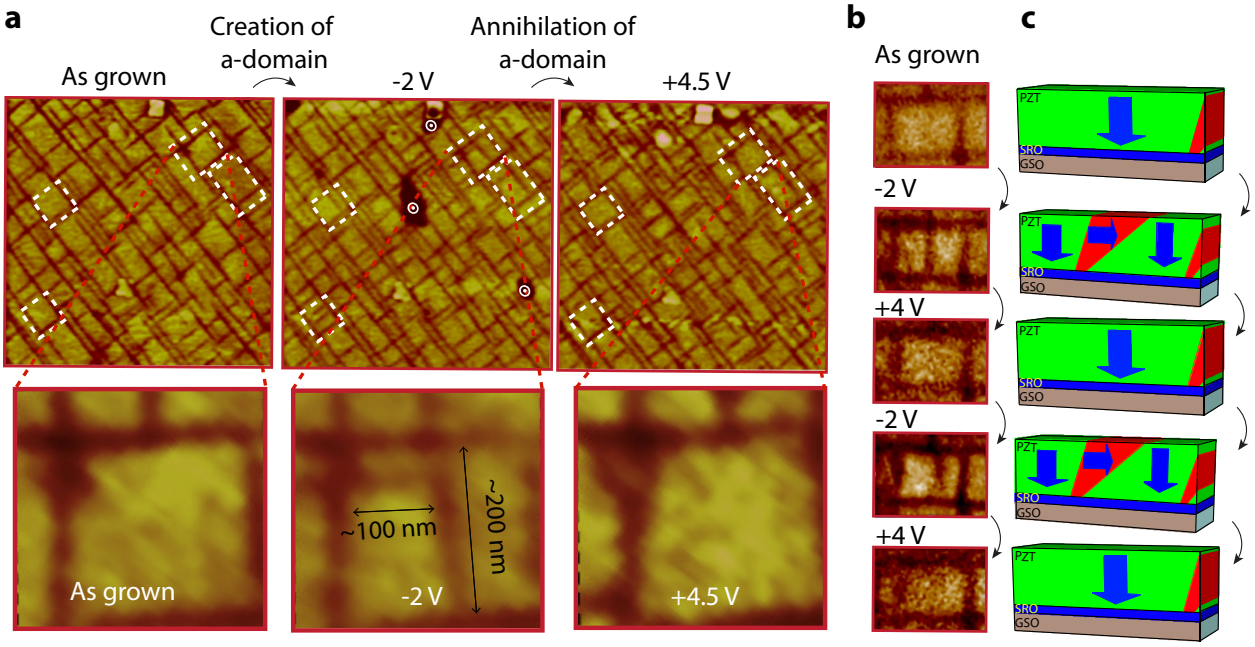


Figure 2.23: *Reversible creation and annihilation of ferroelastic a-domains.* (a) Comparison of the out-of-plane PFM snapshots of the same 2 $\mu$m x 2 $\mu$m area of the 40 nm PZT film in the as-grown state and after an AFM tip has applied -2 V and subsequently +4.5 V on the entire region. The regions where ferroelastic *a*-domain are created or annihilated are indicated by dashed boxes. (b) PFM snapshots of a 300 nm$\times$ 200 nm region, where an *a*-domain is reversibly created and annihilated by applying a voltage sequence -2 V$\rightarrow$+4 V $\rightarrow$-2 V$\rightarrow$+4 V locally. (c) Schematic illustration of the reversible creation and annihilation of an *a*-domain.

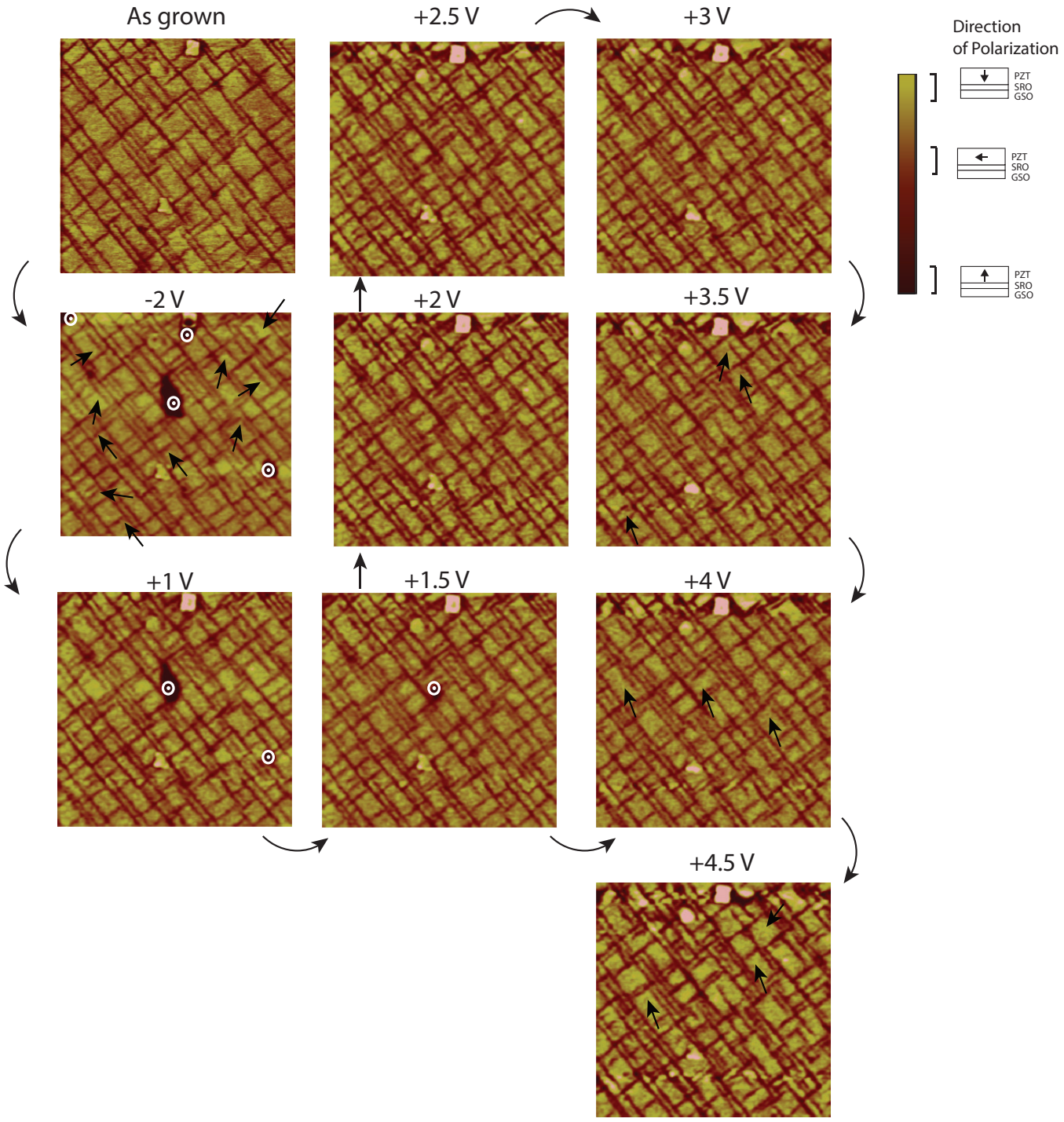


Figure 2.24: *Ferroelastic $c \rightarrow a$ and $a \rightarrow c$ switching:* The out-of-plane PFM snapshots after applying -2 V and then applying subsequently increasing positive DC voltages on the same 2 $\mu$m x 2 $\mu$m area. The regions where ferroelastic switching occurs are indicated by arrows.

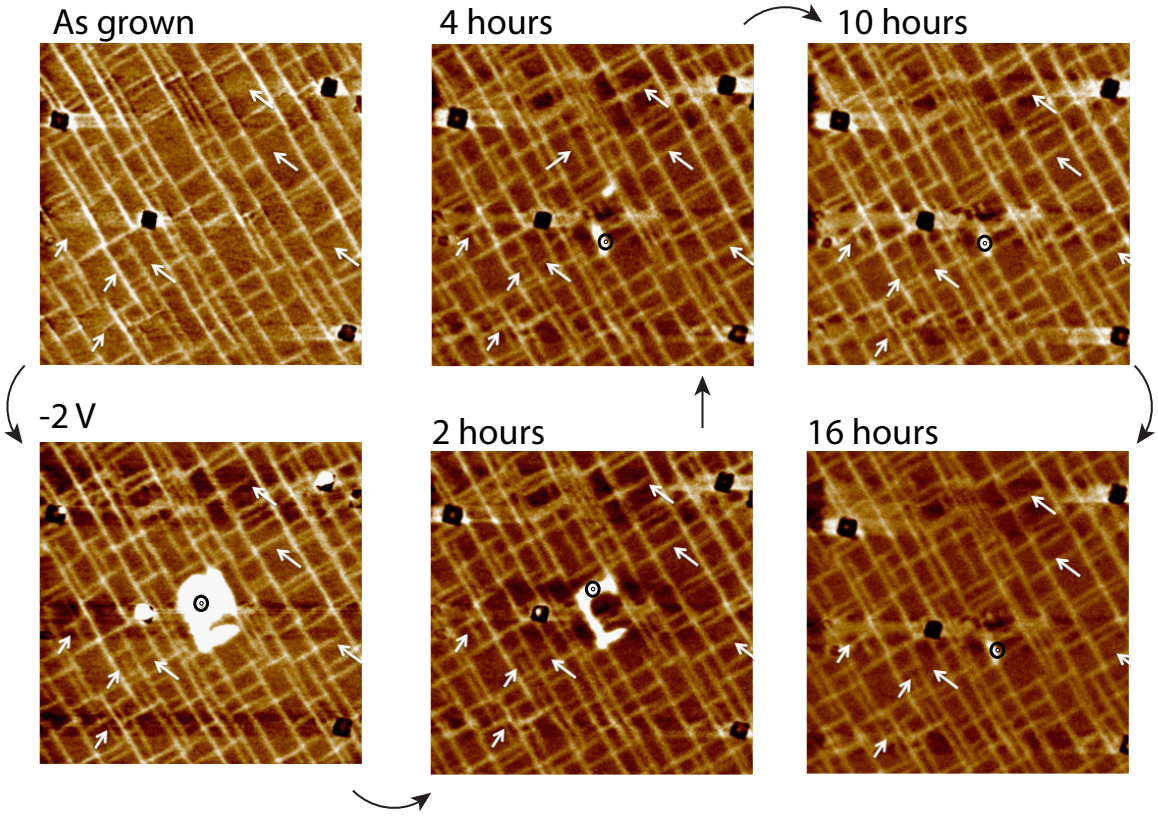


Figure 2.25: Stability of newly formed $a$-domains.

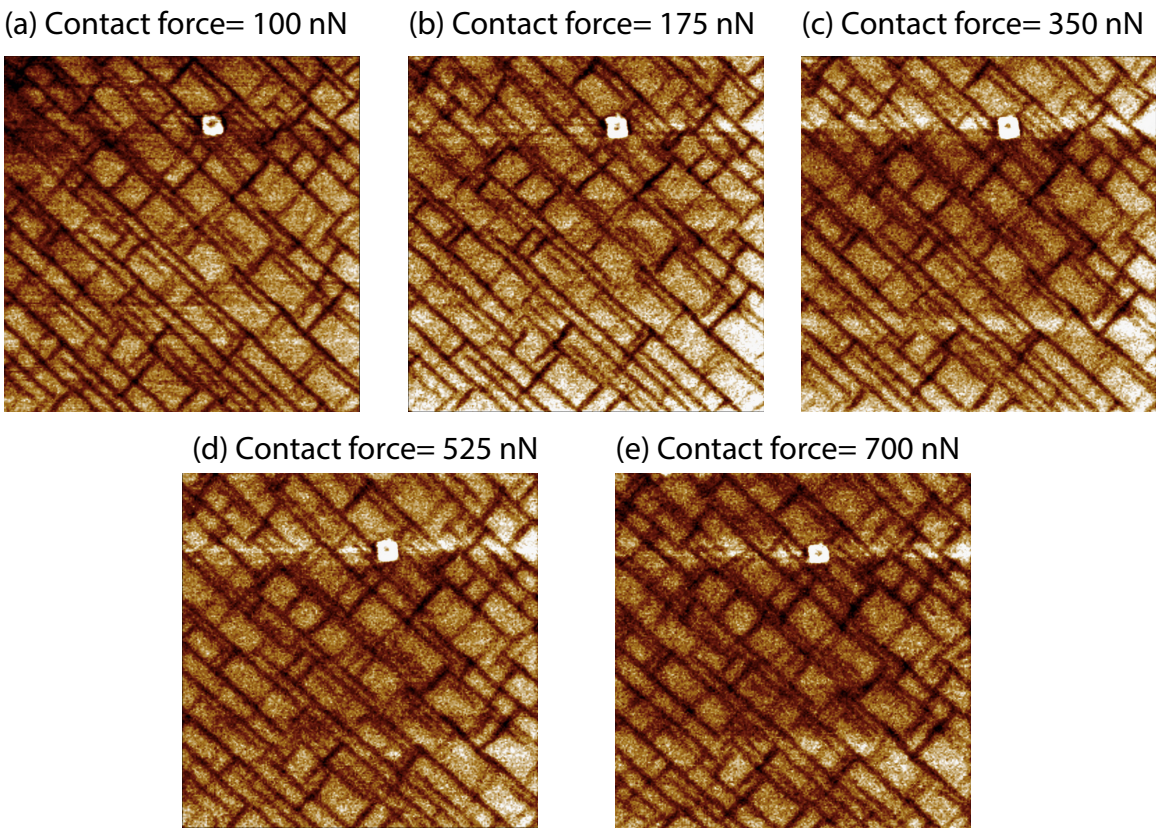


Figure 2.26: The effect of the contact force on the ferroelastic domain pattern.

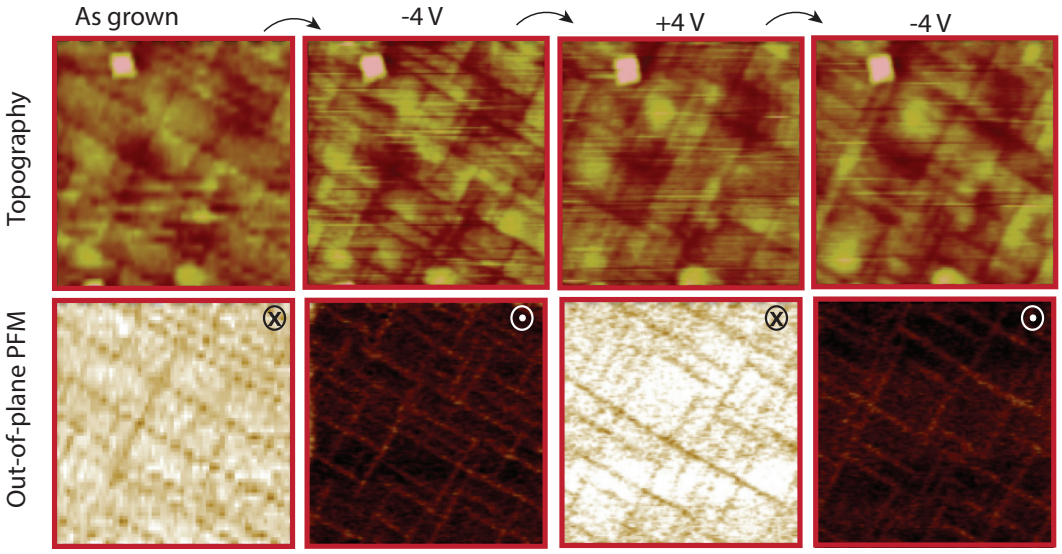


Figure 2.27: *Coupled ferroelastic-ferroelectric switching.* Topography and the out-of-plane piezo-response of the same 1.5 $\mu$m x 1.5 $\mu$m region of the 40 nm PZT film in the as-grown state and after -4 V, +4 V and -4 V were successively applied on the entire region.

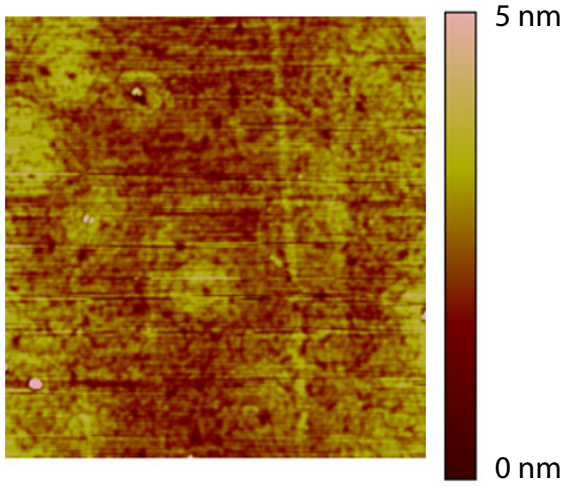


Figure 2.28: AFM topography image of typical PZT-STO sample surfaces showing an RMS roughness less than 0.5 nm.

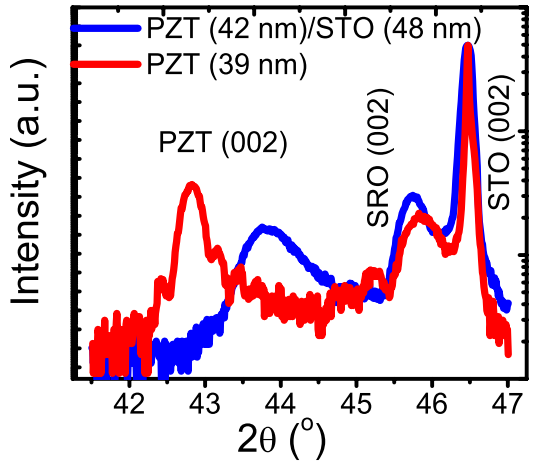


Figure 2.29: XRD $\theta-2\theta$ scans around (002) reflections of a PZT (42 nm)/STO (28 nm)/SRO (30 nm) and a PZT (39 nm)/SRO (30 nm) sample.

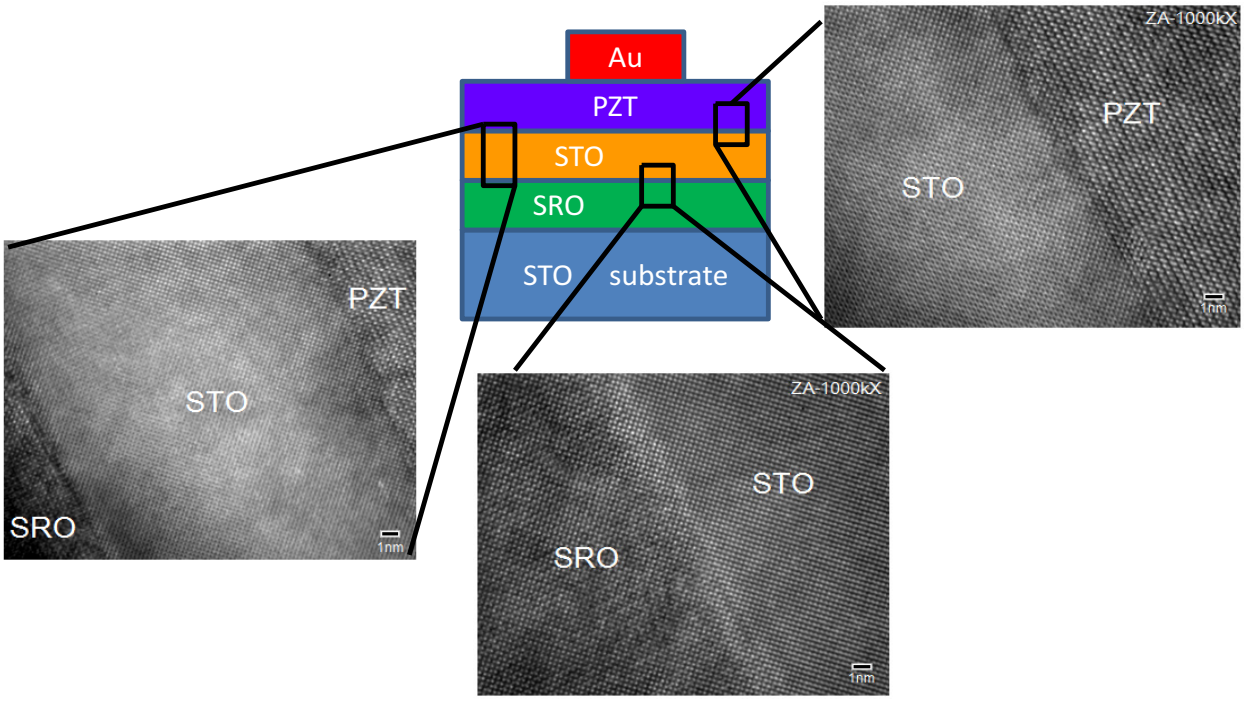


Figure 2.30: Cross-sectional HRTEM images of different interfaces of a PZT-STO sample.

# Chapter 3

# DIRECT MEASUREMENT OF NEGATIVE CAPACITANCE IN A FERROELECTRIC CAPACITOR

This chapter describes the direct measurement of negative capacitance in an isolated ferroelectric capacitor. In chapter 1, we have shown that the negative capacitance state in a ferroelectric is an unstable equilibrium. As a result, the negative capacitance cannot be directly measured by connecting a ferroelectric directly to an LCR meter. In this chapter, we demonstrate the direct experimental measurement of the negative differential capacitance in a thin, single crystalline ferroelectric film, by constructing a simple R-C network and monitoring the voltage dynamics across the ferroelectric capacitor.

In sections 3.1-3.9, we describe the underlying theory of the direct measurement of ferroelectric negative capacitance and the key experimental results. Two new concepts, namely the "characteristic negative capacitance transients" and the "dynamic hysteresis loops", are introduced in section 3.5. The effects of the external circuit parameters such as the voltage pulse amplitude and the external resistor on characteristics negative capacitance transients and the dynamic hysteresis loops are described in sections 3.7 and 3.8, respectively. Section 3.9 deals with the control of the time scale of the negative capacitance transients using the external resistor. Section 3.10 describes a simple 1-D model of the negative capacitance transients and the dynamics hysteresis loop based on the Landau-Khalatnikov equation. Based on the model presented in section 3.10, we extract the intrinsic parameters of the negative capacitor, namely the $\rho$ parameter and the negative capacitance from experimentally measured transients, which is detailed in section 3.11. Section 3.12 presents insights into the relation between the negative capacitance effect and the domain mediated switching mechanisms. Sections 3.13 and 3.14 compare our results with the previously published reports on the negative capacitance effect and ferroelectric switching, respectively. Section 3.15 correlates the structural properties of the PZT films with the negative capacitance transients.

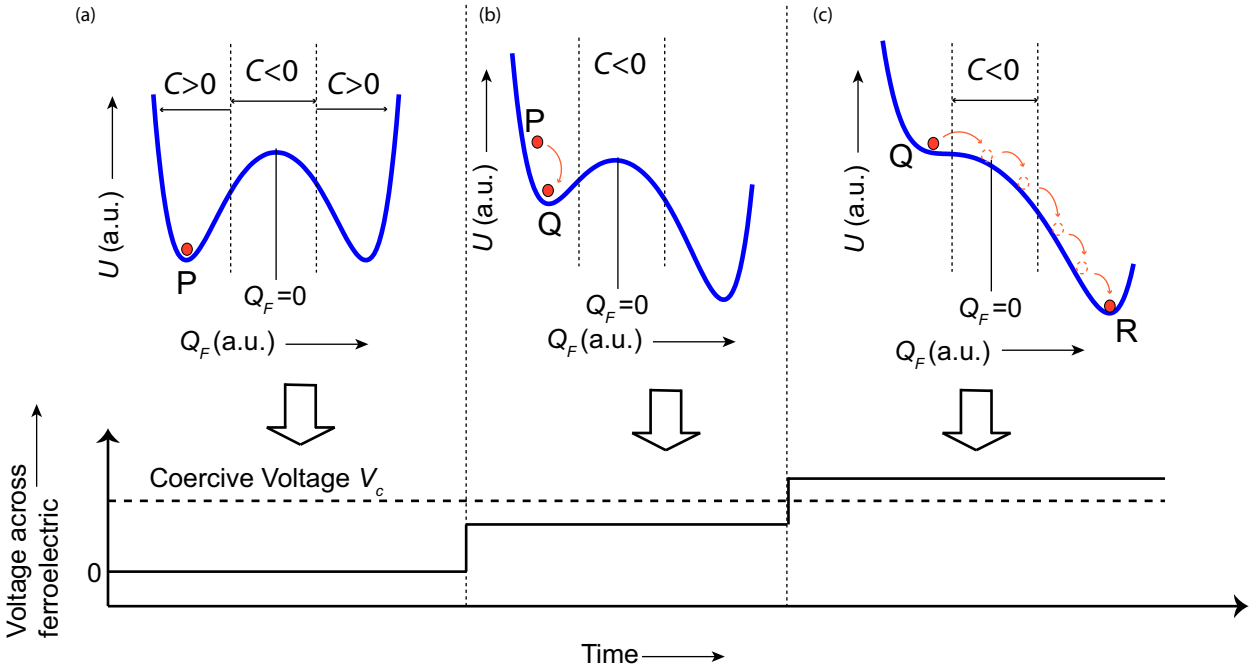


Figure 3.1: *Energy Landscape description of the ferroelectric negative capacitance.* (a) The energy landscape $U$ of a ferroelectric capacitor in the absence of an applied voltage. The capacitance C is negative only in the barrier region around charge $Q_F = 0$. (b,c) The evolution of the energy landscape upon the application of a voltage across the ferroelectric capacitor that is smaller (b) and larger than the coercive voltage $V_c$ (c). If the voltage is larger than the coercive voltage, the ferroelectric polarization rolls down hill through the negative capacitance states. $P$, $Q$ and $R$ represent different polarization states in the energy landscape.

Most of the results presented in this chapter were reported in Khan *et al.* [99].

## 3.1 Dynamics of Ferroelectric Polarization Switching and Negative Capacitance

For a ferroelectric material, whose energy landscape is shown in figure 3.1, the capacitance is negative only in the barrier region around charge $Q_F$=0. Starting from an initial state $P$, as a voltage is applied across the ferroelectric capacitor, the energy landscape is tilted and the polarization will move to the nearest local minimum. Figure 3.1(b) shows this transition for a voltage, which is smaller than the coercive voltage $V_c$. If the voltage is larger than $V_c$, one of the minima disappears and $Q_F$ moves to the remaining minimum of the energy

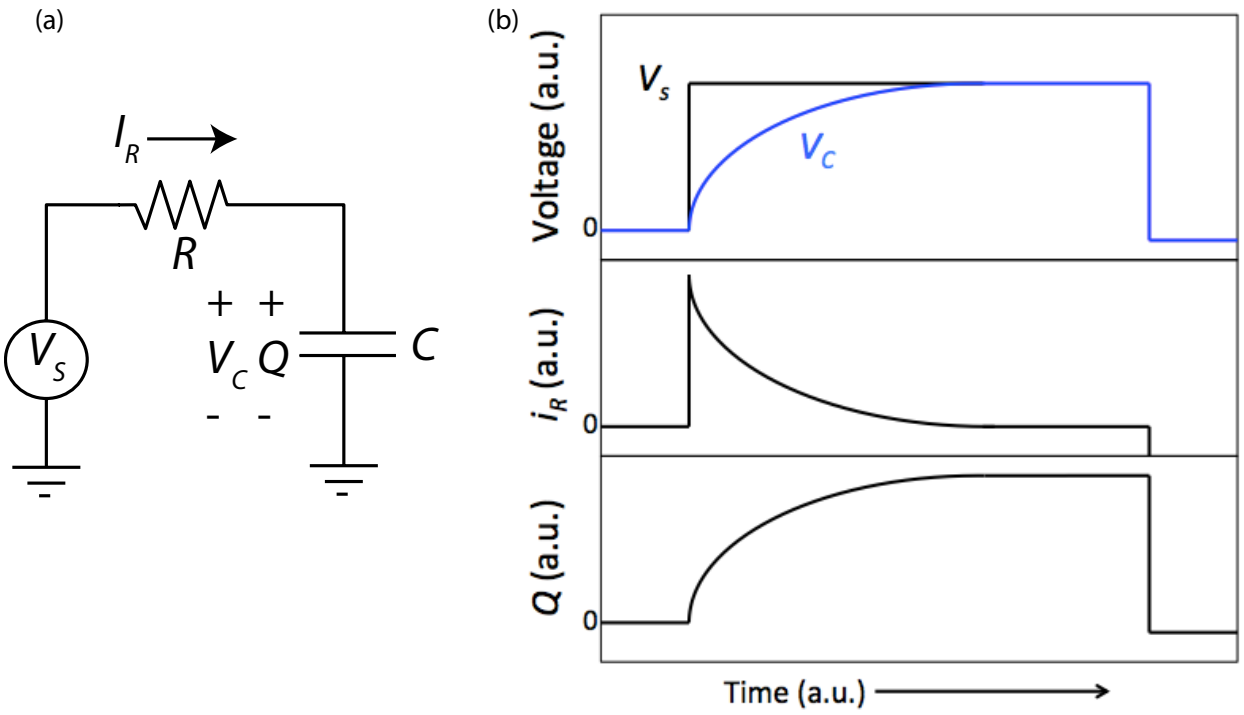


Figure 3.2: *Dynamics in a Regular $R-C$ Series Circuit.* (a) An $R-C$ series network connected to a voltage source. (b) Transients corresponding to the capacitor voltage $V_C$, the stored charge in the capacitor $Q$ and the current through the resistor $i_R$ upon the application of a voltage: $0 \rightarrow V_S$.

landscape (figure 3(c)). Notably as the polarization rolls downhill in figure 3.1(c), it passes through the region where $C = [d^2U/dQ_F^2]^{-1} < 0$. Therefore, while switching from one stable polarization to the other, a ferroelectric material crosses through a region where the differential capacitance is negative. This intuitive picture of the ferroelectric switching allows to directly measure the negative capacitance in a ferroelectric capacitor in a time dynamic fashion, which we describe in the succeeding sections.

## 3.2 Dynamics in a Regular $R-C$ Series Circuit

Before we look into the dynamics of the ferroelectric switching, let us first consider the charge dynamics in a regular series network of a resistor and a capacitor. Figure 3.2(a) shows an $R-C$ circuit connected to a voltage source $V_S$. Upon the application of a voltage pulse: $0 \rightarrow V_S$, the voltage across the capacitor $V_C$ and the charge stored in the capacitor $Q$ increase monotonically with a time constant of $RC$, which is shown in figure 3.2(b). In other words,

$V_C(t) = V_S(1 - e^{-t/RC})$ and $Q(t) = CV_S(1 - e^{-t/RC})$. We note in figure 3.2(b) that, during any infinitesimally small time duration $\Delta t$, the change in the charge $dQ(t)$ and the change in the capacitor $dV_c(t)$ would have the same sign. At a result, at any time $t$ during the transient, $dQ/dV_c$ would be a positive number equal to $C$. In the succeeding sections, we shall see how the charge-voltage relations look for a ferroelectric capacitor during polarization switching.

## 3.3 Experimental Setup

We applied voltage pulses across a series combination of a ferroelectric capacitor and a resistor $R$ and observed the time dynamics of the ferroelectric polarization using an oscilloscope. Figure 3.3(a) shows the schematic diagram of the experimental setup and the electrical connections to the oscilloscope and figure 3.3(b) shows the equivalent circuit diagram. A 60 nm film of ferroelectric $Pb(Zr_{0.2}Ti_{0.8})O_3$ (PZT) was grown on metallic $SrRuO_3$ (60 nm) buffered $SrTiO_3$ substrate using the pulsed laser deposition technique. Square gold top electrodes with a surface area $A$= (30 $\mu$m)$^2$ were patterned on top of the PZT films using standard micro-fabrication techniques. The remnant polarization of the PZT film is measured to be 0.74 C/m$^2$ and the coercive voltages are +2 V and -1.8 V. The PZT capacitor was connected to a voltage pulse source (Agilent 81150A pulse function generator) through an external series resistor $R$. The voltage transients were measured using a digital storage oscilloscope (Tektronix 2024). Top Au and bottom SRO contacts were connected to the probe tips in a probe station. The capacitor $C$ connected in parallel with the ferroelectric capacitor in figure 3.3(b) represents the parasitic capacitance contributed by the probe-station and the oscilloscope in the experimental setup. The extraction of the parasitic capacitance $C$ is detailed in the next section.

## 3.4 Extraction of the Parasitic Capacitance

In order to extract the value of the parasitic capacitance which is referred to as $C$ in figure 3.3(b), voltage pulses were applied across the probe station under open circuit conditions through the resistor $R = 50$ k$\Omega$. Figure 3.4(a) shows the transient response of the circuit for an applied voltage $V_s$ : -5.4 V$\rightarrow$+5.4 V. By fitting the voltage transient across the probes $V_x$ shown in figure 3.4(a) to the equation $V_x(t) = (+5.4 - 2 \times 5.4e^{-t/(RC)})$ V with $R = 50$ k$\Omega$, the value of the parasitic capacitance $C$ is extracted to be $\sim$60 pF. Figure 3.4(b) plots the measured charge-voltage characteristics of the parasitic capacitor.

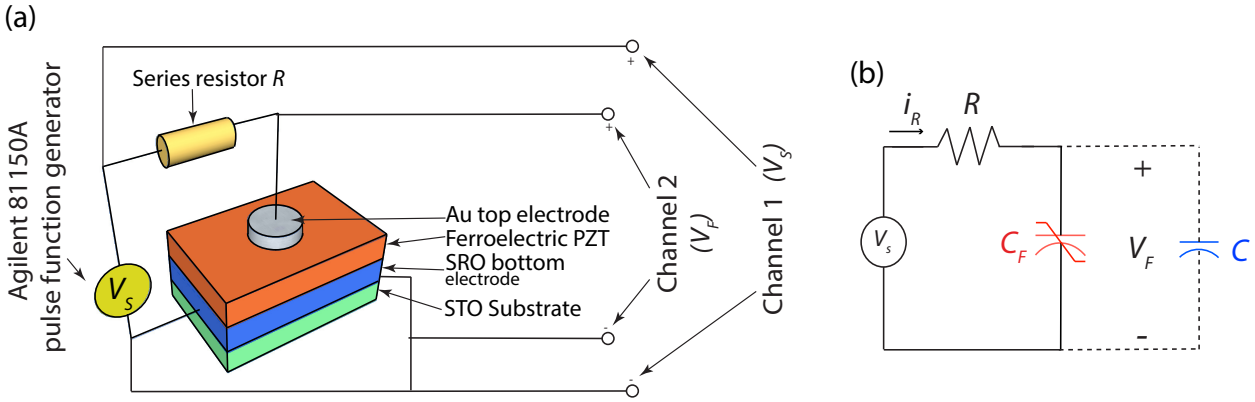


Figure 3.3: *Experimental setup.* (a) Schematic diagram of the experimental setup. (b) Equivalent circuit diagram of the experimental setup. $C_F$, $C$ and $R$ represent the ferroelectric and the parasitic capacitors and the external resistor respectively. $V_S$, $V_F$ and $i_R$ are the source voltage, the voltage across $C_F$ and the current through $R$ respectively.

## 3.5 Negative Capacitance Transients during Ferroelectric Switching and Dynamic Hysteresis Loop

Now we consider the transient response of the ferroelectric-resistor series combination in response to an AC voltage pulse $V_S$: -5.4 V$\rightarrow$ +5.4 V $\rightarrow$ -5.4 V. The total charge in the ferroelectric and the parasitic capacitor at a given time $t$, $Q(t)$, is calculated using $Q(t) = \int_0^t i_R(t)dt$, $i_R$ being the current flowing through $R$. The charge across the ferroelectric capacitor $Q_F(t)$ is calculated using the relation: $Q_F(t) = Q(t) - CV_F(t)$, $V_F$ being the voltage measured across the ferroelectric capacitor. Figure 3.5 shows the transients corresponding to $V_S$, $V_F$, $i_R$ and $Q$. We note in figure 3.5 that after the -5.4 V $\rightarrow$ +5.4 V transition of $V_S$, $V_F$ increases until point $A$, after which it decreases till point $B$. We also note in figure 3.5 that during the same time segment, $AB$, $i_R$ is positive and $Q$ increases. In other words, during the time segment, $AB$, the changes in $V_F$ and $Q$ have opposite signs. As such, $dQ/dV_F$ is negative during $AB$ which points to the fact that the ferroelectric polarization is passing through the unstable negative states. This is in contrast to the dynamics of a regular $R-C$ series circuit shown in figure 3.1(b), where the changes in the charge stored in and the voltage across the capacitor both have the same sign. A similar signature of negative capacitance is observed after the +5.4 V $\rightarrow$ -5.4 V transition of $V_S$ during the time segment $CD$ in figure 3.4. We refer to the transients during the time segments $AB$ and $CD$ as the *characteristic negative capacitance transients*.

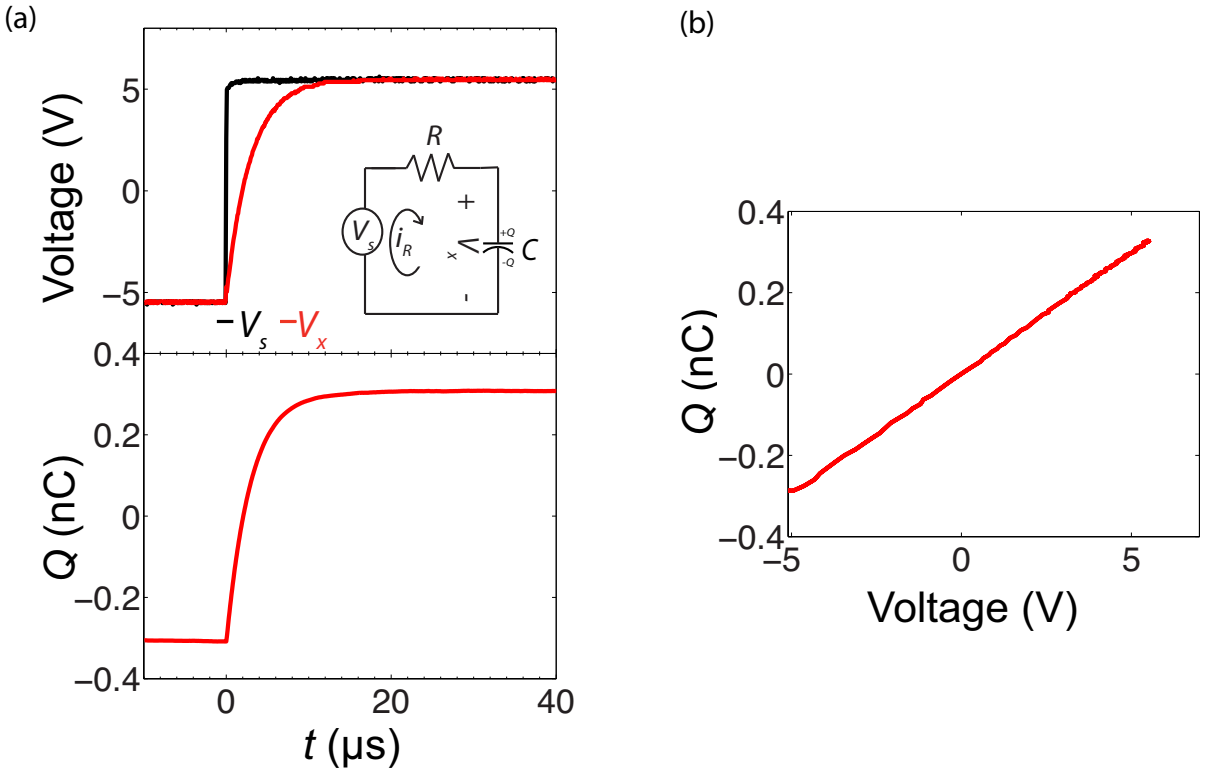


Figure 3.4: *Extraction of parasitic capacitance.* (a) Transient response of the circuit under the open circuit conditions to an AC voltage pulse $V_s$ : -5.4 V $\rightarrow$+5.4 V. (b) The charge-voltage characteristics of the parasitic capacitor.

The charge density of the ferroelectric capacitor or the ferroelectric polarization, $P(t) = Q_F(t)/A$ is plotted as a function of $V_F(t)$ in figure 3.6. We observe in figure 3.6 that the $P(t) - V_F(t)$ curve is hysteretic and in the sections $AB$ and $CD$, the slope of the curve is negative indicating that the capacitance is negative in these regions. We refer to the $P(t) - V_F(t)$ curve measured in the time-dynamic fashion as the *dynamic hysteresis loop*.

## 3.6 Correlation between the ferroelectric switching and the negative capacitance transient

In section 3.1 and figures 3.1(b,c), we have seen that the ferroelectric polarization passes through the negative capacitance region only when the applied voltage is larger than coercive voltage such that a polarization switching event occurs. Here we correlate the experimentally observed characteristic negative capacitance transients with the ferroelectric switching. We

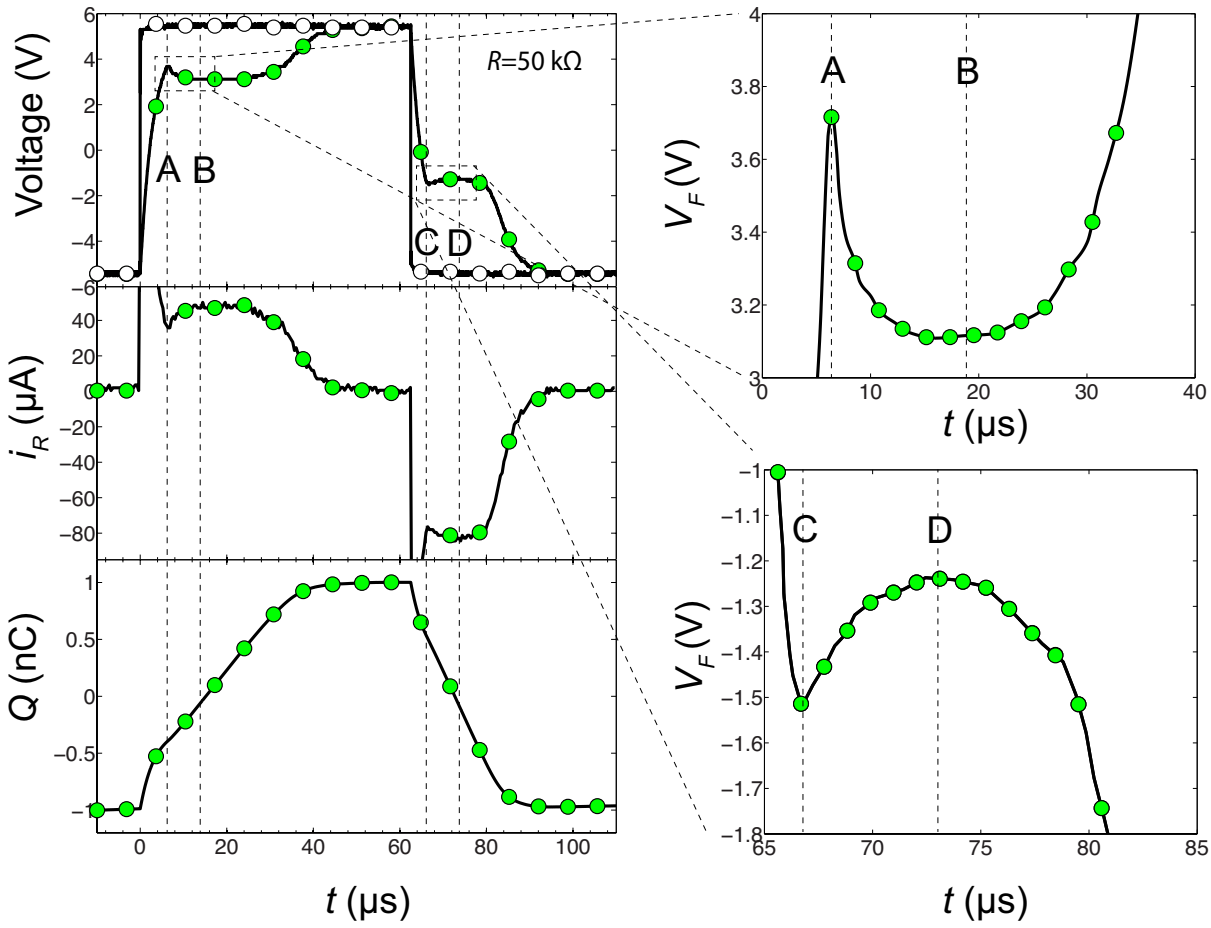


Figure 3.5: *Negative capacitance transients of a Ferroelectric Capacitor.* Transients corresponding to the source voltage $V_S$, the ferroelectric voltage $V_F$ and the charge Q upon the application of an AC voltage pulse $V_S$: -5.4 V$\rightarrow$ +5.4 V $\rightarrow$ -5.4 V. $R$=50 k$\Omega$. The negative capacitance transients are observed during the time segments $AB$ and $CD$.

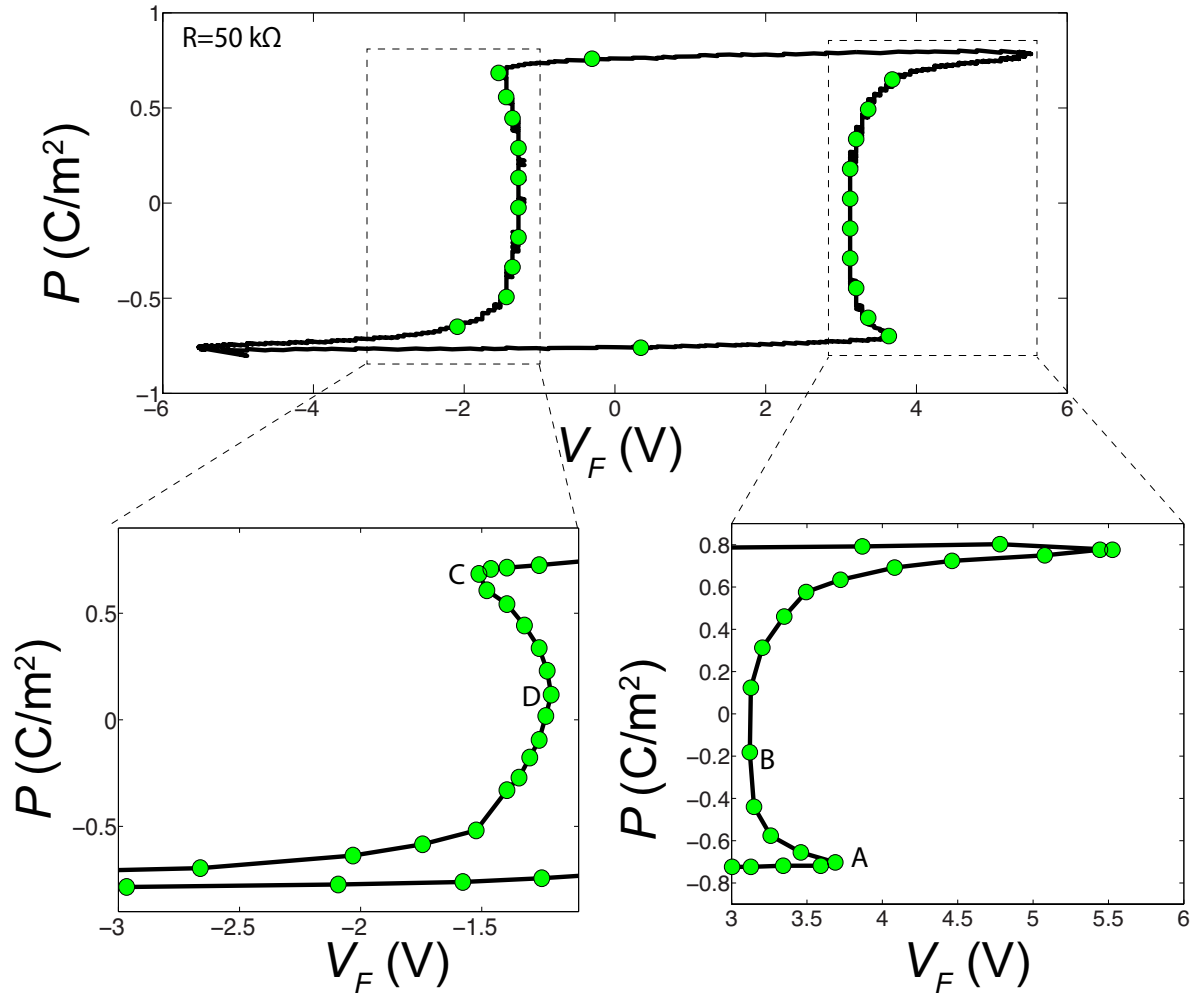


Figure 3.6: *Experimental measurement of Negative Capacitance.* The ferroelectric polarization $P(t)$ as a function of $V_F(t)$ with $R$=50 kΩ for $V_S$: -5.4 V→ +5.4 V → -5.4 V.

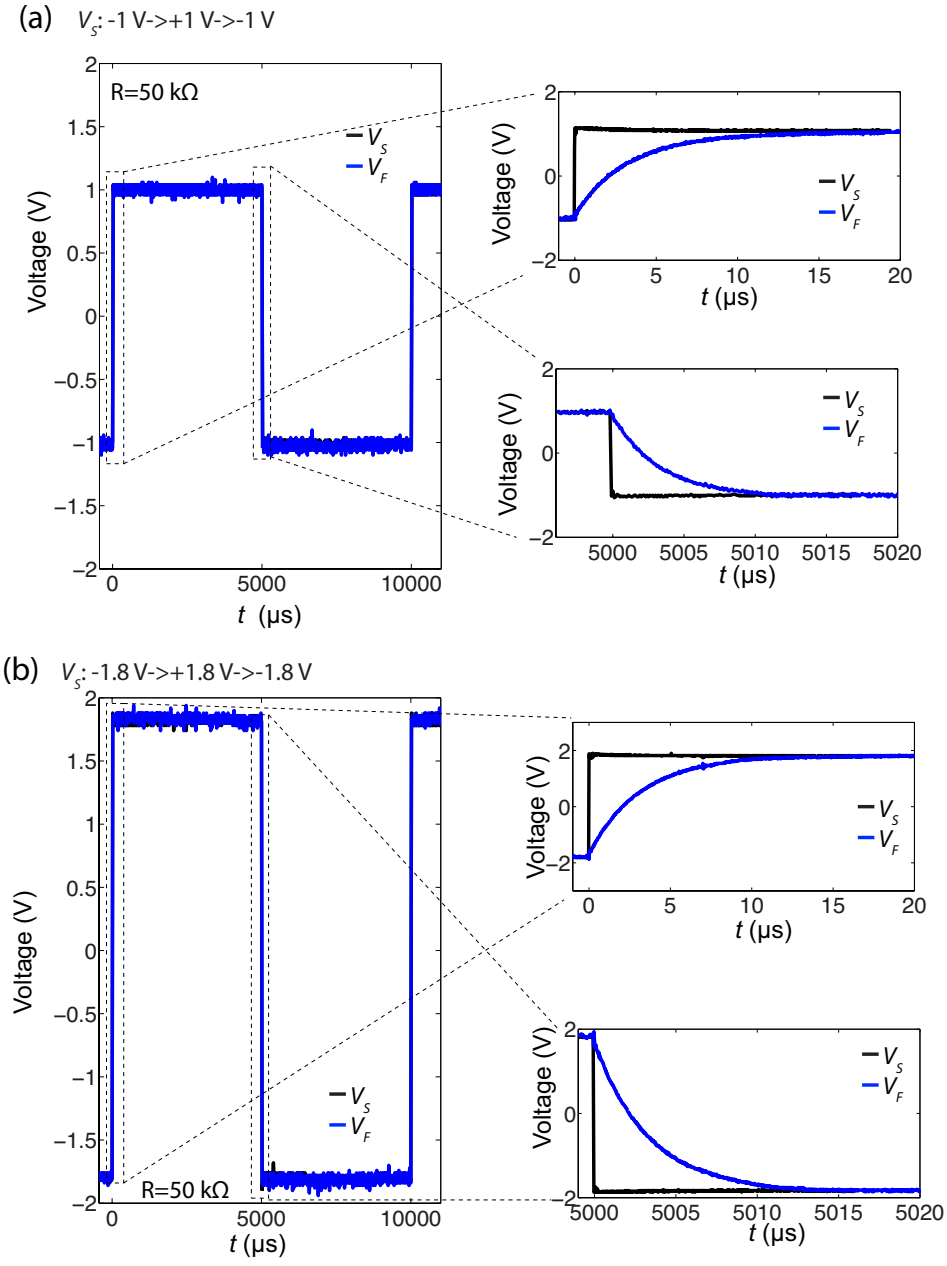


Figure 3.7: Transient response of the series combination of the ferroelectric capacitor and a resistor $R = 50$ kΩ to an AC voltage pulse $V_s$ :-1 V→+1 V→-1 V (a) and $V_s$ :-1.8 V→+1.8 V→-1.8 V (b).

note the following.

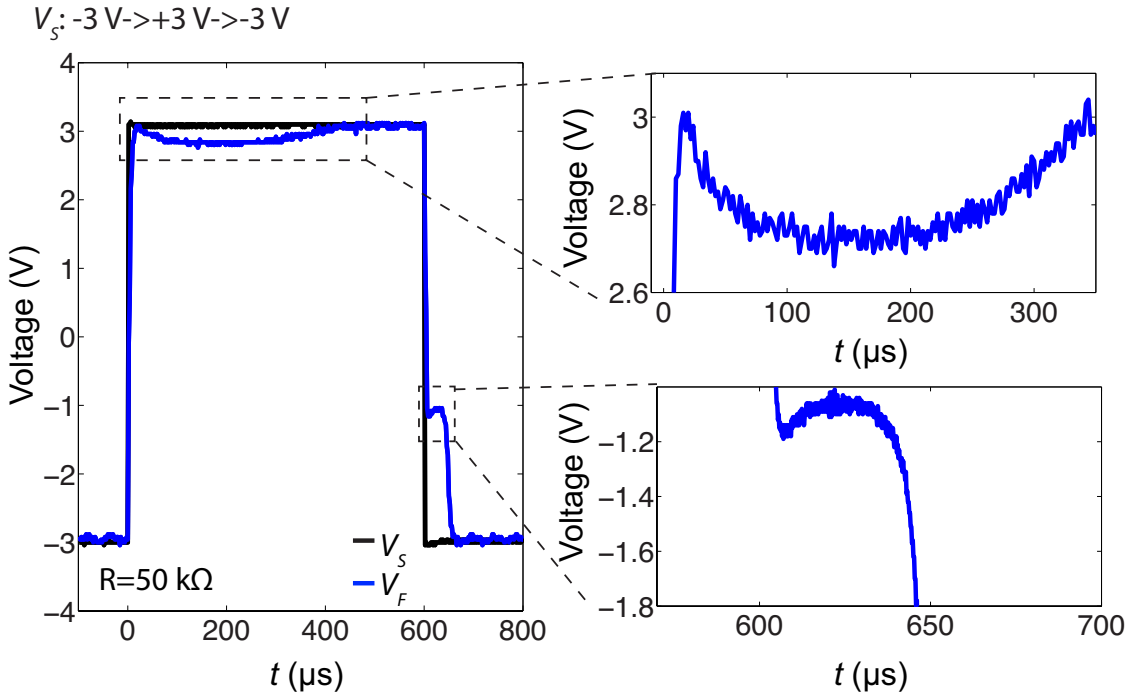


Figure 3.8: Transient response of the series combination of the ferroelectric capacitor and a resistor $R = 50$ kΩ to an AC voltage pulse $V_s$ :-3 V→+3 V→-3 V.

1. When a voltage is applied which is lower than the coercive voltage so that there is no switching of the polarization, we observe a simple capacitive charging of the voltage, as expected from the double well energy landscape of the ferroelectric material and shown in figure 3.1(b). The coercive voltage of our PZT sample is +2 V and -1.8 V. In figure 3.7(a,b), the voltage transients are shown for voltages pulses $V_s$: -1 V→ +1 V → -1 V and $V_s$: -1.8 V→ +1.8 V → -1.8 V respectively. Clearly, there are no negative capacitance transients observed in figure 3.7, since the applied AC voltage amplitude is less the coercive voltage.

2. Now, in the same setup, when a voltage is applied which is larger than the coercive voltage so that the ferroelectric polarization switches its direction, we observe the negative capacitance transient. In figure 3.8, the AC voltage magnitude is larger than the coercive voltage and the negative capacitance transients are observed.

3. To further elucidate the point, we applied successive DC pulses on the PZT sample. In figure 3.9(a), a large negative voltage pulse was first applied to align the polarization away from the PZT/SRO interface and then two successive +6 V pulses were applied. We note in figure 3.9(a) that during the 1st pulse, the switching of polarization occurs which results in the characteristic negative capacitance transient of the ferroelectric voltage $V_F$; on the other hand, during the 2nd pulse, the polarization does not switch

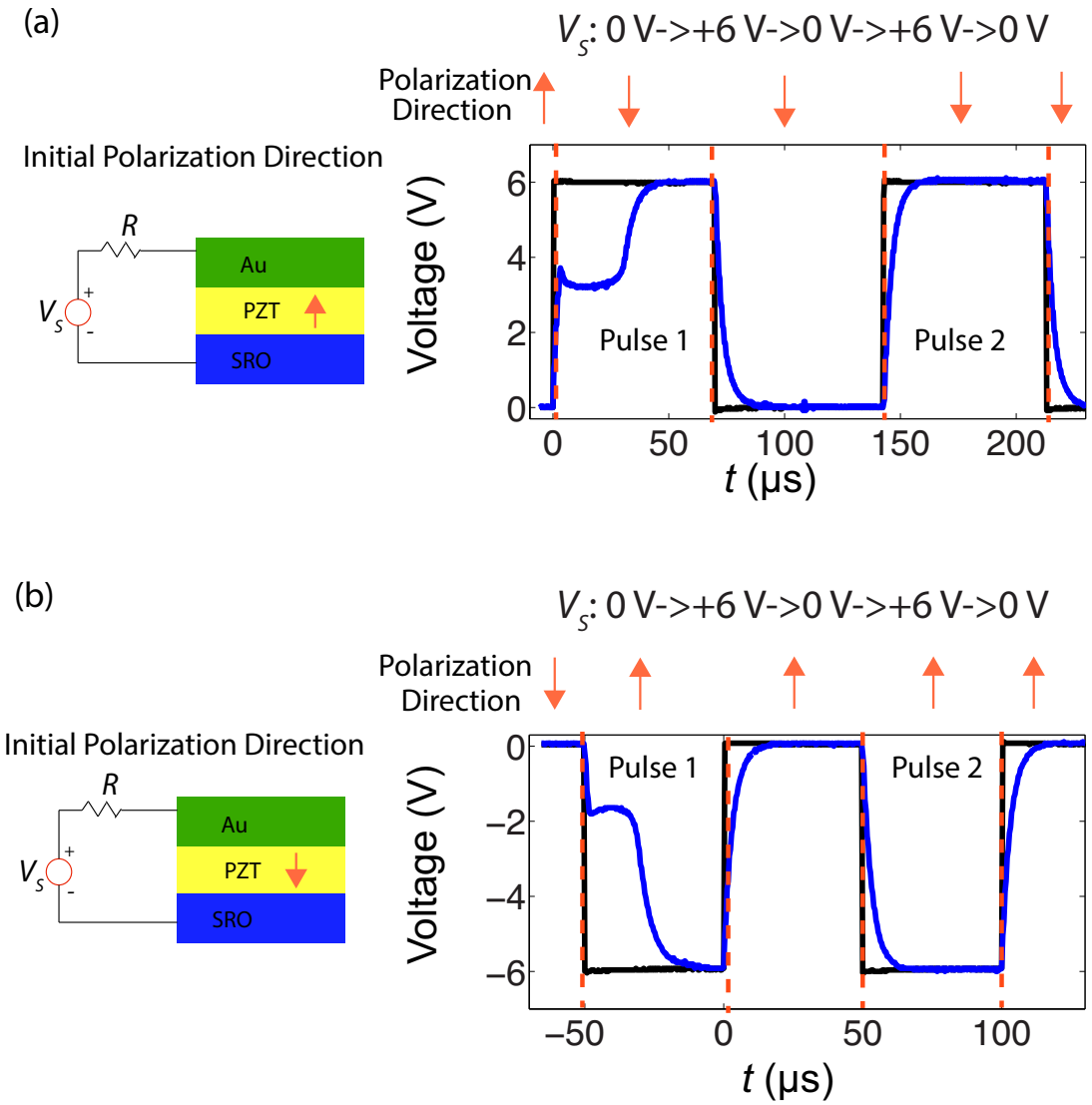


Figure 3.9: Transient response of the series combination of the ferroelectric capacitor and a resistor $R$ = 50 kΩ to two successive DC voltage pulses of $V_s$ : 0 V→ +6 V→0 V (a) and $V_s$ : 0 V→ -6 V→0 V (b). The relative polarization directions at different time are also indicated.

since it had already been aligned with the applied electric field in the previous pulse, and no negative capacitance transient is observed in the $V_F$ waveform during the 2nd pulse. Similar experiment with two successive -6 V pulses is shown in figure 3.9(b).

This correlation between switching and the characteristic transients clearly shows that the characteristic negative capacitance transients are due to the intrinsic ferroelectric switching dynamics and not because of any extrinsic defect dynamics.

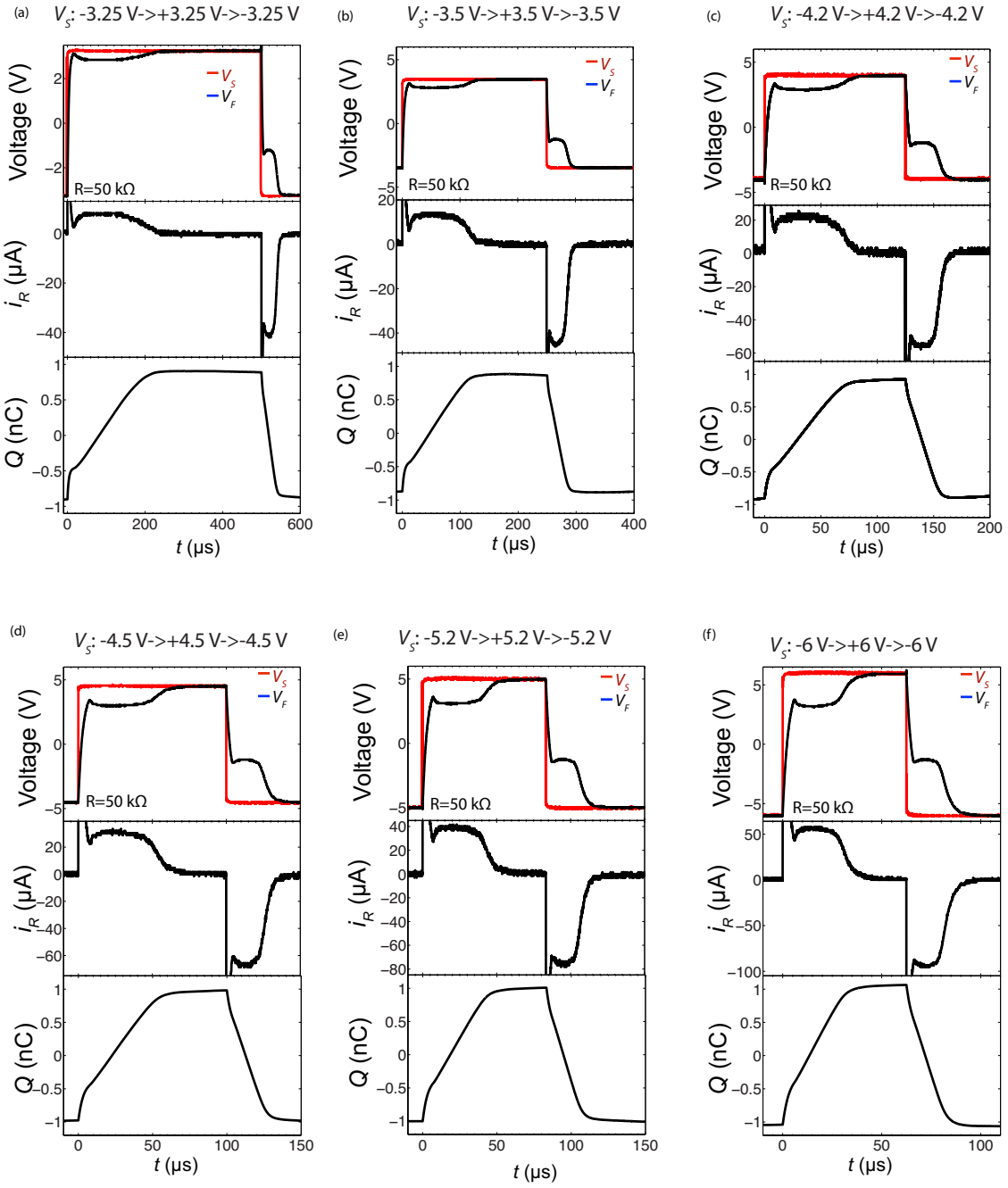


Figure 3.10: Comparison of the transient response of the series combination of the ferroelectric capacitor and a resistor $R = 50$ kΩ to different AC voltage pulses.

## 3.7 Dynamic Hysteresis Curves for Different Voltage Amplitudes

Figures 3.10(a,b,c,d,e) show the transient response of the series combination of the same ferroelectric capacitor and a resistor $R = 50$ kΩ to AC voltage pulses with amplitudes of

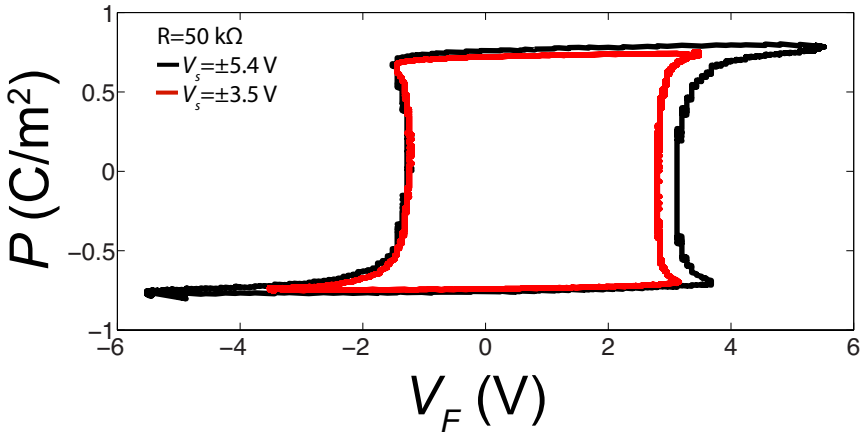


Figure 3.11: Comparison of the $P$-$V_F$ curves for the same circuit for $V_s$ : -3.5 V →+3.5 V→-3.5 V and $V_s$ :-5.4 V→+5.4 V→-5.4 V.

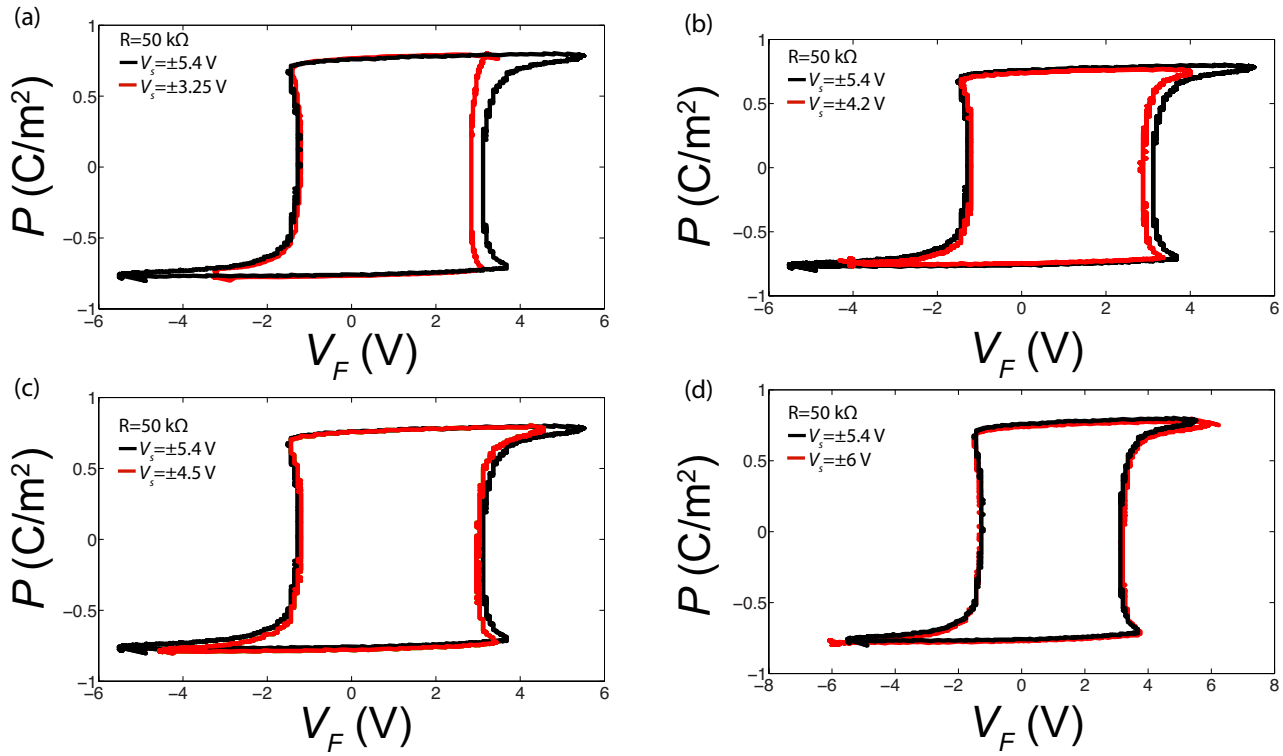


Figure 3.12: Comparison of the $P$-$V_F$ curves corresponding to $V_s$ :-5.4 V→+5.4 V→-5.4 V with that for different other voltage pulses.

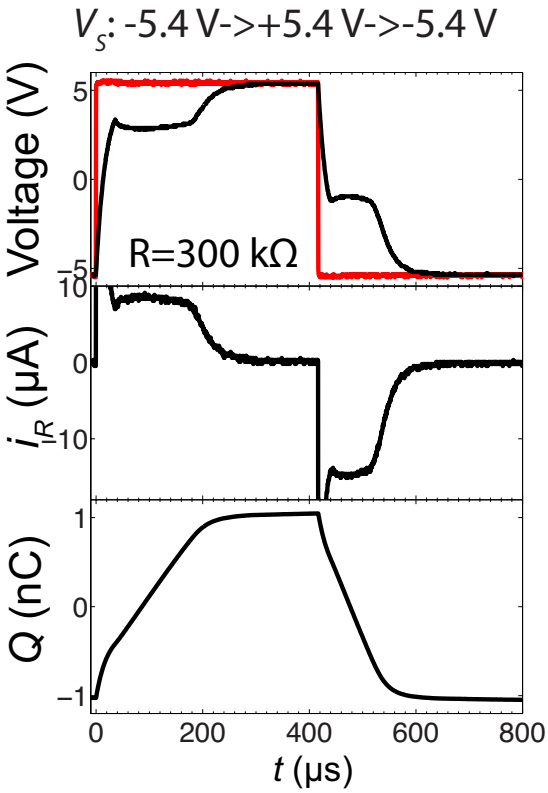


Figure 3.13: Transient response of the series combination of the ferroelectric capacitor and a resistor $R$ = 300 kΩ to an AC voltage pulse $V_s$ :-5.4 V→+5.4 V→-5.4 V.

3.25 V, 3.5 V, 4.2 V, 4.5 V, 5.2 V and 6 V, respectively. Figure 3.11 compares the dynamic hysteresis loops of the same circuit for $V_s$ : -3.5 V →+3.5 V → -3.5 V and $V_s$ :-5.4 V →+5.4 V →-5.4 V. The dynamic hysteresis loops are calculated from the corresponding transient responses following the procedure described in section 3.5. Figure 3.12 compares the $P$-$V_F$ curve corresponding to $V_s$ :-3.5 V→+3.5 V→-3.5 V with that for different other AC voltage pulses. We note in figures 3.11 and 3.12 that for a larger peak voltage, the hysteresis window is wider. We analyze the effect of the applied voltage magnitude in section 3.11.

## 3.8 Dynamic Hysteresis Curves for Different External Series Resistors

Next we analyze the effects of the external series resistance on the dynamic hysteresis loop. Figure 3.13 shows the transient response of the series combination of the ferroelectric capacitor and a resistor $R$ = 300 kΩ to an AC voltage pulse $V_s$ : -5.4 V→+5.4 V→-5.4 V. Figure 3.14 compares the $P$-$V_F$ curves corresponding to $R$=50 kΩ (replotted from figure 3.6) and

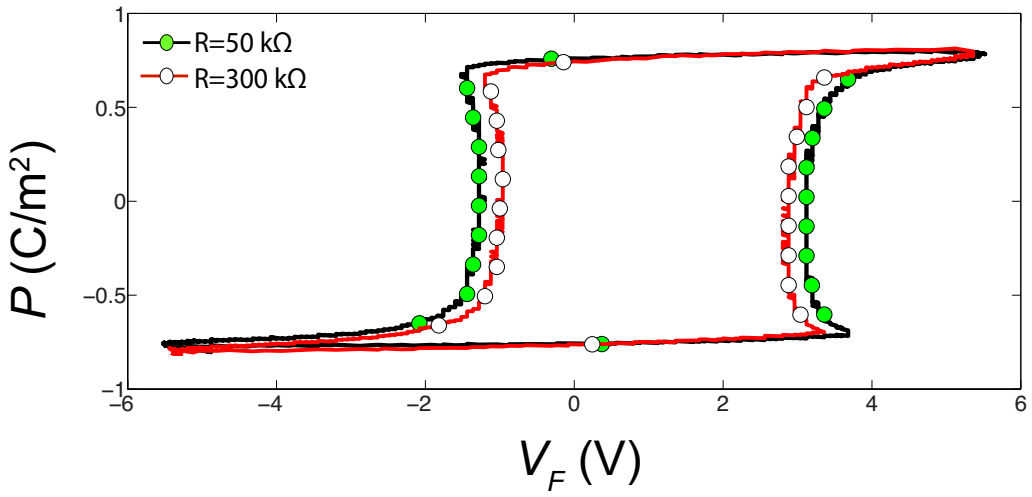


Figure 3.14: Comparison of the $P(t)$-$V_F(t)$ curves corresponding to $R$=50 kΩ and 300 kΩ for $V_s$ :-5.4 V→+5.4 V→-5.4 V.

300 kΩ for $V_s$ : -5.4 V →+5.4 V → -5.4 V. We note in figure 3.14 that for a smaller value of $R$, the hysteresis loop is wider, which we discuss section 3.11.

## 3.9 Time duration of the negative capacitance transients

Figure 3.15(a,b,c,d) show the transient response of the PZT sample to a DC pulse $V_S$: 0 V→ +6 V for $R$=2 kΩ, 25 kΩ, 50 kΩ and 300 kΩ respectively. The time duration of the negative capacitance transient $t_1$ is indicated in the close-up images in figure 3.15(a,b,c,d). Figure 3.16(a,b) plot $t_1$ as a function of $R$ in logarithmic and linear scale respectively. In figure 3.16(a,b), we observe a linear decrease of $t_1$ down to ∼350 ns as $R$ is decreased to 2 kΩ. Figure 3.16(c) shows that the extrapolated $t_1 - R$ curve intersects the $R = 0$ line at $t_1$=19.9 ns. These timescales for switching are similar to what had been observed for domain nucleation and propagation in PZT in earlier reports [100, 101].

## 3.10 Landau-Khalatnikov Simulation of Ferroelectric Switching

A ferroelectric capacitor could be modeled in accordance with the Landau-Khalatnikov equation,

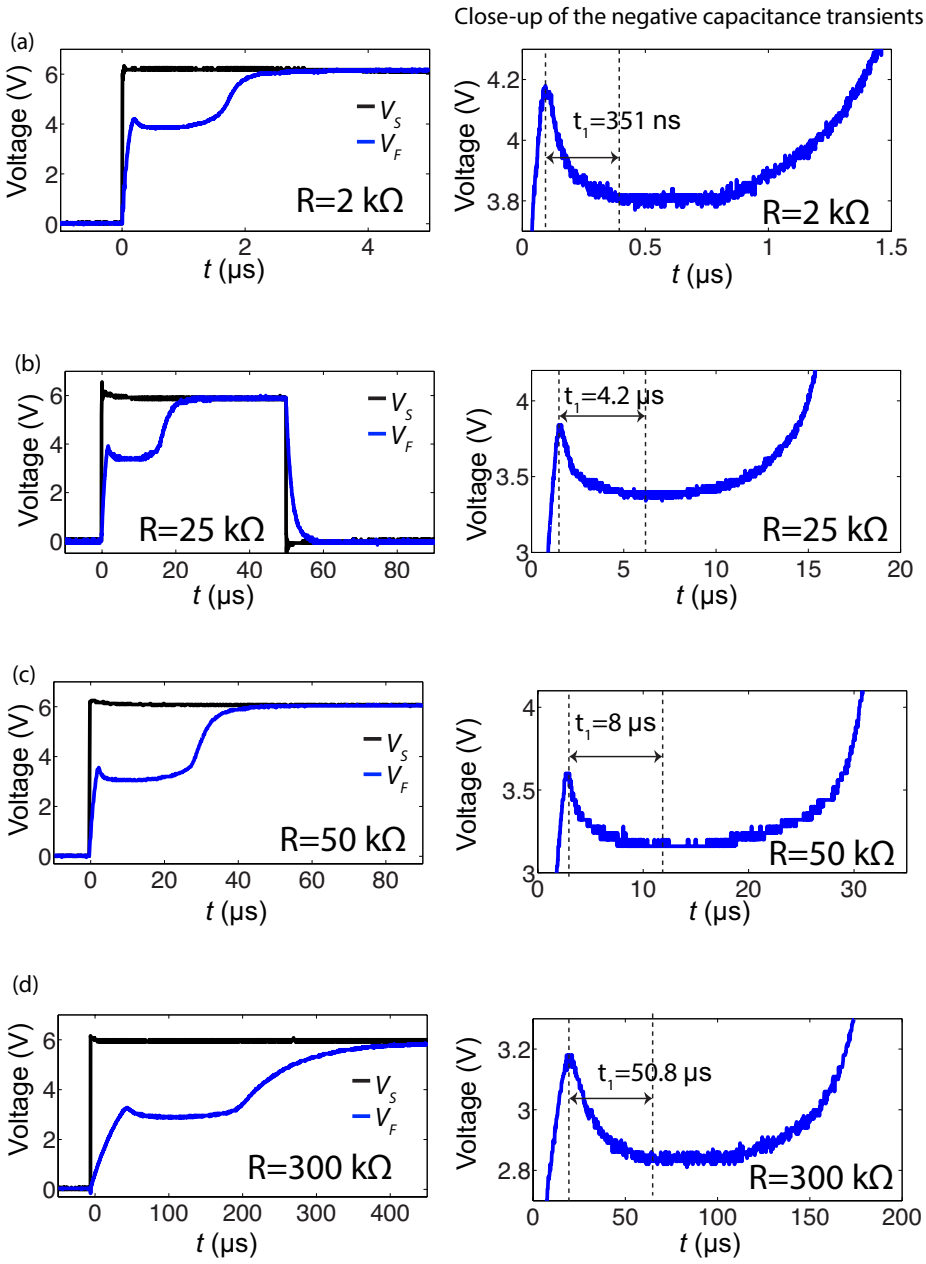


Figure 3.15: Transient response of the PZT sample to a DC pulse $V_S$: 0 V$\rightarrow$ +6 V for $R$=2 kΩ (a), 25 kΩ (b), 50 kΩ (c) and 300 kΩ (d). Before applying each of the pulses, a large negative voltage pulse was applied to set the initial polarization in the appropriate direction.

$$\rho\frac{dQ_F}{dt} = -\frac{dU}{dQ_F} \tag{3.1}$$

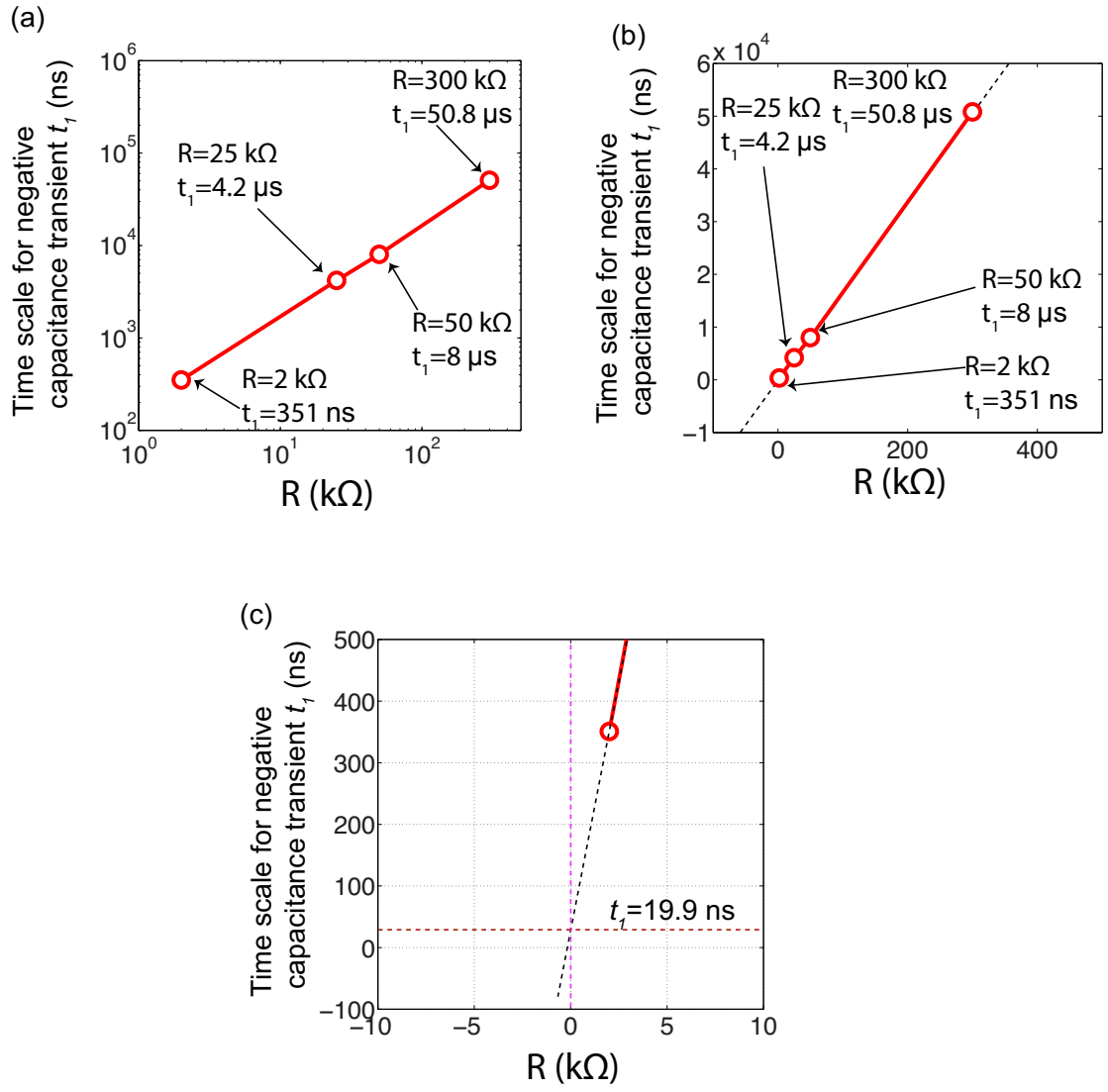


Figure 3.16: (a,b) The time duration of the negative capacitance transient $t_1$ as a function of $R$ in logarithmic (a) and linear scale (b). (c) Extrapolation of $t_1$ vs. $R$ curve to $R = 0$.

$$U = \alpha Q_F^2 + \beta Q_F^4 + \gamma Q_F^6 - Q_F V_F \tag{3.2}$$

where the energy density per unit area . $\alpha$, $\beta$ and $\gamma$ are rescaled anisotropy constant for the ferroelectric capacitor and $\rho$ is a material dependent parameter in the units of $\Omega$ which accounts for the dissipative processes during ferroelectric switching. Equation 3.1 could be rearranged in the following form.

$$V_F(Q_F) = \frac{Q_F}{C(Q_F)} + \rho \frac{dQ_F}{dt} \tag{3.3}$$

Here, $C(Q_F) = 2\alpha Q_F + 4\beta Q_F^3 + 6\gamma Q_F^5$.

In order to relate the rescaled anisotropy constants for the ferroelectric capacitor in equations 3.1 and 3.3 to per unit volume anisotropy constants, we note that, for an applied electric field $E$ across the ferroelectric capacitor, the per unit volume energy of a ferroelectric $U_{pu}$ is given by

$$U_{pu} = \alpha_1 P^2 + \alpha_{11} P^4 + \alpha_{111} P^6 - PE \tag{3.4}$$

where $P$ is the surface charge density or the ferroelectric polarization and $\alpha_1$, $\alpha_{11}$ and $\alpha_{111}$ are the per unit volume anisotropy constants of the material. For a parallel plate capacitor of area $A$ and thickness $d$, the charge $Q_F$ is given by $Q_F = PA$. The voltage across the ferroelectric capacitor $V_F = Ed$ and the free energy of the capacitor $U = U_{pu}Ad$. Hence the energy of the capacitor can be written as

$$\begin{aligned} U &= U_{pu}Ad \\ &= \{\alpha_1(\frac{Q_F}{A})^2 + \alpha_{11}(\frac{Q_F}{A})^4 + \alpha_{111}(\frac{Q_F}{A})^6 - (\frac{Q_F}{A})E\}Ad \\ &= \frac{d\alpha_1}{A}Q_F^2 + \frac{d\alpha_{11}}{A^3}Q_F^4 + \frac{d\alpha_{111}}{A^5}Q_F^6 - Q_F V_F \end{aligned} \tag{3.5}$$

Comparing equation 3.5 with equation 3.2, the following relationships are obtained.

$$\alpha = \frac{d\alpha_1}{A} \tag{3.6}$$

$$\beta = \frac{d\alpha_{11}}{A^3} \tag{3.7}$$

$$\gamma = \frac{d\alpha_{111}}{A^5} \tag{3.8}$$

From equation 3.3, we note that the equivalent circuit for a ferroelectric capacitor consists of an internal resistor $\rho$ and a nonlinear capacitor $C_F(Q_F)$ connected in series. We shall denote $Q_F/C_F(Q_F)$ as the internal ferroelectric node voltage $V_{int}$. Figure 3.17 shows the equivalent circuit corresponding to a ferroelectric capacitor connected to a voltage source through a resistor $R$. Following the experimental setup shown in figure 3.3(b), the parasitic capacitor $C$ is added in parallel to the ferroelectric ($\rho$ in series parallel to the $C_F(Q_F)$ in the simulation. A 60 nm PZT film with square electrodes of area $A$= (30 $\mu$m)$^2$ is taken as the ferroelectric capacitor. The parasitic capacitance $C$=60 pF. $\rho$ is taken as 50 k$\Omega$. The remnant polarization corresponding to these anisotropy constants is $\sim$0.7 C/m$^2$ and the coercive voltage is $\pm$7.5 V. The values of the anisotropy constants ($\alpha_1$, $\alpha_{11}$ and $\alpha_{111}$) for

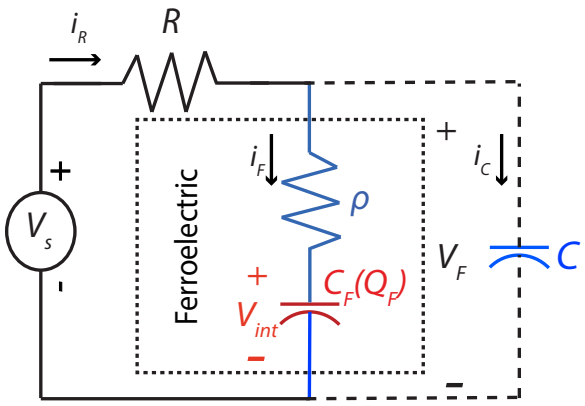


Figure 3.17: *Simulation of the time-dynamics of the ferroelectric switching.* (a) Equivalent circuit diagram of the simulation. $C_F$, $\rho$, $C$ and $R$ represent the ferroelectric capacitor, the internal resistor, the parasitic capacitor and the external resistor respectively. $V_S$, $V_{int}$ and $V_F$ are the voltage across the source, $C_F$ and $C$ respectively and $i_R$, $i_F$ and $i_C$ are the current through $R$, $C_F$ and $C$ respectively.

$Pb(Zr_{0.2}Ti_{0.8})O_3$ are taken from Ref. [39] and are listed below.

$$x = 0.8 \tag{3.9}$$

$$\alpha_1 = \frac{T - T_0}{2\epsilon_0 C_0}, \epsilon = 8.854 \times 10^{-12} \tag{3.10}$$

$$\alpha_{11} = (10.612 - 22.655x + 10.955x^2) \times \frac{10^{13}}{C_0} \tag{3.11}$$

$$\alpha_{111} = (12.026 - 17.296x + 9.179x^2) \times \frac{10^{13}}{C_0} \tag{3.12}$$

$$C_0 = (\frac{2.8339}{1 + 126.56(x - 0.5)^2} + 1.4132) \times 10^5 \tag{3.13}$$

$$T_0 = 462.63 + 843x - 2105.5x^2 + 4041.8x^3 - 3828.2x^4 + 1337.8x^5 \tag{3.14}$$

$$\tag{3.15}$$

Here, all units are in S.I.

The circuit shown in figure 3.17 is simulated by solving the following equations at each time step.

$$0 = V_s(t) - i_R(t)R - (i_R(t) - i_C(t))\rho - V_{int}(t) \tag{3.16}$$

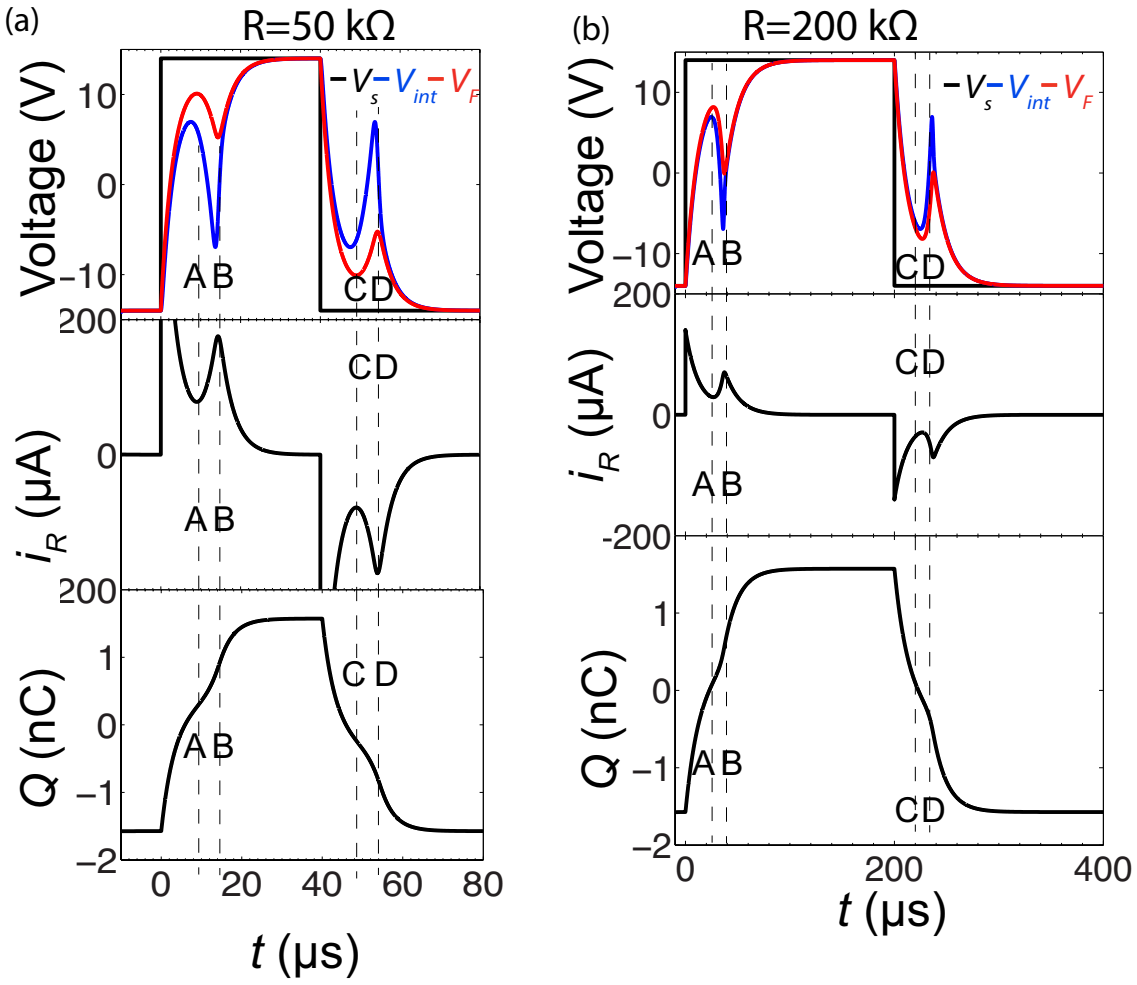


Figure 3.18: The simulated transient response of the series combination of the ferroelectric capacitor and a resistor $R = 200$ kΩ to an AC voltage pulse $V_s$ :-14 V→+14 V→-14 V.

$$0 = V_{int}(t) + (i_R(t) - i_C(t))\rho - \frac{1}{C}\int i_C(t)dt \quad (3.17)$$

$$Q_F(t) = Q_F(t=0) + \int_{t=0}^{t} (i_R(t) - i_C(t))dt \quad (3.18)$$

$$V_{int}(t) = \frac{Q_F(t)}{C_F(Q_F(t))} = 2\alpha Q_F(t) + 4\beta Q_F^3 + 6\gamma Q_F^5 \quad (3.19)$$

$V_F(t)$ is calculated using the relation: $V_F(t) = V_{int}(t) + (i_R(t) - i_C(t))\rho$.

Figure 3.18(a) show the simulated transients corresponding to $V_S$, $V_F$, $V_{int}$, $i_R$ and $Q$

of the series combination of the ferroelectric capacitor and a resistor $R = 50$ kΩ to an AC voltage pulse $V_s$ : -14 V $\rightarrow$+14 V $\rightarrow$ -14 V. In figure 3.18(a), we observe opposite signs of changes in $V_F$ and $Q$ during the time segments $AB$ and $CD$, as was seen experimentally in figure 3.4. Figure 3.19(b) plots the simulated dynamic hysteresis loop ($P - V_F$ curve) and the $P - V_{int}$ curve for $R$= 50 kΩ. To understand the difference between the $P - V_F$ and $P - V_{int}$ curves we note that $V_F = V_{int} + \rho i_F$, with $i_F$ being the current through the ferroelectric branch; the additional resistive voltage drop, $i_F$, results in the hysteresis in the $P - V_F$ curve. Nevertheless, it is clear from figure 3.19(b) that the negative slope of the $P - V_{int}$ curve in a certain range of $P$, due to $C_F$ being negative in that range, is reflected by the negative slope in the $P - V_F$ curve in the segments $AB$ and $CD$.

We also simulated the transients for the same circuit with $R = 200$ kΩ for $V_s$ : -14 V $\rightarrow$+14 V $\rightarrow$ -14 V, which are plotted in figure 3.18(b). The corresponding dynamic hysteresis loops are plotted in figure 3.19(b). We observe that, for a smaller value of $R$, the hysteresis loop of the simulated dynamic hysteresis loop is wider, as was observed experimentally in figure 3.14 and discussed in section 3.8. This is due to the fact that, for a larger $R$, the current through the ferroelectric is smaller, resulting in a smaller voltage drop across $\rho$.

Similarly, in section 3.7, we observed that the larger the magnitude of the applied voltage, the wider the hysteresis loop, which could be explained by the model presented. For a larger peak voltage, a larger current flows into the ferroelectric, thereby increasing the voltage drop across the internal resistance $\rho$.

## 3.11 Dependence of $\rho$ and the negative capacitance on the voltage amplitude

Based on the discussion in the previous section, we first describe a procedure to estimate the value of the parameter $\rho$. Equation 3.3 can be rewritten as follows.

$$V_F(Q_F(t)) = \frac{Q_F(t)}{C_F(Q_F(t))} + \rho i_F(t) \tag{3.20}$$

where $i_F = dQ_F/dt$. Let us compare the dynamics of a ferroelectric capacitor for two different resistors $R_1$ and $R_2$ for the same applied voltage pulse. Let $t_1$ and $t_2$ be the time variables for these two cases, $i_{F1}$ and $i_{F2}$ be the corresponding currents through the ferroelectric capacitor and $V_{F1}$ and $V_{F2}$ be the measured ferroelectric voltages for the resistors $R_1$ and $R_2$ respectively. Hence,

$$V_{F1}(Q_{F1}(t_1)) = \frac{Q_{F1}(t_1)}{C_F(Q_{F1}(t_1))} + \rho i_{F1}(t_1) \tag{3.21}$$

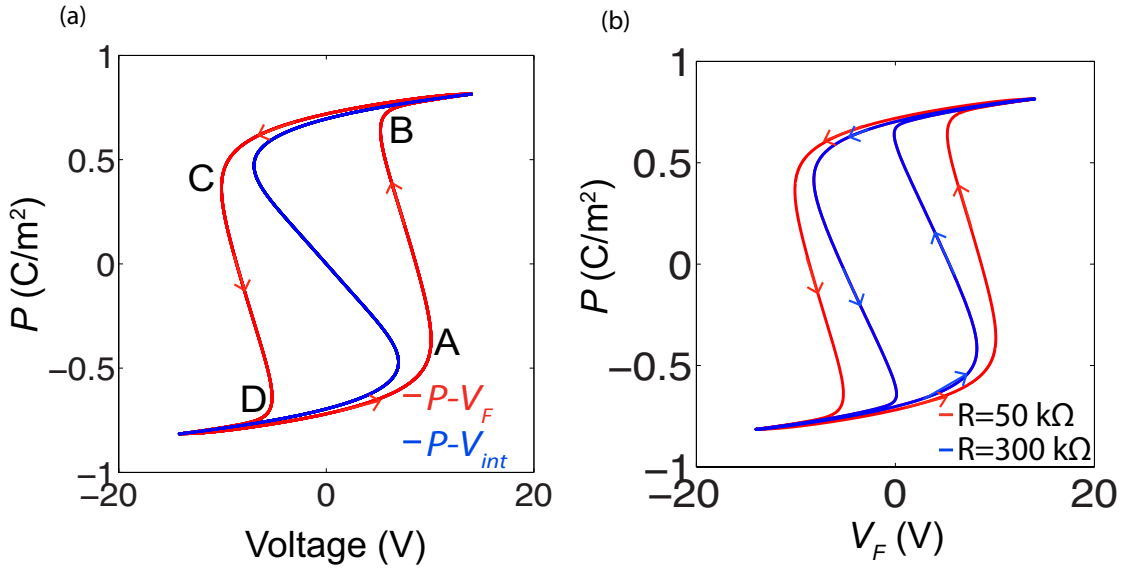


Figure 3.19: (a) The ferroelectric polarization P(t) as a function of $V_F(t)$ and $V_{int}(t)$ for $V_s$ :-14 V→+14 V→-14 V and $R$ = 50 kΩ. (b) Comparison of the simulated $P(t) - V_F(t)$ curves for $R$ = 50 kΩ and 200 kΩ upon the application of $V_s$ :-14 V→+14 V→-14 V.

$$V_{F2}(Q_{F2}(t_2)) = \frac{Q_{F2}(t_2)}{C_F(Q_{F2}(t_2))} + \rho i_{F2}(t_2) \tag{3.22}$$

Let us assume that, in the first experiment with the resistor $R_1$, $Q_{F1}$ reaches a given value $Q$ at $t_1 = \tau_1$, and in the second experiment with $R_2$, $Q_{F2}$ reaches $Q$ at $t_2 = \tau_2$ (i.e. $Q_{F1}(t_1 = \tau_1) = Q_{F2}(t_2 = \tau_2) = Q$). Hence from equation (3.21) and (3.22), the following equation for $\rho$ can be derived.

$$\rho(Q) = \frac{V_{F1}(t_1 = \tau_1) - V_{F2}(t_2 = \tau_2)}{i_{F1}(t_1 = \tau_1) - i_{F2}(t_2 = \tau_2)} = \frac{V_{F1}(Q) - V_{F2}(Q)}{i_{F1}(Q) - i_{F2}(Q)} \tag{3.23}$$

Now we investigate the dependence of $\rho$ and the negative capacitance on the voltage magnitude. Figure 3.20(a,b) show the transient response of the PZT sample to DC pulses of different applied voltage amplitudes for $R$=50 kΩ and 300 kΩ respectively. Before applying each of the pulses shown in figure 3.20, a large negative voltage pulse was applied to set the initial polarization along the appropriate direction. Figure 3.21(a,b) show the $Q_F - V_F$ and $Q_F - i_F$ curves respectively for different applied voltage amplitudes with $R$= 50 kΩ and $R$= 300 kΩ. Figure 3.21(c) shows the value of $\rho$ calculated using equation 3.23 as a function of

$Q_F$ for different voltage amplitudes. Using the extracted value of $\rho$ for a given voltage amplitude, the internal node voltage $V_{int}(Q_F(t)) = Q_F(t)/C_F(Q_F(t)) = V_F(Q_F(t)) - i_F(Q_F(t)) \times \rho$ is calculated. Figure 3.22 shows the corresponding $Q_F - V_{int}$ curves. In figure 3.22, the negative capacitance state of the ferroelectric corresponds to the region under the dashed box. The average value of the negative capacitance $C_{FE}$ is calculated using the equation: $C_{FE} = \Delta Q_F/\Delta V_{int}$, $\Delta Q_F$ and $\Delta V_{int}$ being the changes in the ferroelectric charge and the internal ferroelectric node voltage in the negative capacitance region, respectively.

Figure 3.23(a,b) plot the average $\rho$ and $-C_{FE}$ respectively as functions of the applied voltage amplitude. We note in figure 3.23(a) that the average value of $\rho$ decreases monotonically from a value of $\sim$15 k$\Omega$ with an increasing amplitude of the applied voltage while the magnitude of the negative capacitance $C_{FE}$ remains reasonably constant within the range 400-500 pF.

## 3.12 Domain Mediated Switching Mechanisms and Negative Capacitance

In principle, the 1-D Landau-Khalatnikov equation of ferroelectric switching detailed in section 3.11 corresponds to a single domain scenarios shown in figure 3.24(a). Given the large size of our capacitors (30 $\mu$m $\times$ 30 $\mu$m), the switching invariably happens through domain-mediated mechanisms, which is schematically illustrated in figure 3.24(b). Thus, our results show that, the double well picture aspresented in section 3.1, which is typically associated with a single domain configuration (section 3.11) can still qualitatively predict the experimental outcome. Nonetheless, as long as there is a threshold and subsequent abrupt switching, a negative capacitance effect will ensue. The single domain picture tries to capture the threshold by estimating it through a double-well energy profile and as such provides the mean value of the microscopic parameters.

Most importantly, even in a domain mediated switching, a regime of abrupt switching is present that leads to the negative capacitance transient. The characteristic negative capacitance transients (for example the result shown in figure 3.5) and the experimental $P(t) - V_F(t)$ curves reveal that the negative capacitance effect exists during the initial period of the transient and in a certain range of ferroelectric polarization. For example, in the $P(t) - V_F(t)$ curve shown in figure 3.25, the negative capacitance is observed in the polarization ranges: (-0.46 C/m$^2$, -0.73 C/m$^2$) and (+0.32 C/m$^2$, +0.66 C/m$^2$). This indicates that microscopically an abrupt switching event exists in the initial period of the switching, before the material reverts back to an ordinary-capacitor behavior.

In section 3.12, we have seen that the average value of $\rho$ decreases monotonically with an increasing amplitude of the applied voltage while $|C_{FE}|$ remains reasonably constant within

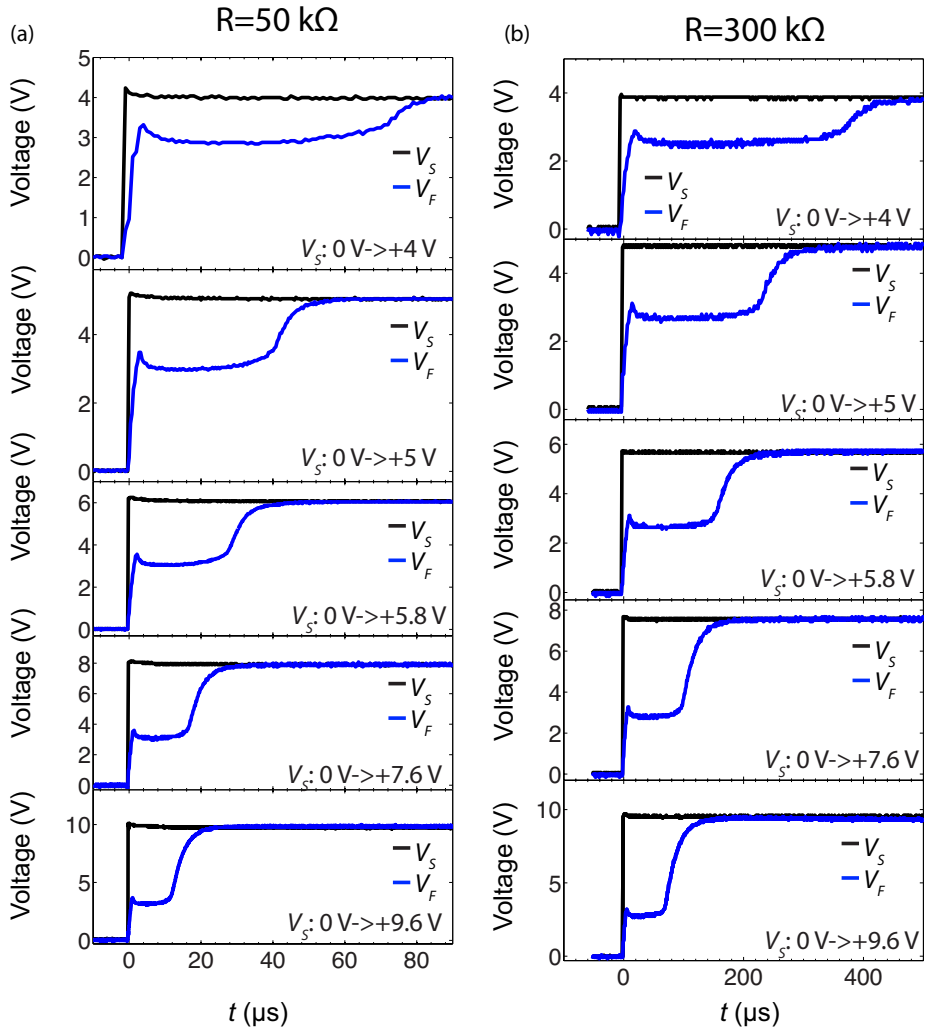


Figure 3.20: Transient response of the PZT sample to DC pulses of different amplitudes for $R$=50 kΩ (a) and 300 kΩ (b). Before applying each of the pulses, a large negative voltage pulse was applied to set the initial polarization along the appropriate direction.

the range 400-500 pF. Intuitively, in a domain-mediated switching process, a larger input voltage results in more domains to nucleate at the onset. Hence, this suggests that this increase in number of initial domains lead to a smaller $\rho$, while the negative capacitance remains fairly independent of it.

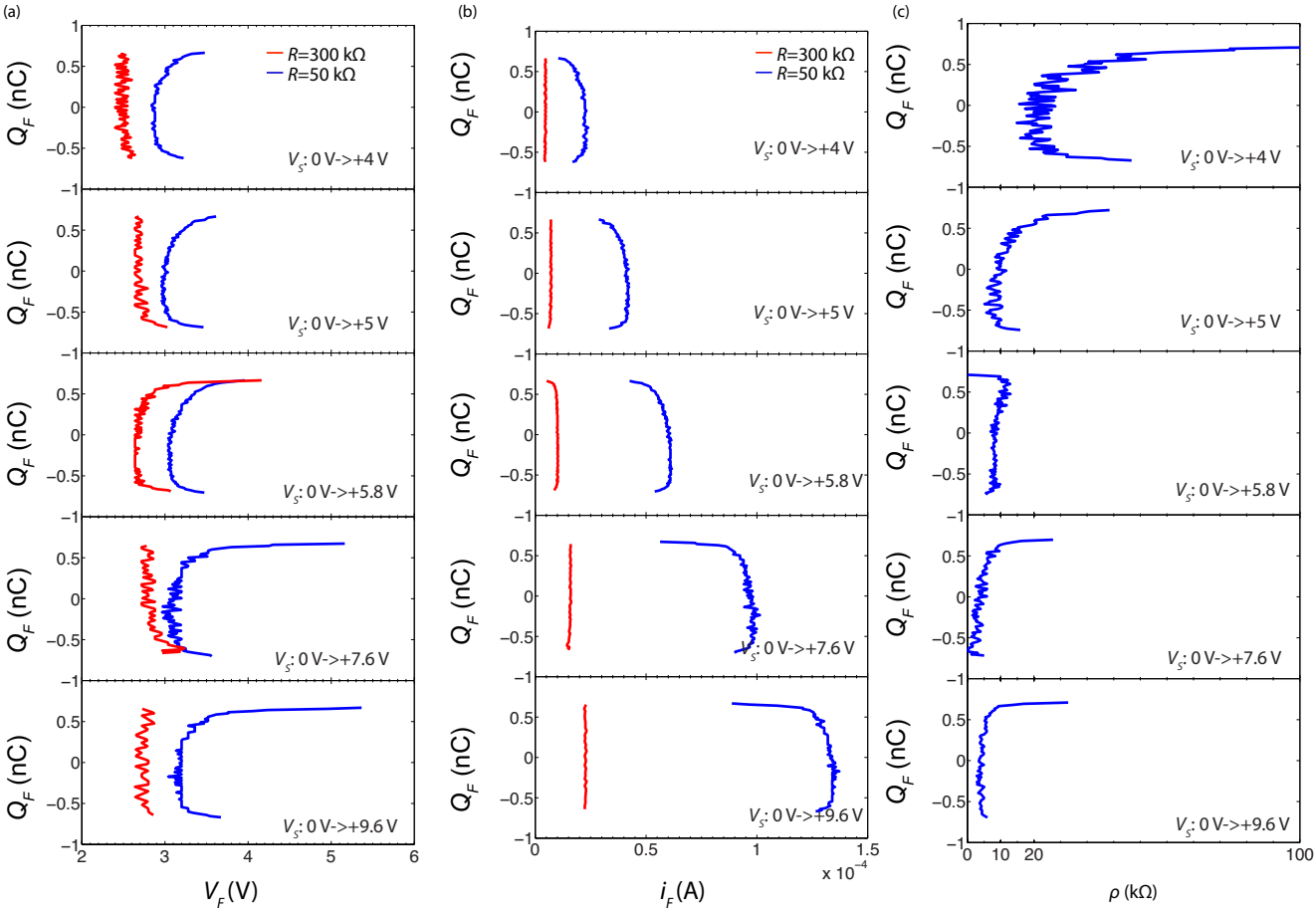


Figure 3.21: (a,b) $Q_F - V_F$ (a) and $Q_F - i_F$ (b) curves for different applied voltage amplitudes with $R$= 50 kΩ and $R$= 300 kΩ. (c) The value of $\rho$ calculated using equation 3.23 as a function of $Q_F$ for different voltage amplitudes.

## 3.13 Comparison with Previously Published Reports on Negative Capacitance and Ferroelectric Switching Dynamics

It is interesting to note that a negative slope in the polarization-voltage characteristic has been predicted since the early days of ferroelectricity [102, 40, 24, 25, 103, 104]. What is even more interesting is that the characteristic negative capacitance transient was actually observed in as early as 1956 by Merz *et al.* (see figure 1 in Ref. [25]). Landauer *et al.* plotted the polarization-voltage curve of a ferroelectric showing the negative capacitance

region in figure 4 of Ref. [24] in 1957. However, a successful measurement of the entire intrinsic hysteresis loop was performed by Bratkovsky *et al.*, albeit only indirectly [104]. An S-like polarization-voltage behavior in one branch of the hysteresis has been measured in a transistor structure [105]. In contrast, our results provide a direct measure of the intrinsic hysteresis and negative capacitance of the material.

Note that, in our study of ferroelectric switching dynamics, the dynamics is intentionally slowed down by adding a large series resistance $R$. The addition of a series resistance ($R$) is critically important in revealing the negative capacitance region in the dynamics. An appreciable voltage drop across the series resistance $R$ allows the voltage across the ferroelectric capacitor to be measured without being completely dominated by the source voltage-in the limit when $R \rightarrow 0$, the voltmeter would be directly connected across the voltage source. Most model studies on ferroelectric switching [25, 106, 107, 108] have been done in the latter limit-where the ferroelectric capacitor is directly connected across a voltage source (or through a small resistance).

## 3.14 Comparison of the negative capacitance calculated from dynamic measurement and stabilization experiments

It is interesting to compare the directly measured value of negative capacitance and the extracted value in Khan et al.[109] The value of negative capacitance of PZT film in the PZT(28 nm)/STO(48 nm) bilayer extracted in Ref. [109] is within -10 and -30 $\mu$F/cm$^2$. In comparison, the capacitance per unit area of a 60 nm PZT film measured in the current work is $\sim$-55 $\mu$F/cm$^2$. If it is normalized to the same thickness of PZT (28 nm) in Ref. [109], it is $\sim$-110 $\mu$F/cm$^2$. Therefore, the values are in the same ballpark. This is remarkable given the fact that the two experiments were done on completely two different batches of samples grown at different conditions. Therefore, the values obtained in these two different approaches namely the current dynamic measurement of isolated PZT and stabilized negative capacitance in PZT-STO series combination are completely consistent.

Notably, the polarization and strain in a ferroelectric material are fundamentally coupled.[39] In a bi-layer, the depolarization field felt by the ferroelectric material leads to suppression of polarization, which then reorganizes the strain which in turn changes the polarization again. Ultimately, the ferroelectric will be stabilized such that the polarization, depolarizing field and strain find a self-consistent solution. This also depends on the polarizability, screening etc. of the dielectric material. Thus when a negative capacitance is stabilized by a dielectric capacitor in series, the effective negative capacitance could be somewhat different from that measured from the '$S$' curve in an isolated ferroelectric. Therefore, in a stabilized structure, it will be necessary to measure the effective negative capacitance

in-situ by looking at the enhancement of capacitance as shown in Ref. [109, 110].

## 3.15 Correlation between Structural Properties and Negative Capacitance Transients

In chapter 2 section 2.12, we showed that the electrical properties of PZT films are strongly correlated to the X-ray diffraction rocking curve full-width-half-maximum (FWHM). Figure 3.26 shows the X-ray diffraction rocking curve measurement around the PZT (002) peak of the same 60 nm PZT film for which the negative transients are observed in the preceding sections in this chapter. The FWHM of PZT (002) rocking curve is less than 0.1 °, which points to the high crystalline quality of this film. Figure 3.27(a, b, c, d) show the dielectric constant-voltage and the admittance angle-voltage characteristics of the PZT(60 nm)/SRO(60 nm)/STO(001) at 1 kHz, 10 kHz, 100 kHz and 1 MHz respectively. In figure 3.27(a-e), we observe that the admittance angle is $\sim 90^0$ at all frequencies. Figure 3.28 shows the dielectric constant $\varepsilon_r$ as a function the AC electric field $E_0$ at 10 kHz. We observe that as the AC electric field is increased from 10 kV/cm to ∼120 kV/cm, the dielectric constant increases by a mere 0.4% for this sample. The correlation between the low FWHM and the low frequency dispersion, small Rayleigh coefficient in this sample is consistent with results in presented in chapter 2 section 2.12 and figures 2.17 and 2.18.

Next we look into another PZT sample whose FWHM is ∼0.3 ° (see figure 3.29(a). Figure 3.29(b) shows the $V_F$ transients corresponding to voltage pulses $V_S$: 0 V → +5.8 V and 0 V → +10 V. We note in figure 3.29(b) that no characteristic transients are observed in this sample. Thus, the comparison of the transient response of PZT samples with low FHWM and large FWHM suggests the characteristic negative capacitance transients ensue in PZT films with high crystalline quality.

## 3.16 Conclusions

The key results reported in this chapter are listed below.

1 We have presented the first direct measurement technique of negative capacitance in an isolated ferroelectric capacitor. We have introduced two new fundamental concepts in negative capacitance, namely the characteristic negative capacitance transients and the dynamic hysteresis loop.

2 We studied how the negative capacitance transients and the dynamic hysteresis loops vary with the external circuit parameters such as the external resistor and the voltage

pulse amplitude.

3 The results were qualitatively explained using a 1-D Landau-Khalatnikov model. The key insight obtained is that, even though the ferroelectric switching invariably occurs through domain mediated mechanisms in our samples, the negative capacitance effect, which is predicted based on a single domain double-well energy well picture, is still robust in such situations. This indicates that microscopically abrupt switching events are copiously present during the early parts of the switching dynamics.

## 3.17 Suggestions for Future Work

1 The microscopic details of ferroelectric switching dynamics could be studied using multiple techniques such as using atomic force microscopy [111] and X-ray diffraction [112]. In combination with the time dynamic measurement presented in this chapter, such techniques could reveal important information of the microscopic details of the characteristic negative transients (for example, the abrupt/correlated switching events during the early part of the switching dynamics that result in the characteristic transients).

2 The concept of negative capacitance goes beyond the ferroelectrics and and can be applied in general to any two-level system separated by an intrinsic barrier [26, 27, 28, 29, 30]. The technique presented herein could serve as a canonical test for negative capacitance in any such system.

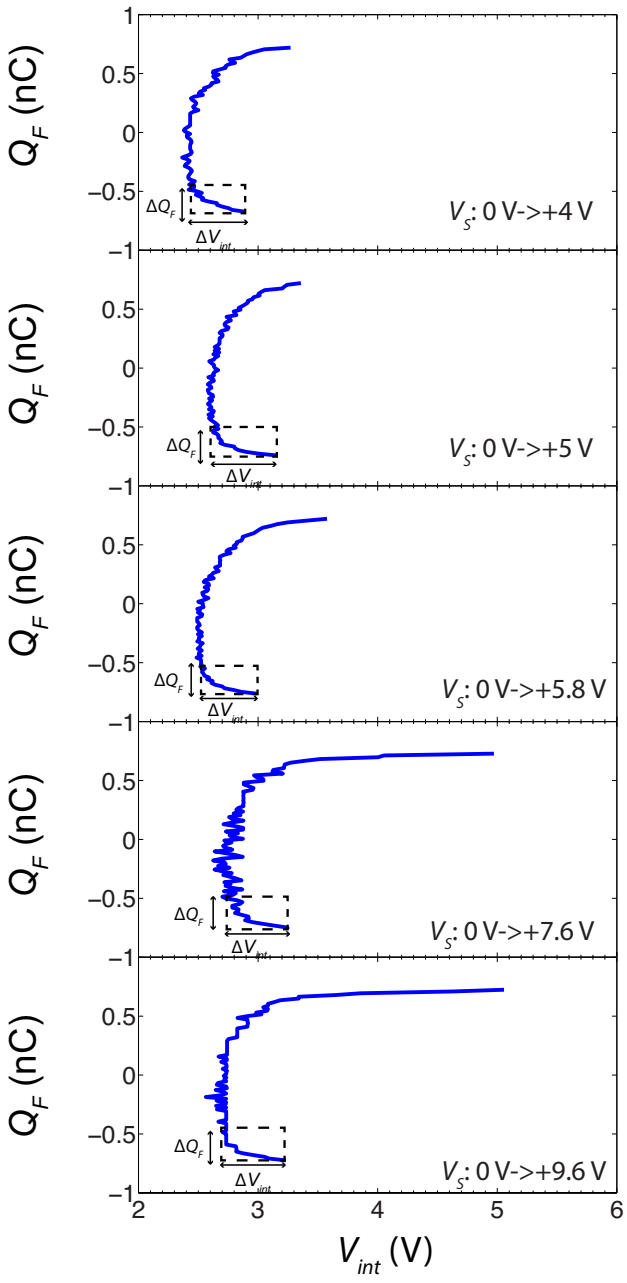


Figure 3.22: $Q_F - V_{int}$ curves for different voltage pulses. The negative capacitance state of the ferroelectric corresponds to the region under the dashed box.

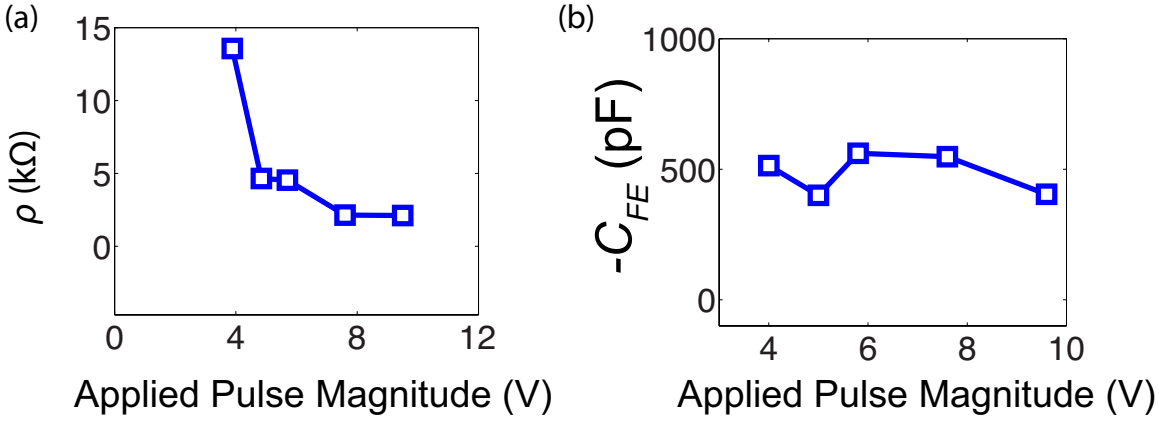


Figure 3.23: Average $\rho$ (a) and $-C_{FE}$ (b) as functions of the applied voltage magnitude.

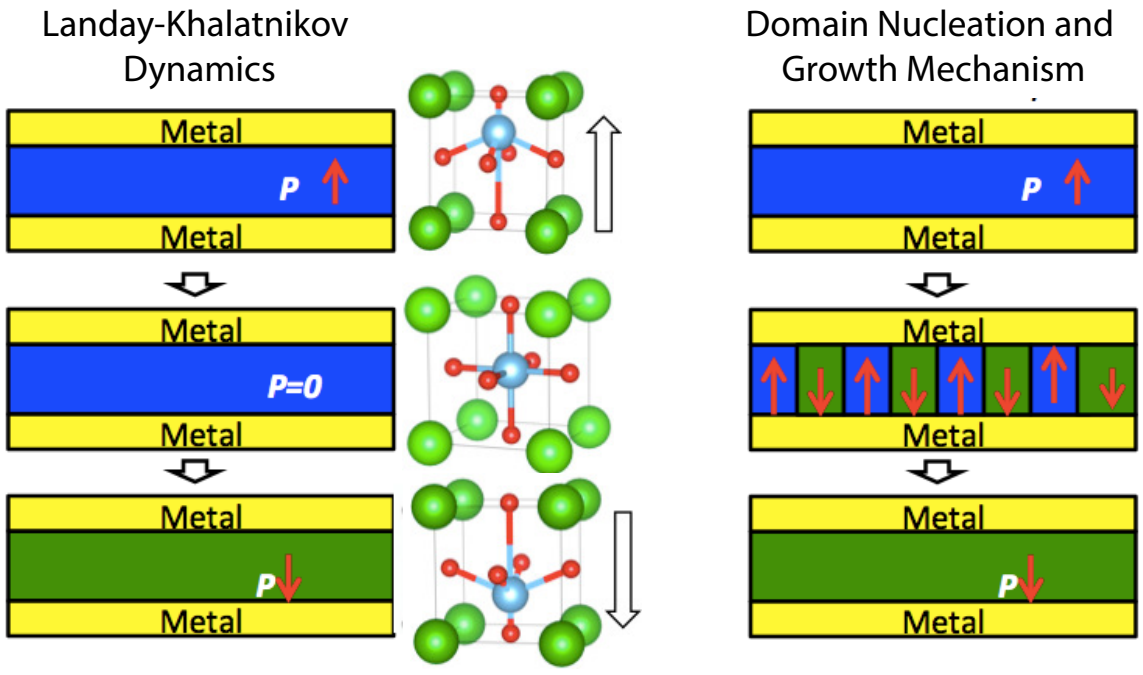


Figure 3.24: Schematic illustration of ferroelectric switching in the single domain fashion (a) and through domain mediated mechanisms (b).

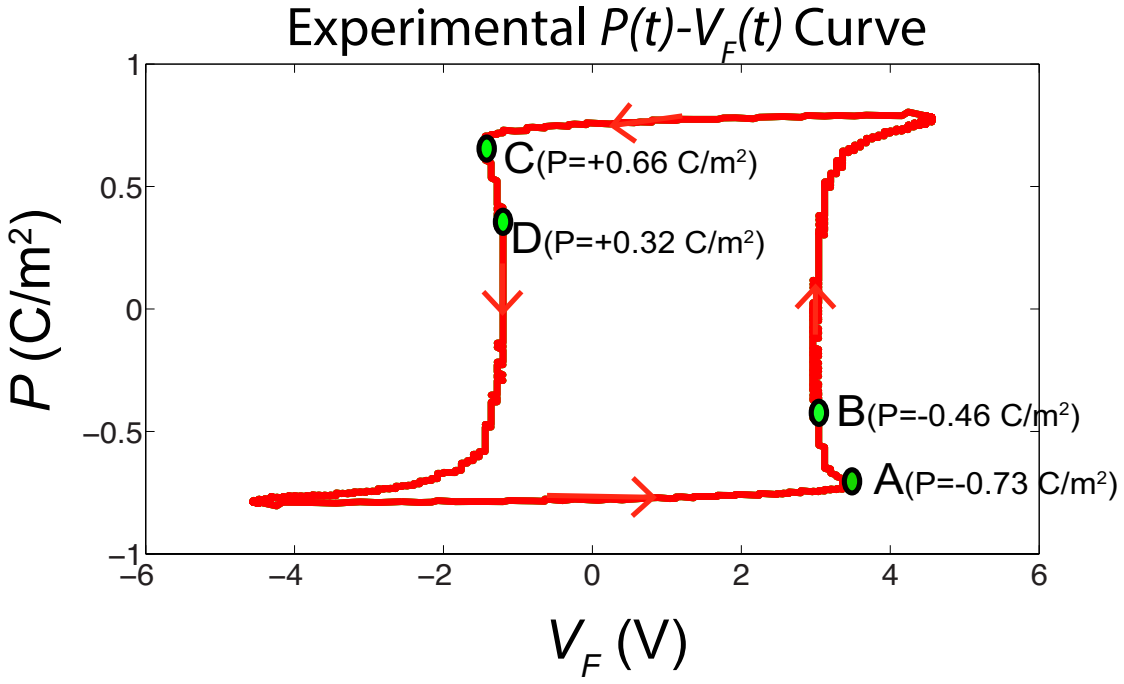


Figure 3.25: The dynamic hysteresis loop showing the polarization range of negative capacitance state. This loop is a replotted version of the same shown in figure 3.6.

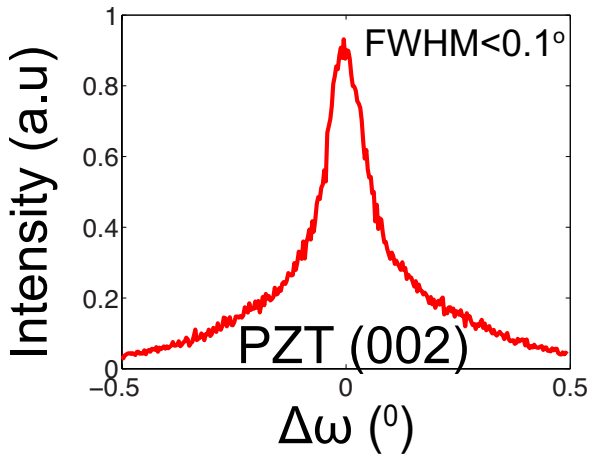


Figure 3.26: X-ray diffraction rocking curve measurement around the PZT (002) peak of the 60 nm PZT film.

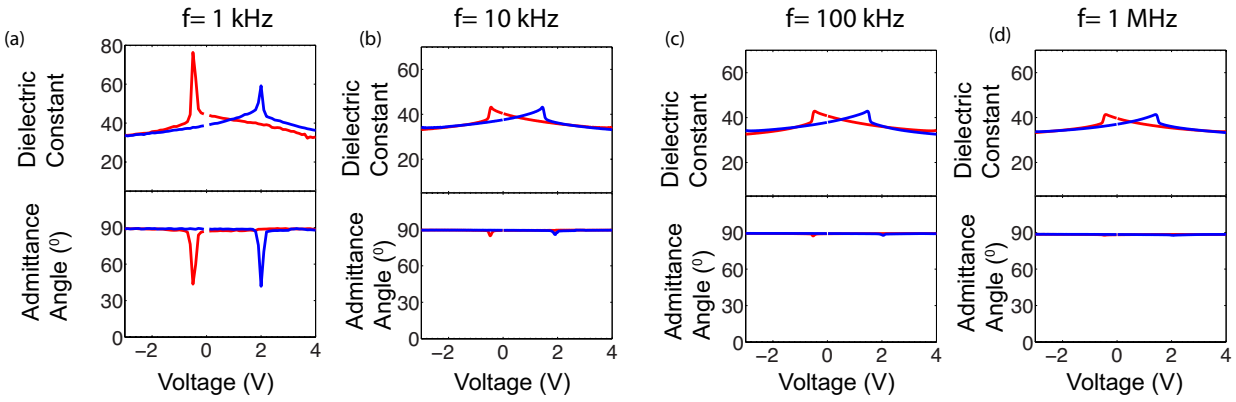


Figure 3.27: (a,b,c,d) Dielectric constant-voltage and the admittance angle-voltage characteristics of the PZT sample at 1 kHz (a), 10 kHz (b), 100 kHz (c) and 1 MHz (d).

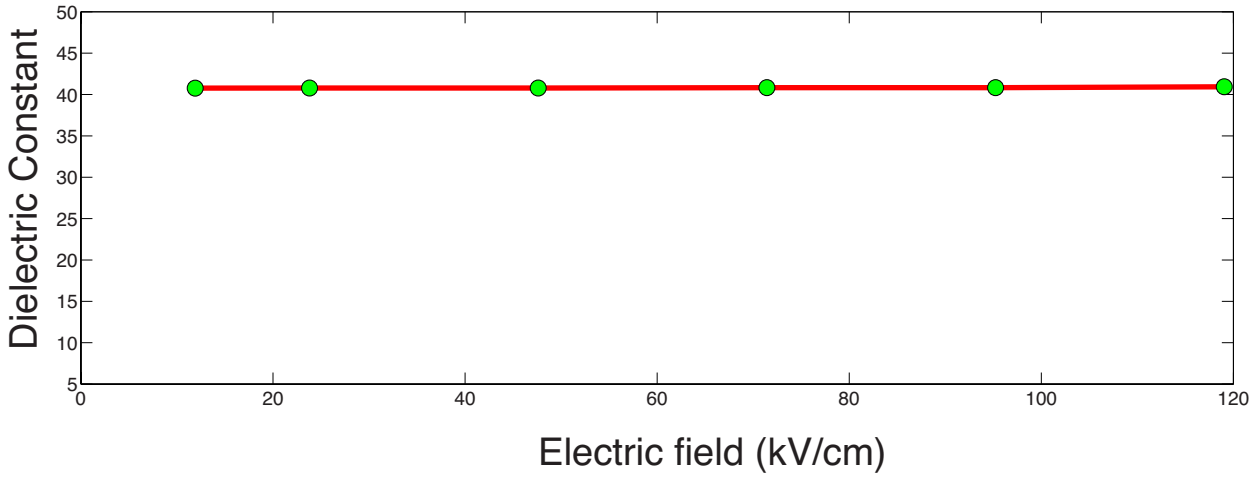


Figure 3.28: The dielectric constant $\varepsilon_r$ as a function the AC electric field $E_0$ at 10 kHz.

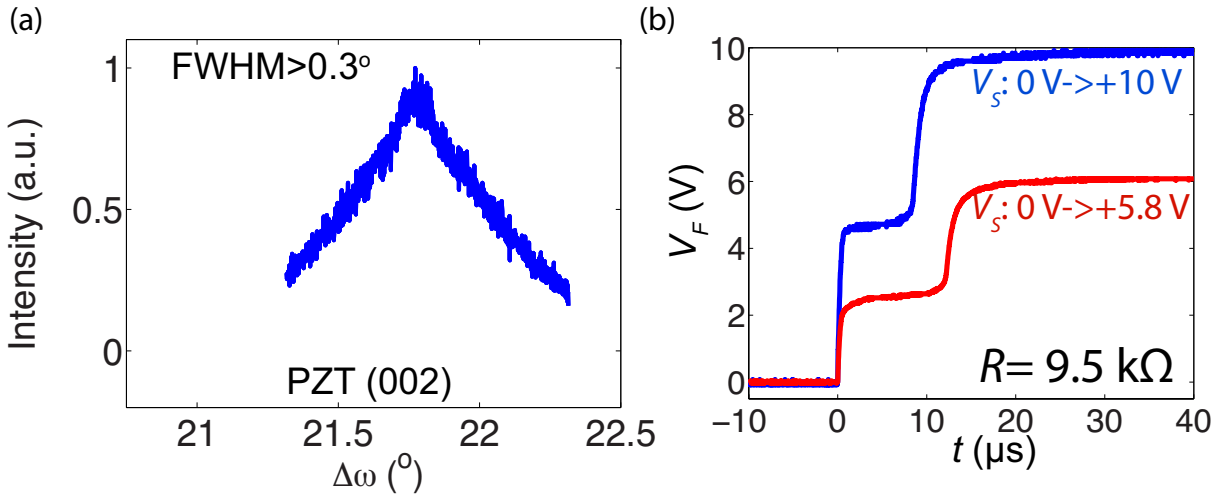


Figure 3.29: (a) X-ray diffraction rocking curve measurement around the PZT (002) peak of a PZT film with FWHM $> 0.3°$. (b) $V_F$ transients corresponding to voltage pulses $V_S$: 0 V $\rightarrow$ +5.8 V and 0 V $\rightarrow$ +10 V. $R$=9.5 k$\Omega$.

# Chapter 4

# STABILIZATION OF NEGATIVE CAPACITANCE: CAPACITANCE ENHANCEMENT IN FERROELECTRIC-DIELECTRIC HETEROSTRUCTURES

In the previous chapters, we have seen that the ferroelectric negative capacitance is an unstable state and, in an isolated ferroelectric capacitor, the negative capacitance states can be accessed only in a time-dynamic fashion. This chapter describes the stabilization of the ferroelectric negative capacitance state by putting a positive capacitor in series. The significance of the results presented in this chapter lies in the fact the fact that, to reduce the subthreshold swing in a field-effect transistor, the ferroelectric negative capacitance is required to be stabilized. The in-series positive capacitor could be the semiconductor channel capacitor in a negative capacitance field-effect-transistor or a dielectric capacitor in a ferroelectric-dielectric heterostructure. In this chapter, we take recourse to the latter approach where we take ferroelectric $Pb(Zr_{0.2}Ti_{0.8})O_3$-dielectric $SrTiO_3$ heterostructure as a model system. The stabilization of the ferroelectric negative capacitance in a ferroelectric-dielectric heterostructure results in an enhancement of the equivalent capacitance of the heterostructure over that of the constituent dielectric, which we demonstrate experimentally.

In this chapter, we start with the general theory of the stabilization of the negative capacitance state in a ferroelectric-dielectric heterostructure in section 4.1. Section 4.2 details the experimental demonstration of the capacitance enhancement in a ferroelectric $Pb(Zr_{0.2}Ti_{0.8})O_3$-dielectric $SrTiO_3$ heterostructure capacitor due to the stabilized state of the ferroelectric negative capacitance. In section 4.3, we describe a model based on the 1-D Landau theory a generic ferroelectric-dielectric heterostructure and qualitatively explain the experimentally observed temperature dependence of the negative capacitance effect.

Most of the results presented in the chapter was reported in Khan *et al.* [113].

## 4.1 Theory of Stablization of Ferroelectic Negative Capacitance in a Ferroelectric-Dielectric Heterostucture

The negative capacitance in a ferroelectric capacitor can be stabilized in a ferroelectric-dielectric heterostructure schematically shown in figure 4.1(a). Figure 4.1(b) shows the equivalent circuit diagram of the ferroelectric-dielectric heterostructure capacitor. $C_{FE}$ and $C_{DE}$ stand for the ferroelectric and dielectric capacitance, respectively. Since the capacitors are in series, the same amount of charge $Q$ accumulates across of each of the capacitors. Hence, at a given $Q$, the total energy of the series combination $U_{FE+DE}$ is the sum of the energies of the ferroelectric and the dielectric ($U_{FE}$ and $U_{DE}$ respectively). In other words, $U_{FE+DE}(Q) = U_{FE}(Q) + U_{DE}(Q)$. At equilibrium, the series combination stabilizes at a charge $Q$ that minimizes the total energy of the system. Figures 4.1(c,d) show the energy landscapes of the ferroelectric and the dielectric and the series combination for two different cases. The charge rests at the minima of the ferroelectric-dielectric energy landscape. Note in figures 4.1(c,d) that *the equilibrium $Q$ corresponds to the negative capacitance region in the ferroelectric energy landscape, which points to the fact that the ferroelectric has been stabilized in the negative capacitance state.* Figure 4.1(e) shows a case where the dielectric capacitance is such that the negative capacitance state is not stabilized since the equilibrium $Q$ lies outside the negative capacitance region of the ferroelectric energy landscape.

Now the question is what the macroscopic signature of stabilization of the ferroelectric negative capacitance in a ferroelectric-dielectric heterostructure is. To understand that, we note that, according to the laws of electrostatics and circuits theory, the equivalent capacitance of a series combination of two positive capacitors will be smaller than each of them. In a ferroelectric-dielectric heterostructure, this classical law could be broken since $C_{FE+DE} = (C_{FE}^{-1} + C_{DE}^{-1})^{-1}$ could be larger than $C_{DE}$ if $C_{FE}$ is negative and $|C_{FE}| > C_{DE}$. Based on the energy based definition of capacitance ($C = (d^2U/dQ^2)^{-1}$), at given $Q$, the flatter the energy landscape is, the larger the capacitance is. In figures 4.1(c,d), we note that at the $Q$ corresponding to minima/minimum, the ferroelectric-dielectric energy landscape at the minima is flatter than that of the dielectric indicating that in both of these cases $C_{FE+DE} > C_{DE}$. On the other hand, in figure 4.1(e), where the negative capacitance is not stabilized, the ferroelectric-dielectric energy landscape at the minima is less flat than that of the dielectric indicating that $C_{FE+DE} < C_{DE}$ in this case.

It is interesting to note that temperature could be used as a tuning parameter for the ferroelectric negative capacitance. In the Landau description of the ferroelectric, the temperature ($T$) dependence in the energy $U_{FE} = \alpha Q^2 + \beta Q^4 + \gamma Q^6$ comes through the parameter $\alpha = a_\circ(T - T_c)$, where $a_\circ$ is a positive material dependent parameter and $T_c$ is the Curie temperature. For given ferroelectric-dielectric heterostructure, the ferroelectric negative capacitance could be transformed from stable state to an unstable one by simply changing

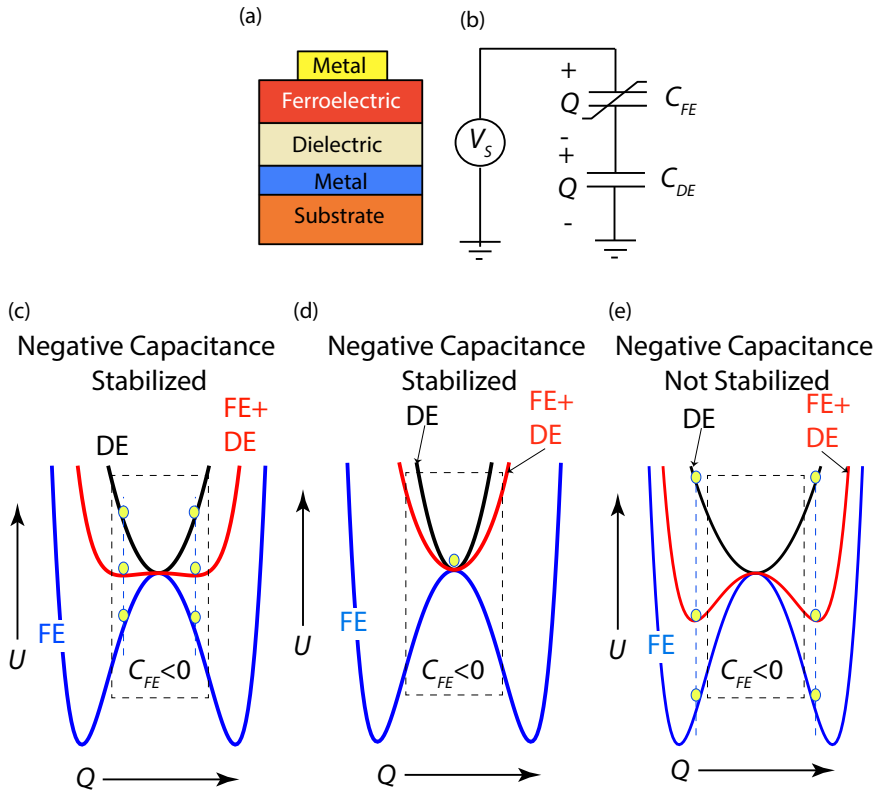


Figure 4.1: *Stabilization of ferroelectric negative capacitance.* (a) Schematic diagram of a ferroelectric-dielectric heterostructure capacitor. (b) Equivalent circuit diagram of a ferroelectric-dielectric heterostructure. (c,d,e) Energy landscapes of the ferroelectric and the dielectric and the series combination for three different cases. In the cases presented in figures (c,d), the ferroelectric negative capacitance state has been stabilized. For the case presented in figure (e), the ferroelectric negative capacitance state has not been stabilized. In figure (c), ferroelectric-dielectric landscape still has two minima, which means that, in this case, the ferroelectric-dielectric heterostructure still behaves like a ferroelectric with a smaller spontaneous polarization and a smaller hysteresis window. On the other hand, in figure (d), where the dielectric capacitance is smaller (the dielectric energy landscape is less flat) than that in figure 4.1(c), ferroelectric-dielectric landscape has a single minimum, and as result, it is behaves like a dielectric.

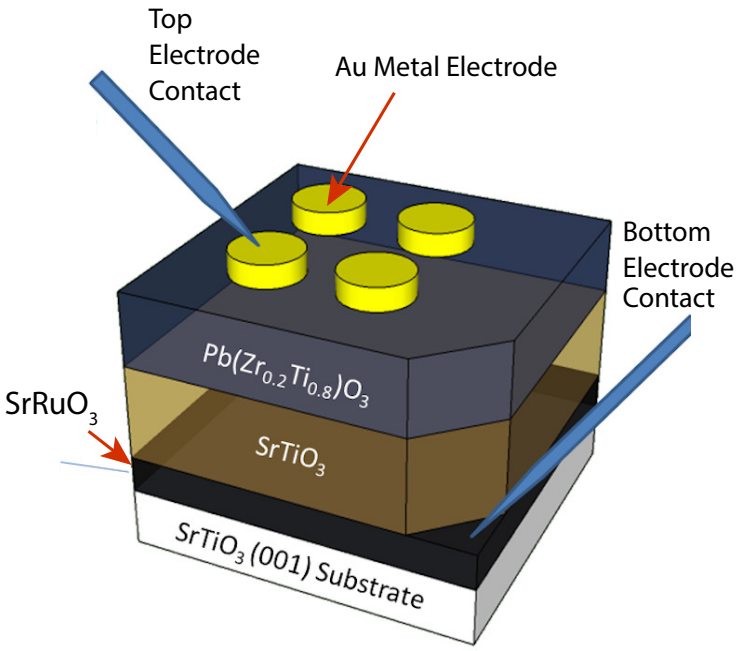


Figure 4.2: Schematic diagram of the ferroelectric $Pb(Zr_{0.2}Ti_{0.8})O_3$-dielectric $SrTiO_3$ capacitor. Au and $SrRuO_3$ (SRO) are used as top and bottom contacts respectively.

temperature, which we will demonstrate in the succeeding sections.

## 4.2 Experimental Demonstration of Stabilization of Negative Capacitance and Capacitance Enhancement in Ferroelectric-Dielectric Heterostructures

Let us first consider a ferroelectric $Pb(Zr_{0.2}Ti_{0.8})O_3$ (28 nm)-dielectric $SrTiO_3$ (48 nm) heterostructure grown on metallic $SrRuO_3$ buffered $SrTiO_3$ (001) substrate. The growth of the sample is described in chapter 2 and the schematic diagram of the measurement is shown in figure 4.2. Capacitance measurements were performed using an HP 4194A Impedance/Gain-Phase Analyzer. Figure 4.3 shows the $C-V$ characteristics at 100 kHz of a PZT (28 nm)-STO (48 nm) heterostructure capacitor at different temperatures and compares it to the capacitance of a 48 nm STO. We note in figure 4.3(a) that, at room temperature (30 °C), the capacitance of the PZT (28 nm)-STO (48 nm) is smaller than that of the constituent STO (48 nm) layer. This points to the fact that, at room temperature, the PZT layer acts as a positive dielectric. However, in figure 4.3(b), we observe that, at 300 °C, the capacitance of

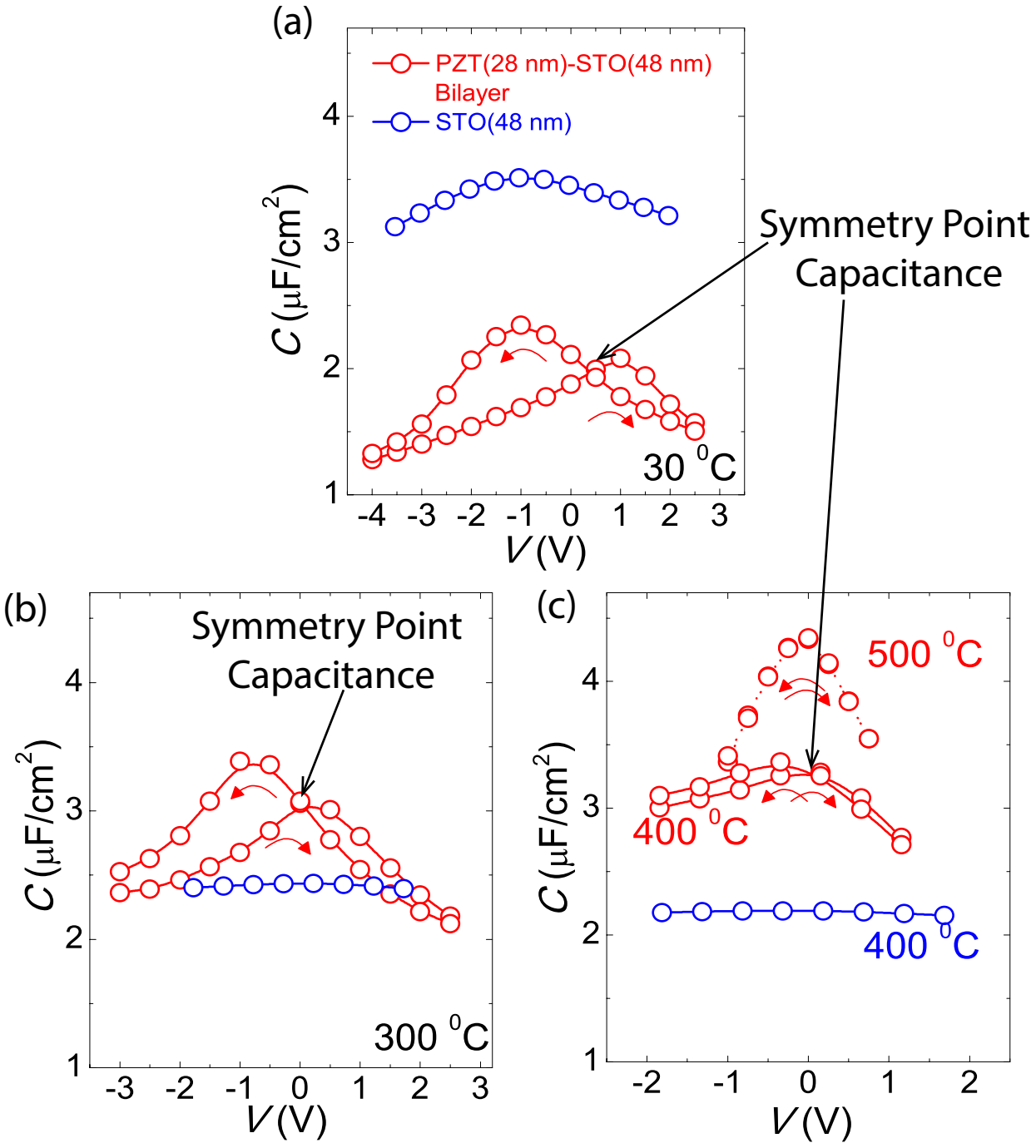


Figure 4.3: Comparison of $C - V$ characteristics of a PZT (28 nm)-STO (48 nm) and an STO (48 nm) sample at room temperature (30 °C) (a), 300 °C (b) and 400 and 500 °C.

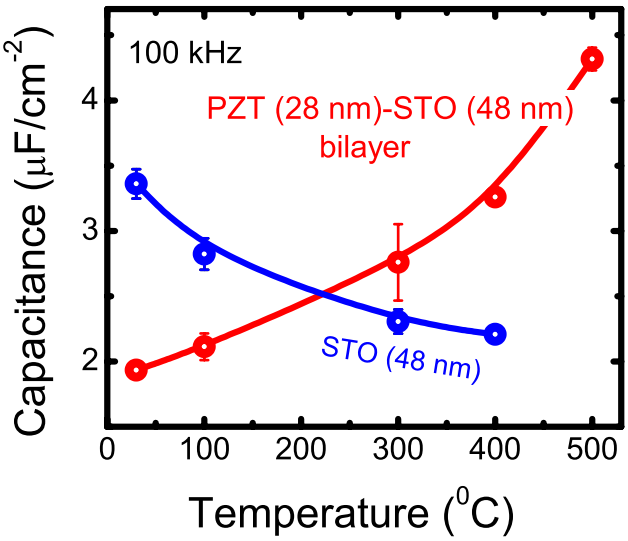


Figure 4.4: Capacitances of the samples at the symmetry point as functions of temperature measured at 100 kHz. Symmetry point refers to the cross point of the $C-V$ curves obtained during upward and downward voltage sweeps.

the PZT (28 nm)-STO (48 nm) hetero-capacitor is larger than that of the constituent STO (48 nm) layer indicating that the 28 nm PZT layer acts a negative capacitor. We observe in figure 4.3(c) that the enhancement of capacitance in the PZT-STO heterostructure is even larger at 400 and 500 °C.

Figure 4.4 shows the "symmetry point capacitance" of the PZT-STO heterostructure and the constituent dielectric STO as a function of temperature. Here "symmetry point capacitance" refers to the capacitance at the cross-point of the $C-V$ curves obtained during the upward and downward voltage sweeps (indicated in figure 4.3). We note in figure 4.4 that the capacitance of 48 nm STO decreases monotonically with temperature, while that of PZT (28 nm)-STO (48 nm) heterostructure increases monotonically with temperature. The capacitance of PZT (28 nm)-STO (48 nm) heterostructure is larger than that of the constituent 48 nm STO at temperatures over ∼225 °C.

Based on the experimentally measured values of the capacitances,we now extract the value of ferroelectric capacitance $C_{PZT}$ and the voltage amplification at the PZT-STO interface. Voltage amplification ratio at the PZT-STO interface is the ratio of the voltage across the STO to the total voltage applied across the PZT-STO heterostructure, which is given by $r = (1 + C_{STO}/C_{PZT})$. Figure 4.5 shows the extracted capacitance of the PZT in the heterostructure and the calculated voltage amplification factor $r$ at the PZT-STO interface. We note in figure 4.5 that the PZT capacitance is negative and the amplification factor $r$ is larger than 1 above 225 °C.

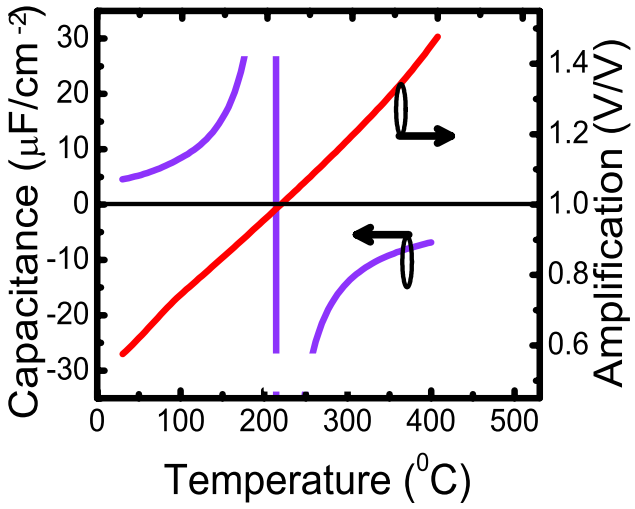


Figure 4.5: Extracted PZT capacitance in the bilayer and the calculated amplification factor at the FE-DE interface.

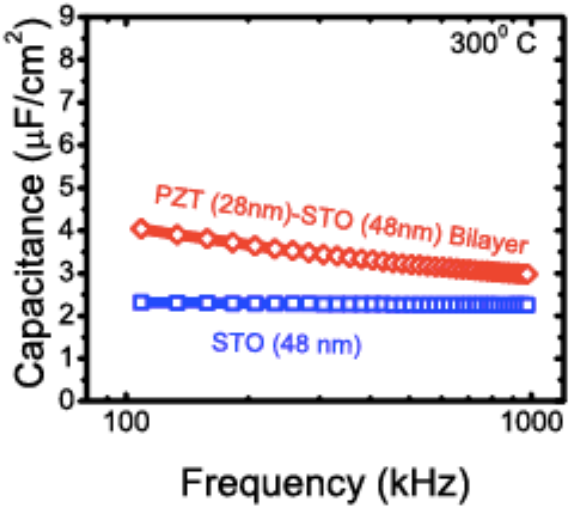


Figure 4.6: Capacitance of the PZT (28 nm)-STO (48 nm) heterostructure and the STO (48 nm) layer as a function of frequency at 300 °C.

Figure 4.6 shows the capacitance of the PZT (28 nm)-STO (48 nm) heterostructure and the STO (48 nm) layer as a function of frequency at 300 °C. Figure 4.6 shows the enhancement in capacitance is retained even at 1 MHz, thereby indicating that defect mediated processes are minimal, if any and, therefore, the enhanced capacitance cannot be attributed to such effects.

Figure 4.7(a) compares the capacitance of thee different PZT-SRO heterostructures (sample no 2-4) with that of the constituent STO at different temperatures. Also plotted in figure 4.7(a) is the capacitance of an isolated STO (sample 1) and an isolated PZT sample (sample 5). The capacitance of the constituent STO in each of the heterostructures is shown by small horizontal line. We observe in figure 4.7(a) that all the PZT-SRO heterostructures show an enhancement of the capacitance at higher temperatures. Figure 4.7(b) shows the admittance angle $\theta$ of the same samples. The dissipation factor $D(= \cot\theta)$ in all the devices remains reasonably low confirming that capacitance measurements are not compromised by leakage.

## Calibration of $SrTiO_3$ Dielectric Constant

$SrTiO_3$ dielectric constant varies strongly with growth conditions. Hence, there is a concern whether the STO dielectric constant in isolated STO layer is lower than that in the PZT-STO heterostructure. In fact, our measured STO dielectric constant at room temperature ($\sim$200) is lower than the highest reported STO (50 nm) permittivity ($\sim$300) [114], which raises the possibility that there exists a dead layer at the Au-STO interface that may reduce the intrinsic dielectric constant of STO and that is absent in Au-PZT interface in the bilayers. In this regard, it is to be noted that bilayer capacitance enhancement is not observed at high temperatures only and to the best of our knowledge, temperature dependence of $\epsilon_r$ of single crystal STO thin films (50-100 nm) on SRO buffered STO (001) substrate at higher than 300 K has not been reported in literature. Hence, in order to benchmark our measurements at high temperatures against standard values, we simulated unstrained STO dielectric constant using Landau theory, which is plotted in figure 4.8. The highest value of unstrained STO dielectric constant was reported in Jang *et al.* [114], which is also plotted in figure 4.8. We note in figure 4.8 that the simulated STO $\epsilon_r$ is in excellent agreement with the measured $\epsilon_r$ reported by Jang *et al.* [114]. Using X-ray diffraction spectroscopy techniques, we determined that STO in both bilayers and STO-only samples are unstrained, which is expected since the STO and SRO in-plane lattice constants are very closely matched to each other. Figure 4.9(a) shows the temperature dependence of STO simulated using Landau theory (tagged as "STO (simulation)") and compares that with our measured dielectric constants of STO (tagged as "STO (measured)") and PZT-STO bilayer. It is important to note in figure 4.9(a) that simulated and measured permittivities are in the same range at elevated temperature where the capacitance enhancement in the PZT-STO heterostructure is observed. By noting that $C_{PZT-STO} = \epsilon_{PZT-STO}/(d_{PZT} + d_{STO})$ and $C_{STO} = \epsilon_{STO}/d_{STO}$, $C_{PZT-STO} \geq C_{STO}$ requires $\epsilon_{PZT-STO} > \epsilon_{STO}(1 + d_{PZT}/d_{STO})$. In figure 4.3(a), $\epsilon_{STO}(1 + d_{PZT}/d_{STO})$ curves for the measured STO dielectric constant and the simulated STO dielectric constant are also plotted and tagged "Required $\epsilon$ (measured)" and "Required $\epsilon$ (simulation)", respectively. We note in figure 4.9(a) that even we consider the simulated STO dielectric constant, the dielectric constant curve of the PZT-STO heterostructure crosses over the "Required $\epsilon$ (simulation)" curve at above 300 °C. Hence, at elevated temperatures, the dielectric enhancement

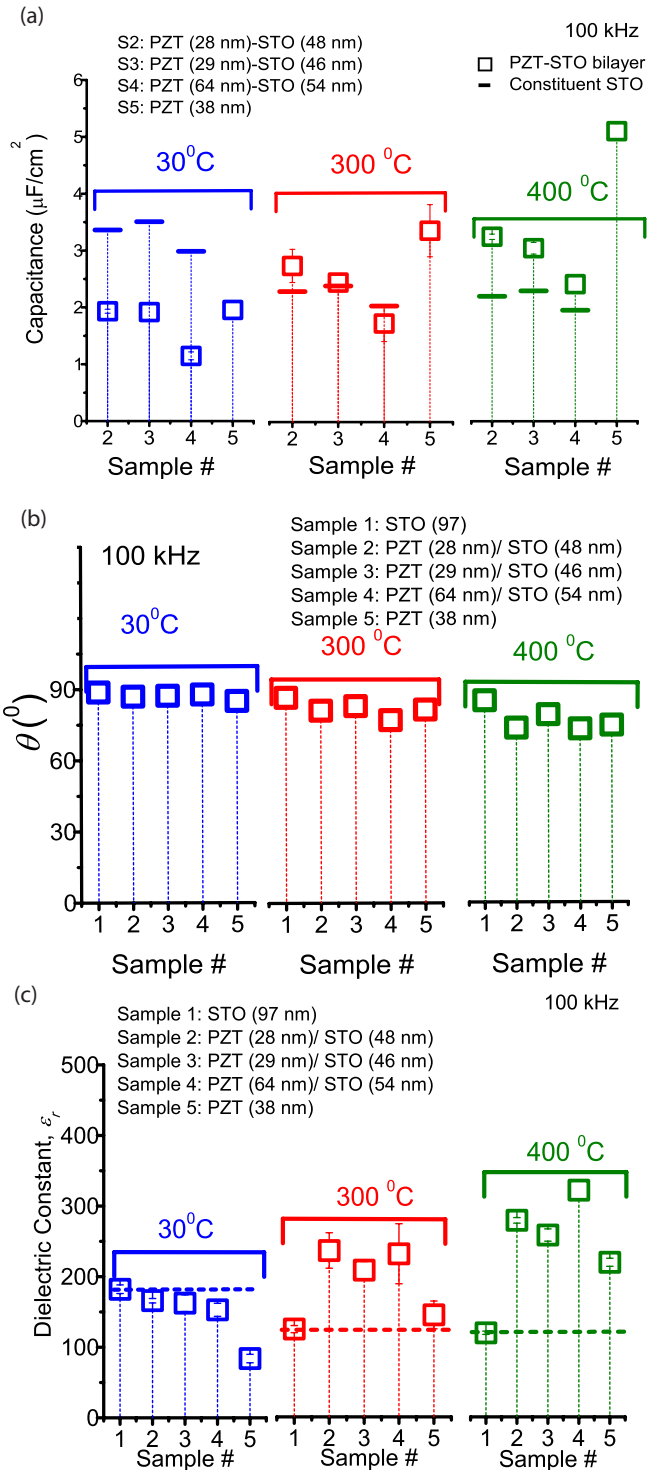


Figure 4.7: Comparison of capacitance (a), the admittance angles (b), and dielectric constant (c) of several PZT-STO samples with those of STO and PZT at 100 kHz at different temperatures. In (b), the capacitance of the constituent STO in each of the bilayers is shown by small horizontal line.

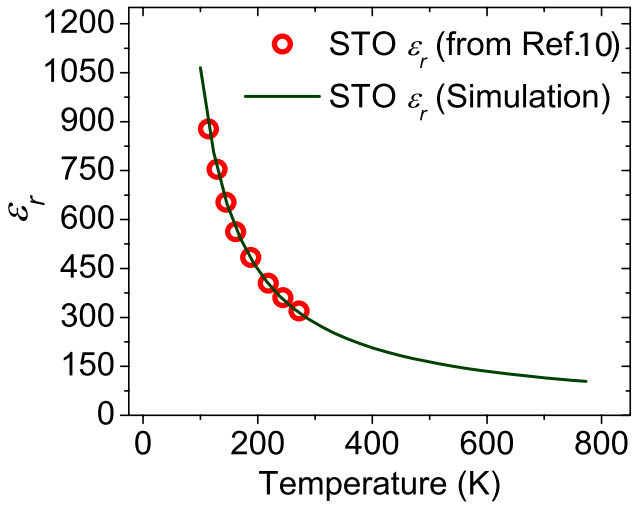


Figure 4.8: Comparison of STO dielectric constant simulated using Landau model with measure dielectric constant of 50 nm STO reported in Ref. 21.

of PZT-STO bilayer is large enough to yield capacitance enhancement, even if we compare the measured PZT-STO bilayer capacitance with the simulated STO capacitance, which is shown in figure 4.9(b).

Another point that needs to be considered is the thickness dependence of STO permittivity. Since the breakdown electric field of STO is smaller than that of PZT, it poses a problem when the bi-layer capacitance is compared to that of an isolated STO layer over the same voltage range. To overcome this problem, we have used a 97 nm STO as our controlled sample. The permittivity for isolated STO was measured from this sample. Consequently the capacitance of 48 nm STO was calculated using the measured permittivity of the 97 nm sample. It is well known that STO permittivity goes down with decreasing thickness. Therefore, we have overestimated the capacitance of isolated STO layer and *underestimated* the capacitance enhancement that we show in figures 4.9(a) and 4.9(b). If we directly use the measured capacitances from a 48 nm thick STO sample, the capacitance enhancement can be found at *room temperature*. In figures 4.9(a) and 4.9(b), this is what we illustrate by "lower bound".

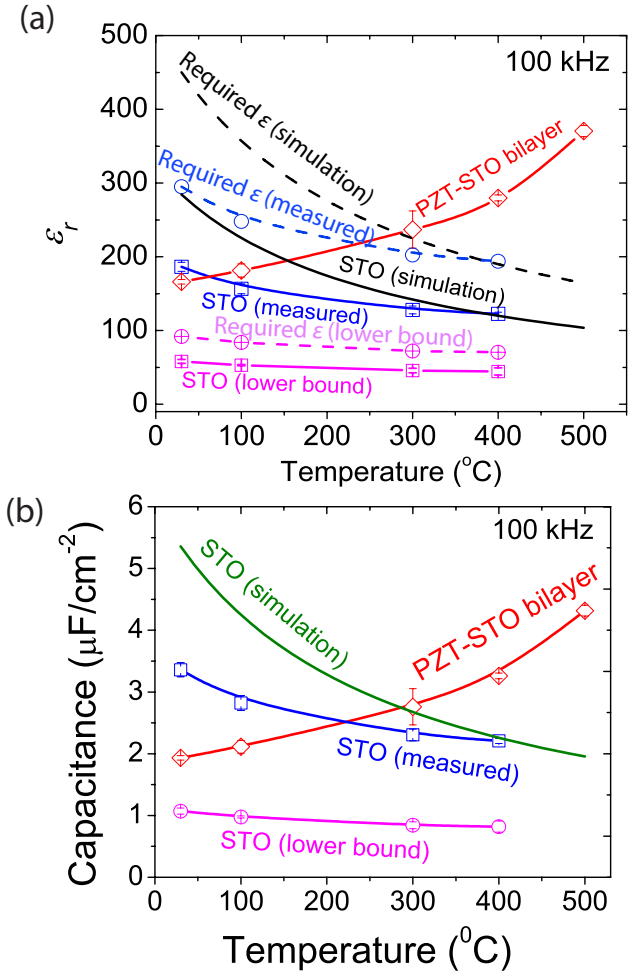


Figure 4.9: Comparison of dielectric constant (a) and capacitance (b) of a PZT (28 nm)-STO (48 nm) sample with those of STO samples at 100 kHz as functions of temperature. In (a), curves tagged 'Required $\epsilon$' refers to the required bilayer dielectric constant to achieve $C_{PZT-STO} = C_{STO}$ at a certain temperature. The lower bound of STO dielectric constant and capacitance correspond to those measured from the 48 nm STO sample.

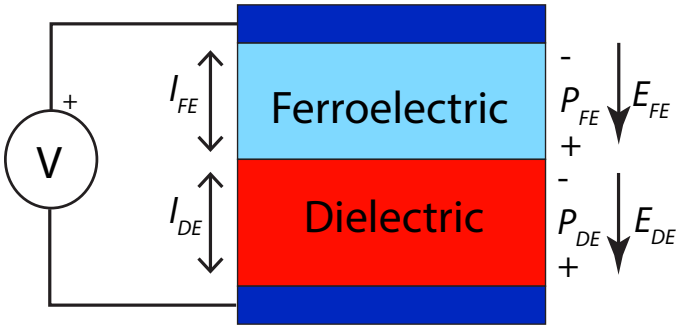


Figure 4.10: Schematic diagram of a ferroelectric-dielectric heterostructure.

## 4.3 Theoretical Model of Capacitance Enhancement

### Model

Let us consider a series combination of a Ferroelectric (FE) and a dielectric (DE) capacitor. For this example, we shall consider PZT (Lead Zirconate Titanate: $PbZr_{0.2}Ti_{0.8}O_3$) as the ferroelectric layer and STO (Strontium Titanate: $SrTiO_3$) as the dielectric layer. Figure 4.10 shows the schematic diagram of a ferroelectric(FE)-dielectric(DE) heterostructure. $l_f$ and $l_d$ are the FE and DE layer thicknesses, respectively. If the total voltage across the FE-DE series capacitor network is $V$, according to the Kirchhoff's law,

$$V = V_f + V_d = E_f l_f + E_d l_d \tag{4.1}$$

Here, the subscripts, $f$ and $d$, refer to FE and DE, respectively. $V_f = E_f l_f$ and $V_d = E_d l_d$ are the voltages across the FE and DE layers respectively. Also, applying Gauss's law at the interface between FE and DE, one obtains the following equation for the surface charge density, $Q$.

$$Q = \epsilon_0 E_f + P_f = \epsilon_0 E_d + P_d \tag{4.2}$$

Here, $P_i$ is the charge per unit area or polarization of the $i$-th layer.

It is important to understand the dielectric polarization term $P_d$. The following two cases are considered for simulations.

1 For a linear dielectric, $P_d = \epsilon_0(\epsilon_d - 1)E_d$. In such a case, the right hand side of equation 4.2 becomes $\epsilon_0\epsilon_d E_d$.

2 For a non-linear dielectric such as $SrTiO_3$, $P_d = f(E_d)$, where $E_d = f^{-1}(P_d) = 2\alpha_{1,d}P_d + 4\alpha_{11,d}P_d^3 + 6\alpha_{111,d}P_d^5 + 8\alpha_{1111,d}P_f^7$. $\alpha_{1,d}$, $\alpha_{11,d}$, $\alpha_{111,d}$ and $\alpha_{1111,d}$ are the dielectric anisotropy coefficients. In this case, the relative dielectric constant of the DE layer, $\epsilon_d$ is buried in the electric field dependence of $P_d$ and, hence, the coefficient of

$E_d$ in the right hand side of equation 4.2 is simply $\epsilon_0$.

Similarly, for the FE layer, $E_f = 2\alpha_{1,f}P_f + 4\alpha_{11,f}P_f^3 + 6\alpha_{111,f}P_f^5 + 8\alpha_{1111,f}P_f^7$ in equation 4.2. Here, $\alpha_{1,f}$, $\alpha_{11,f}$, $\alpha_{111,f}$ and $\alpha_{1111,f}$ are the ferroelectric anisotropy coefficients. The relative dielectric constant of the FE layer, $\epsilon_f$ is buried in the electric field dependence of $P_f$.

The total energy of the combination per unit surface area can be written as,

$$\begin{aligned} U_{f+d} &= l_f\left(\alpha_{1,f}P_f^2 + \alpha_{11,f}P_f^4 + \alpha_{111,f}P_f^6 + \alpha_{1111,f}P_f^8 - E_fP_f\right) \\ &\quad + l_d\left(\alpha_{1,d}P_d^2 + \alpha_{11,d}P_d^4 + \alpha_{111,d}P_d^4 + \alpha_{1111,d}P_f^6 - E_dP_d\right) \end{aligned} \tag{4.3}$$

The advantage of writing the energy function of a DE also like that of a FE, as it has been done in Equation 4.3, is the fact that this equation equally applies to a dielectric or a paraelectric material. Since STO is indeed paraelectric, equation 4.3 is particularly appropriate.

Combining equations 4.1, 4.2 and 4.3, the following equation for $U_{f+d}$ can be derived.

$$\begin{aligned} U_{f+d} = \quad & l_f\left(\alpha_{1,f}P_f^2 + \alpha_{11,f}P_f^4 + \alpha_{111,f}P_f^6 + \alpha_{1111,f}P_f^8\right) \\ & + l_d\left(\alpha_{1,d}P_d^2 + \alpha_{11,d}P_d^4 + \alpha_{111,d}P_d^6 + \alpha_{1111,d}P_d^8\right) \\ & - V\frac{P_fl_f + P_dl_d}{l_f + l_d} + \frac{l_fl_d\left(P_f - P_d\right)^2}{\epsilon_fl_f + \epsilon_dl_d} \end{aligned} \tag{4.4}$$

We note that a similar expression for the total energy in FE-DE heterostructure was derived by Dawber *et al.* [115].

For a given voltage $V$, the state of the combined FE-DE network can be found by minimizing the total energy given by Equation 4.4 with respect to polarizations in FE and DE. This will provide the polarization and electric fields in individual layers. The total capacitance of the FE-DE series network can then be calculated from $C = dQ/dV$. The effective capacitance of the FE and DE layers at a given $V$ can also be calculated using $C_i = dQ/dV_i$ $(i \equiv f, d)$. The algorithm for the solution is described in the next subsection.

## Algorithm

This subsection describes the algorithm for solving the equations presented in the previous subsection. For clarity, some of the equations presented in the previous subsection are

repeated here. $V$ is the voltage applied across the heterostructure. $l_i$, $P_i$ and $E_i$ are respectively the thickness, the polarization and the electric field in the $i$-th layer ($i \equiv$ f, d). $x$ and $y$ are volume fractions of FE and DE layers respectively in the heterostructure.

$$x = \frac{l_f}{l_d + l_f}; y = \frac{l_d}{l_d + l_f} \tag{4.5}$$

Applying Kirchhoff's voltage law and Gauss law in this heterostructure, following relations are obtained.

$$E_f \cdot l_f + E_d \cdot l_d = V \tag{4.6}$$

$$\epsilon_0 E_f + P_f = \epsilon_0 E_d + P_d \tag{4.7}$$

Equation 4.6 and 4.7 are solved to obtain the following relations for the electric fields.

$$E_f = \frac{V}{l_f + l_d} - \frac{P_f - P_d}{\epsilon_0} y \tag{4.8}$$

$$E_d = \frac{V}{l_f + l_d} + \frac{P_f - P_d}{\epsilon_0} x \tag{4.9}$$

The free energy per unit volume of the FE layer is given by the following relation.

$$\begin{aligned} U_f &= \alpha_{1,f} P_f^2 + \alpha_{11,f} P_f^4 + \alpha_{111,f} P_f^6 + \alpha_{1111,f} P_f^8 - E_f P_f \\ &= (\alpha_{1,f} + \frac{y}{\epsilon_0}) P_f^2 + \alpha_{11,f} P_f^4 + \alpha_{111,f} P_f^6 + \alpha_{1111,f} P_f^8 - \frac{y}{\epsilon_0} P_d P_f \\ &\quad - \frac{V}{l_f + l_d} P_f \end{aligned} \tag{4.10}$$

Here, $\alpha_{1,f}$, $\alpha_{11,f}$, $\alpha_{111,f}$ and $\alpha_{1111,f}$ are the ferroelectric anisotropy coefficients.

Similarly, the free energy per unit volume of the DE layer is given by the following relation.

$$\begin{aligned} U_d &= \alpha_{1,d} P_d^2 + \alpha_{11,d} P_d^4 + \alpha_{111,d} P_d^6 + \alpha_{1111,d} P_d^8 - E_d P_d \\ &= (\alpha_{1,d} + \frac{x}{\epsilon_0}) P_d^2 + \alpha_{11,d} P_d^4 + \alpha_{111,d} P_d^6 + \alpha_{1111,d} P_d^8 - \frac{x}{\epsilon_0} P_f P_d \\ &\quad - \frac{V}{l_f + l_d} P_d \end{aligned} \tag{4.11}$$

Here, $\alpha_{1,d}$, $\alpha_{11,d}$, $\alpha_{111,d}$ and $\alpha_{1111,d}$ are the dielectric anisotropy coefficients.

Defining $E = \frac{V}{l_f + l_d}$ and using equation 4.10 and 4.11, the free energy per unit surface area of the FE-DE heterostructure $U_{f+d} = xU_f + yU_d$ can expressed as follows

$$U_{f+d} = (l_f + l_d)(x \cdot (f_f(P_f) - E \cdot P_f) + y \cdot (f_d(P_d) - E \cdot P_d) + \frac{xy}{2\epsilon_0}(P_f - P_d)^2) \tag{4.12}$$

The equilibrium values of $P_f$ and $P_d$ minimizes $U_{f+d}$ for which the following relation needs to be satisfied.

$$\frac{\partial U_{f+d}}{\partial P_f} = \frac{\partial U_{f+d}}{\partial P_d} = 0 \tag{4.13}$$

From equation 4.13, the following relations are derived.

$$\frac{\partial f_f}{\partial P_f} + \frac{y}{\epsilon_0}(P_f - P_d) - E = 0 \tag{4.14}$$

$$\frac{\partial f_{DE}}{\partial P_d} - \frac{x}{\epsilon_0}(P_f - P_d) - E = 0 \tag{4.15}$$

where, $f_i = \alpha_{1,i}P_i^2 + \alpha_{11,i}P_i^4 + \alpha_{111,i}P_i^6 + \alpha_{1111,i}P_i^8$, $i \equiv$ f, d.

Solution of equation 4.14 and 4.15 for a given $V$ or $E$ gives the equilibrium values of $P_f$ and $P_d$. We solved equation 4.14 and 4.15 using a MATLAB code that implements a Newton-Raphson routine. The steps are follows.

1. Assume a value of $P_f$ which we refer to as $P_{f,guess}$.

2. For $P_f = P_{f,guess}$, the value of the function on the left hand side of equation 11, $F_{guess}$ is calculated using the following the relations.

$$P_{d,guess} = P_{f,guess} + \frac{\epsilon_0}{y}\frac{\partial f_f}{\partial P_f}(P_{f,guess}) + \frac{\epsilon_0}{y}E \tag{4.16}$$

$$F_{guess} = \frac{\partial f_d}{\partial P_d}(P_{d,guess}) - \frac{x}{\epsilon_0}(P_{f,guess} - P_{d,guess}) - E \tag{4.17}$$

3. $\frac{dF_{guess}}{dP_f}$ is calculated at $P_f = P_{f,guess}$ using relations 4.18-4.21.

$$P^{\delta}_{f,guess} = P_{f,guess} + \delta; \delta \to 0 \tag{4.18}$$

$$P^{\delta}_{d,guess} = P^{\delta}_{f,guess} + \frac{\epsilon_0}{y}\frac{\partial f_f}{\partial P_f}(P^{\delta}_{f,guess}) + \frac{\epsilon_0}{y}E \tag{4.19}$$

$$F^{\delta}_{guess} = \frac{\partial f_d}{\partial P_d}(P^{\delta}_{d,guess}) - \frac{x}{\epsilon_0}(P^{\delta}_{f,guess} - P^{\delta}_{d,guess}) - E \tag{4.20}$$

$$\frac{dF_{guess}}{dP_f} = \lim_{\delta \to 0}\frac{F^{\delta}_{guess} - F_{guess}}{\delta} \tag{4.21}$$

4. The assumed value of $P_f$ is updated using the following relations. $\gamma < 1$ is the update coefficient.

$$\Delta P_{f,guess} = -\frac{F_{guess}}{\frac{dF_{guess}}{dP_f}} \tag{4.22}$$

$$P^{new}_{f,guess} = P_{f,guess} + \Delta P_{f,guess} \cdot \gamma \tag{4.23}$$

5. Steps 1-4 are repeated until $\Delta P_{f,guess} \rightarrow 0$.

For ferroelectric PZT, the values of the anisotropy constants are taken from [116] and are listed below.

$$x = 0.8 \tag{4.24}$$
$$\alpha_{1,f} = \frac{T - T_0}{2\epsilon_0 C_0}, \epsilon = 8.854 \times 10^{-12} \tag{4.25}$$
$$\alpha_{11,f} = (10.612 - 22.655x + 10.955x^2) \times \frac{10^{13}}{C_0} \tag{4.26}$$
$$\alpha_{111,f} = (12.026 - 17.296x + 9.179x^2) \times \frac{10^{13}}{C_0} \tag{4.27}$$
$$C_0 = (\frac{2.8339}{1 + 126.56(x - 0.5)^2} + 1.4132) \times 10^5 \tag{4.28}$$
$$T_0 = 462.63 + 843x - 2105.5x^2 + 4041.8x^3 - 3828.2x^4 + 1337.8x^5 \tag{4.29}$$
$$\alpha_{1111,f} = 0 \tag{4.30}$$

For dielectric STO, the values of the anisotropy constants are also taken from [116] and are listed below.

$$\alpha_{1,d} = 7.06(T - 35.5) \times 10^5 \tag{4.31}$$
$$\alpha_{11,d} = 1.7 \times 10^9 \tag{4.32}$$
$$\alpha_{111,d} = \alpha_{1111,f} = 0 \tag{4.33}$$

In equation 4.24-4.33, all units are in S.I.

## Temperature Dependence of Negative Capacitance Effect in a Ferroelectric-Dielectric Heterostructure

A ferroelectric material is sensitive to the temperature due to the coefficient $\alpha$ being proportional to $T$. This is the main reason why the negative capacitance is temperature dependent. For all practical purposes, in a FE-DE-bilayer, the system would adopt a nearly uniform polarization throughout all the layers resulting in $Q \approx P_f \approx P_d$. This is due to the fact that the last term in equation 4.4, which represents the electrostatic energy arising due to the polarization mismatch at the interface is costly in energy. Equation 4.4 can be simplified as

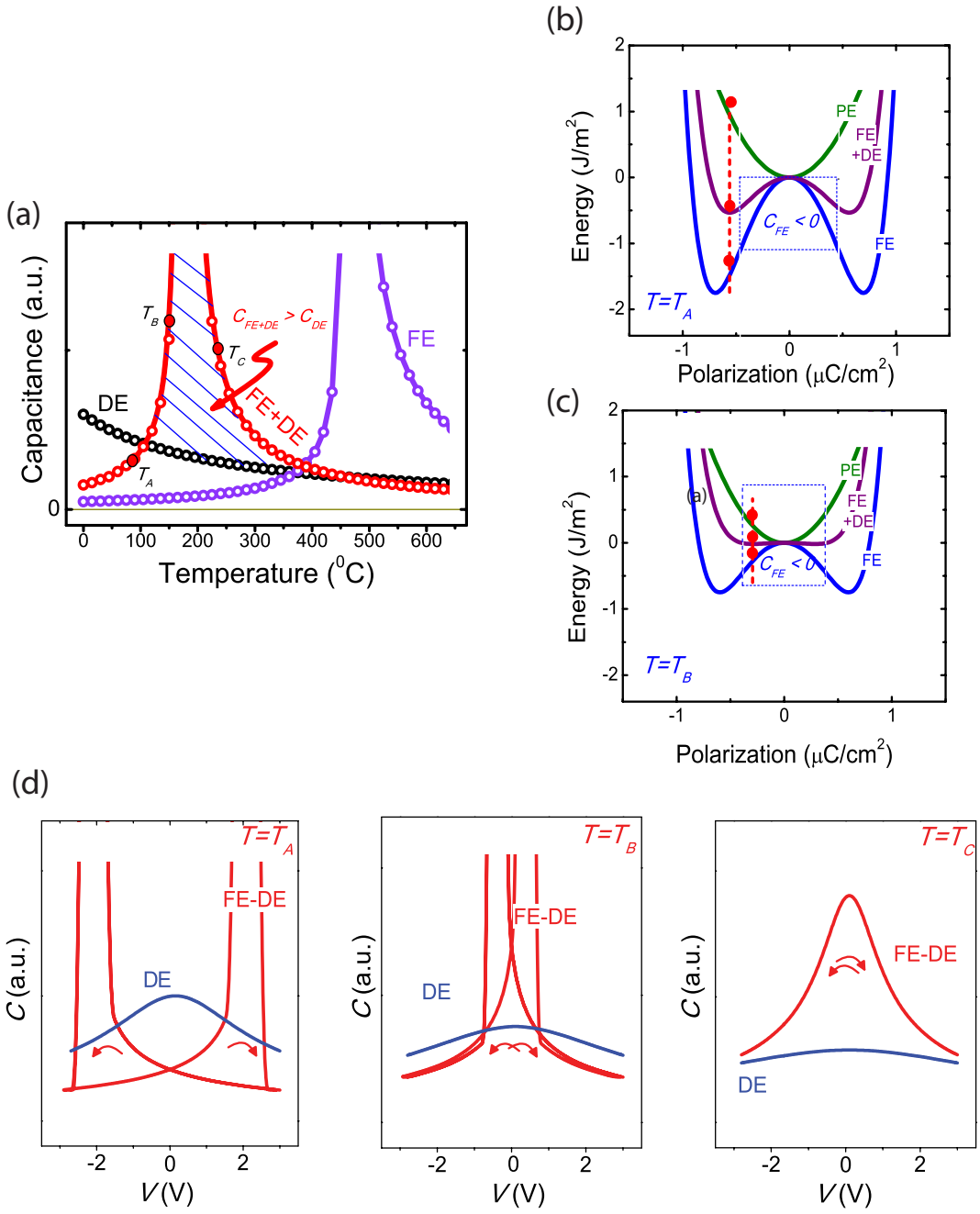


Figure 4.11: (a) Simulated capacitance of a PZT-STO bi-layer capacitor, an isolated STO and an isolated PZT with a thickness of $t_{PZT}$ as a function of temperature. $t_{PZT}$:$t_{STO}$ = 4:1. The temperature corresponding to the singularity in PZT capacitance corresponds to its Curie temperature. Note that capacitance-temperature characteristics of the PZT-STO bilayer capacitor has a similar shape as that of a PZT capacitor with a lower Curie temperature. (b,c) Energy landscapes of the series combination at two different temperatures, $T_A$ (b) and $T_B$ (c). (d) Calculated $C-V$ characteristics of a STO capacitor and a PZT-STO heterostructure capacitor (thickness ratio 4:1) at $T = T_A, T_B$ and $T_C$.

$$\begin{aligned} U_{f+d} &= l_f\left(\alpha_{1,f}Q^2+\alpha_{11,f}Q^4+\alpha_{111,f}Q^6+\alpha_{1111,f}Q^8\right) \\ &\quad +l_d\left(\alpha_{1,d}Q^2+\alpha_{11,d}Q^4+\alpha_{111,d}Q^6+\alpha_{1111,d}Q^8\right)-VQ \end{aligned} \tag{4.34}$$

From equation 4.34, one can easily see that when a DE is added in series with FE, a positive quantity ($\alpha_{1,d}l_d/l_f > 0$) is added to the $\alpha_{1,f}$ coefficient of the ferroelectric . One way to understand the impact of this addition of positive energy is to recognize that it reduces the "effective" Curie temperature of the ferroelectric material, by reducing the total negative energy in the combined system. Figure 4.11(a) shows the simulated capacitance of a FE-DE (PZT-STO) heterostructure as a function of temperature and compares it to the capacitance of DE (STO). Indeed, simulated capacitance vs temperature shows a shift of the effective Curie temperate towards the left for the FE-DE heterostructure in comparison to isolated FE.

In order to explain the temperature dependence in more details, we resort to energy landscapes, as shown in figures 4.11(b) and 4.11(c), for two different temperatures, $T_A$ and $T_B$. For a ferroelectric material, as the temperature increases, the double wells of energy landscape come closer together and become shallower and flatter making the ferroelectric capacitance increase. At the Curie temperature, the double wells develop into a single minimum, the capacitance peaks and a FE-to-DE phase transition occurs. Beyond Curie temperature, the energy landscape in the DE phase again becomes steeper around the single minima making the capacitance decrease with the temperature. Interestingly, the exact same thing happens when, rather than changing the temperature, a dielectric is added in series. If temperature is increased, the $\alpha_{1,f}$ coefficient for the ferroelectric material increases by $\alpha_0 T$. On the other hand, if a dielectric material is added, the same coefficient increases by $\alpha_{1,d}l_d/l_f$ (see Equation 4.4). For a conventional dielectric $\alpha_{1,d} = 1/(2\epsilon_0\epsilon_d), \alpha_{11,d} = \alpha_{111,d} = 0$. Because of this duality, the negative capacitance effect in a FE-DE layer shows the temperature dependence seen in figure 4.11(a). On the other hand, this means that temperature can be used as an effective tuning parameter for characterization and probing of negative capacitance.

Note that the capacitance is not negative everywhere in the energy landscape of ferroelectric material. The portion where capacitance is indeed negative is shown by the dashed box in figures 4.11(b) and 4.11(c). The idea is to add enough positive energy in the system from the DE so that the total energy will be minimized at a $(U, Q)$ coordinate where ferroelectric capacitance is negative. There are three distinct regions of operation that are of interest for negative capacitance. First at $T = T_A$, the added energy from the dielectric alone is not large enough to stabilize the ferroelectric material in a negative capacitance region (see figure 4.11(b)). If now the temperature is increased from $T_A$ to $T_B$, the combined energy moves to the point of minimum energy inside the dashed box and hence negative capacitance is

expected (see figures 4.11(c)). But note that the total energy still shows small double wells. This means, despite negative capacitance operation and capacitance enhancement, a hysteresis should be observed. This is the second mode of operation. Now if the temperature is further increased to $T_C$, the positive energy will be large enough to completely eliminate the double well and make the combined energy look like a paraelectric or dielectric (shown by the tag 'DE' in figures 4.11(b) and 4.11(c)). In this third region of operation we shall find a capacitance enhancement and also the operation will be hysteresis free. Figure 4.11(d) shows capacitance-voltage simulations for PZT-STO heterostructure at $T_A, T_B$ and $T_C$, as described above. At $T_A$, PZT-STO shows hysteresis in $C-V$ characteristics and PZT-STO capacitance is smaller than of the STO capacitor around $V = 0$. The peaks in $C-V$ characteristics in PZT-STO correspond to polarization switching and are not related to the negative capacitance effect. At $T_B$, the PZT-STO hysteresis has decreased and equivalent capacitance is larger than that of the STO capacitor around zero bias condition. Therefore the negative capacitance operation can now be observed but it is accompanied by hysteresis. Finally, at a further elevated temperature, $T_C$, the PZT-STO capacitance becomes much larger than that of PZT and the hysteresis completely goes away. This is the most desired mode of operation. Note in our experimental results presented in figure 4.3(c), the PZT-STO $C-V$ characteristics is hysteresis free at 500 °C.

## 4.4 Conclusions

In summary, we have experimentally demonstrated that, in a crystalline ferroelectric-dielectric series capacitance network, the total capacitance, contrary to what happens in a classical series combination, could be larger than the constituent dielectric capacitance. Through the combined experimental-simulation study presented herein, we show that the observed enhancement of the capacitance in the ferroelectric-dielectric capacitor corresponds to the stabilization of the ferroelectric negative capacitance. An understanding of the temperature dependent behavior of the negative capacitance phenomenon is also developed based on simple 1-D Landau-Devonshire formalism.

## 4.5 Future Directions

1 *Towards room temperature capacitance enhancement:* The capacitance enhancement in the $Pb(Zr_{0.2}Ti_{0.8})O_3$-$SrTiO_3$ heterostructure was observed at elevated temperatures only. This is due to the fact that the bulk Curie temperature of PZT is ∼450 °C; but when grown on $SrTiO_3$ substrate, it Curie temperature increases by almost 400 °C to above 850 °C due to the compressive strain imposed by $SrTiO_3$. The temperature range of the capacitance enhancement is closely related to the ferroelectric Curie temperature. The higher the Curie temperature, the higher the temperature for on-set of capacitance

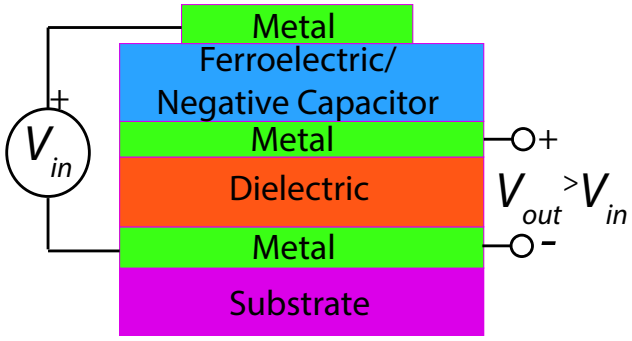


Figure 4.12: A passive voltage amplifier.

enhancement. Hence, by using a ferroelectrics with smaller Curie temperature such as $BaTiO_3$ and $(Ba_xSr_{1-x})TiO_3$, the capacitance enhancement could be observed at room temperature.

2 *Passive voltage amplification:* By introducing an intermediate metallic layer between the ferroelectric and the dielectric layer in a heterostructure, a passive voltage amplifier could be implemented. Figure 4.12 shows the schematic diagram of such an amplifier. The input voltage $V_{in}$ is amplified at the internal metal layer ($V_{out} = V_{in} \times (1 + C_{DE}/C_{FE})^{-1}$).

3 *Capacitance enhancement in ferroelectric-semiconductor heterostructures:* The capacitance enhancement in ferroelectric-semiconductor heterostructure is the first signature of stabilized ferroelectric negative capacitance to be detected in a negative capacitance field-effect-transistor.

# Chapter 5

# MODELING OF FERROELECTRIC NEGATIVE CAPACITANCE FIELD EFFECT TRANSISTOR

In this chapter, we present a design methodology of ferroelectric (FE) negative capacitance FETs (NCFETs) based on the concept of capacitance matching. We propose a new mode of NCFET operation, called the "antiferroelectric mode." In an antiferroelectric NCFET, a significant boost in the on-current can be obtained in exchange for a nominal hysteresis besides achieving sub-60mV/dec subthreshold operation. Design considerations for different device parameters (FE thickness, EOT, source/drain overlap and gate length) are explored. It is suggested that relative improvement in device performance due to FE negative capacitance becomes more significant in very short channel length devices because of the increased drain-to-channel coupling.

Section 5.1 describes the simulation procedure of the negative capacitance field-effect-transistor. The concept of capacitance matching for the design of a negative capacitance field-effect-transistor is presented in section 5.2. Section 5.2 also introduces the concept of the antiferroelectric model of NCFET operation. Section 5.3 presents the effects of different device parameters, such as ferroelectric thickness, equivalent oxide thickness, source and drain overlaps and gate length, on the performance on NCFET.

Most of the results presented in this paper was reported in reference [117].

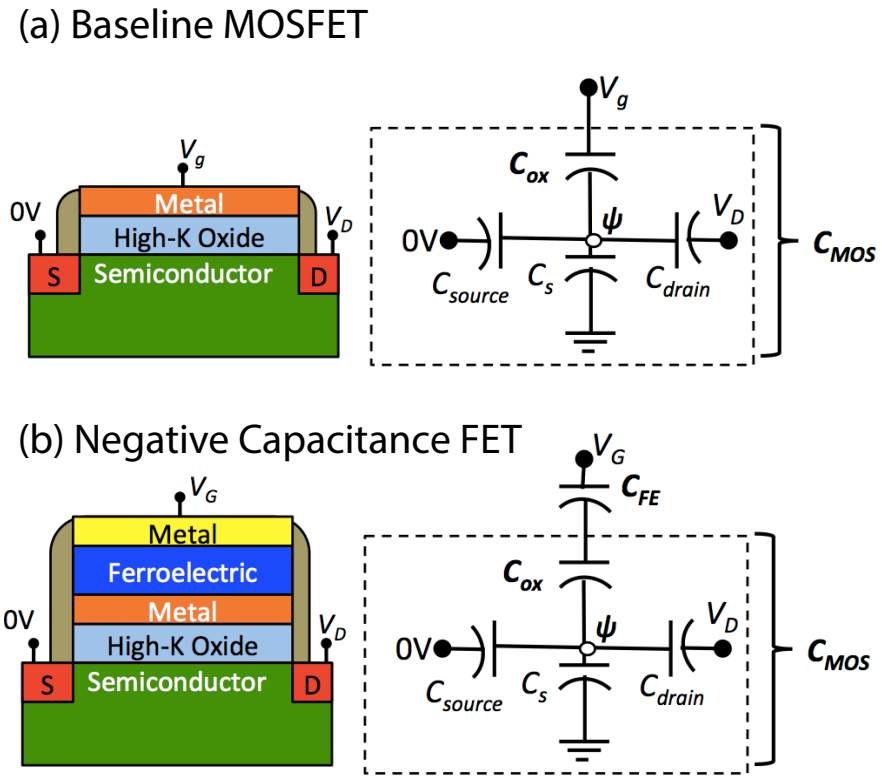


Figure 5.1: Schematic diagram of the baseline MOSFET (a) and the negative capacitance field-effect-transistor (b). In the negative capacitance FET, a ferroelectric negative capacitance oxide is integrated into the gate oxide stack through a metallic buffer layer.The equivalent capacitance circuit model of the MOSFET and NCFET are also shown.

## 5.1 Modeling Framework of Negative Capacitance FET

Figure 5.1(a,b) show the schematic diagram of the a bulk Si MOSFET and a negative capacitance FET, respectively. Bulk Si MOSFET with high-K gate oxide in figure 5.1(a) is referred to as the the baseline MOSFET. In the negative capacitance FET shown in figure 5.1(b), the ferroelectric oxide is assumed to be deposited on a commensurate metallic template grown on the oxide of the baseline MOSFET [118]. The intermediate metallic layer between the ferroelectric and the high-K gate oxide is chosen following the experimental device [119], which we refer to as the floating gate with a voltage of $V_g$. The voltage at the outer gate is $V_G$. This floating gate averages out the non-uniform potential profile along the source-drain direction as well as any charge non-uniformity coming from domain formation in the FE. Thus as long as the MOSFET is concerned, the FE looks like a mono-domain dipole. This experimental structure therefore justifies using a 1-D landau model for the FE.

The intrinsic MOSFET is simulated using TCAD Sentaurus software taking into account the 2-D electrostatics. Dynamic nonlocal path band-to-band model, standard Shockley-Reed-Hall recombination and drift-diffusion model are used and Fermi-Dirac statistics is assumed in the MOSFET simulation. Source/drain junction depth is 10 nm.

To calculate the characteristics of the NCFET, the baseline MOSFET is simulated for a given combination of internal gate voltage $V_g$ and the drain voltage $V_D$. The voltage drop across of the ferroelectric is calculated as $V_{FE}(Q) = (2\alpha Q + 4\beta Q^3 + 6\gamma Q^5) \times t_{FE}$, where $\alpha$, $\beta$, $\gamma$ are the ferroelectric anisotropy constants and $Q$ is the charge in the channel calculated using the TCAD simulation at the given $V_g$ and $V_D$ condition which is reflected at the internal gate. The voltage at the external gate $V_G(Q) = V_{FE}(Q) + V_g(Q)$. $Pb(Zr_{0.5}Ti_{0.5})O_3$ is considered as the FE. The anisotropy constants for $Pb(Zr_{0.5}Ti_{0.5})O_3$ are taken from reference [116] and are listed below.

$$x = 0.5 \tag{5.1}$$

$$\alpha_1 = \frac{T - T_0}{2\epsilon_0 C_0}, \epsilon = 8.854 \times 10^{-12} \tag{5.2}$$

$$\alpha_{11} = (10.612 - 22.655x + 10.955x^2) \times \frac{10^{13}}{C_0} \tag{5.3}$$

$$\alpha_{111} = (12.026 - 17.296x + 9.179x^2) \times \frac{10^{13}}{C_0} \tag{5.4}$$

$$C_0 = (\frac{2.1716}{1 + 500.05(x - 0.5)^2} + 0.131x + 2.01) \times 10^5 \tag{5.5}$$

$$T_0 = 462.63 + 843x - 2105.5x^2 + 4041.8x^3 - 3828.2x^4 + 1337.8x^5 \tag{5.6}$$

Here, all units are in S.I.

## 5.2 The Capacitance Tuning Perspective

In order to understand the design methodology of a negative capacitance FET, we show the equivalent capacitance model of a FET in figure 5.1(a). In figure 5.1(a), $C_{ox}$ and $C_s$ are the oxide and the semiconductor capacitance, respectively and $C_{source}$ and $C_{drain}$ represent the source and drain coupling capacitance to the channel, respectively. $C_{MOS} = C_{ox}||(C_s + C_{source} + C_{drain})$. Figure 5.1(b) shows the schematic diagram of a negative capacitance FET where a ferroelectric negative capacitance oxide is integrated into the gate oxide stack through a metallic buffer layer. The ferroelectric capacitance $C_{FE}$ is negative. The key to negative capacitance effect is that the negative differential capacitance of the FE ($C_{FE} < 0$) compensates the positive capacitances ($C_{MOS} > 0$) in the device such that the resulting gate

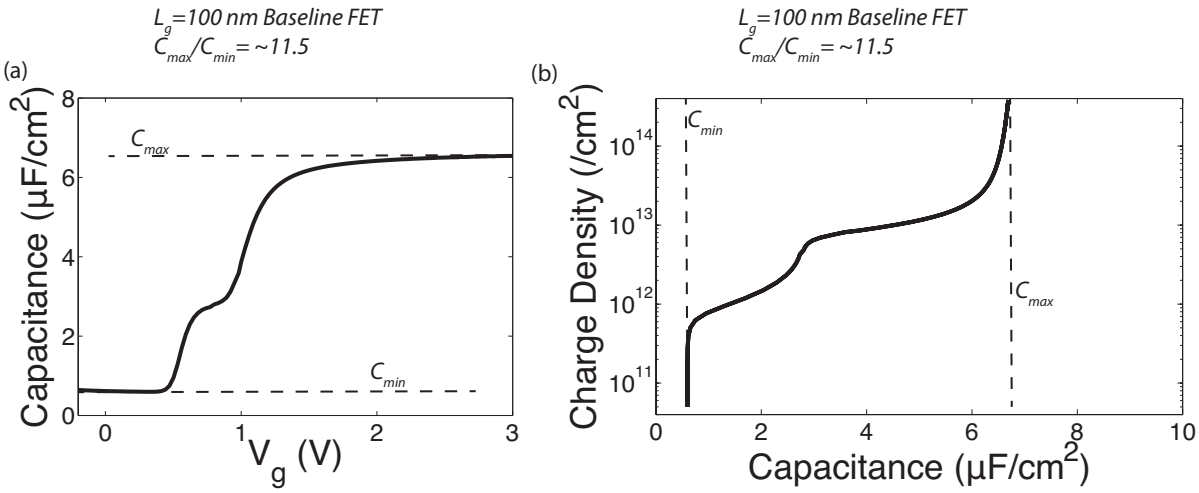


Figure 5.2: Capacitance-gate voltage characteristics (a) and charge density-capacitance characteristics of the baseline MOSFET. $L_g$=100 nm. The ratio of the inversion and depletion capacitance $C_{max}/C_{min}$=∼11.5.

capacitance, $C_G = (C_{FE}^{-1} + C_{MOS}^{-1})^{-1}$ can be made larger than $C_{MOS}$. In such a case, the body factor can be calculated as

$$m = \frac{dV_G}{d\psi} = (1 + \frac{C_{MOS}}{C_{FE}})(1 + \frac{C_s + C_{source} + C_{drain}}{C_{ox}}) \tag{5.7}$$

We note in equation 5.7, by matching $C_{FE}$ to $C_{MOS}$ which refers to the condition: -$C_{FE} \approx C_{MOS}$ and $-C_{FE} > C_{MOS}$, subthreshold swing $SS = m \times 60$ mV/dec could be made arbitrarily smaller than 60 mV/dec. A perfect matching between $C_{FE}$ and $C_{MOS}$ would result in an ideal switch with $SS$=0 mV/dec. $C_{MOS}$ (-$C_{FE} = C_{MOS}$ and $-C_{FE} > C_{MOS}$).

Now the question is: "Is it possible to match the ferroelectric capacitance and the MOSFET capacitance?" In order to answer this question, figure 5.2(a) show $C_{MOS}$-$V_g$ and $Q$-$C_{MOS}$ characteristics of a $L_g$=100 nm baseline MOSFET. We note in figure 5.2(a) that between the depletion and inversion the MOSFET capacitance changes by an order of magnitude. As result, innovative approach is necessary to design a NCFET.

Figure 5.3(a) shows the $Q$-$V_G$ characteristics of a NCFET for different ferroelectric thicknesses $t_{FE}$. Figure 5.3(b) shows $C_{MOS}$ and $-C_{FE}$ for these cases. It is interesting to note that while for $t_{FE}$=150 nm, the $Q-V_G$ curve is non-hysteretic and resembles that of a regular MOS capacitor with a smaller EOT, for the other two cases, $Q - V_G$ curve has two different

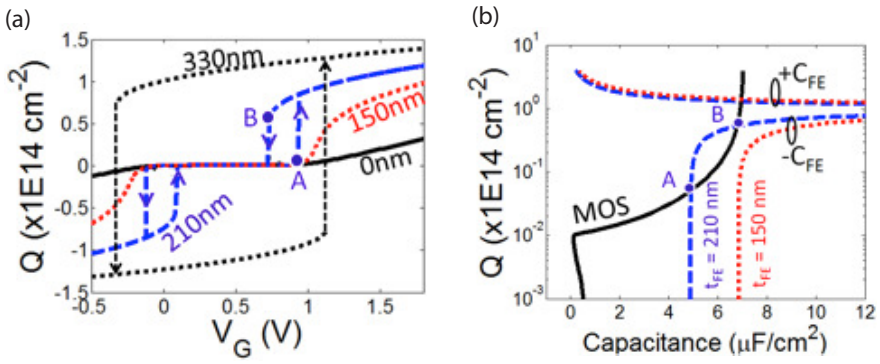


Figure 5.3: (a) Evolution of $Q - V_G$ characteristics with FE thickness. (b) Comparison of MOS capacitance and FE capacitance as functions of $Q$ for different $t_FE$.

types of hysteresis. For $t_{FE}$=210 nm, it has butterfly type dual hysteresis loops, which is a characteristic feature of antiferroelectric type materials [6]. With further increase in $t_{FE}$, the width of the hysteresis loops increases and at a critical $t_{FE}$, they merge together to form a usual ferroelectric single hysteresis loop (for example see the case for $t_{FE}$=330 nm). The origin of this thickness dependence is that $C_{FE}$ and $C_{MOS}$ are both non-linear (figure 5.3(c)) and they cannot be matched in the entire range of $Q$ from depletion to accumulation. For $Q$ values, where -$C_{FE} < C_{MOS}$, the equivalent $C_G$ become negative and hence the system becomes unstable and shows bi-stability. In order to elucidate this point, we note in 5.3(b), for $t_{FE}$=150 nm, the condition: $-C_{FE} > C_{MOS}$ is satisfied and hence the corresponding $Q - V_G$ curves do not have any hysteresis. On the other hand, for $t_{FE}$=210 nm, $C_{MOS}$ exceeds $-C_{FE}$ between the $Q$ values corresponding to points $A$ and $B$ (figure 5.3(b)). Hence, as shown in figure 5.3(a), hysteretic jumps occur in the $Q - V_G$ curve of the $t_{FE}$=210 nm case at the $Q$ values corresponding to points $A$ and $B$ in figure 5.3(b). The origin of AFE type dual hysteresis is that for certain $t_{FE}$, there can be multiple disconnected ranges of $Q$ values where the condition: $-C_{FE} < C_{MOS}$ is satisfied. AFE behavior is obtained for a certain range of FE thickness. The key difference between AFE and FE type hysteresis in a NC-MOS capacitor is that in the former case, all three regions of MOS operation (depletion, accumulation and inversion) can be accessed by sweeping $V_G$, while in the latter case, the device switches between the accumulation and inversion and the depletion region (the off state) cannot be accessed by changing $V_G$.

Figure 5.4(a,b) show the $Q - V_G$ and $I_D - V_G$ characteristic, respectively, of an AFE type NCFET for two different $V_D$. It is interesting to note that the hysteresis loops in $Q - V_G$ and $I_D - V_G$ can be dynamically controlled by drain voltage, $V_D$. It is due to the fact that $Q$ and $C_{MOS}$ changes with $V_D$ because of the electrostatic coupling of the channel to the drain. This, together with the fact that the shape of the hysteresis is dictated by relative magnitudes of $C_{MOS}$ and $C_{FE}$ means that the hysteresis in $Q - V_G$ and $I_D - V_G$ characteristics

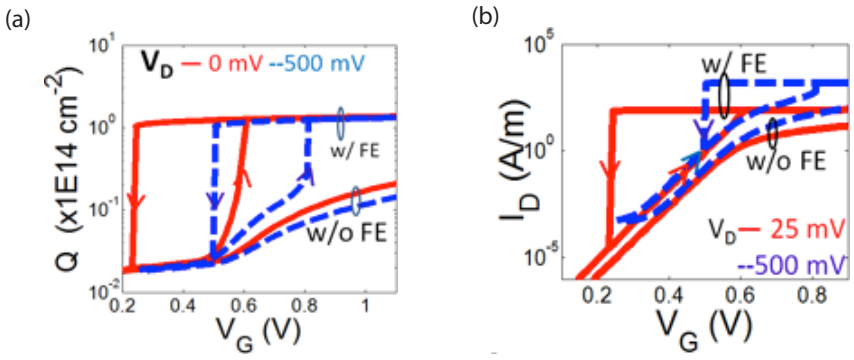


Figure 5.4: *Dynamic hysteresis control by $V_D$ in an AFE NCFET.* $Q - V_G$ (a) and $I_D - V_G$ (b) characteristics of the NCFET for different $V_D$. $t_{FE} = 210$ nm.

can be modulated dynamically by $V_D$. This gives rise to interesting possibilities of using such dynamic hysteresis control for novel memory functionalities in the same device structure.

## 5.3 Performance Tuning

### Ferroelectric Thickness Optimization

Figure 5.5(a-d) show the effect of $t_{FE}$ on the performance of AFE type NCFETs. We note in figure 5.5(a,b) is that in the presence of AFE type hysteresis, the significant boost in on-current is achieved with respect to the intrinsic MOSFET and $I_{on}$ (current in the upper branch of hysteresis) is almost independent of VG. One can take advantage of this AFE behavior by choosing the gate metal workfunction properly so that the hysteresis loop is positioned to fit completely within the supply voltage $V_{DD}$ window. Figure 5.5(c) shows that apart from boosting the on-current, the subthreshold swing is also improved with the addition of the FE. Figure 5.5(c) summarizes the overall effect of $t_{FE}$ on device performance by relating the on-off ratio to $t_{FE}$ for a given $V_D$. In this calculation, it was made sure that the hysteresis loops fit within the $V_G$ swing at the given $V_D$. Notably, at the on-set of hysteresis, on-off-ratio (and $I_{on}$) becomes independent of $t_{FE}$. Now that increase in $t_{FE}$ improves the subthreshold slope in the lower current regime and boosts $I_{on}$ by hysteretic jumps while increasing the hysteresis width, the design challenge is to optimize $t_{FE}$ so that on-off ratio is maximized while maintaining the hysteresis width smaller than the voltage swing.

Figure 5.6 summarizes the optimization of AFE NCFET performance with respect to $t_{FE}$. Figure 5.6(a) plots the maximum on-current achievable in a NCFET at different power supply voltages $V_{DD}$ (=$V_G$=$V_D$) and $I_{off}$=1 nA/$\mu$m and 100 nA/$\mu$m by optimizing the FE thickness. The corresponding optimal $t_{FE}$ at different $V_{DD}$ is shown in figure 5.6(b). The

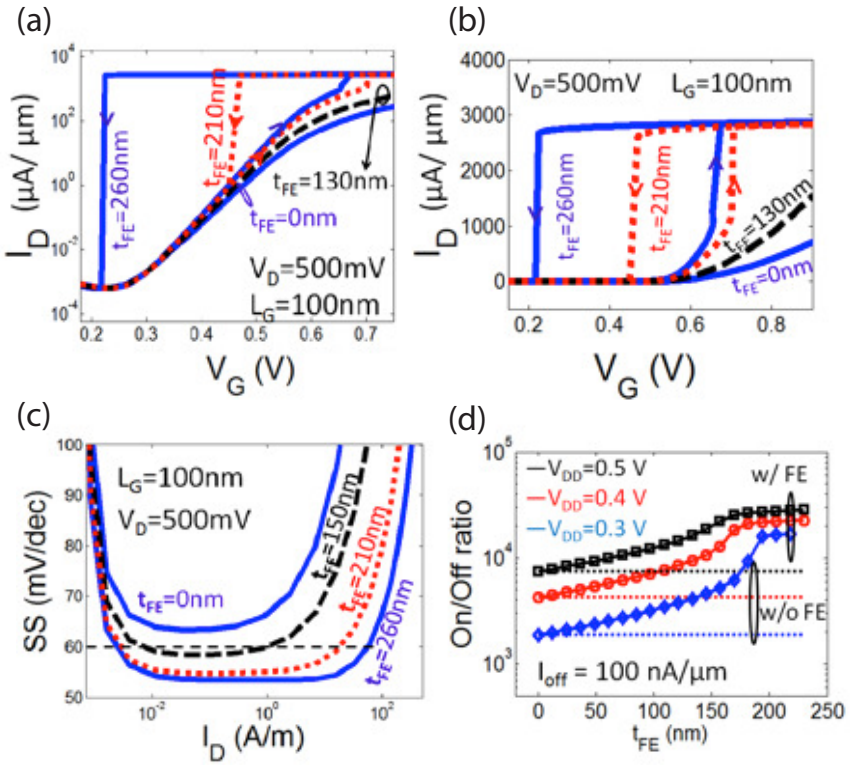


Figure 5.5: *Effect of $t_{FE}$ on Antiferroelectric type $I_D - V_G$ Characteristics.* (a,b) $I_D - V_G$ curves in logarithmic (a) and linear scale (b) for different $t_{FE}$. (c) Ramp up subthrehold slope (=$d(log_{10}I_D)/dV_G$) as a function of $I_D$ for different $t_{FE}$. (d) On-off ratio as a function of $t_{FE}$ for different $V_{DD}$ (=$V_G$=$V_D$) with $I_{off}$ set at 100 nA/$\mu$m.

optimal $t_{FE}$ decreases with the scaling of $V_{DD}$ due to the fact that the width of hysteresis loop will also have to decrease to accommodate the hysteresis loop within the $V_G$ swing=$V_{DD}$. We observe ins figure 5.6(a) that by optimizing $t_{FE}$ for a given $V_{DD}$, almost an order of magnitude increase in $I_{on}$ can be achieved compared to that in the baseline MOSFET. For example, in figure 5.6(a), for $I_{off}$=100 nA/$\mu$m, $I_{on}$ at $V_{DD}$=225 mV in the optimized NCFET is the same as that in the intrinsic MOSFET at $V_{DD}$=500 mV. This indicates that $V_{DD}$ can be scaled to much smaller voltages in NCFETs than possible in the conventional MOSFETs. We also note in figure 5.6(a) that for $I_{off}$=1 nA/$\mu$m, between $V_{DD}$=350 mV and 500 mV, the maximum $I_{on}$ achievable in the optimized NCFETs is the same as that for the optimized NCFET for $I_{off}$=100 nA/$\mu$m. Figure 5.6(c) shows $I_{on}$ vs on-off ratio in a NCFET for different $t_{FE}$. Note in figure 5.6(c) that for $t_{FE}$=210 nm, $I_{on}$ is independent of the on-off ratio (and $I_{off}$). This is due to the fact that after the on-set of hysteresis, $I_{on}$ is almost independent of $V_G$. Utilizing this fact, a unique NCFET can be designed where $I_{on}$ is independent of $I_{off}$ for a certain range of $V_{DD}$.

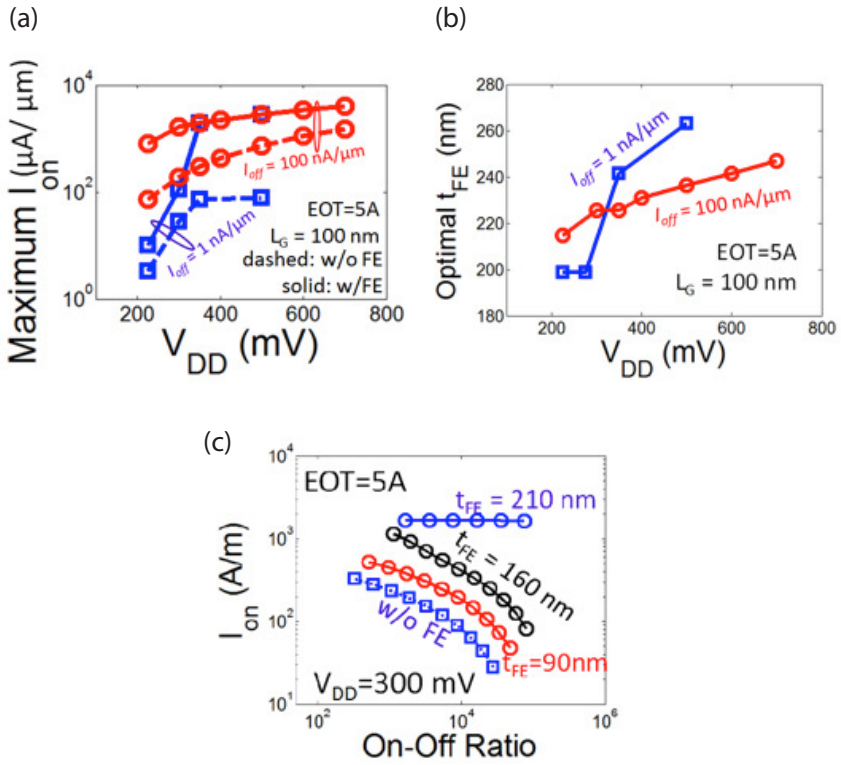


Figure 5.6: *Performance Optimization by FE thickness.* (a) Maximum on-current (a) achievable in a NCFET at different power supply voltages, $V_{DD}$ (=$V_G$=$V_D$) and $I_{off}$=1 nA/$\mu$m and 100 nA/$\mu$m by optimizing the FE thickness. (b) The optimal $t_{FE}$ at different $V_{DD}$. (c) $I_{on}$ vs on-off ratio in a NCFET for different $t_{FE}$.

## Effect of Equivalent Oxide Thickness (EOT)

EOT is an important design parameter for NCFET, because an interfacial amorphous $SiO_2$ layer is inevitable in the gate stack due to the process related issues [4,8]. Figure 5.7 summarizes the optimization of AFE NCFET performance with respect to EOT. Figure 5.3(a) plots on-current $I_{on}$ as a function of $t_{FE}$ for NCFETs with different EOTs for $I_{off}$=100 nA/$\mu$m and $V_{DD}$=300 mV. We note in figure 5.7(a) that although a larger EOT results in a smaller $I_{on}$ for a given $V_{DD}$, by using a ferroelectric of an optimal $t_FE$, the same maximum $I_{on}$ can be achieved in devices with different EOTs. For example, $I_{on}$ in the baseline MOSFET for EOT=20 $\mathring{A}$ is almost 4 times less than that for EOT=5$\mathring{A}$, but in the corresponding NCFETs same $I_{on}$ can be achieved by using $t_{FE}$= 200 nm and 600 nm for EOT = 5 $\mathring{A}$ and 20 $\mathring{A}$ respectively. Figure 5.7(b,c) plot maximum $I_{on}$ and optimum $t_{FE}$ (c) for different EOT devices as functions of $V_{DD}$ for $I_{off}$ = 100 nA/$\mu$m. We note in figure 5.7(c) that the optimal $t_{FE}$ scales linearly with the EOT in the intrinsic device. This is due to the fact that since an increase in EOT decreases $C_{MOS}$, a larger $t_{FE}$ is required to compensate the increase in

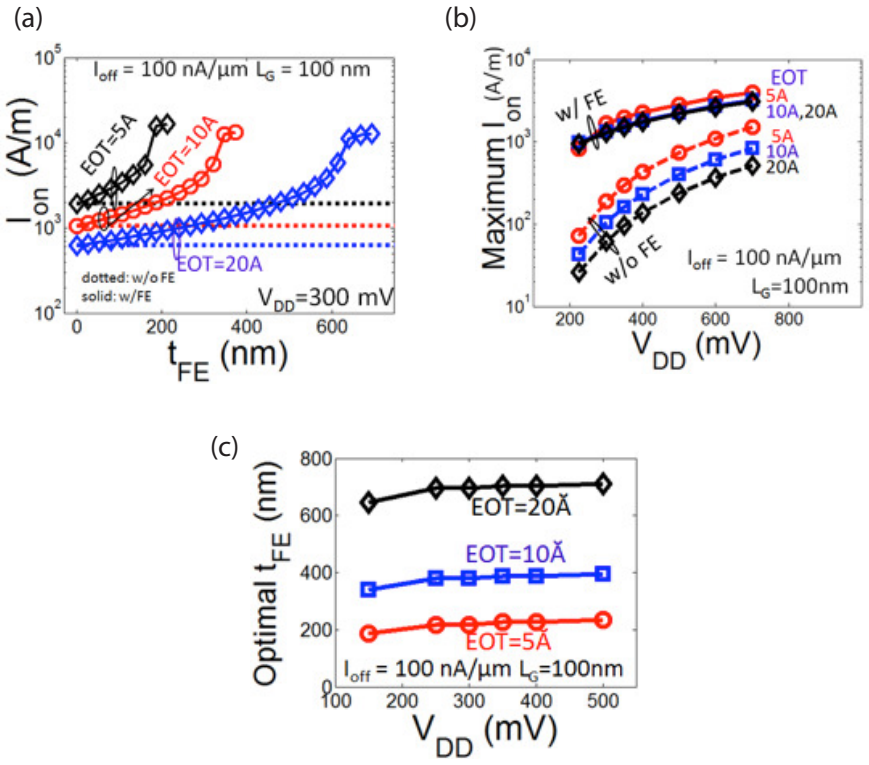


Figure 5.7: *Equivalent oxide thickness as a critical NCFET design parameter.* (a) On-current $I_{on}$ as a function of $t_{FE}$ for NCFETs with different EOTs for $I_{off}$=100 nA/$\mu$m and $V_{DD}$=300 mV. (b,c) Maximum $I_{on}$ (b) and optimum $t_{FE}$ (c) for different EOT devices as functions of $V_{DD}$ for $I_{off}$ = 100 nA/$\mu$m.

$C_{MOS}$.

## Source and Drain Overlap

Source and drain overlaps contribute additional capacitances to MOS structure ($C_{MOS}$) and hence overlaps can be utilized as important design parameters. Figure 5.8(a,b) compares $I_D-V_G$ characteristics of the baseline MOSFET and a NCFET with $t_{FE}$=210 nm for different source and drain overlaps, respectively. It is interesting to note in figure 5.8 that $I_D - V_G$ characteristics of the baseline MOSFET is independent of the length of the overlap; however, $I_D-V_G$ characteristics of the NCFET is strongly varies depending on the overlap location and length. For example, we observe in figure 5.8(a,b) that, without an overlap, the subthreshold swing of NCFET is identical to that of the baseline MOSFET at low current levels. In figure 5.8(a), we observe that as an source overlap is introduced, the subthreshold swing of NCFET is significantly improved compared to that of the baseline MOSFET. This is because of the fact that with additional source overlap capacitance, $C_{MOS}$ is better matched

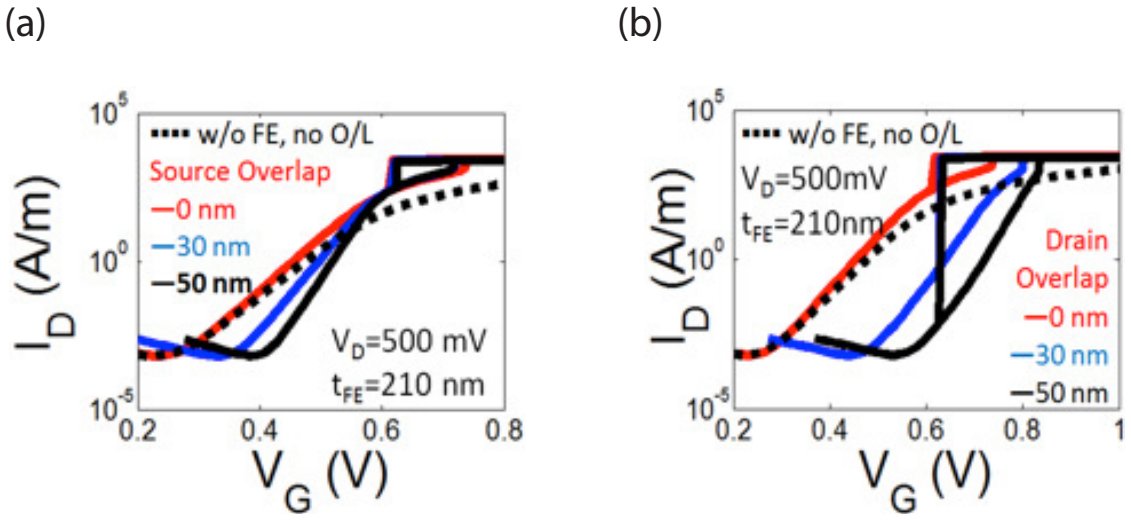


Figure 5.8: *Source and Drain Overlap Effects.* $I_D - V_G$ characteristics of a NCFET with $t_{FE}$=210 nm for different source (a) and drain (b) overlaps. $L_G$=100 nm, $V_D$= 500 mV.

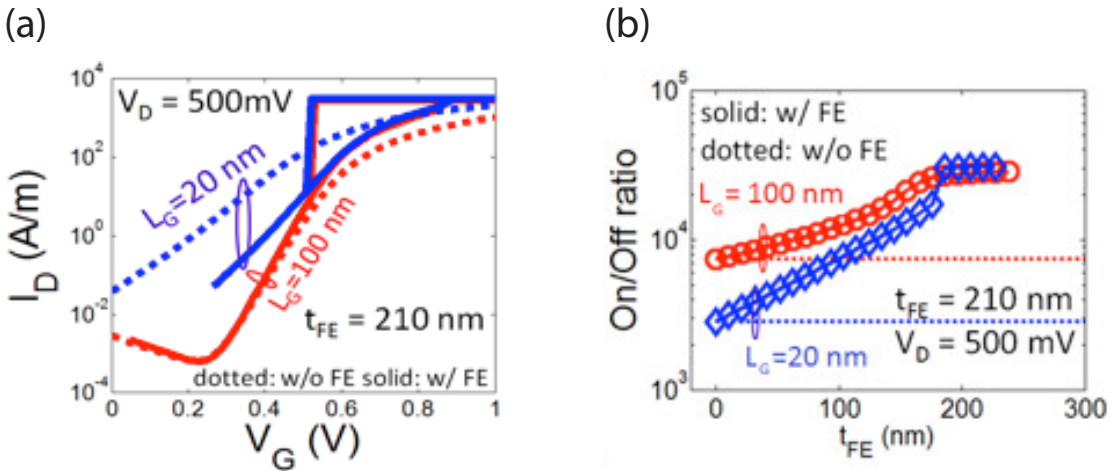


Figure 5.9: *Effect of $L_G$ scaling.* (a) Comparison of $I_D - V_G$ characteristics of NCFETs with $t_{FE}$=210 nm with two different gate lengths, $L_G$=20 nm and 100 nm. (b) On-off ratio as a function of $t_{FE}$ for two different $L_G$.

to $C_{FE}$ resulting in further decrease in subthreshold swing. A comparison between figures 5.8(a) and 5.8(b) shows that, with a drain overlap, the shape of the hysteresis changes, while source overlap has no effect on the hysteresis shape. The reason for this, as was confirmed by detailed simulations, is that the source overlap adds significant capacitance in the subthreshold region while drain overlap increases the capacitance in a much larger range of $Q$.

### Gate Length Scaling

Although in an ultra-scaled device, performance is severely degraded due to short channel effects, the charge density $Q$ and $C_{MOS}$ in the subthreshold regime is increased significantly in a scaled device due to the increased drain coupling to the channel. Resulting increase in $C_{MOS}$ could result in a better matching to the FE capacitance and greater performance improvement for the same $t_{FE}$ in an ultra-scaled device. Figure 5.9(a) compares $I_D - V_G$ characteristics of NCFETs with $t_{FE}$=210 nm with two different gate lengths: $L_G$=20 nm and 100 nm. We note in figure 5.9(a) that the same thickness of the ferroelectric results in a better improvement of the subthreshold characteristics of the $L_G$=20 nm device than that of the $L_G$=100 nm device. Figure 5.9(b) plots the on-off ratio as a function of $t_{FE}$ for two different $L_G$ for $I_{off}$ = 100 nA/$\mu$m. We observe in figure 5.9(b) that, for the same $t_{FE}$ in NCFETs with $L_G$=20 and 100 nm, same on-off ratio can be achieved although the baseline MOSFET with $L_G$=20 nm has significantly lower on-off ratio. This suggests that the improvement in the device performance due to the negative capacitance effects could be stronger as device dimensions are scaled down.

## 5.4 Conclusions

The key findings presented in this chapter are as follows.

1 We have shown that capacitance matching is a powerful design concept for negative capacitance MOSFETs.

2 An NCFET can be designed to have either (a) non-hysteretic or (b) antiferroelectric behavior. The key design philosophy presented herein is that the unique antiferroelectric property can allow for very large on-off ratio in exchange for hysteresis. By designing the hysteresis to fit within the VDD window by tuning tFE, this effect can be utilized as a logic device.

3 Gate overlap capacitances can be tuned to improve the NCFET performance significantly.

5 Finally, increased drain coupling in ultra-scaled devices enhances the device performance more significantly for shorter channel devices.

## 5.5 Suggestions for Future Work

1 In the NCFET model presented herein, a floating gate was employed to make sure the 1-D Landau model is a reasonable assumption for the ferroelectric. For logic operations, such a floating gate is not desirable. A full 2-D model of the ferroelectric oxide could eliminate the necessity of the floating gate for modeling purposes.

2 Compact models of NCFETs could be developed following the procedure presented in this chapter. Such models would be useful to project the performance enhancement in circuits using NCFETs.

3 Dynamic control of antiferroelectric hysteresis loops by drain voltage could enable novel memory devices.

4 Our results show that the desired thickness of the ferroelectric is of the order of 100 nm. An investigation of the ferroelectric oxides which could reduce the optimal ferroelectric thickness down to $\sim$ 10 nm would be necessary.

# Chapter 6

# CONCLUSIONS AND FUTURE WORK

## 6.1 Conclusions

The key result presented in this work is "Negative Capacitance Has Been Detected!" [120] In chapter 1 section 1.7, we made a point that although the concept of negative capacitance is fundamental of the theory of ferroelectrics, this phenomenon was never experimentally demonstrated before primarily due to its unstable nature. Now that the negative capacitance has been experimentally measured in a ferroelectric $Pb(Zr_{0.2}Ti_{0.8})O_3$ films, we hope that the results presented in this thesis would set the stage for utilizing this phenomenon for breakthroughs in ultra-low power computing. The main results are listed below.

1 *Direct measurement on negative capacitance:* Negative capacitance is directly measured by constructing a simple series network of a ferroelectric $Pb(Zr_{0.2}Ti_{0.8})O_3$ capacitor and an external resistor. When a voltage is applied across this series network, the voltage across the ferroelectric capacitor was observed to decrease with time-in exactly the opposite direction to which voltage for a regular positive capacitor should change. Two fundamental concepts-namely the "characteristic negative capacitance transients" and the "dynamic hysteresis loops"- have been proposed, which give quantitive measure of the negative capacitance phenomenon. The effects of different parameters such as the external resistance and voltage pulse amplitude on the negative capacitance phenomena are also investigated. These results are presented in chapter 3 and reported in [99].

2 *Stabilization of negative capacitance:* Stabilization of the negative capacitance in ferroelectric $Pb(Zr_{0.2}Ti_{0.8})O_3$-dielectric $SrTiO_3$ heterostructures is experimentally demonstrated. In contrast to the classical theory of electrostatics, we observed that the equivalent capacitance of a series combination of a ferroelectric and a dielectric capacitor is larger than that of the constituent dielectric capacitor. This points to the fact

the the ferroelectric capacitor acts as an effective negative capacitor in such a circuit. The results are analyzed based on a simple 1-D Landau-Devonshire model. The effects of temperature on the negative capacitance phenomena are also investigated. These results are presented in chapter 4 and reported in reference [113].

3 *Design of negative capacitance field-effect-transistors:* A design framework of negative capacitance field-effect-transistors (NCFET) has also been presented. A new mode of NCFET operation-called the antiferroelectric mode is proposed, where a significantly boost of the on-current and a sub-60 mV/dec subthreshold characteristics is obtained in exchange for a nominal hysteresis. The effects of different design parameters such ferroelectric thickness, source/drain overlap and gate length on the NCFET performance are also analyzed. These results are presented in chapter 5 and reported in reference [117].

4 *Voltage controlled decoupled ferroelastic switching:* We have reported for the first time a voltage controlled reversible creation and annihilation of $a$-axis oriented $\sim$10 nm wide ferroelastic nanodomains without a concurrent ferroelectric 180° switching of the surrounding $c$-domain matrix in archetypal ferroelectric $Pb(Zr_{0.2}Ti_{0.8})O_3$ thin films by using the piezo-response force microscopy technique. In previous studies, the coupled nature of ferroelectric switching and ferroelastic rotation has made it difficult to differentiate the underlying physics of ferroelastic domain wall movement. Our observation of distinct thresholds for ferroelectric and ferroelastic switching allowed us investigate the ferroelastic switching cleanly and demonstrate a new degree of nanoscale control over the ferroelastic nanodomains. These results are presented in chapter 2 and reported in reference [31].

5 *The nature of polarization-strain coupled:* We have studied the effects of epitaxial strain on spontaneous polarization of strained 40 nm $Pb(Zr_{0.2}Ti_{0.8})O_3$ films by growing them on three different substrates, names $SrTiO_3$ (001), $DyScO_3$ (110) and $GdScO_3$. Our work shows that, while, in the tetragonality range $c_c/a_c$ = 1.05-1.09, PZT remnant polarization is nearly independent of the tetragonality, in the range $c_c/a_c$ = 1.041-1.05, remnant polarization is found to show a much stronger functional dependence. This points to the fact that the strain sensitivity of the polarization even in the same ferroelectric material can depend on the value of tetragonality and the sensitivity is larger for smaller values of the tetragonality. These results are presented in chapter 2.

6 *Effects of strain relaxation on the dielectric properties of ferroelectric thin films:* We also studied the effects of strain relaxation of dielectric properties of 40 nm $Pb(Zr_{0.2}Ti_{0.8})O_3$ films grown on $SrTiO_3$ substrates. A drastic increase in defect and dislocation density due to strain relaxation is observed in epitaxial PZT films with tetragonality $c/a <$ 1.07 grown on STO substrates, which results in a significant frequency dispersion of the dielectric constant and a strong Rayleigh type behavior in those samples. For a

given combination of a ferroelectric thin film and a substrate, tetragonality $c_c/a_c$ is a quantitative measure of the degree to which epitaxial strain has been relaxed in the film and the extent of extrinsic contributions to the dielectric properties can be predicted from the value of $c_c/a_c$. These results are presented in chapter 2 and reported in reference [32].

## 6.2 Suggestions for Future Work

1 *Negative capacitance in CMOS compatible $HfO_2$ based ferroelectrics:* Ferroelectricity has recently been discovered in annealed polycrystalline $HfO_2$ when doped with a variety of elements such as Si, Zr, La, Sr, Al, Y etc. [121, 122, 123, 124, 125, 126, 127, 128, 129, 130, 131, 121, 132, 133, 134, 135, 136, 137, 138, 139, 140]. This material system has a number of properties desirable for device applications, such as (1) robust ferroelectricity at 10 nm thickness range unlike their predecessors: perovskite based ferroelectrics, (2) tunability of the spontaneous polarization and the coercive voltage through the control of doping level, dopant species and the annealing conditions and (3) CMOS compatibility. While these materials have opened a floodgate for activities, most of the efforts are confined to memory applications. Investigation of negative capacitance effects in $HfO_2$ based ferroelectrics could bring about new opportunities for ultra-low power computing.

2 *Negative capacitance in antiferroelectric materials:* An antiferroelectric crystal consists of two ferroelectric sublattices in which the spontaneous dipoles are antiparallel or quasi-antiparallel resulting in a macroscopic zero spontaneous polarization [141, 142, 143]. The interaction between the adjacent sublattices in antiferroelectric would result in an interesting negative capacitance phenomenon where the negative slope regions in the charge-voltage characteristics are separated by a region of positive capacitance around $P$=0. The disconnected negative capacitance regions in an antiferroelectric charge-voltage characteristics results in a butterfly double hysteresis loop. Intrinsic (homogeneous) switching has been predicted in antiferroelectrics, for which a stronger negative capacitance effect is expected in these materials [143, 144].

3 *Passive voltage amplification:* By introducing an intermediate metallic layer between the ferroelectric and the dielectric layer in a heterostructure, a passive voltage amplifier could be implemented. Figure 6.2 shows the schematic diagram of such an amplifier. The input voltage $V_{in}$ is amplified at the internal metal layer ($V_{out} = V_{in} \times (1 + C_{DE}/C_{FE})^{-1}$).

4 *Microscopic details of negative capacitance* The microscopic details of negative capacitance dynamics could be studied using multiple techniques such as using atomic force

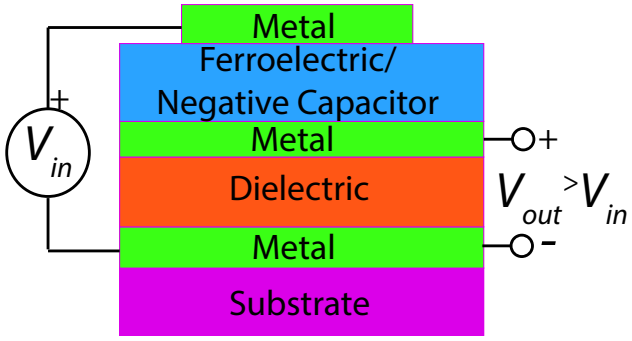


Figure 6.1: A passive voltage amplifier.

microscopy [111] and X-ray diffraction [112]. In combination with the time dynamic measurement presented in chapter 3, such techniques could reveal important information of the microscopic details of the characteristics negative transients (for example, the abrupt/correlated switching events during the early part of the switching dynamics that result in the characteristic transients).

5 *Phase field based modeling of ferroelectric-dielectric heterostructures* Theoretical modeling of the ferroelectric-dielectric heterostructures presented in chapter 4 was performed using 1-D Landau-Devonshite formalism. A 3-D phase field based approach to modeling could give more insights in the stabilization of negative capacitance in such heterostructures [145, 146].
:

6 *Modeling of ferroelectric switching dynamics:* The time-dynamic measurement of negative capacitance in a ferroelectric capacitance was modeled using the Landau-Khalatnikov equation in chapter 3. Such a model assumes a single domain switching. In reality, switching dynamics involves domain mediated mechanisms in ferroelectric capacitors. Hence, a study of ferroelectric switching based on multi scale models involving atomistic molecular dynamics and coarse-grained Monte Carlo simulations could reveal the effects of domain nucleation and growth mechanisms on the characteristic negative capacitance transients [147].

7 *Modeling of negative capacitance transistors:* In chapter 4, a floating gate was assumed in the negative capacitance field-effect-transistor to screen out the non-uniformity of electrostatic potential at the ferroelectric-dielectric interface and to make sure the assumption of a mono-domain ferroelectric is a reasonable one. However, for practical logic applications, a floating gate is not desirable since it could float to any potential depending on the leakage current and the switching cycles. Hence, to remove the mono

domain assumption, ferroelectric oxide in a negative capacitance field-effect-transistor could be modeled using the 3-D phase field approach. This, in turn, could lead to a design framework of negative capacitance field-effect-transistor which does not require a floating gate.

8 *Alternative negative capacitance systems:* The concept of negative capacitance goes beyond the ferroelectrics and can be applied in general to any two-level system separated by an intrinsic barrier [26, 27, 28, 29, 30]. The time-dynamic measurement technique of negative capacitance presented in chapter 3 could serve as a canonical test for negative capacitance in any such system.

# Bibliography


[1] J. Whitney and P. Delforge. *Data Center Efficiency Assessment*. Available online: http://www.nrdc.org/energy/files/data-center-efficiency-assessment-IP.pdf. National Resource Defense Council, Aug 2014. Retrieved: 5 May, 2015.

[2] *24 Electronic Products Per Household – Got Recycling?* Available online: http://www.forbes.com/sites/tjmccue/2013/01/02/24-electronic-products-per-household-got-recycling/. Forbes magazine. Retrieved: 5 May, 2015.

[3] D. Evans. *The Internet of Things How the Next Evolution of the Internet Is Changing Everything*. Available online: http://www.cisco.com/web/about/ac79/docs/innov/IoT_IBSG_0411FINAL.pdf. Internet Business Solutions Group , 2011. Retrieved: 12 May, 2015.

[4] Martin Hilbert and Priscila López. "The worldÕs technological capacity to store, communicate, and compute information". In: *Science* 332.6025 (2011), pp. 60–65.

[5] *Energy in the United States*. Available online: http://en.wikipedia.org/wiki/Energy_in_the_United_States. Retrieved: 5 May, 2015.

[6] James M Kaplan, William Forrest, and Noah Kindler. *Revolutionizing data center energy efficiency*. Tech. rep. Technical report, McKinsey & Company, 2008.

[7] Richard Brown et al. "Report to congress on server and data center energy efficiency: Public law 109-431". In: *Lawrence Berkeley National Laboratory* (2008).

[8] Eric Pop. "Energy dissipation and transport in nanoscale devices". In: *Nano Research* 3.3 (2010), pp. 147–169.

[9] *The International Technology Roadmap for Semiconductors*. Available online: http://itrs.net/. Retrieved: 5 May, 2015.

[10] Andrew Danowitz et al. "CPU DB: recording microprocessor history". In: *Communications of the ACM* 55.4 (2012), pp. 55–63.

[11] *50 Years of Moore's Law*. Available online: http://www.intel.com/content/www/us/en/silicon-innovations/moores-law-technology.html. Retrieved: 5 May, 2015.

[12] Thomas N Theis and Paul M Solomon. "ItÕs time to reinvent the transistor!" In: *Science* 327.5973 (2010), pp. 1600–1601.

[13] Thomas N Theis and Paul M Solomon. "In Quest of the" Next Switch": Prospects for Greatly Reduced Power Dissipation in a Successor to the Silicon Field-Effect Transistor". In: *Proceedings of the IEEE* 98.12 (2010), pp. 2005–2014.

[14] Ralph K Cavin et al. "Energy barriers, demons, and minimum energy operation of electronic devices". In: *Fluctuation and Noise letters* 5.04 (2005), pp. C29–C38.

[15] Victor V Zhirnov et al. "Limits to binary logic switch scaling-a gedanken model". In: *Proceedings of the IEEE* 91.11 (2003), pp. 1934–1939.

[16] Sanjay Banerjee et al. "A new three-terminal tunnel device". In: *IEEE Electron Device Letters* 8.8 (1987), pp. 347–349. ISSN: 0741-3106. DOI: 10.1109/EDL.1987.26655.

[17] Chenming Hu et al. "Green Transistor - A VDD Scaling Path for Future Low Power ICs". In: *International Symposium on VLSI Technology, Systems and Applications, 2008. VLSI-TSA 2008.* 2008, pp. 14–15. DOI: 10.1109/VTSA.2008.4530776.

[18] K. Gopalakrishnan, Peter B. Griffin, and James D. Plummer. "Impact ionization MOS (I-MOS)-Part I: device and circuit simulations". In: *IEEE Transactions on Electron Devices* 52.1 (2005), pp. 69–76. ISSN: 0018-9383. DOI: 10.1109/TED.2004.841344(410)52.

[19] Hei Kam and Tsu-Jae King Liu. "Pull-In and Release Voltage Design for Nanoelectromechanical Field-Effect Transistors". In: *IEEE Transactions on Electron Devices* 56.12 (2009), pp. 3072–3082. ISSN: 0018-9383. DOI: 10.1109/TED.2009.2032617.

[20] M. Enachescu et al. "Ultra low power NEMFET based logic". In: *2013 IEEE International Symposium on Circuits and Systems (ISCAS)*. 2013, pp. 566–569. DOI: 10.1109/ISCAS.2013.6571905.

[21] Sayeef Salahuddin and Supriyo Datta. "Use of Negative Capacitance to Provide Voltage Amplification for Low Power Nanoscale Devices". In: *Nano Letters* 8.2 (2008). PMID: 18052402, pp. 405–410. DOI: 10.1021/nl071804g. eprint: http://pubs.acs.org/doi/pdf/10.1021/nl071804g. URL: http://pubs.acs.org/doi/abs/10.1021/nl071804g.

[22] LE Cross and RE Newnham. "History of ferroelectrics". In: *J Am Ceram* 11 (1987), pp. 289–305.

[23] Gene H Haertling. "Ferroelectric ceramics: history and technology". In: *Journal of the American Ceramic Society* 82.4 (1999), pp. 797–818.

[24] Rolf Landauer. "Electrostatic considerations in BaTiO3 domain formation during polarization reversal". In: *Journal of Applied Physics* 28.2 (1957), pp. 227–234.

[25] Walter J Merz. "Switching time in ferroelectric BaTiO3 and its dependence on crystal thickness". In: *Journal of Applied Physics* 27.8 (1956), pp. 938–943.

[26] JP Eisenstein, LN Pfeiffer, and KW West. "Negative compressibility of interacting two-dimensional electron and quasiparticle gases". In: *Physical review letters* 68.5 (1992), p. 674.

[27] M AbdelGhany and T Szkopek. "Extreme sub-threshold swing in tunnelling relays". In: *Applied Physics Letters* 104.1 (2014), p. 013509.

[28] Muhammad Masuduzzaman and Muhammad Ashraful Alam. "Effective nanometer airgap of NEMS devices using negative capacitance of ferroelectric materials". In: *Nano letters* 14.6 (2014), pp. 3160–3165.

[29] Raj K Jana, Gregory L Snider, and Debdeep Jena. "On the possibility of sub 60 mV/decade subthreshold switching in piezoelectric gate barrier transistors". In: *physica status solidi (c)* 10.11 (2013), pp. 1469–1472.

[30] Justin C Wong and Sayeef Salahuddin. "Can piezoelectricity lead to negative capacitance?" In: *Electron Devices Meeting (IEDM), 2014 IEEE International*. IEEE. 2014, pp. 13–5.

[31] Asif Islam Khan et al. "Voltage-Controlled Ferroelastic Switching in Pb (Zr0. 2Ti0. 8) O3 Thin Films". In: *Nano letters* 15.4 (2015), pp. 2229–2234.

[32] Asif Islam Khan et al. "The effects of strain relaxation on the dielectric properties of epitaxial ferroelectric Pb (Zr0. 2Ti0. 8) TiO3 thin films". In: *Applied Physics Letters* 105.2 (2014), p. 022903.

[33] D Dijkkamp et al. "Preparation of Y-Ba-Cu oxide superconductor thin films using pulsed laser evaporation from high Tc bulk material". In: *Applied Physics Letters* 51.8 (1987), pp. 619–621.

[34] R Ramesh et al. "Epitaxial growth of ferroelectric bismuth titanate thin films by pulsed laser deposition". In: *Applied physics letters* 57.15 (1990), pp. 1505–1507.

[35] JS Horwitz et al. "Insitu deposition of epitaxial PbZrxTi (1- x) O3 thin films by pulsed laser deposition". In: *Applied physics letters* 59.13 (1991), pp. 1565–1567.

[36] Robert Eason. *Pulsed laser deposition of thin films: applications-led growth of functional materials*. John Wiley & Sons, 2007.

[37] Hans M Christen and Gyula Eres. "Recent advances in pulsed-laser deposition of complex oxides". In: *Journal of Physics: Condensed Matter* 20.26 (2008), p. 264005.

[38] Milton Ohring. *Materials science of thin films*. Academic press, 2001.

[39] Karin M Rabe, Charles H Ahn, and Jean-Marc Triscone. *Physics of ferroelectrics: a modern perspective*. Vol. 105. Springer Science & Business Media, 2007.

[40] Malcolm E Lines and Alastair M Glass. *Principles and applications of ferroelectrics and related materials*. Clarendon press Oxford, 2001.

[41] Landolt-Börnstein. *Numerical Data and Functional Relationships in Science and Technology, edited by K.-H. Hellwege and A. M. Hellwege*. Ed. by K.-H. Hellwege and A. M. Hellwege. Vol. 16. Springer, Berlin, 1981.

[42] V Nagarajan et al. "Thickness dependence of structural and electrical properties in epitaxial lead zirconate titanate films". In: *J. Appl. Phys.* 86.1 (1999), pp. 595–602.

[43] JH Haeni et al. "Room-temperature ferroelectricity in strained SrTiO3". In: *Nature* 430.7001 (2004), pp. 758–761.

[44] M. D. Biegalski. "Ph.D. thesis". In: *The Pennsylvania State University* (2006).

[45] V Nagarajan et al. "Dynamics of ferroelastic domains in ferroelectric thin films". In: *Nature Mater.* 2.1 (2002), pp. 43–47.

[46] Peng Gao et al. "Atomic-scale mechanisms of ferroelastic domain-wall-mediated ferroelectric switching". In: *Nature Comm.* 4 (2013).

[47] Jun Ouyang et al. "Engineering of Self-Assembled Domain Architectures with Ultrahigh Piezoelectric Response in Epitaxial Ferroelectric Films". In: *Adv. Func. Mater.* 17.13 (2007), pp. 2094–2100.

[48] A Roelofs et al. "Depolarizing-field-mediated $180^0$ switching in ferroelectric thin films with $90^0$ domains". In: *Appl. Phys. Lett.* 80.8 (2002), pp. 1424–1426.

[49] J Karthik, AR Damodaran, and LW Martin. "Effect of $90^0$ Domain Walls on the Low-Field Permittivity of Pb(Zr0.2Ti0.8)$O_3$ Thin Films". In: *Phys. Rev. Lett.* 108.16 (2012), p. 167601.

[50] Levente J. Klein et al. "Domain dynamics in epitaxial $Pb(Zr_{0.2}Ti_{0.8})O_3$ films studied by piezoelectric force microscopy". In: *J. Vacuum Sci. Tech. B* 28.4 (2010), C5A20–C5A23.

[51] Ruijuan Xu et al. "Ferroelectric polarization reversal via successive ferroelastic transitions". In: *Nature materials* 14.1 (2015), pp. 79–86.

[52] C. B. Sawyer and C. H. Tower. "Rochelle Salt as a Dielectric". In: *Phys. Rev.* 35 (3 1930), pp. 269–273. DOI: 10.1103/PhysRev.35.269. URL: http://link.aps.org/doi/10.1103/PhysRev.35.269.

[53] Ho Nyung Lee et al. "Suppressed dependence of polarization on epitaxial strain in highly polar ferroelectrics". In: *Physical review letters* 98.21 (2007), p. 217602.

[54] R. E. Eitel, T. R. Shrout, and C. A. Randall. "Nonlinear contributions to the dielectric permittivity and converse piezoelectric coefficient in piezoelectric ceramics". In: *Journal of Applied Physics* 99.12, 124110 (2006), pp. –. DOI: http://dx.doi.org/10.1063/1.2207738. URL: http://scitation.aip.org/content/aip/journal/jap/99/12/10.1063/1.2207738.

[55] Cz Pawlaczyk et al. "Fatigue, rejuvenation and self-restoring in ferroelectric thin films". In: *Integrated Ferroelectrics* 9.4 (1995), pp. 293–316.

[56] D. V. Taylor and D. Damjanovic. "Evidence of domain wall contribution to the dielectric permittivity in PZT thin films at sub-switching fields". In: *Journal of Applied Physics* 82.4 (1997).

[57] NA Pertsev, AG Zembilgotov, and AK Tagantsev. "Effect of mechanical boundary conditions on phase diagrams of epitaxial ferroelectric thin films". In: *Phys. Rev. Lett.* 80.9 (1998), p. 1988.

[58] K. J. Choi et al. "Enhancement of Ferroelectricity in Strained BaTiO3 Thin Films". In: *Science* 306.5698 (2004), pp. 1005–1009. DOI: 10.1126/science.1103218.

[59] Claude Ederer and Nicola A Spaldin. "Effect of epitaxial strain on the spontaneous polarization of thin film ferroelectrics". In: *Phys. Rev. Lett.* 95.25 (2005), p. 257601.

[60] Ho Nyung Lee et al. "Suppressed dependence of polarization on epitaxial strain in highly polar ferroelectrics". In: *Phys. Rev. Lett.* 98.21 (2007), p. 217602.

[61] V Nagarajan et al. "Misfit dislocations in nanoscale ferroelectric heterostructures". In: *Applied Physics Letters* 86.19 (2005), pp. 192910–192910.

[62] IB Misirlioglu et al. "Defect microstructures in epitaxial PbZr0. 2Ti0. 8O3 films grown on (001) SrTiO3 by pulsed laser deposition". In: *Journal of materials science* 41.3 (2006), pp. 697–707.

[63] Dal-Hyun Do et al. "Structural visualization of polarization fatigue in epitaxial ferroelectric oxide devices". In: *Nature materials* 3.6 (2004), pp. 365–369.

[64] S. Gariglio et al. "Strain relaxation and critical temperature in epitaxial ferroelectric Pb(Zr0.20Ti0.80)O3 thin films". In: *Appl. Phys. Lett.* 90.20 (2007), pp. –.

[65] Valanoor Nagarajan et al. "Scaling of structure and electrical properties in ultrathin epitaxial ferroelectric heterostructures". In: *Journal of applied physics* 100.5 (2006), p. 051609.

[66] RE Eitel, TR Shrout, and CA Randall. "Nonlinear contributions to the dielectric permittivity and converse piezoelectric coefficient in piezoelectric ceramics". In: *Journal of applied physics* 99.12 (2006), p. 124110.

[67] H Lu et al. "Mechanical writing of ferroelectric polarization". In: *Science* 336.6077 (2012), pp. 59–61.

[68] Peng Gao et al. "Ferroelastic domain switching dynamics under electrical and mechanical excitations". In: *Nature Comm.* 5 (2014).

[69] AL Roitburd. "Equilibrium structure of epitaxial layers". In: *Phys. Stat. Sol. a* 37.1 (1976), pp. 329–339.

[70] Alexander L Roytburd. "Thermodynamics of polydomain heterostructures. I. Effect of macrostresses". In: *J. Appl. Phys.* 83.1 (1998), pp. 228–238.

[71] W Pompe et al. "Elastic energy release due to domain formation in the strained epitaxy of ferroelectric and ferroelastic films". In: *J. Appl. Phys.* 74.10 (1993), pp. 6012–6019.

[72] A. H. G. Vlooswijk et al. "Smallest $90^0$ domains in epitaxial ferroelectric films". In: *Appl. Phys. Lett.* 91.11, 112901 (2007), p. 112901. DOI: http://dx.doi.org/10.1063/1.2783274. URL: http://scitation.aip.org/content/aip/journal/apl/91/11/10.1063/1.2783274.

[73] Ludwig Feigl et al. "Controlled stripes of ultrafine ferroelectric domains". In: *Nature communications* 5 (2014).

[74] Dillon D Fong et al. "Ferroelectricity in ultrathin perovskite films". In: *Science* 304.5677 (2004), pp. 1650–1653.

[75] Ramaroorthy Ramesh and Nicola A Spaldin. "Multiferroics: progress and prospects in thin films". In: *Nature materials* 6.1 (2007), pp. 21–29.

[76] Tuomas H. E. Lahtinen, Jussi O. Tuomi, and Sebastiaan van Dijken. "Pattern Transfer and Electric-Field-Induced Magnetic Domain Formation in Multiferroic Heterostructures". In: *Adv. Mater.* 23.28 (2011), pp. 3187–3191. ISSN: 1521-4095.

[77] Jan Seidel et al. "Conduction at domain walls in oxide multiferroics". In: *Nature Materials* 8.3 (2009), pp. 229–234.

[78] Tomas Sluka et al. "Free-electron gas at charged domain walls in insulating BaTiO3". In: *Nature communications* 4 (2013), p. 1808.

[79] Jill Guyonnet et al. "Conduction at domain walls in insulating Pb(Zr0. 2Ti0. 8) O3 thin films". In: *Advanced Materials* 23.45 (2011), pp. 5377–5382.

[80] SY Yang et al. "Above-bandgap voltages from ferroelectric photovoltaic devices". In: *Nature Nanotechnology* 5.2 (2010), pp. 143–147.

[81] Y Ivry et al. "Flux closure vortexlike domain structures in ferroelectric thin films". In: *Phys. Rev. Lett.* 104.20 (2010), p. 207602.

[82] Chun-Lin Jia et al. "Direct observation of continuous electric dipole rotation in flux-closure domains in ferroelectric Pb (Zr, Ti) O3". In: *Science* 331.6023 (2011), pp. 1420–1423.

[83] Yachin Ivry et al. "Unexpected Controllable Pair-Structure in Ferroelectric Nanodomains". In: *Nano letters* 11.11 (2011), pp. 4619–4625.

[84] Raymond GP McQuaid et al. "Exploring vertex interactions in ferroelectric flux-closure domains". In: *Nano letters* 14.8 (2014), pp. 4230–4237.

[85] Gustau Catalan et al. "Domain wall nanoelectronics". In: *Reviews of Modern Physics* 84.1 (2012), p. 119.

[86] G Le Rhun et al. "Increased ferroelastic domain mobility in ferroelectric thin films and its use in nano-patterned capacitors". In: *Nanotech.* 17.13 (2006), p. 3154.

[87] Wei Li and Marin Alexe. "Investigation on switching kinetics in epitaxial Pb(Zr0.2Ti0.8)O3 ferroelectric thin films: Role of the 90Âř domain walls". In: *Appl. Phys. Lett.* 91.26, 262903 (2007), p. 262903. DOI: http://dx.doi.org/10.1063/1.2825414. URL: http://scitation.aip.org/content/aip/journal/apl/91/26/10.1063/1.2825414.

[88] Zhengkun Ma et al. "Effect of $90^0$ domain movement on the piezoelectric response of patterned $Pb(Zr0.2Ti0.8)O_3/SrTiO_3$/Si heterostructures". In: *Appl. Phys. Lett.* 87.7 (2005), pp. 072907–072907.

[89] Lang Chen et al. “Formation of $90^0$ elastic domains during local 180ą switching in epitaxial ferroelectric thin films”. In: *Appl. Phys. Lett.* 84.2 (2004), pp. 254–256.

[90] Yachin Ivry et al. “90ą domain dynamics and relaxation in thin ferroelectric/ferroelastic films”. In: *Phys. Rev. B* 81.17 (2010), p. 174118.

[91] Yachin Ivry et al. “Nucleation, growth, and control of ferroelectric-ferroelastic domains in thin polycrystalline films”. In: *Phys. Rev. B* 86.20 (2012), p. 205428.

[92] Varatharajan Anbusathaiah et al. “Labile ferroelastic nanodomains in bilayered ferroelectric thin films”. In: *Adv. Mat.* 21.34 (2009), pp. 3497–3502.

[93] RGP McQuaid et al. “Mesoscale flux-closure domain formation in single-crystal BaTiO3”. In: *Nature Comm.* 2 (2011), p. 404.

[94] S. H. Baek et al. “Ferroelastic switching for nanoscale non-volatile magnetoelectric devices”. In: *Nature Mat.* 9.4 (2010), pp. 309–314.

[95] Nina Balke et al. “Deterministic control of ferroelastic switching in multiferroic materials”. In: *Nature Nano.* 4.12 (2009), pp. 868–875.

[96] Rajeev Ahluwalia et al. “Manipulating Ferroelectric Domains in Nanostructures Under Electron Beams”. In: *Phys. Rev. Lett.* 111.16 (2013), p. 165702.

[97] Ja Kyung Lee et al. “Direct observation of asymmetric domain wall motion in a ferroelectric capacitor”. In: *Acta Mater.* 61.18 (2013), pp. 6765–6777.

[98] L Feigl et al. “Compliant ferroelastic domains in epitaxial Pb (Zr, Ti) O3 thin films”. In: *Applied Physics Letters* 104.17 (2014), p. 172904.

[99] Asif Islam Khan et al. “Negative capacitance in a ferroelectric capacitor”. In: *Nature materials* 14.2 (2015), pp. 182–186.

[100] Alexei Gruverman, D Wu, and JF Scott. “Piezoresponse force microscopy studies of switching behavior of ferroelectric capacitors on a 100-ns time scale”. In: *Physical review letters* 100.9 (2008), p. 097601.

[101] JF Scott et al. “Switching kinetics of lead zirconate titanate submicron thin-film memories”. In: *Journal of applied physics* 64.2 (1988), pp. 787–792.

[102] LD Landau and IM Khalatnikov. “On the anomalous absorption of sound near a second-order phase transition point”. In: *Dokl. Akad. Nauk SSSR*. Vol. 96. 1954, pp. 469–472.

[103] AM Bratkovsky and AP Levanyuk. “Very large dielectric response of thin ferroelectric films with the dead layers”. In: *Physical Review B* 63.13 (2001), p. 132103.

[104] AM Bratkovsky and AP Levanyuk. “Depolarizing field and ÒrealÓ hysteresis loops in nanometer-scale ferroelectric films”. In: *Applied physics letters* 89.25 (2006), pp. 253108–253108.

[105] Giovanni A Salvatore, Alexandru Rusu, and Adrian M Ionescu. "Experimental confirmation of temperature dependent negative capacitance in ferroelectric field effect transistor". In: *Applied Physics Letters* 100.16 (2012), pp. 163504–163504.

[106] J Li et al. "Ultrafast polarization switching in thin-film ferroelectrics". In: *Applied physics letters* 84.7 (2004), pp. 1174–1176.

[107] PK Larsen et al. "Nanosecond switching of thin ferroelectric films". In: *Applied physics letters* 59.5 (1991), pp. 611–613.

[108] An Quan Jiang et al. "Subpicosecond domain switching in discrete regions of Pb (Zr0. 35Ti0. 65) O3 thick films". In: *Advanced Functional Materials* 22.10 (2012), pp. 2148–2153.

[109] Asif Khan et al. "Experimental evidence of ferroelectric negative capacitance in nanoscale heterostructures". In: *Applied Physics Letters* 99.11 (2011), pp. 113501–113501.

[110] Daniel JR Appleby et al. "Experimental observation of negative capacitance in ferroelectrics at room temperature". In: *Nano letters* 14.7 (2014), pp. 3864–3868.

[111] Th Tybell et al. "Domain Wall Creep in Epitaxial Ferroelectric P b (Z r 0.2 T i 0.8) O 3 Thin Films". In: *Physical review letters* 89.9 (2002), p. 097601.

[112] Alexei Grigoriev et al. "Nanosecond domain wall dynamics in ferroelectric Pb (Zr, Ti) O 3 thin films". In: *Physical review letters* 96.18 (2006), p. 187601.

[113] Asif Islam Khan et al. "Experimental evidence of ferroelectric negative capacitance in nanoscale heterostructures". In: *Applied Physics Letters* 99.11 (2011), p. 113501.

[114] H. W. Jang et al. "Ferroelectricity in Strain-Free $SrTiO_3$ Thin Films". In: *Phys. Rev. Lett.* 104 (19 2010), p. 197601. DOI: 10.1103/PhysRevLett.104.197601. URL: http://link.aps.org/doi/10.1103/PhysRevLett.104.197601.

[115] Matthew Dawber et al. "Tailoring the properties of artificially layered ferroelectric superlattices". In: *Advanced Materials* 19.23 (2007), pp. 4153–4159.

[116] Karin Maria Rabe, Charles H. Ahn, and Jean-Marc Triscone. *Physics of ferroelectrics: a modern perspective*. Vol. 105. Springer, 2007. (Visited on 11/24/2013).

[117] Asif I Khan et al. "Ferroelectric negative capacitance MOSFET: Capacitance tuning & antiferroelectric operation". In: *Electron Devices Meeting (IEDM), 2011 IEEE International*. IEEE. 2011, pp. 11–3.

[118] RA McKee, FJ Walker, and MF Chisholm. "Crystalline oxides on silicon: the first five monolayers". In: *Physical Review Letters* 81.14 (1998), p. 3014.

[119] A. Rusu et al. "Metal-Ferroelectric-Meta-Oxide-semiconductor field effect transistor with sub-60mV/decade subthreshold swing and internal voltage amplification". In: *Electron Devices Meeting (IEDM), 2010 IEEE International*. IEEE. 2010, pp. 16.3.1–16.3.4. DOI: 10.1109/IEDM.2010.5703374.

[120] Gustau Catalan, David Jiménez, and Alexei Gruverman. "Ferroelectrics: Negative capacitance detected". In: *Nature Materials* 14.2 (2015), pp. 137–139.

[121] TS Boscke et al. "Ferroelectricity in hafnium oxide thin films". In: *Applied Physics Letters* 99.10 (2011), pp. 102903–102903.

[122] Stefan Mueller et al. "Incipient Ferroelectricity in Al-Doped HfO2 Thin Films". In: *Advanced Functional Materials* 22.11 (2012), pp. 2412–2417.

[123] J Müller et al. "Ferroelectricity in yttrium-doped hafnium oxide". In: *Journal of Applied Physics* 110.11 (2011), p. 114113.

[124] Stefan Mueller et al. "Reliability characteristics of ferroelectric thin films for memory applications". In: *Device and Materials Reliability, IEEE Transactions on* 13.1 (2013), pp. 93–97.

[125] Johannes M§ller et al. "Ferroelectricity in simple binary ZrO2 and HfO2". In: *Nano letters* 12.8 (2012), pp. 4318–4323.

[126] Johannes Muller et al. "Nanosecond Polarization Switching and Long Retention in a Novel MFIS-FET Based on Ferroelectric". In: *Electron Device Letters, IEEE* 33.2 (2012), pp. 185–187.

[127] TS Böscke et al. "Phase transitions in ferroelectric silicon doped hafnium oxide". In: *Applied Physics Letters* 99.11 (2011), p. 112904.

[128] J Muller et al. "Ferroelectricity in HfO 2 enables nonvolatile data storage in 28 nm HKMG". In: *VLSI Technology (VLSIT), 2012 Symposium on*. IEEE. 2012, pp. 25–26.

[129] J Müller et al. "Ferroelectric Zr0. 5Hf0. 5O2 thin films for nonvolatile memory applications". In: *Applied Physics Letters* 99.11 (2011), p. 112901.

[130] S Mueller et al. "Ferroelectricity in Gd-doped HfO2 thin films". In: *ECS Journal of Solid State Science and Technology* 1.6 (2012), N123–N126.

[131] T Olsen et al. "Co-sputtering yttrium into hafnium oxide thin films to produce ferroelectric properties". In: *Applied Physics Letters* 101.8 (2012), p. 082905.

[132] Ekaterina Yurchuk et al. "HfO2-based Ferroelectric Field-Effect Transistors with 260 nm channel length and long data retention". In: *Memory Workshop (IMW), 2012 4th IEEE International*. IEEE. 2012, pp. 1–4.

[133] Dayu Zhou et al. "Insights into electrical characteristics of silicon doped hafnium oxide ferroelectric thin films". In: *Applied Physics Letters* 100.8 (2012), p. 082905.

[134] Dayu Zhou et al. "Wake-up effects in Si-doped hafnium oxide ferroelectric thin films". In: *Applied Physics Letters* 103.19 (2013), p. 192904.

[135] Min Hyuk Park et al. "Ferroelectricity and Antiferroelectricity of Doped Thin HfO2-Based Films". In: *Advanced Materials* 27.11 (2015), pp. 1811–1831.

[136] T Schenk et al. “Strontium doped hafnium oxide thin films: Wide process window for ferroelectric memories”. In: *Solid-State Device Research Conference (ESSDERC), 2013 Proceedings of the European*. IEEE. 2013, pp. 260–263.

[137] Min Hyuk Park et al. “Effect of forming gas annealing on the ferroelectric properties of Hf0. 5Zr0. 5O2 thin films with and without Pt electrodes”. In: *Applied Physics Letters* 102.11 (2013), p. 112914.

[138] Sergiu Clima et al. “Identification of the ferroelectric switching process and dopant-dependent switching properties in orthorhombic HfO2: A first principles insight”. In: *Applied Physics Letters* 104.9 (2014), p. 092906.

[139] Dominik Martin et al. “Ferroelectricity in Si-Doped HfO2 Revealed: A Binary Lead-Free Ferroelectric”. In: *Advanced Materials* 26.48 (2014), pp. 8198–8202.

[140] Stefan Mueller et al. “Performance investigation and optimization of Si: HfO 2 FeFETs on a 28 nm bulk technology”. In: *Applications of Ferroelectric and Workshop on the Piezoresponse Force Microscopy (ISAF/PFM), 2013 IEEE International Symposium on the*. IEEE. 2013, pp. 248–251.

[141] Charles Kittel. “Theory of antiferroelectric crystals”. In: *Physical Review* 82.5 (1951), p. 729.

[142] Kenkichi Okada. “Phenomenological theory of antiferroelectric transition. i. second-order transition”. In: *Journal of the Physical Society of Japan* 27.2 (1969), pp. 420–428.

[143] LE Cross. “Antiferroelectric-Ferroelectric Switching in a Simple ÒKittelÓ Antiferroelectric”. In: *Journal of the Physical Society of Japan* 23.1 (1967), pp. 77–82.

[144] James F Scott. “Switching of ferroelectrics without domains”. In: *Advanced Materials* 22.46 (2010), pp. 5315–5317.

[145] YL Li et al. “Phase-field model of domain structures in ferroelectric thin films”. In: *Appl. Phys. Lett.* 78.24 (2001), pp. 3878–3880.

[146] Long-Qing Chen. “Phase-field models for microstructure evolution”. In: *Annual review of materials research* 32.1 (2002), pp. 113–140.

[147] Young-Han Shin et al. “Nucleation and growth mechanism of ferroelectric domain-wall motion”. In: *Nature* 449.7164 (2007), pp. 881–884.